Searches for direct pair production of third generation squarks, and dark matter, in final states containing $b-$jets and $E_{\mathrm{T}}^{\mathrm{miss}}$ using the ATLAS detector at the LHC

UNIVERSITY OF LIVERPOOL

Thesis submitted in accordance with the requirements of
the University of Liverpool for the degree of Doctor in Philosophy
by

John Anders

Department of Physics,
Oliver Lodge Laboratory
University of Liverpool

September 2017

Abstract

This thesis documents the results of analyses performed searching for BSM processes in final states consisting of $b-$tagged jets and missing transverse energy ($E_{\mathrm{T}}^{\mathrm{miss}}$) using the ATLAS detector at the Large Hadron Collider.

The results of searches for the direct pair production of bottom squarks decaying via $\tilde{b} \rightarrow b + \tilde{\chi}_1^0$ are presented. The first search used 3.2 fb^{-1} of Run 2 data at a centre-of-mass energy ($\sqrt{s}$) of 13 TeV and placed exclusion limits on sbottom masses up to 840 GeV for massless neutralinos [1]. The updated search uses a total integrated luminosity of 36.1 fb^{-1} and provides sensitivity to heavier sbottom masses, excluding sbottom masses up to 950 GeV for $m_{\tilde{\chi}_1^0} = 1$ GeV.

Two searches for the pair production of third generation squarks decaying asymmetrically in the one-lepton 2-$b-$jets and $E_{\mathrm{T}}^{\mathrm{miss}}$ final state are presented. The Run 1 search, using an integrated luminosity of 20.3 fb^{-1} collected at $\sqrt{s} = 8$ TeV, placed exclusion limits in pMSSM scenarios with m_{Ql3} excluded between 340 and 680 GeV for $\mu = 110$ GeV. Exclusion limits are also placed in simplified model scenarios, where $m_{\tilde{t}}$ is excluded between 300 and 510 GeV for $m_{\tilde{\chi}_1^0}$ =110 GeV assuming $\Delta m(\tilde{\chi}_1^{\pm}, \tilde{\chi}_1^0) = 5$ GeV [2]. The Run 2 search, performed using 36.1 fb^{-1} collected at $\sqrt{s} = 13$ TeV, placed limits in simplified model scenarios, with sbottom masses up to 800 GeV excluded considering neutralinos of mass 110 GeV. A statistical combination of this analysis and the 36.1 fb^{-1} sbottom analysis extends this exclusion to 880 GeV for $m_{\tilde{\chi}_1^0} = 110$ GeV. The results of these analyses is scheduled to be published in Summer 2017.

Finally a search for direct dark matter production in association with $b-$jets, in the 0-lepton, 2 $b-$jets and $E_{\mathrm{T}}^{\mathrm{miss}}$ final state using 13.3 fb^{-1} of Run 2 ($\sqrt{s} = 13$ TeV) data is presented. Cross section upper limits are placed, in simplified model scenarios, on a range of scalar and pseudoscalar masses assuming a dark matter mass of 1 GeV [3].

Declaration

This thesis is the result of my own work, except where explicit reference is made to the work of others, and has not been submitted for another qualification to this, or any other, university. This thesis does not exceed the word limit for the respective Degree Committee.

John Anders

Acknowledgements

Before I start writing a large list of people to thank, I'll start by apologising for missing anybody out. The number of people who have either contributed to the work shown in this thesis; or have provided welcome distraction from work, is quite large and adding everyone in would probably push this document to beyond 300 pages.

Firstly many thanks to my family, especially my parents and sister, primarily for putting up with me over the holiday periods where I was supposedly taking time off, but spent most of it working. Also a huge thank you to the many friends who have provided support throughout the last four years, including but not limited to Danny, Mike, Alex, Rosie, Fionn, Jenna, Flanagan, Coops and Mike. Obviously the largest thank you in this category goes to Sarah, who had to live with me while writing up, generally looked after me, and was very forgiving about me leaving the country to be in Geneva, causing me to miss most of the important dates in our relationship... sorry about that.

Moving onto the physicists. A huge thank you to Carl for programming assistance and moral support; and to Steve and Ellis for the interesting coffee conversations. Thank you to the Liverpool ATLAS group for continued assistance throughout my PhD. Additional thanks to Jan for proofreading my thesis. Thanks also must go to everyone from the Liverpool HEP group who attempted to lift the bubble chamber shield, contributing to our Netherlands-esque run of losing three consecutive finals. Special thanks to the 16/17 squad who finally ended our cup final hoodoo, allowing me to retire from the competition on top. Special thank you to Calum for being good company throughout all of the analyses that we ended up working on together, and thanks to the whole of the sbottom analysis group. At this point I have to especially thank Kãrlis, who after living with me in our first year, then spending a year with me in Geneva, and finally spending countless weekends working 7-days a week next to me in office whilst writing up, must be sick of the sight of me and very thankful that I've finally left.

And finally, the largest thanks must go to my supervisor Monica who, throughout working with me, has dealt with my general stupidity, the plethora of coding errors, the time it was so hot in Geneva that I couldn't function properly, and more recently my slight "mocking" of her programming skills. Without her excellent supervision the work contained within would not have been possible, and I would be (to quote her) "stuck selling flowers at the side of the road".

Contents

List of Figures

List of Tables

Chapter 1

Introduction

The Standard Model (SM) of particle physics has proven to be a robust framework to describe the natural world. It has been placed under more and more scrutiny during the years of data-taking by the experiments at the Large Hadron Collider (LHC) but, as of yet, remains the most complete picture of nature that we possess. This is not to say that the theory is without fault, as it does not explain everything that we see in nature. Significant effort is made to investigate Beyond the Standard Model (BSM) physics, seeking to further our understanding of the universe. Searches for evidence of Supersymmetry (SUSY) or other BSM physics plays a significant part in the research programs for the two general purpose detectors, ATLAS and CMS, at the LHC.

This thesis[1] proceeds as follows. The first chapter introduces the SM, building from the electromagnetic Lagrangian, through to the Higgs mechanism and electroweak symmetry breaking. Problems with the SM are discussed, and the theory of SUSY is discussed as a possible extension of the SM. Additionally a generic dark matter production model, as searched for at the LHC, is introduced.

This is followed by a brief introduction of the LHC complex, and a more in-depth overview of the ATLAS (A Toroidal LHC ApparatuS) detector. This chapter culminates in a review of the author's work developing an application for the online recovery of Semiconductor Tracker (SCT) modules.

A chapter introducing the requirements taken into account when modelling physical processes follows, including the considerations made when building a Monte Carlo generator. This chapter also contains the author's work investigating: the interference effects

[1] For the purposes of this thesis the convention $\hbar = c = 1$ is used throughout.

between the single-top and $t\bar{t}$ processes; and producing a parameterisation to estimate the modelling uncertainties associated with the V+jets ($V = W/Z$) processes.

Subsequently the physics objects used in the analyses are presented, with the differences between the Run 1 and Run 2 definitions noted. This chapter also contains a comprehensive overview of the kinematic variables used in the analyses.

Three analysis chapters follow from the above, each containing the results of searches for BSM physics. In all cases, the author has contributed to the analyses covering a variety of aspects which include the definition of the event selection optimised to maximise signal over SM background yields, the estimate of the SM background using partially data-driven techniques, the estimate of the systematic uncertainties and the statistical interpretations of the results. The most relevant contributions concerning the above topics are reported.

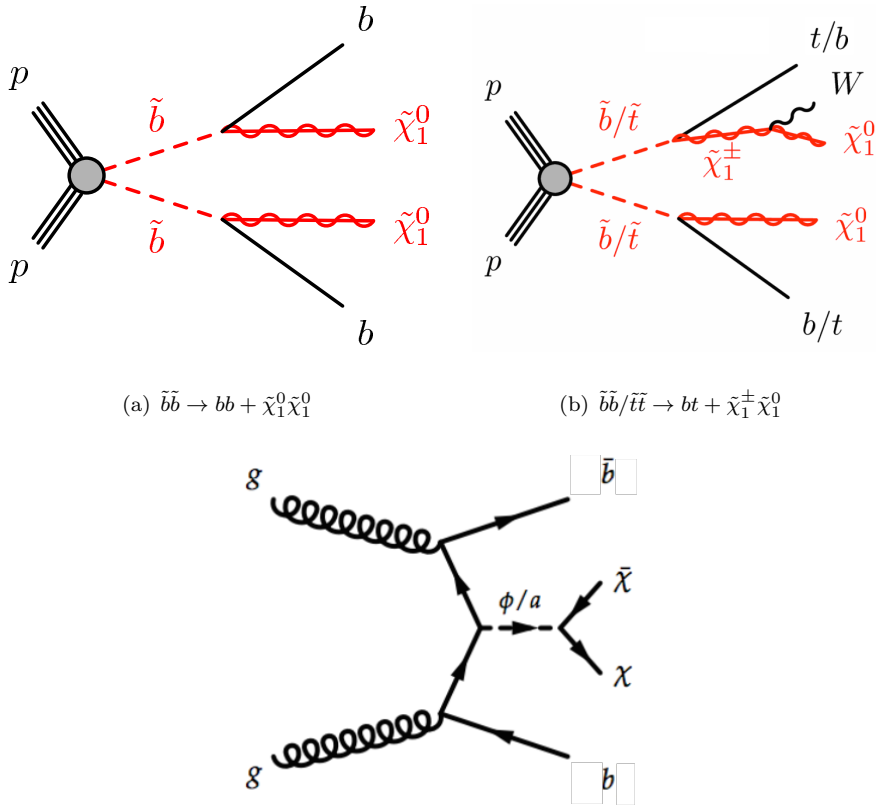

(a) $\tilde{b}\tilde{b} \to b\bar{b} + \tilde{\chi}_1^0\tilde{\chi}_1^0$

(b) $\tilde{b}\tilde{b}/\tilde{t}\tilde{t} \to bt + \tilde{\chi}_1^{\pm}\tilde{\chi}_1^0$

(c) Direct DM production

FIGURE 1.1: Diagrams of the BSM processes investigated within this thesis. (a) Direct sbottom pair production: $\tilde{b}\tilde{b} \to b\bar{b} + \tilde{\chi}_1^0\tilde{\chi}_1^0$ (Chapter 6). (b) Direct sbottom/stop pair production decaying asymmetrically via $\tilde{b}\tilde{b}/\tilde{t}\tilde{t} \to bt + \tilde{\chi}_1^{\pm}\tilde{\chi}_1^0$ (Chapter 7). (c) Direct production of dark matter, (Chapter 8).

The first analysis chapter contains the results of the Run 2 searches for direct sbottom

pair production, as seen in Figure 1.1(a), in the 0-lepton, 2-$b-$jets and $E_{\mathrm{T}}^{\mathrm{miss}}$ final state. The first of these searches was performed using the $3.2\,\mathrm{fb}^{-1}$ of luminosity collected during 2015. The second search is an improvement and an update of the previous analysis using the full 2015 and 2016 dataset with a total luminosity of $36.1\,\mathrm{fb}^{-1}$.

The second analysis chapter documents two searches performed to target more complex signal models where more than one decay mode is kinematically allowed. Such scenarios, referred to as asymmetric (or "mixed") scenarios, arise from either bottom or top squark pair production and this is shown in Figure 1.1(b). These searches were performed in the one-lepton, two-$b-$jet and $E_{\mathrm{T}}^{\mathrm{miss}}$ final state. The first of the analyses presented uses the Run 1 dataset comprising a total luminosity of $20.1\,\mathrm{fb}^{-1}$ at a centre of mass energy $\sqrt{s} = 8\,\mathrm{TeV}$. The author has led the update of this analysis using the 2015+2016 Run 2 dataset, building on the Run 1 analysis and targeting similar models at a higher centre of mass energy, $\sqrt{s} = 13\,\mathrm{TeV}$.

The final analysis chapter presents a search performed using the Run 2 data investigating direct dark matter production in association with $b-$jets. The final state investigated contains 0-leptons, 2-$b-$jets and $E_{\mathrm{T}}^{\mathrm{miss}}$. The full 2015 dataset ($3.2\,\mathrm{fb}^{-1}$) and a partial 2016 dataset ($11.1\,\mathrm{fb}^{-1}$) is used resulting in a total luminosity of $13.3\,\mathrm{fb}^{-1}$.

The presented analyses using the full Run 1 and partial Run 2 datasets have been published in Ref. [2], Ref. [1] and Ref [3]. The analyses using the full Run 2 dataset are in the final stages of approval within the ATLAS collaboration.

Chapter 2

Theoretical Overview

In this chapter an overview of the building blocks of the Standard Model of particle physics is discussed. This includes an overview of the Lagrangians for quantum electrodynamics and quantum chromodynamics and finally the Lagrangian for the electroweak force. An overview of the Higgs mechanism and spontaneous symmetry breaking is provided, resulting in the full formalism of the Standard Model. Shortfalls in the Standard Model and unanswered questions, such as the Higgs hierarchy problem and the nature of dark matter, are discussed, before introducing supersymmetry as a possible solution to these questions.

2.1 Fundamental Particles

The Standard Model (SM) is a theory of interactions between the fermionic particles and three of the four fundamental forces: electromagnetism (EM); the strong force; and the weak force. The SM also implies the existence of the Higgs boson which is required to generate the masses of the weak vector bosons. An overview of the particles as described by the SM is presented in Table 2.1.

The forces present in the SM arise due to symmetries relating the quantum numbers of particles and the conservation of these quantum numbers dictated by Noether's theorem. For example, the discovery of baryons composed of three of the same type of fermion (for example the Δ^{++} baryon consisting of three up-type quarks) requires the introduction of a new quantum number (referred to as colour), in order for the state to satisfy the Pauli exclusion principle. The introduction of the colour charge implied a symmetry, leading to the description of strong force.

Fermions					
Generation	Name	Label	Spin	Charge [e]	Mass
I	Up-quark	u	1/2	+2/3	2.2 MeV
	Down-quark	d	1/2	-1/3	4.7 MeV
	Electron	e	1/2	-1	0.511 MeV
	Electron-neutrino	ν_e	1/2	0	< 2 eV
II	Charm-quark	c	1/2	+2/3	1.27 GeV
	Strange-quark	s	1/2	-1/3	96 MeV
	Muon	μ	1/2	-1	105 MeV
	Muon neutrino	ν_μ	1/2	0	< 2 eV
III	Top-quark	t	1/2	+2/3	174.2 GeV
	Bottom-quark	b	1/2	-1/3	4.18 GeV
	Tau	τ	1/2	-1	1.78 GeV
	Tau-neutrino	ν_τ	1/2	0	< 2 eV
Bosons					
Force	Name	Label	Spin	Charge [e]	Mass
Electromagnetic	Photon	γ	1	0	0
strong	Gluon	g	1	0	0
weak	W-boson	$W^\pm$	1	± 1	80.4 GeV
weak	Z-boson	Z^0	1	0	91.2 GeV
–	Higgs Boson	h	0	0	125.1 GeV

TABLE 2.1: An overview of the particles described by the SM. Particle masses taken from [5].

Fermions are the constituents of matter, and have intrinsic spin, s, of 1/2. Everyday matter such as protons, neutrons and atomic nuclei are composed of the lightest fermions, referred to as the first generation fermions. The heavier fermions of the second and third generations are produced predominantly in high energy particle collisions. Fermions can be further categorised into particles that can interact via the strong force, known as quarks, and particles that do not interact via the strong force, known as leptons.

The quarks themselves can be categorised into up-type quarks (u, c, t) which have electromagnetic charge $+2/3$, and down-type quarks (d, s, b) which have charge $-1/3$. Quarks also carry the colour charge and exist in a colour triplet, enabling interactions via the strong force. The left-handed up- and down-type quarks can interact via the weak force, as they form part of a weak isospin doublet. All quarks, except the top-quark, undergo hadronisation after a period of time resulting in baryons or mesons. As the

top-quark is much more massive than the other quarks, with a lifetime $\tau_t \approx 0.5 \times 10^{24}$ s, it decays via the weak force before it can hadronise.

Similarly to the up- and down-type quarks, the left-handed leptons also form isospin doublets under the weak force. The charged leptons (e, μ, τ) have electromagnetic charge -1, whereas the neutrinos (ν_e, ν_μ, ν_τ,) are chargeless.

The vector bosons (γ, g, $W^\pm$, Z^0) are force mediators and have intrinsic spin of 1. In the SM, the vector bosons are exchange particles, for example two particles interacting via the electromagnetic force will exchange a photon. The concept of gauge invariance suggests that all force mediators should be massless, as is the case for the photon and gluon. This is not the case for the W and Z bosons which have mass, but are not allowed to have Dirac mass terms in the Lagrangian. The Higgs mechanism is required to generate the W and Z masses. The Higgs boson is the only known fundamental scalar ($s = 0$) and unlike the other bosons in the SM, the Higgs boson is not associated directly with one of the fundamental forces. Instead, the Higgs is an excitation of the Higgs field. The Higgs field permeates through the universe and interacts (via the Higgs boson) with particles to provide mass to the massive particles, allowing the W and Z bosons to have mass terms and also obey gauge invariance.

As alluded to above, the main guiding principle in the construction of the SM is the concept of gauge invariance. The interactions described by the SM arise due to the requirement that the forces are locally gauge invariant. Local gauge invariance implies that the interactions are invariant under local gauge transformations. The SM is built by applying local gauge invariance to the three forces, and in doing so the interactions between the fermions and the bosons arise naturally. The SM can be written in shorthand as $\mathrm{SU(3)_C} \times \mathrm{SU(2)_L} \times \mathrm{U(1)_Y}$, with each component corresponding to the symmetry group which generates the interactions (eg $\mathrm{SU(3)_C}$ corresponding to colour, $\mathrm{SU(2)_L}$ corresponding to weak-isospin and $\mathrm{U(1)_Y}$ corresponding to the hypercharge).

The derivations of quantum electrodynamics (QED), quantum chromodynamics (QCD) and electroweak (EW) unification closely follow Ref. [6]. As an initial step in building the SM Lagrangian it is intuitive to begin with the simplest interactions described by the SM: QED.

2.2 Quantum Electrodynamics

The Lagrangian for QED can be formed by starting with the Dirac Lagrangian and applying local gauge invariance. It is easily recognised that under a global phase transformation (α) of the wavefunction, ψ, of the form $\psi(x) \rightarrow \psi'(x) = e^{i\alpha}\psi(x)$, Equation 2.1, which contains the Dirac mass term m, is invariant.

$$\mathcal{L}_{Dirac} = i\bar{\psi}\gamma^{\mu}\partial_{\mu}\psi - m\bar{\psi}\psi. \tag{2.1}$$

However under a local phase transformation of the form $\psi(x) \rightarrow \psi'(x) = e^{i\alpha(x)}\psi(x)$ this is not the case, as can be seen in Equation 2.2.

$$\begin{aligned}
\mathcal{L}_{Dirac} \rightarrow \mathcal{L}'_{Dirac} &= i\bar{\psi}'\gamma^{\mu}\partial_{\mu}\psi' - m\bar{\psi}'\psi' \\
&= i\bar{\psi}e^{-i\alpha(x)}\gamma^{\mu}\partial_{\mu}[e^{i\alpha(x)}\psi] - m\bar{\psi}e^{-i\alpha(x)}e^{i\alpha(x)}\psi \\
&= i\bar{\psi}e^{-i\alpha(x)}\gamma^{\mu}(e^{i\alpha(x)}\partial_{\mu}\psi + ie^{i\alpha(x)}\psi\partial_{\mu}[\alpha(x)]) - m\bar{\psi}\psi \\
&= i\bar{\psi}\gamma^{\mu}\partial_{\mu}\psi - m\bar{\psi}\psi + \bar{\psi}\gamma^{\mu}\psi\partial_{\mu}[\alpha(x)].
\end{aligned} \tag{2.2}$$

In order to construct a locally gauge invariant Dirac Lagrangian, the derivative of the wavefunction must transform in the same manner as the wavefunction itself, $D_{\mu}\psi(x) \rightarrow D'_{\mu}\psi'(x) = e^{i\alpha(x)}D_{\mu}\psi(x)$. To do this, the covariant derivative D_{μ} is defined as:

$$D_{\mu} = \partial_{\mu} + ieA_{\mu}. \tag{2.3}$$

The gauge field (A_{μ}) is introduced, which transforms as:

$$A_{\mu} \rightarrow A'_{\mu} = A_{\mu} - \frac{1}{e}\partial_{\mu}\alpha(x). \tag{2.4}$$

The Dirac Lagrangian can then be rewritten with the covariant derivative, which introduces the A_{μ} term into the Lagrangian, corresponding to the photon, or in a more generic case, the mediator of the force. The associated kinetic energy term is given by:

$$F_{\mu\nu} = ie([\partial_{\mu}A_{\nu}] - [\partial_{\nu}A_{\mu}]). \tag{2.5}$$

By introducing the covariant derivative into the Lagrangian, it can be shown that the Lagrangian is now invariant under local gauge transformation:

$$\begin{aligned}
\mathcal{L}_{Dirac} \rightarrow \mathcal{L}'_{Dirac} &= i\bar{\psi}'\gamma^\mu D'_\mu \psi' - m\bar{\psi}'\psi' \\
&= i\bar{\psi}e^{-i\alpha(x)}\gamma^\mu(\partial_\mu + ieA_\mu - i\partial_\mu\alpha(x))[e^{i\alpha(x)}\psi] - m\bar{\psi}e^{-i\alpha(x)}e^{i\alpha(x)}\psi \\
&= i\bar{\psi}e^{-i\alpha(x)}\gamma^\mu(e^{i\alpha(x)}\partial_\mu\psi + ieA_\mu e^{i\alpha(x)}\psi \\
&- ie^{i\alpha(x)}\psi\partial_\mu[\alpha(x)] + ie^{i\alpha(x)}\psi\partial_\mu[\alpha(x)]) - m\bar{\psi}\psi \\
&= i\bar{\psi}\gamma^\mu D_\mu\psi - m\bar{\psi}\psi.
\end{aligned} \tag{2.6}$$

A complete Lagrangian for QED can now be obtained by adding in the kinetic energy term $-\frac{1}{4}F_{\mu\nu}F^{\mu\nu}$:

$$\mathcal{L}_{EM} = -\frac{1}{4}F_{\mu\nu}F^{\mu\nu} + i\bar{\psi}\not{D}\psi - m\bar{\psi}\psi. \tag{2.7}$$

It is seen that by forcing the Lagrangian to be locally gauge invariant and hence introducing the covariant derivative, interactions between the force (A_μ) and the matter fields (ψ) arise naturally.

It is at this stage that it is useful to investigate a scenario where a Dirac mass term is introduced into the Lagrangian for the mediator. For brevity, only the transformation of the Dirac mass term is considered, as the invariance of the terms in the above Lagrangian has already been demonstrated:

$$\begin{aligned}
\mathcal{L} &= m^2 A_\mu A^\mu \\
\mathcal{L} \rightarrow \mathcal{L}' &= m^2 A'_\mu A'^\mu \\
&= m^2(A_\mu - \frac{1}{e}\partial_\mu\alpha(x))(A^\mu - \frac{1}{e}\partial^\mu\alpha(x)) \\
&\neq m^2 A_\mu A^\mu.
\end{aligned} \tag{2.8}$$

It is seen that the introduction of a direct Dirac mass term into the Lagrangian is not locally gauge invariant. Another important aspect characterising the QED Lagrangian, is the commutation relation between the covariant derivatives taken at two different gauges:

$$\begin{aligned}
[D_\mu, D_\nu] &= (\partial_\mu + ieA_\mu)(\partial_\nu + ieA_\nu) - (\partial_\nu + ieA_\nu)(\partial_\mu + ieA_\mu) \\
&= [\partial_\mu, \partial_\nu] + ie([\partial_\mu, A_\nu] - [\partial_\nu, A_\mu]) \\
&= ieF_{\mu\nu}.
\end{aligned} \tag{2.9}$$

Due to the abelian nature of QED, it can be seen that the commutator reduces to the classical EM result.

2.3 Quantum Chromodynamics

The Lagrangian for quantum chromodynamics (QCD) can be built in a similar manner to the QED Lagrangian, using the concept of gauge invariance. However further experimentally verified considerations must also be taken into account:

- quarks are the constituents of hadrons;
- quarks are fermions which can interact via the colour charge;
- the colour charge obeys an SU(3) symmetry;
- the colour interaction is mediated by the gluon, which does not interact via any other force.

Requiring the colour charge to obey an SU(3) symmetry suggests that a QCD Lagrangian can be constructed based upon non-Abelian SU(3) Yang-Mills theory [7]. This requires that the fermion wavefunctions (Dirac spinors) are written as 3-vectors consisting of the three colours ψ_f:

$$\psi_f = \begin{pmatrix} \psi_r \\ \psi_g \\ \psi_b \end{pmatrix}, \bar{\psi^f} = (\bar{\psi^r}, \bar{\psi^g}, \bar{\psi^b}). \tag{2.10}$$

Following from the above, a QCD Lagrangian can be constructed of the form:

$$\mathcal{L}_{\text{QCD}} = -\frac{1}{4} F^a_{\mu\nu} F^{\mu\nu}_a + \sum_f \bar{\psi}^f_i (i\not{D}_{ij} - m_f \delta_{ij}) \psi^f_j. \tag{2.11}$$

The QCD Lagrangian is summed over the quark flavours (f) and the colour charges (a). The covariant derivative and field strength tensor for QCD are also slightly different with respect to QED:

$$D^\mu_{ij} \equiv \partial^\mu \delta_{ij} + i g_s t^a_{ij} A^\mu_a. \tag{2.12}$$

$$F^a_{\mu\nu} \equiv \partial_\mu A^a_\nu - \partial_\nu A^a_\mu - g_s f_{abc} A^b_\mu A^c_\nu. \tag{2.13}$$

The gauge coupling (g_s) term present in both Equations 2.12 and 2.13 is similar to the charge in QED and regulates the strength of the interaction. The covariant derivative contains the three colour matrices (t^a_{ij}) which are the generators of the SU(3) group. The definition of the field tensor contains terms proportional to the coupling, which correspond to a self-interaction between the mediators of the field. Further to this, these terms contain the structure constants of the SU(3) algebra (f_{abc}), which are defined via the commutation relations:

$$[t_a, t_b] = i f_{abc} t_c. \tag{2.14}$$

A very important property of QCD is that the gauge coupling, is dependent upon the momentum transfer of a process (Q^2):

$$g_s^2(Q^2) = \frac{4\pi}{\beta_0 \ln(\frac{Q^2}{\Lambda^2_{\mathrm{QCD}}})}, \tag{2.15}$$

known as a running coupling ($\alpha_s = g_s^2/4\pi$), this relationship is shown in Equation 2.15. This leads to two important physical observations, asymptotic freedom and confinement.

In the asymptotic limit at high energies ($Q^2 \to \infty$), it can be seen from Equation 2.15 and Figure 2.1 that the strong coupling tends to 0. It is in this regime that QCD calculations are performed as quarks and gluons can be treated as quasi-free particles. The range where the assumption that quarks and gluons are free is known as perturbative QCD (pQCD). For physics at the LHC, α_S is evaluated at the characteristic scale of the interaction being considered, for example, for Z^0 boson production α_S is evaluated at the Z-mass with a value of 0.118. Contrastingly, at low energies ($Q^2 \to \Lambda^2_{\mathrm{QCD}}$) the strong coupling tends to infinity. Λ_{QCD} is known as the hadronisation scale and is usually taken to be around the pion mass ($\approx$200 MeV). A consequence of this behaviour is that only colourless states are observed in nature, as at low energies coloured states hadronise. The physical representation of this is that bare quarks and gluons are not observed directly in particle detectors. Instead they are observed as a flow of hadrons, known as a jet.

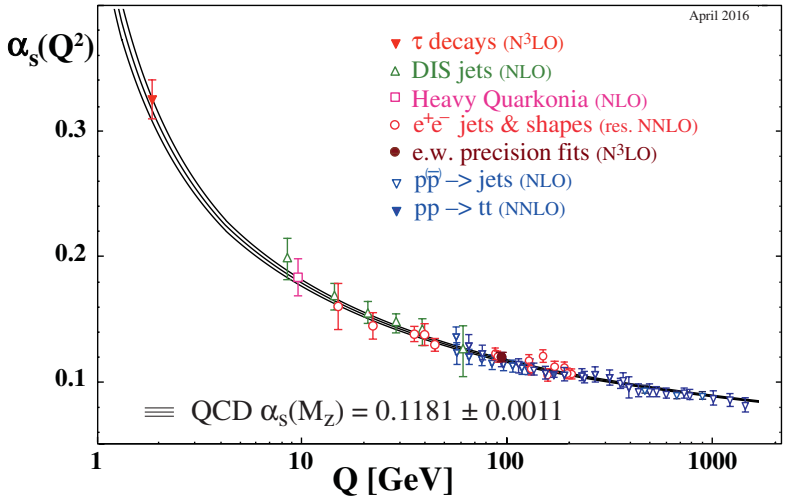

FIGURE 2.1: Theoretical expectation and experimental measurements of the strong coupling constant (α_s) as a function of the momentum transfer of a process (Q^2). Taken from [5].

The modelling of proton-proton collisions requires additional information due to the energy dependence of the strong coupling and the substructure of the proton. Aspects involved in the modelling of proton-proton collisions are discussed in Section 4.

2.4 Electroweak Unification

The weak force can be constructed in a similar manner to QCD, via a non-Abelian Yang-Mills SU(2) theory, modelling the interactions between the left-handed fermions. The electromagnetic and weak interactions are themselves manifestations of the Electroweak (EW) force. When unifying the electromagnetic and weak forces into a single interaction described by a Yang-Mills theory [8, 9, 10], the symmetry group is $\mathrm{SU(2)_L} \times \mathrm{U(1)_Y}$, corresponding to the $\mathrm{SU(2)_L}$ group of the weak force and the $\mathrm{U(1)_Y}$ group which is similar to electromagnetism, however now the force acts upon the hypercharge ($Y = 2(Q - T_3)$, where T_3 is the third component of weak isospin), with the coupling g_Y. As such, the mediator of this force is no longer the photon, and instead the mediator is represented by B_μ. The EW Lagrangian can be written in the form:

$$\mathcal{L}_{EW} = -\frac{1}{4} W^i_{\mu\nu} W^{\mu\nu}_i - \frac{1}{4} B_{\mu\nu} B^{\mu\nu} + \bar{\psi}(i\not{D} - m)\psi. \tag{2.16}$$

It differs from the EM Lagrangian as there are now multiple field terms: $W^i_{\mu\nu}$ which corresponds to $\mathrm{SU}(2)_L$, the group of the weak isospin interaction interacting with only the left-handed fermions; and $B_{\mu\nu}$, the field corresponding to the U(1) hypercharge. The corresponding covariant derivative and kinetic terms are:

$$D_\mu \equiv \partial_\mu + \frac{ig_{\mathrm{W}}}{2}\vec{\tau}.\vec{W}_\mu + ig_{\mathrm{Y}}\frac{Y}{2}B_\mu, \tag{2.17}$$

$$W^i_{\mu\nu} = \partial^\mu W^i_\nu - \partial^\nu W^i_\mu - g_{\mathrm{W}}\epsilon^{ijk}W^j_\mu W^k_\nu. \tag{2.18}$$

The $B_{\mu\nu}$ term is of the same form as $F_{\mu\nu}$ in Equation 2.9. The field tensor term for the weak force follows a similar structure to that of QCD, requiring the summation over the three SU(2) gauge fields and also includes a self-interaction term proportional to the coupling (g_{W}). The self-interaction term again arises due to the non-Abelian nature of the SU(2) group, and this term also contains the structure constants of the group (ϵ^{ijk}). The covariant derivative is also similar to QCD, containing the three generators of the group ($\vec{\tau}$).

An important aspect to note is that the weak components of the Lagrangian act only on the left-handed isospin doublets (Equation 2.19) of the Standard Model, whereas the hypercharge components act on both the left- and right-handed components. The right-handed components are singlets under the $\mathrm{SU}(2)_L$ symmetry:

$$\psi_{\mathrm{Left}} = \begin{pmatrix} e^-_L \\ \nu^e_L \end{pmatrix}, \begin{pmatrix} \mu^-_L \\ \nu^\mu_L \end{pmatrix}, \begin{pmatrix} \tau^-_L \\ \nu^\tau_L \end{pmatrix}, \begin{pmatrix} d_L \\ u_L \end{pmatrix}, \begin{pmatrix} s_L \\ c_L \end{pmatrix}, \begin{pmatrix} b_L \\ t_L \end{pmatrix} \tag{2.19}$$

$$\psi_{\mathrm{Right}} = e_R, \mu_R, \tau_R, d_R, u_R, s_R, c_R, b_R, t_R. \tag{2.20}$$

The direct inclusion of a Dirac mass term for the B_μ and $W^{0,1,2}_\mu$ fields is irreconcilable with local gauge invariance. However, the physically observed photon and weak vector bosons are the mass eigenstates of the W_μ and B_μ fields. It is this incompatibility which requires the introduction of another method to produce massive gauge bosons, known as the Higgs mechanism.

Before introducing the Higgs mechanism, it is possible to foreshadow the relationships between the mediator states used in the Lagrangian, and the physical states, shown in Equation 2.21. The photon and Z-boson are related to the W^3_μ and B_μ states by the weak mixing angle (θ_W):

$$\begin{aligned} W^{\pm} &= 1/\sqrt{2}(W_{\mu}^{1} \pm iW_{\mu}^{2}), \\ \gamma &= W_{\mu}^{3}\sin\theta_W + B_{\mu}\cos\theta_W, \\ Z^0 &= W_{\mu}^{3}\cos\theta_W + B_{\mu}\sin\theta_W. \end{aligned} \tag{2.21}$$

The W-bosons are charged ($Q = \pm 1$) and the Z^0 and γ are neutral.

2.5 The Higgs Mechanism

Local gauge invariance was integral in the construction of the Lagrangians that have been considered in earlier sections. It can be shown that by adding a Dirac mass term to either the QCD or EW Lagrangians the princple of local gauge invariance is broken. For QED and QCD this is not a problem, as the respective vector bosons for these forces are massless. However, for the massive electroweak bosons this poses a problem. As the concept of local gauge invariance is well founded, with the experimentally verified predictions of QED and QCD, it is desirable to propose an alternative mechanism to generate the $W^{\pm}$ and Z^0 masses conserving the principle of local gauge invariance. The Higgs mechanism [11, 12, 13] was originally formulated in 1964 and is explained in the following.

2.5.1 Spontaneous Symmetry Breaking

Consider a Klein-Gordon Lagrangian for a scalar field with a modified mass term, μ, and a field self-interaction term λ:

$$\mathcal{L}_H = \frac{1}{2}\partial_\mu\phi\partial^\mu\phi + \frac{1}{2}\mu^2\phi^2 - \frac{1}{4}\lambda^2\phi^4. \tag{2.22}$$

When compared to the unmodified Klein-Gordon Lagrangian, it is seen that this modified Lagrangian has an unphysical (complex) mass term. Comparing Equation 2.22 to a generic Lagrangian of the form $\mathcal{L} = \mathcal{T} - \mathcal{U}$, $\mathcal{T}$ corresponds to the kinetic energy term ($\frac{1}{2}\partial_\mu\partial^\mu$), and the potential term ($\mathcal{U}$) can be written as:

$$\mathcal{U}(\phi) = -\frac{1}{2}\mu^2\phi^2 + \frac{1}{4}\lambda^2\phi^4, \tag{2.23}$$

which can be graphically represented as shown in Figure 2.2.

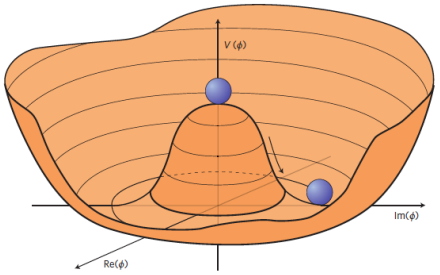

FIGURE 2.2: Graphical representation of the Higgs potential. Taken from [14].

The ground state of this potential is then found by expanding around the minima. Considering a one-dimensional case there are three possible values where $\frac{\partial \mathcal{U}}{\partial \phi} = 0$: $\phi = 0$; and $\phi = \pm\frac{\mu}{\lambda}$. By inspection of this potential it can be seen that $\phi = 0$ corresponds to a maxima, whilst $\phi = \pm\frac{\mu}{\lambda}$ correspond to two minima. It is now possible to rewrite the Lagrangian for this field in terms of a new variable η:

$$\eta = \phi \pm \frac{\mu}{\lambda} \tag{2.24}$$

The rewritten Lagrangian takes the form:

$$\mathcal{L}_H = \frac{1}{2}\partial_\mu \eta \partial^\mu \eta + \frac{1}{2}\mu^2\eta^2 \pm \mu\lambda\eta^3 - \frac{\lambda^2\eta^4}{4} - \frac{\mu^4}{4\lambda^2}. \tag{2.25}$$

The Lagrangian now contains a mass term ($\frac{1}{2}\mu^2\eta^2$) with the correct sign, corresponding to a field with a boson of mass $m = \sqrt{2\mu}$. The higher order terms in η are the field self-coupling terms corresponding to triple and quartic couplings.

Upon comparing Equation 2.25 to Equation 2.22, the rewritten Lagrangian is no longer invariant under the transformation $\eta \to -\eta$. The symmetry of the Lagrangian has been broken by the act of chosing to work with one of the ground (or vacuum) states. This is known as spontaneous symmetry breaking.

2.5.2 Spontaneous Symmetry Breaking of the SU(2) group

Extending the scalar singlet in the previous example to a complex scalar SU(2) doublet, will lead to the spontaneous symmetry breaking of the SU(2) group, and eventually a method for the generation of the W and Z boson masses. The required form of the complex scalar doublet is:

$$\phi = \begin{pmatrix} \phi_a \\ \phi_b \end{pmatrix} = \begin{pmatrix} \phi_1 + i\phi_2 \\ \phi_3 + i\phi_4 \end{pmatrix}, \tag{2.26}$$

leading to a Lagrangian for this field of the form:

$$\mathcal{L}_H = \frac{1}{2}(\partial_\mu \phi)^\dagger (\partial^\mu \phi) + \frac{1}{2}\mu^2(\phi^\dagger \phi) - \frac{1}{4}\lambda^2(\phi^\dagger \phi)^2. \tag{2.27}$$

Requiring the above Lagrangian to be invariant under local SU(2) transformations implies the introduction of the covariant derivative and field terms defined in Equations 2.17 and 2.18 respectively. The Lagrangian now becomes:

$$\begin{aligned} \mathcal{L}_H = \frac{1}{2}[(\partial_\mu + \frac{ig_{\mathrm{W}}}{2}\vec{\tau}.\vec{W}_\mu + ig_{\mathrm{Y}}\frac{Y}{2}B_\mu)\phi]^\dagger[(\partial^\mu + \frac{ig_{\mathrm{W}}}{2}\vec{\tau}.\vec{W}^\mu + ig_{\mathrm{Y}}\frac{Y}{2}B^\mu)\phi] \\ + \frac{1}{2}\mu^2(\phi^\dagger\phi) - \frac{1}{4}\lambda^2(\phi^\dagger\phi)^2 - \frac{1}{4}W_{\mu\nu}W^{\mu\nu} - \frac{1}{4}B_{\mu\nu}B^{\mu\nu}. \end{aligned} \tag{2.28}$$

Using the same approach introduced in the previous section, it is found that the potential is minimised when $\phi^\dagger\phi = -\mu^2/\lambda^2$. A gauge is chosen, such that $\phi_1 = \phi_2 = \phi_4 = 0$, with $\phi_3 = -\mu^2/\lambda^2 \equiv v^2$, where v is known as the vacuum expectation value (VEV). For this particular gauge, when expanded around the minima, Equation 2.26 becomes:

$$\phi_0 = \begin{pmatrix} 0 \\ v \end{pmatrix} = \begin{pmatrix} 0 \\ v + h(x) \end{pmatrix}. \tag{2.29}$$

By substituting the above minimised field term into Equation 2.28 and expanding the terms in a similar manner to Equation 2.25, it is found that the equation contains a mass term for the $\phi-$field, corresponding to a scalar boson with $m_h = \sqrt{2\lambda v^2}$.

2.5.3 The origin of the W & Z Boson masses

With the Lagrangian described in Equation 2.28, it is now possible to "give" mass to the W and Z bosons, by taking the covariant derivative terms:

$$\frac{1}{2}[(\partial_\mu + \frac{ig_{\mathrm{W}}}{2}\vec{\tau}.\vec{W}_\mu + ig_{\mathrm{Y}}\frac{Y}{2}B_\mu)\phi]^\dagger[(\partial^\mu + \frac{ig_{\mathrm{W}}}{2}\vec{\tau}.\vec{W}^\mu + ig_{\mathrm{Y}}\frac{Y}{2}B^\mu)\phi]. \tag{2.30}$$

Expanding the above equation by performing the summation over the SU(2) generators, introducing the ground-state Higgs field, and defining $h.c$, as the Hermitian conjugate leads to:

$$\frac{1}{8}\begin{pmatrix} g_{\mathrm{W}}W_\mu^3 + g_{\mathrm{Y}}B_\mu & g_{\mathrm{W}}(W_\mu^1 - iW_\mu^2) \\ g_{\mathrm{W}}(W_\mu^1 + iW_\mu^2) & -g_{\mathrm{W}}W_\mu^3 + g_{\mathrm{Y}}B_\mu \end{pmatrix}\begin{pmatrix} 0 \\ v \end{pmatrix} + h.c. \tag{2.31}$$

The physical $W^\pm$ are then defined as a linear superposition of the W_1 and W_2 fields of the forms: $W_\mu^\pm = \frac{1}{\sqrt{2}}(W_\mu^1 \pm iW_\mu^2)$. Expanding the above expression and including the Hermitian conjugate terms, yields:

$$\frac{1}{4}v^2 g_{\mathrm{W}}^2(W_\mu^+ W^{\mu-}) + \frac{v^2}{8}(g_{\mathrm{Y}}B_\mu - g_{\mathrm{W}}W_\mu^3)(g_{\mathrm{Y}}B^\mu + g_{\mathrm{W}}W^{\mu\,3}). \tag{2.32}$$

The first term in this expression is identified as the mass term for the $W^\pm$ fields, corresponding to $m_{\mathrm{W}} = \frac{1}{2}g_{\mathrm{W}}v$. The final term in the expression concerns the Z^0 boson and photon and can be rewritten in matrix form as:

$$\frac{v^2}{8}\begin{pmatrix} W_\mu^3 & B_\mu \end{pmatrix}\begin{pmatrix} g_{\mathrm{W}}^2 & -g_{\mathrm{Y}}g_{\mathrm{W}} \\ -g_{\mathrm{Y}}g_{\mathrm{W}} & g_{\mathrm{Y}}^2 \end{pmatrix}\begin{pmatrix} W^{\mu\,3} \\ B^\mu \end{pmatrix}. \tag{2.33}$$

This 2×2 matrix can then be diagonalised to give the massless photon state (A_μ) and the physical $Z-$boson state (Z^0), with mass given by:

$$m_Z = \frac{v}{2}\sqrt{g_{\mathrm{Y}}^2 + g_{\mathrm{W}}^2}. \tag{2.34}$$

Due to the dependence of m_W on the weak-coupling, it is possible to write a relationship between the W and Z boson masses. Equation 2.21, previously introduced the weak mixing angle, also known as the Glashow-Weinberg angle, θ_{W}, which can be defined as either $\sin(\theta_W) \equiv g_{\mathrm{Y}}/\sqrt{g_{\mathrm{W}}^2 + g_{\mathrm{Y}}^2}$ or $m_{\mathrm{W}} = m_{\mathrm{Z}}\cos(\theta_{\mathrm{W}})$.

This relationship acts as a powerful theoretical prediction of the $\mathrm{SU(2)_L}\times\ \mathrm{U(1)}_Y$ theory, as contained within is the unification of the electromagnetic and weak forces and the spontaneous symmetry breaking provided by the Higgs mechanism.

2.5.4 The origin of the Fermion Masses

An additional attribute of the Higgs field is that it also gives rise to the fermion masses in a simple manner, by introducing Yukawa mass terms into the Lagrangian. The terms can be written of the kind:

$$g_f\bar{\psi}_L\phi\psi_R, \tag{2.35}$$

Where g_f is the Yukawa coupling between the fermion and the Higgs field, and the ψ terms correspond to the wavefunction of the fermion. After spontaneous symmetry breaking, in the ground state of the Higgs potential, this becomes:

$$g_f \frac{v}{\sqrt{2}} \bar{\psi}_L \phi \psi_R, \tag{2.36}$$

resulting in a mass term for the fermion:

$$m_f = \frac{g_f v}{\sqrt{2}}. \tag{2.37}$$

The Yukawa couplings, and hence the fermion masses, are not predicted in the SM and must be experimentally measured.

2.6 The Standard Model

A compact formalism of the SM Lagrangian is shown in Equation 2.38. Contained within the equation are the kinetic terms of the three fundamental forces ($\mathrm{SU}(3)_C \times \mathrm{SU}(2)_L \times \mathrm{U}(1)_Y$), the interactions between the fermions and the forces (contained within the coveriant derivative term), the Yukawa terms related to the fermion masses, and the Higgs kinetic and field terms.

$$\begin{aligned} \mathcal{L}_{SM} = & -\frac{1}{4} F_{\mu\nu} F^{\mu\nu} \\ & + i\bar{\psi} \not{D} \psi + h.c \\ & + \psi_i y_{ij} \psi_j \phi + |D_\mu \phi|^2 - V(\phi). \end{aligned} \tag{2.38}$$

The predictions from the above Lagrangian are experimentally verified to an incredible degree by many experiments and across a wide range of energy scales. Figure 2.3 shows the cross section predictions for a variety of SM processes as measured by the ATLAS experiment. The cross sections are related to the probability of a given process occuring, and are further discussed in Chapter 4.1.1. The grey boxes are the theoretically predicted cross sections at the relevant energy scale for the processes under consideration and the coloured boxes are the experimentally measured values for the cross section. As seen in the plot there is remarkable consistency between the theoretical predictions and the experimentally measured values.

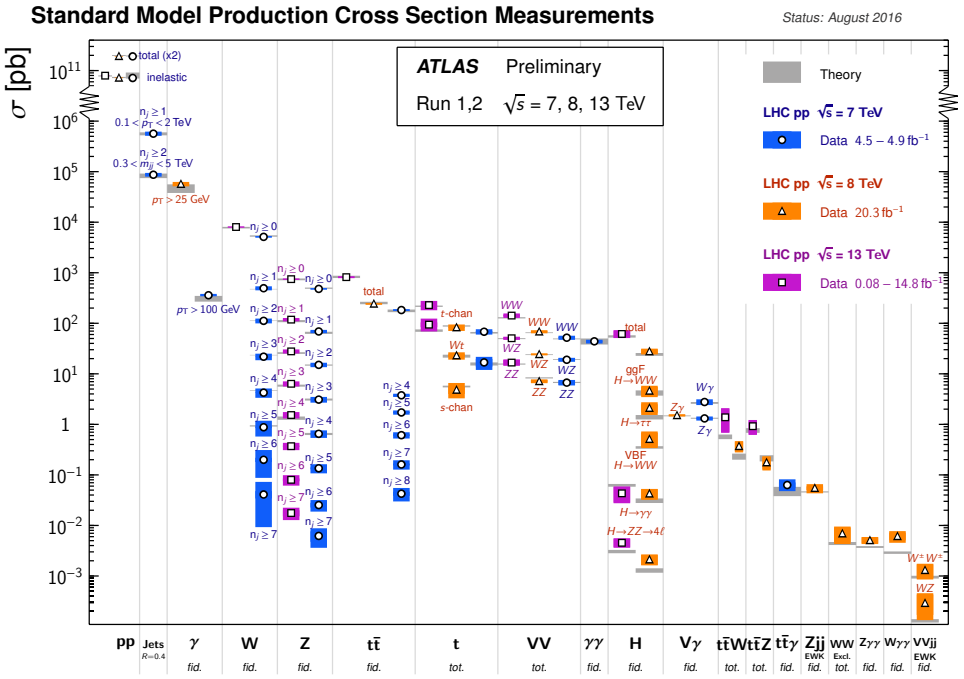

FIGURE 2.3: An overview of the cross section predictions taken from the SM (in grey) compared to the experimentally measured values at $\sqrt{s} = 7, 8, 13$ TeV (blue, orange and purple respectively).
Taken from [15]

With the discovery of the Higgs Boson in 2012 [16, 17, 18, 19], with mass $m_h \approx 125\,\text{GeV}$ the final piece of the SM was confirmed, validating the theory of electroweak symmetry breaking and the concept of gauge invariance.

2.6.1 Open questions

Even with the discovery of the Higgs boson many questions remain unanswered. In fact, the very discovery of the Higgs boson causes a new problem to arise, known as the hierarchy problem [20, 21, 22, 23].

An intuitive way to consider the hierarchy problem is to postulate that there is no new physics between the current electroweak scale (taken to be the Higgs mass) and the Planck scale (where gravity is equally as strong as the other forces) $m_{Planck} \approx 10^{19}\,\text{GeV}$. Assuming that there exists a fundamental theory which unifies the SM and gravity, then the ratio of the EW symmetry breaking scale and Planck scale is very small ($m_h/m_{Planck} \approx 10^{-17}$) which seems unnatural.

A more mathematically rigorous way of evaluating this is to consider quantum loop corrections to the Higgs mass known as the technical hierarchy problem. Particles that

gain mass by the Higgs mechanism are involved in quantum loop corrections to the physical Higgs mass. Equation 2.39 considers the first order correction to the Higgs mass from a fermion (f).

$$\Delta m_h^2 = -\frac{g_f^2}{8\pi^2}(\Lambda_{\mathrm{UV}}^2 +) - 6m_f^2 \ln(\Lambda_{\mathrm{UV}}/m_f) + ... \tag{2.39}$$

To regulate the loop integral an energy scale cut-off is introduced (Λ_{UV}) which is the energy scale at which new physics would be present. If, in this scenario the scale at which new physics is introduced is the Planck scale ($\Lambda = m_{\mathrm{Planck}}$) and the correction to the Higgs mass is calculated for the top-quark, then the magnitude of the correction is of the order 30 times larger than the known value of $\Delta m_h \approx 90\,\mathrm{GeV}$. This discrepancy between the measured value and the theoretically predicted value is one hint that new physics must exist somewhere between the electroweak and Planck scales.

Astronomical observations also provide hints of new physics beyond the Standard Model (BSM). Measurement of galactic rotation curves represent the orbital velocities of stars in galaxies and the distance of the star from the galactic centre. When comparing the rotation curve expected due to the luminous matter present in the galaxy, with the observed rotational curve, there is a discrepancy which implies additional, non-luminous matter present in these galaxies [24]. This extra matter, known as Dark Matter (DM) due to the fact it does not interact with light, remains unexplained in the SM.

The theoretical predictions of the SM are generally in very good agreement with a wide range of experimentally measured values however, some discrepancies are known. Another hint of BSM physics is related to the anomalous magnetic moment of the muon. The Dirac equation predicts a magnetic moment of the muon $g_\mu = 2$ at tree level. When taking into account higher order corrections from SM particles, the magnetic moment of the muon is expected to increase slightly. The contribution to the magnetic moment from the higher order corrections is known as the anomalous magnetic moment, and is defined as:

$$a_\mu = \frac{g_\mu - 2}{2}. \tag{2.40}$$

Using Equation 2.41, the magnetic moment of the muon can be determined experimentally to a very high precision by measuring the precession frequency of muons in a magnetic field, such as when in a storage ring.

$$\vec{M} = g_\mu \frac{e}{2m_\mu} \vec{S}. \tag{2.41}$$

Previous experiments have measured a discrepancy between the theoretical value of a_μ and the experimental value, measured to be $\approx 3.4 - 3.6\sigma$ [25]. A further measurement of the anomalous magnetic moment of the muon is planned in 2018 with the g-2 experiment in Fermilab [26]. If the discrepancy between the experimental value and the theoretical value persists, it could suggest extra non-SM particles involved in the loop corrections.

A final unresolved question arises when considering the possibility of developing a grand-unified theory (GUT). When creating a GUT it is supposed that the three forces currently explained by the SM are representations of a single force. If this is the case, then the running couplings related to the forces in the SM should all converge at a certain energy. If the couplings as currently described by the SM are extrapolated to higher energies then it is seen that the three forces do not converge at the same point. To correct this, BSM physics can contribute to the running of the couplings, allowing the forces to converge at the same point.

2.7 Supersymmetry

There are many possible ways to propose BSM physics. For example, a simple method to provide a candidate for DM and its interactions would be to insert new terms into the SM Lagrangian that directly satisfy the postulated DM interactions. An example of this is discussed in Section 2.8.

Another method to generate BSM physics is to continue with the previous theme of symmetries, as the concept of symmetry was an integral component in the creation of the SM. The concept of supersymmetry (SUSY) [27, 28, 29, 30, 31, 32, 33, 34] introduces an internal symmetry between bosons and fermions, such that a fermionic state can change to a bosonic state, and vice versa. The following derivations closely follow Ref. [35].

Introducing a symmetry of this form is not arbitrary, as the Coleman-Mandula theorem [36] states thats that there is no non-trivial way to extend the Poincaré algebra (generators of Lorentz boosts and rotations) when considering three space-like and one time-like dimension, and maintain non-zero scattering amplitudes. The theorem postulates that the only non-trivial mix of Poincaré and internal symmetries is the product of the two ($Poincaré \times Internal$). Thankfully there is a loophole in the theorem, due to

the axiom that the internal symmetries considered were bosonic in their nature. When considering a fermionic operator (the type of operator that would be required to change a boson into a fermion), the Coleman-Mandula theorem no longer prevents the inclusion of this symmetry. As such, it is possible to introduce an operator (Q) to transform between fermionic and bosonic states:

$$Q|\psi_{\text{Boson}}\rangle \propto |\psi_{\text{Fermion}}\rangle \qquad Q|\psi_{\text{Fermion}}\rangle \propto |\psi_{\text{Boson}}\rangle \tag{2.42}$$

This new symmetry introduces a group orthogonal to the SM, leading to a representation of the form $\text{SU}(3)_C \times \text{SU}(2)_L \times \text{U}(1)_Y \times \text{SUSY}$. The orthogonality of this group implies that the SM quantum numbers of a particle will not change when that particle undergoes a SUSY transformation. This increases the number of degrees of freedom in the theory and doubles the number of particles. The consequences of this are two-fold, the first being that for each particle in the SM there exists a supersymmetric version of the particle, known as a superpartner. The superpartners have identical mass and quantum numbers, but differ by half a unit of spin. The second consequence is that the SM particles and their superpartners can be placed in supermultiplets. There are two types of supermultiplet, chiral multiplets, and gauge multiplets.

The SM fermions are one component of a chiral multiplet, with the other component being their scalar superpartner. The naming convention of the supersymmetric particles present in the chiral multiplets is to introduce the pre-fix "s" for scalar, and example of this is the *stop* which is the superpartner of the top quark. The SM vector bosons are one component of the gauge multiplets, with the other component being the relevent spin-$\frac{1}{2}$ superpartner. The convention for the super partners in this case is that "ino" is appended to the end of the boson name, for example the superpartner of the gluon, becomes the *gluino*.

The final particle that remains to be placed in a supermultiplet is the Higgs boson. In the SM there exists one Higgs doublet. The doublet couples with the up-type quarks and its charge conjugate couples with the down-type quarks. When introducing the superpotential, this is no longer allowed due to charge conservation requirements.

Instead an extended Higgs sector is required as a prelude to SUSY, which requires two doublets. One doublet (H_u) gives masses to the up-type quarks, and the other doublet (H_d) gives masses to the down-type quarks. These two doublets introduce four gauge eigenstates: H_u^0, H_d^0, H_u^+ and H_u^- which mix to form the mass eigenstates: h^0, H^0, A^0

and $H^{\pm}$. In this scenario the lighest CP even mass eigenstate (h^0) is the SM Higgs boson and the other mass eigenstates are decoupled at high masses. It is the gauge eigenstates introduced by the extended Higgs sector that are placed into multiplets with their SUSY counterpart. Continuing the previously defined nomenclature, the superpartners of the Higgs bosons are referred to as Higgsinos.

Names	Symbol	spin 0	spin $\frac{1}{2}$	$SU(3)_C \times SU(2)_L \times U(1)_Y$
squarks, quarks	Q	$(\tilde{u_L}, \tilde{d_L})$	(u_L, d_L)	$(3, 2, \frac{1}{6})$
(3 families)	u	$\tilde{u_r}^*$	$u_L^\dagger$	$(3, 1, -\frac{2}{3})$
	d	$\tilde{d_r}^*$	$d_R^\dagger$	$(3, 1, \frac{1}{3})$
sleptons, leptons	L	$(\tilde{\nu}, \tilde{e_L})$	(ν, e_L)	$(1, 2, -\frac{1}{2})$
(3 families)	e	$\tilde{e_r}^*$	$e_L^\dagger$	$(1, 1, 1)$
Higgsinos, Higgs	H_u	(H_u^+, H_u^0)	$(\tilde{H_u^+}, \tilde{H_u^0})$	$(1, 2, +\frac{1}{2})$
	H_d	(H_d^0, H_d^-)	$(\tilde{H_d^0}, \tilde{H_d^-})$	$(1, 2, -\frac{1}{2})$

TABLE 2.2: An overview of the chiral supermultiplet groupings required by Supersymmetry. The table presents the eigenstates under the SUSY transformation, which do not correspond to the mass eigenstates, which are described in Table 2.4.

Names	spin $\frac{1}{2}$	spin 1	$SU(3)_C \times SU(2)_L \times U(1)_Y$
gluino, gluon	$\tilde{g}$	g	(8,1,0)
winos, W-bosons	$\tilde{W}^{\pm}$ $\tilde{W}^0$	$W^{\pm}W^0$	(1,3,0)
bino, B-boson	$\tilde{B}^0$	B^0	(1,1,0)

TABLE 2.3: An overview of the gauge supermultiplet groupings required by Supersymmetry. As in the previous table, this table shows the eigenstates under the SUSY transformation, which do not correspond to the mass eigenstates, which are described in Table 2.4

Tables 2.2 and 2.3 give an overview of the supermultiplet groupings of particles and sparticles required in the minimal supersymmetric standard model (MSSM).

2.7.1 Mass Eigenstate Mixing

An aspect of SUSY as it would present itself in nature is the difference between the gauge eigenstates of the theory and the mass eigenstates. The superpartners that are represented in the chiral and gauge multiplets of Tables 2.2 and 2.3 are not necessarily the physical mass eigenstates.

Table 2.4 contains the gauge and mass eigenstates of SUSY and the extended Higgs sector. There is mixing between the neutral electroweak gaugino and higgsino eigenstates to produce four neutral particles, referred to as "neutralinos"($\tilde{\chi}^0_{1,2,3,4}$). Mixing also occurs between the charged electroweak and Higgsino eigenstates to produce two "chargino" states ($\tilde{\chi}^{\pm}_{1,2}$). Mixing is also present in the squark sector, the amount of which is related to the masses of the relevant SM particles, and as such is only significant for the top and bottom squarks and the tau sleptons. The gauge eigenstates of the stop are denoted by $\tilde{t}_L$ and $\tilde{t}_R$. The left and right terms here do not refer to the "handedness" of the particle, but instead refer to the handedness of its SM partner. The gauge eigenstates of the stop mix to form two mass eigenstates ($\tilde{t}_1, \tilde{t}_2$), with the $\tilde{t}_1$ the lighter state. As the superpartner of the left-handed bottom quark ($\tilde{b}_L$) is placed in a doublet with the $\tilde{t}_L$, similar mixing occurs between the sbottom gauge eigenstates, to produce two mass eigenstates ($\tilde{b}_1, \tilde{b}_2$); and the stau gauge eigenstates, producing again two mass eigenstates ($\tilde{\tau}_1, \tilde{\tau}_2$).

Names	Spin	R_P	Gauge Eigenstates	Mass Eigenstates
Higgs Bosons	0	+1	$H^0_u, H^0_d, H^+_u, H^-_d$	$h^0, H^0, A^0, H^{\pm}$
squarks	0	-1	$\tilde{u}_L, \tilde{u}_R, \tilde{d}_L, \tilde{d}_R$	same
			$\tilde{s}_L, \tilde{s}_R, \tilde{c}_L, \tilde{c}_R$	same
			$\tilde{t}_L, \tilde{t}_R, \tilde{b}_L, \tilde{b}_R$	$\tilde{t}_1, \tilde{t}_2, \tilde{b}_1, \tilde{b}_2$
sleptons	0	-1	$\tilde{e}_L, \tilde{e}_R, \tilde{\nu}_e$	same
			$\tilde{\mu}_L, \tilde{\mu}_R, \tilde{\nu}_\mu$	same
			$\tilde{\tau}_L, \tilde{\tau}_R, \tilde{\nu}_\tau$	$\tilde{\tau}_1, \tilde{\tau}_2, \tilde{\nu}_\tau$
neutralinos	$\frac{1}{2}$	-1	$\tilde{B}^0, \tilde{W}^0, \tilde{H}^0_u, \tilde{H}^0_d$	$\tilde{\chi}^0_1, \tilde{\chi}^0_2, \tilde{\chi}^0_3, \tilde{\chi}^0_4$
charginos	$\frac{1}{2}$	-1	$\tilde{W}^{\pm}, \tilde{H}^+_u, \tilde{H}^-_d$	$\tilde{\chi}^{\pm}_1, \tilde{\chi}^{\pm}_2$
gluino	$\frac{1}{2}$	-1	$\tilde{g}$	same

TABLE 2.4: An overview of the gauge and mass eigenstates of the SUSY particles and the extended Higgs sector.

2.7.2 Unification

A beneficial aspect of SUSY is that it leads naturally to the unification of the strong and electroweak forces. The evolution of the couplings in the SM are shown in Figure 2.4. It can be seen that the evolution of the couplings as a function of energy does not converge (dashed line), which contradicts the prediction that there is a GUT scale where the forces unify. The addition of sparticles results in extra contributions to the

renormalisation of the couplings. These extra contributions change the evolution of the couplings such that at very high energies the couplings converge (solid line), suggesting the unification of the forces.

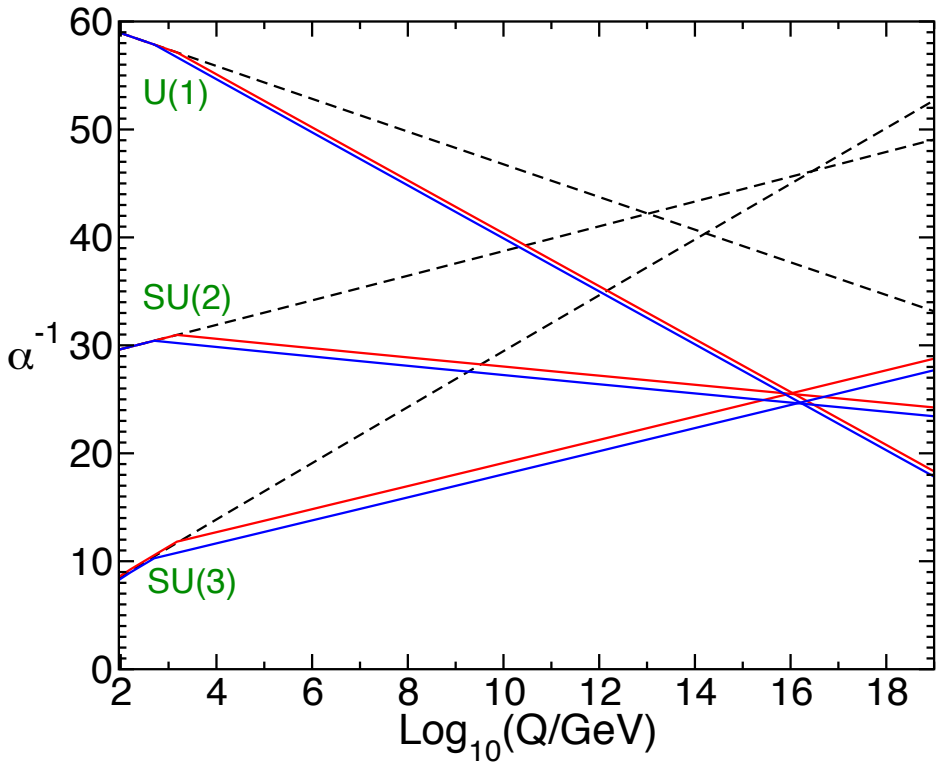

FIGURE 2.4: Evolution of the couplings in the SM (dashed) and SUSY (solid, with various sparticle mass assumptions).
Taken from [35].

2.7.3 SUSY Breaking

The masses of the superpartners are known not to be the same as the SM particles at the energy scales currently investigated. For example, no particles have been observed consistent with a spin 0 electron at the mass 511 keV. This implies that SUSY must be a broken symmetry at the electroweak scale.

The concept of symmetry breaking has been previously discussed with regards to the Higgs Lagrangian. A similar method can also be applied to the SUSY Lagrangian to break the symmetry. Assuming that the super potential is symmetric about the origin, but is no longer symmetric (a non-zero vacuum expectation value) when in the ground state, results in different masses for the individual components of the supermultiplets. In order to maintain the beneficial aspects of the theory, whilst breaking the symmetry, the SUSY Lagrangian must be written in the form:

$$\mathcal{L} = \mathcal{L}_{SUSY} + \mathcal{L}_{soft} \tag{2.43}$$

The $\mathcal{L}_{SUSY}$ term contains all of the gauge and Yukawa couplings, while the $\mathcal{L}_{soft}$ term contains only positive mass/gauge parameters, as a consequence of requiring the energy of the ground state to be positive.

2.7.4 Solution to the Hierarchy Problem

The introduction of a boson (fermion) of equal quantum numbers and mass to each SM fermion (boson) can now be used in order to solve the hierarchy problem discussed in Section 2.6.1. When assessing the quantum corrections to the Higgs mass from the introduction of SUSY, the contributions from the superpartners must be taken into account. Equation 2.39 displays the correction to the Higgs mass due to the coupling between a fermion (g_f) and the Higgs. However the contribution from the superpartner (a scalar in this case) also enters via loop corrections. The correction due to the coupling of a scalar particle to the Higgs is seen in Equation 2.44.

$$\Delta m_h^2 = \frac{g_s}{8\pi^2}(\Lambda_{\mathrm{UV}}^2 - 2m_s^2 \ln(\Lambda_{\mathrm{UV}}/m_s) + ...) \tag{2.44}$$

There is a sign difference between the fermion correction and the bosonic correction, implying that the introduction of the superpartner can cancel the contribution of the SM particles. More explicitly, Equation 2.45 demonstrates that with the assumption that the mass of the fermions and bosons are the same (the couplings are related as $g_f^2 = -g_s$) then the contributions will cancel perfectly, leaving only the bare Higgs mass.

$$\Delta m_h^2 = \frac{\lambda_f^2}{4\pi^2}[(m_f^2 - m_s^2)\ln(\Lambda_{\mathrm{UV}}/m_s) + 3m_f^2 \ln(m_s/m_f)] \tag{2.45}$$

The requirement that SUSY must be a broken symmetry in the form of Equation 2.43, allows for the cancellation described above to still occur, assuming the mass scale of the breaking provides contributions to the Higgs mass, as in Equation 2.46. The mass of the "soft" breaking term cannot be too large, in order to solve the hierarchy problem without resorting to fine tuning of the SUSY parameters.

$$\Delta m_h^2 = m_{soft}^2[\frac{\lambda_f^2}{16\pi^2}\ln(\Lambda_{\mathrm{UV}}/m_{soft}) + ...] \tag{2.46}$$

2.7.5 Naturalness

Breaking the SUSY potential results in the sparticles possessing different masses compared to their SM counterparts, however there are no fixed requirements on what the sparticle masses should be. The concept of naturalness [37] can be used as a guideline to create a general SUSY mass hierachy. A possible way to envisage naturalness is via the tree-level relation:

$$-\frac{m_Z^2}{2} = |\mu|^2 + m_{H_u}^2, \tag{2.47}$$

where the $m_{H_u}^2$ term is the Higgsino mass term and μ is the higgino mass parameter. Any sparticles which would contribute to the right hand side have values that are related and can be set to preseve the observed scale of electroweak symmetry breaking.

This implies that the higgsinos must be light (as they are guided by the μ parameter). In addition the sparticles that contribute to loop corrections to the Higgsino mass, such as the stop (via one loop corrections Δm_1^2), and also the gluinos (via two loop corrections Δm_2^2), must be light. The contributions to the correction to the higgs mass are illustrated below in Equation 2.48, showing that to first and second order the stop and gluinos contribute to the higgs mass. In addition to a light stop, the sbottom mass is also expected to be small as the top and bottom quarks reside in a weak isospin doublet in the SM.

$$\begin{aligned} \Delta m_1^2 &\propto \log(m_{\tilde{t}}) \\ \Delta m_2^2 &\propto \log(1/m_{\tilde{g}}) \end{aligned} \tag{2.48}$$

The implications of naturalness suggest the third generation sparticles (the stop and sbottom) and the gluinos have masses of around the TeV scale. The first and second generation squarks are allowed to have a very high mass, and can be treated as decoupled from the gluinos and third generation squarks.

2.7.6 R-Parity

Introducing a theory that increases the number of particles, and hence couplings, can result in theoretical predictions that conflict with experimental observations. A consequence of SUSY is that a coupling is introduced that would lead to proton decay within seconds, whereas experimental measurements have placed stringent limits on the proton lifetime of $> 2.3 \times 10^{33}$ s [38]. One way to satisfy the proton lifetime in the context of

SUSY is to introduce a new quantum number, referred to as R-parity (R_p), defined in Equation 2.49, which must be conserved in all interactions. R-parity is calculated at a vertex using the spin (s), baryon number (B) and lepton number (L) of the particles entering and exiting the vertex.

$$R_P = (-1)^{2s+3B+L} \tag{2.49}$$

The introduction of R-parity disallows all lepton number violating terms in the SUSY Lagrangian and thus prevents rapid proton decay. A consequence of R-parity conservation for collider experiments is that SUSY particles must be produced in pairs. The initial state of a pp collision is $R_P = 1$, and to conserve R-parity, two SUSY particles must be produced to conserve R-parity. Subsequent decays of the sparticles produced in the interaction must also maintain R-parity, such that the lightest supersymmetric particle (LSP) must be stable. The LSP in R-parity conserving scenarios can be a candidate for Dark Matter. In the models considered in this Thesis the LSP is the lightest neutralino $\tilde{\chi}_1^0$.

2.7.7 Constraints on SUSY from previous measurements

Many direct searches for SUSY have been performed by a variety of experiments with no significant signs of SUSY, limits were placed on parameters in the SUSY phase space. In addition to this, limits can also be placed on SUSY models from precision measurements and, for scenarios that provide a DM candidate, cosmological measurements. Due to the wide variety of SUSY models available, with many differences between them, the constraints in this section will be discussed in relation to the phemonenologcal Minimal Supersymmetric Standard Model (pMSSM).

Unlike GUT theories, which attempt to evolve a set of minimal parameters down to the EW scale, the pMSSM seeks to describe SUSY at the EW scale using a set of 19 experimentally or theoretically motivated parameters, described in Table 2.5 [39].

Parameter	Description
$\tan(\beta)$	Ratio of the VEVs of the two Higgs doublet fields, expected to lie between $1 \leq \tan\beta \leq m_t/m_b$.
M_{A}	Mass of the pseudoscalar Higgs boson (A)
μ	Higgsino/Higgs mass parameter
M_1, M_2, M_3	Bino, wino and gluino mass parameters
$m_{\tilde{q}}, m_{\tilde{u}_R}, m_{\tilde{d}_R}, m_{\tilde{l}}, m_{\tilde{e}_R}$	First/second generation sfermion masses
$m_{\tilde{Q}}, m_{\tilde{t}_R}, m_{\tilde{b}_R}, m_{\tilde{L}}, m_{\tilde{\tau}_R}$	Third generation sfermion masses
A_t, A_b, A_τ	Third generation trilinear couplings

TABLE 2.5: An overview of the parameters in the pMSSM. The range of expected values for $\tan\beta$ is taken from [40].

2.7.7.1 Precision Measurements

The introduction of a set of new heavy particles would imply changes to the SM predicted cross sections of many processes. Precision flavour physics, and the measurement of the branching ratios (BR) of very rare loop processes can provide insight into possible BSM physics, including SUSY. For example the branching ratio of the rare SM process $B_S \to \mu\mu$ can be enhanced by the presence of SUSY particles in loop processes. Examples of the extra loops that will contribute are shown in Figure 2.5. The measurement of BR($B_S \to \mu\mu$) provides limits on the these possible BSM contributions [41] as the measurement is found to be consistent with the SM expectation. However this is just one possible decay that could be enhanced by SUSY particles and there are many SUSY models that do not include enhancements in this channel.

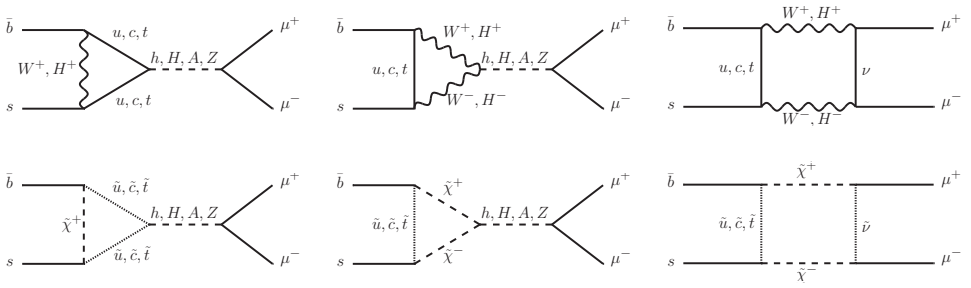

FIGURE 2.5: Examples of the SUSY contributions to BR($B_S \to \mu\mu$). Taken from [42].

2.7.7.2 Cosmological Constraints

With the assumption of R-parity conserving SUSY providing a candidate for DM, constraints on SUSY can also be provided by cosmological measurements. Whilst SUSY can provide a DM candidate, this is not the only necessity in order to explain the abundance of DM in the universe, as it must also explain the DM relic density. The DM relic density is the amount of DM that remained after the universe expanded to a level where the probability of DM annihilation becomes very low, measured to be 26% [43] by the Planck collaboration. In order to satisfy the relic density provided by this measurement, assuming that DM arises from weakly interacting massive particles (WIMPs), constraints can be placed on key pMSSM variables, such as the LSP mass. These constraints can prevent the predicted DM mass in pMSSM models from being too large, however smaller values of the LSP mass are acceptable if significant mixing occurs between the gauginos.

2.7.8 Collider Constraints

Searches for the direct production of R-parity conserving SUSY particles have been a major component of the physics programmes of many particle colliders. Focusing on the LHC-era, searches for direct sparticle production can be split into multiple categories depending upon the sparticle that is being seached for. In this thesis the main focus is on the direct pair production of the third generation squarks, the stop and sbottom.

When performing a search for third generation squarks, most analyses use simplified model scenarios. In these scenarios additional assumptions are made, such as the branching ratio for the decay under consideration is 100%, and that no other sparticles other than those which are under consideration are present. Whilst these scenarios are not representative of how SUSY would present itself in nature, they are useful as a tool to search in a generally model independent manner. Examples of two simplified models that are searched for are shown in Figure 2.6.

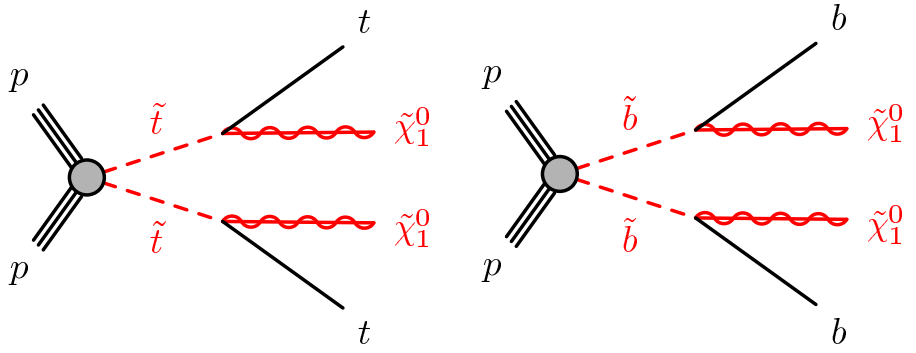

(a) $\tilde{t} \to t + \tilde{\chi}_1^0$ (b) $\tilde{b} \to b + \tilde{\chi}_1^0$

FIGURE 2.6: Representative diagrams of the simplified model scenarios considered when performing searches.

Figure 2.7, shows the ATLAS limits on simplified model scenarios at the end of Run 1 for both stop and sbottom pair production, assuming a BR of 100% for the decay to a top-/bottom-quark, (where the top-quark can also be offshell) and $\tilde{\chi}_1^0$ [2].

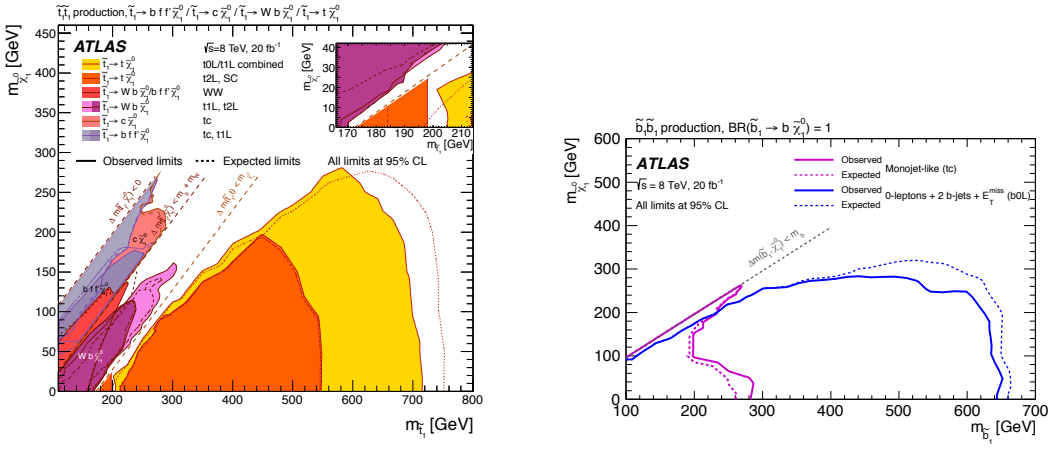

(a) ATLAS Limits on various stop decay scenarios.

(b) ATLAS Limits on a simplified sbottom decay scenario.

FIGURE 2.7: ATLAS third generation squark exclusion limits at the end of Run 1. Taken from [2].

2.8 Generic Dark Matter Models

The astrophysical observation of DM, previously introduced as a open question in the SM, suggests that DM is non-baryonic. The abundance of DM has been measured by the Planck collaboration and corresponds to 26% of the mass-energy content of the universe [43], the nature of which we know very little about. One of the best motivated

candidates for a DM is a weakly interacting massive particle (WIMP). If this is the case, then it may be possible to produce DM directly at the LHC.

Different approaches can be used to investigate direct DM production. Effective Field Theories (EFTs) can be used with the interactions described by contact operators in an EFT framework [44, 45, 46]. The validity of these models requires the assumption that the mass of the mediator between the SM and the dark sector is much larger than the energy scale of the interaction. This is valid for direct and indirect dark matter searches, as the energy of the interaction is much lower than the energy scale of the mediator, for example in direct detection measurements the collision of DM with atomic nuclei which is $\mathcal{O}$(keV) [47].

If the interaction between the SM and the DM particles is at an energy similar to the centre of mass energy of the collision, then EFTs are no longer valid, and simplified models must be used where the mediator between the SM and DM is considered. When producing a simplified model there are a variety of assumptions that must be made, whilst also maintaining a UV complete theory. Primarily the assumptions are related to the properties and interactions of the mediator. The mediator is taken to be either a scalar (ϕ), or a pseudoscalar (a) where the associated scalar is decoupled. The simplified model scenarios are considered to be the most appropriate method to model direct DM production at the current LHC energies [48, 49]. Due to the assumptions made when producing the simplified model scenarios it is non-trivial to compare the results of a direct DM search and a collider DM search. To place results produced with the simplified model scenarios on the same footing at the direct detection results requires further assumptions to be placed on the simplified model scenarios. These additional assumptions enable the model to be evolved down to the same scale as the interactions expected in the direct detection experiments.

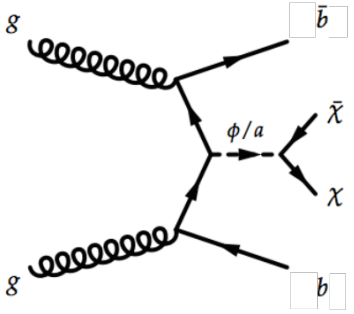

FIGURE 2.8: Feynman diagram for an example of simplified model DM production in association with $b-$quarks, with either a scalar (ϕ) or pseudoscalar (a) mediator.

A representative Feynman diagram of an example simplified model is shown in Figure 2.8. The couplings between the mediator and both, the fermionic sector, and the dark sector are taken to be Yukawa-like. The simplified model scenario can be fully described by four parameters: the DM-mediator coupling, g_χ; the fermion-mediator coupling, g_f; the mediator mass m_ϕ; and the DM mass m_χ. An additional assumpution of equal couplings $g_\chi = g_f = g$ can be made for simplicity. This scenario provides an agnostic method to investigate DM production in a collider environment, whilst introducing as few extra unknown parameters as possible.

Chapter 3

The ATLAS Detector

This chapter contains a brief introduction to the Large Hadron Collider (LHC), including an overview of the accelerator stages required to inject a particle into the LHC. The concept of luminosity is introduced. Finally, an indepth review of the ATLAS detector systems is given, including a breakdown of the detector sub-systems, the trigger and data acquisition (DAQ) systems.

3.1 The Large Hadron Collider

The LHC is a hadron-hadron synchrotron collider situated on the Franco-Swiss border at CERN. The LHC has the capability to collide protons at centre of mass energies of up to 14 TeV. The Run 1 operational energies of 7 and 8 TeV were the highest energy (proton) collisions ever performed; this was then increased to 13 TeV for Run 2. LHC operations began in 2010 (at 7 TeV) in the 26.6 km long LEP [50] tunnel at an average depth of 100 m, and the first collisions occurred in December 2009. The LHC is able to perform both proton-proton collisions and collisions involving lead ions (proton-lead or lead-lead). For the purposes of this thesis only proton-proton collision events are considered.

The CERN accelerator chain is shown in Figure 3.1. Protons are first accelerated in the pre-accelerator chain [51] before they are able to enter the LHC. At the beginning of the complex, hydrogen atoms are ionised in order to produce protons. These protons are injected into LINAC2 and accelerated up to 50 MeV using a series of Radio-Frequency (RF) cavities. From LINAC2 the protons then enter the Booster where they reach an energy of 1.4 GeV. After the Booster, the particles enter the Proton Synchrotron (PS)

reaching an energy of 25 GeV. It is in the PS that the protons are formed into bunches, thanks to the acceleration provided by RF cavities. After the PS, the protons enter the Super Proton Synchrotron (SPS), which is the penultimate accelerator before the protons enter the LHC. The SPS accelerates protons to an energy of 450 GeV, while maintaining the bunch structure, and then injects the protons into the LHC.

Beams of protons are injected into the LHC ring in both clockwise and anti-clockwise directions allowing for collisions at the four Interaction Points (IPs) corresponding to the ATLAS, CMS, LHCb and ALICE experiments. Each beam is accelerated by 8 RF cavities and follows a curved trajectory around the ring due to 1232 superconducting dipole magnets which operate at a temperature of 1.9 K. Additional focusing magnets (quadrupoles, sextupoles and higher orders) are also installed around the ring to provide optical corrections to the beam.

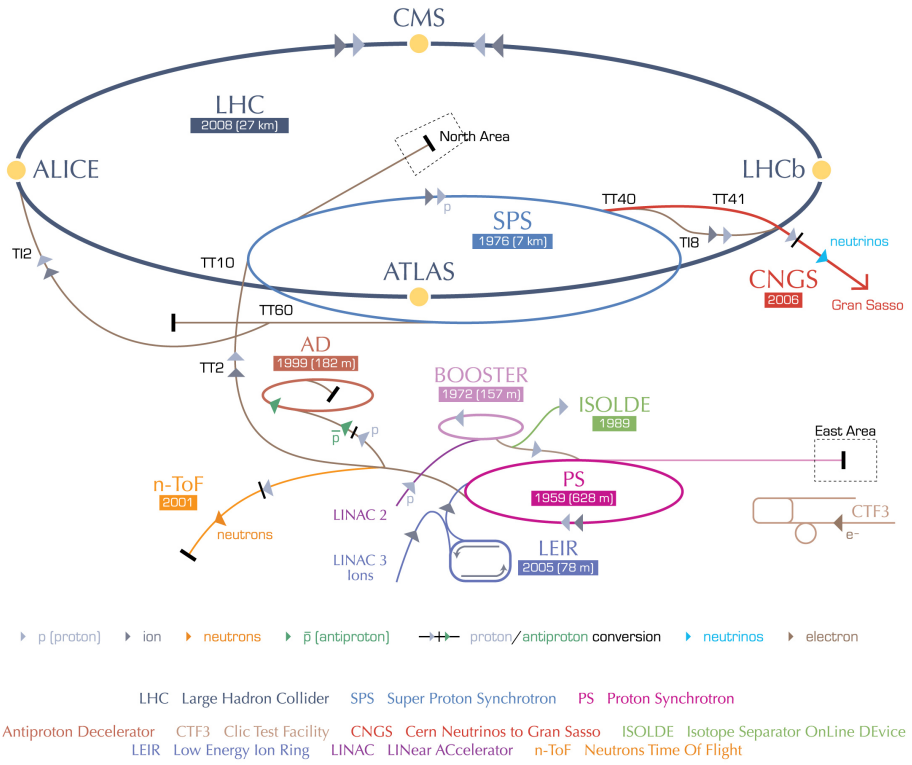

FIGURE 3.1: An overview of the CERN accelerator complex. Protons are accelerated in stages, reaching a higher energy at each stage. The protons begin at the LINAC2, and are accelerated in the Booster, PS and SPS before entering the LHC. Taken from [52]

.

3.2 Luminosity

In order to calculate the number of expected events for a given process both the cross-section (σ) and the integrated luminosity (L) must be known. The integrated luminosity is a measure of the total number of collisions that occur over a period of time, which is calculated as the integral, with respect to time, of the instantaneous luminosity ($\mathcal{L}$). The number of expected events for a process (X) is then given by:

$$N_{\text{Total Events}}(pp \to X) = \sigma_{(pp\to X)} L = \sigma_{(pp\to X)} \int \mathcal{L} dt \tag{3.1}$$

$$\mathcal{L} = \frac{N_b^2 n_b f_{\text{rev}} \gamma_r}{4\pi \epsilon_n \beta^*} F \tag{3.2}$$

The instantaneous luminosity is entirely dependent upon accelerator parameters, [53], and for a proton-proton collider is given by Equation 3.2. In this equation N_b is the number of protons per bunch, n_b is the number of bunches per beam, f_{rev} is the revolution frequency, γ_r is the relativistic gamma factor, ϵ_n is the normalised transverse beam emmision at the IP, β^* is the beta function describing the beam envelope at the IP, and F is a geometric luminosity reduction factor caused by crossing angle between the beams at the IP.

The calculation of the total luminosity is performed as a sum over a number of "luminosity blocks", which are the smallest time interval for which the instantaneous luminosity is calculated [54].

$$L = \sum_{i}^{N_{LB}} \mathcal{L}_i \cdot \Delta t_i. \tag{3.3}$$

Each luminosity block corresponds to a time period of $\approx 1\,\text{minute}$. Equation 3.3 presents the total integrated luminosity as the sum of the number of luminosity blocks (N_{LB}), the integrated luminosity calculated per block ($\mathcal{L}_i$) and the time-period for each block (Δt_i).

3.3 The ATLAS Detector

The ATLAS detector [55] is one of two 4π general purpose detectors (GPD) on the LHC ring. Among the main physics goals of ATLAS are the discovery and measurement of the Higgs boson, searches for BSM physics, and precision measurements of SM processes.

With such a wide ranging physics programme, the detector must be capable of fufilling a set of general requirements to adequately measure physics objects:

- Tracking detectors providing good charged particle momentum measurement enabling particle reconstruction. This also enables the identification of both $b-$jets originating from $b-$quarks from the reconstruction of a secondary vertex.
- Electromagnetic (EM) and hadronic calorimeter systems for the measurement and identification of electrons, photons and jets. These systems are also required to accurately measure the total transverse energy in an event. The total transverse energy is required to calculate the missing transverse momentum ($E_{\mathrm{T}}^{\mathrm{miss}}$) in the x-y plane, as defined in Section 3.3.1, using momentum conservation, which is of great importance to many BSM physics searches.
- A muon spectrometer system for muon identification and good momentum resolution up to a very high transverse momentum.
- A trigger system to efficiently record a wide variety of physics processes based upon the presence of certain objects, whilst also allowing for a reasonable readout rate.
- A fast data acquisition (DAQ) system to readout the data collected by the detector with a high data-quality (DQ) efficiency.

Satisfying the above requirements guided the design of the detector. ATLAS consists of multiple detector systems, shown in Figure 3.2, which are grouped into four subsystems.

The closest sub-system to the beampipe is the Inner Detector (ID), allowing for charged particle tracking in ATLAS. The ID consists of two silicon based detectors: the pixel detector, which makes use of silicon pixels, and is the closest detector to the beampipe; and the Semi-Conductor Tracker (SCT) detector, which consists of silicon strips. The final ID subdetector is the Transition Radiation Tracker (TRT) composed of gaseous straw tube trackers. The ID sub-system is encased in a 2 T magnetic field provided by a solenoid magnet on the outside of the ID environment. For Run 2 an Insertable B-Layer (IBL) was installed as an additional component of the pixel detector, providing an extra layer of pixel sensors closer to the IP.

Beyond the solenoid magnet is the calorimeter sub-system: the EM calorimeter, consisting exclusively of Liquid Argon (LAr) sampling calorimeters; and the hadronic

calorimeter, formed of scintillator-tile calorimeters in the central region and LAr calorimeters in the end-caps. The solenoid and barrel EM calorimeters are placed in the same cryostat to provide the required cooling for the LAr.

The outermost layer of the detector is the muon spectrometer, consisting of tracking chambers and a toroidal magnetic field generated by three magnets, two in the end-caps and one in the central region.

For the remainder of this chapter a more detailed overview of the ATLAS detector sub-systems is presented, in order of increasing distance from the beam-pipe.

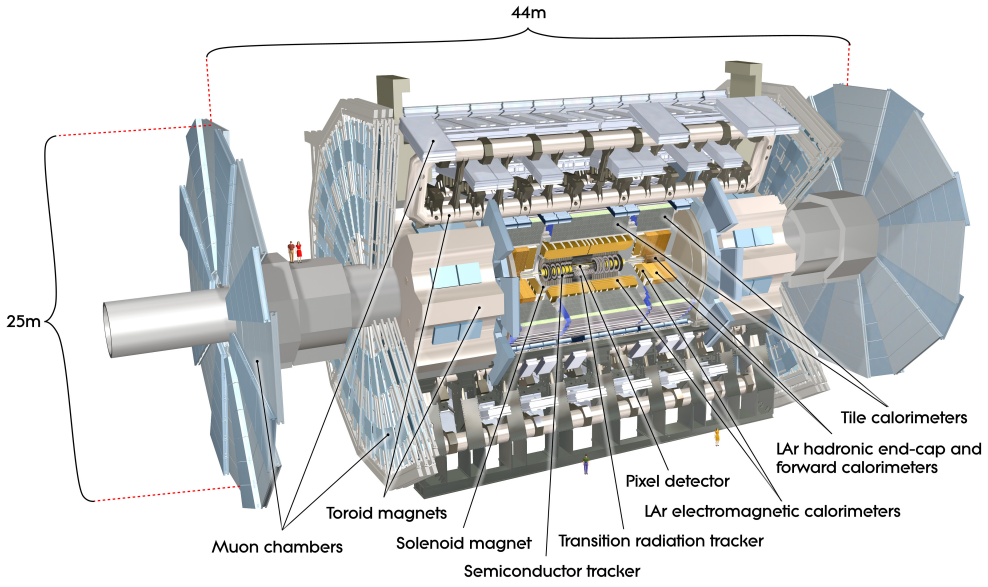

FIGURE 3.2: Cut-away view of the ATLAS detector, with each detector system labelled. The detector systems are grouped into four sub-systems: the Inner Detector, EM calorimeters, hadronic calorimeters, and the muon spectrometer. Taken from [55].

3.3.1 ATLAS Coordinate System

Before proceeding with a detector overview, it is useful to describe the right-handed coordinate system used by ATLAS. The origin of the coordinate system is defined as the nominal interation point. The z-axis is defined by the beam pipe direction, with the x-y plane orthogonal to the beam direction. The positive x- and y- axes are defined as pointing towards the centre of the LHC ring and upwards, respectively. In terms of event kinematics it is more beneficial to use the azimuthal angle (ϕ) defined around the z-axis, and the polar angle (θ) which is the angle from the z-axis. In place of the polar angle the pseudorapidity (for massless particles), η, and rapidity (for massive particles),

y, are used as differences in pseudorapidity ($\Delta\eta$) are invariant with respect to boosts along the z-axis, and are defined in Equations 3.4a and 3.4b respectively.

$$\eta = \ln \tan \frac{\theta}{2}, \tag{3.4a}$$

$$y = \frac{1}{2} \ln \Big(\frac{E + p_Z}{E - p_Z} \Big), \tag{3.4b}$$

ΔR, the distance between two particles in the pseudorapidity-azimuthal angle space, is defined in Equation 3.5.

$$\Delta R = \sqrt{\Delta\phi^2 + \Delta\eta^2}. \tag{3.5}$$

Finally when considering the momentum of physics objects, the transverse momentum (p_{T}) is usually used, which is the projection of the momentum onto the transverse (x-y) plane. The missing transverse momentum $E_{\mathrm{T}}^{\mathrm{miss}}$ is defined as the absolute value of the vectorial sum of the p_{T} of all objects in the detector and is further explained in Section 5.1.6.

3.4 Inner Detector

The ID sub-system, Figure 3.3, is the closest sub-system to the IP and consists of three complementary detectors: the pixel detector, the semiconductor tracker (SCT), and the transition radiation tracker (TRT). The three main purposes of the ID are the identification of primary and secondary vertices, charged particle position and momentum measurements, and electron identification. Table 3.1 shows the resolution of the individual components of the ID sub-system.

The resolution of charged tracks in the ID subsystem provides a transverse momentum resolution of $4.8 \times 10^{-2} \cdot p_{\mathrm{T}}$ [%] for electrons [56] and between 4-20% for muons when only considering the ID. If information from the muon spectrometer is included the transverse momentum resolution for muons is between 4-10% [57].

During Run 1, the radius of the ID was $5 < r < 120\,\mathrm{cm}$, with a longitudinal distance of 6.2 m, providing pseudorapidity coverage of $|\eta| < 2.5$. During the first LHC long shutdown the IBL [58] was added to the detector. The introduction of the IBL provided an additional layer of pixel sensors at a radius of 3 cm away from the beam. This extra layer of pixels provides further tracking information, allowing for improved identification of secondary vertices, greatly improving $b-$jet identification.

The ID region is fully encased in an 2 T solenoidal magnetic field, which is generated by a solenoid magnet located outside the TRT. The two silicon based detectors (the pixel detector and SCT) are cooled to a temperature of around $-20°$ C to provide the optimal operating conditions for the sensors.

Detector Component	Sensor element size [μm]	Intrinsic resolution [μm]
IBL	50 × 250	8 × 40
Pixel	50 × 400	10 × 115
SCT	80	17
TRT	4000	130

TABLE 3.1: An overview of the intrinsic accuracy of the ID components. The sensor element size corresponds to the active detector component of the sensor. The sensor element size and intrinsic resolution are given in terms of (R-ϕ,z) for the IBL and pixel detectors, and (R-ϕ) for the SCT and TRT. Taken from [59]

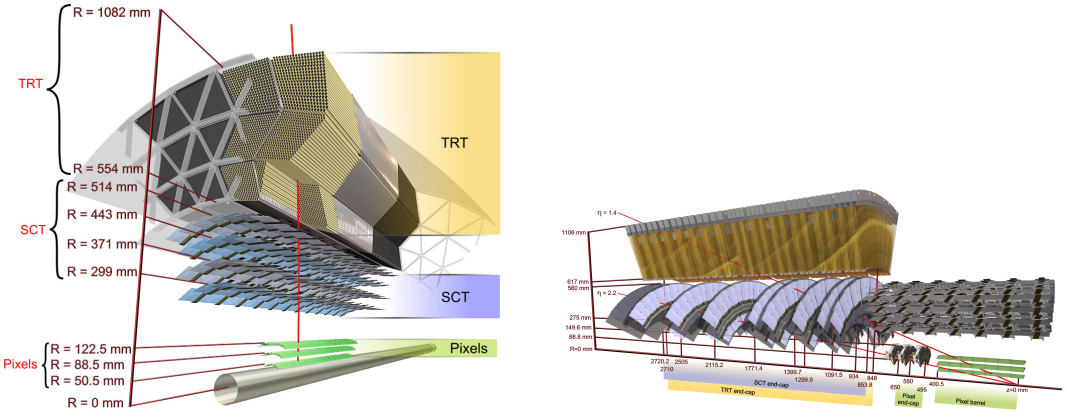

(a) Cross section view.

(b) Longitudinal view.

FIGURE 3.3: Cross-sectional and longitudinal views of the ATLAS ID sub-system during Run 1.

3.4.1 Pixel Detector

The closest sub-detector to the beampipe is the pixel detector, consisting of 1744 identical silicon pixel modules. The pixel sensors are 250 μm thick, with dimensions $19 \times 63\,\text{mm}^2$, resulting in an intrinsic accuracy of 10 μm in the R, ϕ plane and 115 μm along the z-axis. The detector is divided into three barrel layers and two end-caps each composed of three disks.

3.4.1.1 Insertable B-Layer (IBL)

Prior to the beginning of Run 2, it was expected that there would be some degradation of the pixel detector barrel layers from the high radiation environment close to the beam-pipe. This is due to radiation damage causing the loss of charge carriers in the active material reducing the number of hits in the pixel detector. In order to counteract these losses the IBL was scheduled to be installed between Run 1 and Run 2. The IBL was successfully installed and commissioned during 2015. The IBL consists of 224 pixel sensors arranged in a single barrel layer. The sensors are of a different design to the modules used in the pixel detector with dimensions $21 \times 19\,\text{mm}^2$ and thickness $200\,\mu\text{m}$ [60].

3.4.2 Semiconductor Tracker (SCT)

The SCT is a silicon strip detector stationed outside the pixel detector. The SCT consists of 4088 modules, split over 4 barrel layers (2112 modules) and two end-caps with nine disks each (1976 modules per end-cap). The general structure of all modules is the same, however, different designs are used for the barrel and end-caps. Each module consists of two strip layers with a mean strip pitch of $80\,\mu\text{m}$ and a stereoangle of 40 mrad between the layers. This provides an intrinsic accuracy of $17\,\mu\text{m}$ in R, ϕ coordinates and $580\,\mu\text{m}$ in the z direction.

3.4.3 Transition Radiation Tracker (TRT)

The final ID sub-system is the TRT, a gaseous straw tube tracking detector situated outside the SCT. The TRT straws are 4 mm in diameter with an intrinsic accuracy of $130\,\mu\text{m}$ per straw in the R, ϕ plane. Similarly to the other ID sub-systems the TRT is split into a barrel region and two end-cap regions. The barrel region contains 73 straw planes of length 144 cm, that are parallel to the beampipe. The end-cap straws are arranged radially in wheels around the beampipe, with straw length 37 cm. Each straw is inter-leaved with transition radiation material and when a charged particle passes through the material boundaries it will emit transition radiation, this provides electron identification information up to $|\eta| < 2.0$ using the transition radiation emitted by the electron. This information is complementary to the measurements from the electromagnetic calorimeters.

3.5 Calorimetry Systems

The calorimetry sub-systems are situated outside the ID and solenoid magnet, shown in Figure 3.4. There are two types of calorimetry used in ATLAS: the electromagnetic (EM) calorimeter, which is placed immediately outside the solenoid, measures the energy of photons and electrons from EM interactions between the particles and the calorimeter material; and the hadronic calorimeter, placed outside the EM calorimeter, which measures the energy of hadrons from strong interactions between the hadrons and the calorimeter material. Due to the amount of material that is required in the ID and to better correct for energy losses caused by particles passing through the calorimeter materials, a presampler is placed in front of all components of the EM calorimeter. The measurements provided by the presampler allows any initial energy lost to be taken into account when calculating the energy in the shower.

Two calorimetry technologies are employed in ATLAS: liquid Argon (LAr) calorimeters, that require cryogenic cooling; and tile calorimeters, consisting of steel as the absorber and scintillator as the active medium. The EM calorimeter is composed exclusively of LAr calorimeters, whereas the hadronic calorimeter system uses tile calorimeters for the barrel region and LAr calorimeters in the end-caps.

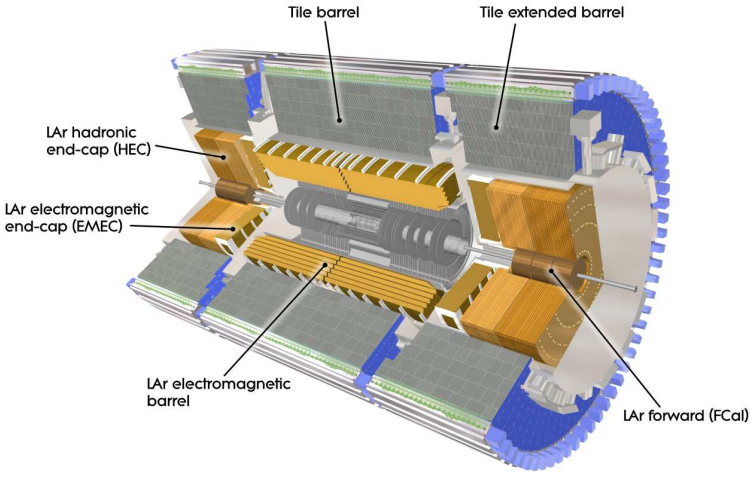

FIGURE 3.4: An overview of the ATLAS calorimetry sub-system. The calorimeter components which use LAr as the active medium are shown in gold, which includes all of the EM calorimeter systems and the forward hadronic calorimeters. The components of the system that use tile scintillators as the active medium are shown in silver. Taken from [55].

The total range covered by the calorimeter systems is $|\eta| < 4.9$, and this coverage is provided by a combination of the barrel and end-cap sections for both systems. Another

important aspect of the calorimeter systems is the thickness, as the calorimeters must be thick enough to contain electromagnetic and hadronic showers. The calorimeter thickness is chosen to be a sufficient amount of interaction lengths (λ) such that the majority of hadronic particle energy would be expected to be expended in the calorimeter. The interaction length is the average length required in which the energy of a hadronic particle will decrease by a factor of $1/e$ due to hadronic interactions. The combined thickness of the calorimeter systems is 11 interaction lengths, which reduces punch-through (showers escaping the calorimeter). This thickness also ensures an accurate calculation of the $E_{\mathrm{T}}^{\mathrm{miss}}$.

The energy resolution requirements of both the EM and hadronic calorimeters are shown in Table 3.2, with the (noise subtracted) energy resolution described by a function of the form:

$$\frac{\sigma(E)}{E} = \frac{a}{\sqrt{E[GeV]}} \oplus b, \tag{3.6}$$

Where a corresponds to the stochastic term related to the shower evolution and b is a constant term taking into account calorimeter response.

Detector Component	Energy Resolution ($\sigma(E)/E$)
EM Calorimeter	$10\%/\sqrt{E} \oplus 0.7\%$
Hadronic Calorimeter Barrel	$50\%/\sqrt{E} \oplus 3\%$
Hadronic Calorimeter Endcap	$100\%/\sqrt{E} \oplus 10\%$

TABLE 3.2: An overview of the energy resolution of the calorimetry systems.

3.5.1 Electromagnetic Calorimeters

As previously stated, the EM calorimeter sub-system is composed entirely of LAr calorimeters. The EM calorimeters are split into three sections: the barrel and two end-caps. The barrel section consists of two half-barrels composed of 1024 accordion-shaped lead absorbers, a sketch of an example barrel module is shown in Figure 3.5. The barrel modules are segmented into three layers with decreasing granularity. The total coverage provided by the barrel calorimeter is $|\eta| < 1.475$. The total thickness of a barrel module (at $|\eta| = 0$) is 22 radiation lengths (X_0), which increases to a maximum of $33\,\mathrm{X}_0$ at $|\eta| = 1.3$. The radiation length X_0 is defined in a similar manner to the interaction length, and is a measure of the electromagnetic energy lost in a material, with

one radiation length corresponding to the distance over which a particle loses $1/e$ of its electromagnetic energy.

The end-cap sections are each composed of two co-axial wheels (referred to as the inner and outer wheels), which are further subdivided into eight accordion-shaped modules. Each end-cap provides further coverage of $1.375 < |\eta| < 3.2$. The end-cap modules are segmented into two layers, again with decreasing granularity. The minimum active thickness of the inner (outer) wheel is $26\,\mathrm{X}_0$ ($24\,\mathrm{X}_0$), which increases to a maximum of $36\,\mathrm{X}_0$ ($38\,\mathrm{X}_0$) as $|\eta|$ increases from 2.5 to 3.2 (1.475 to 2.5).

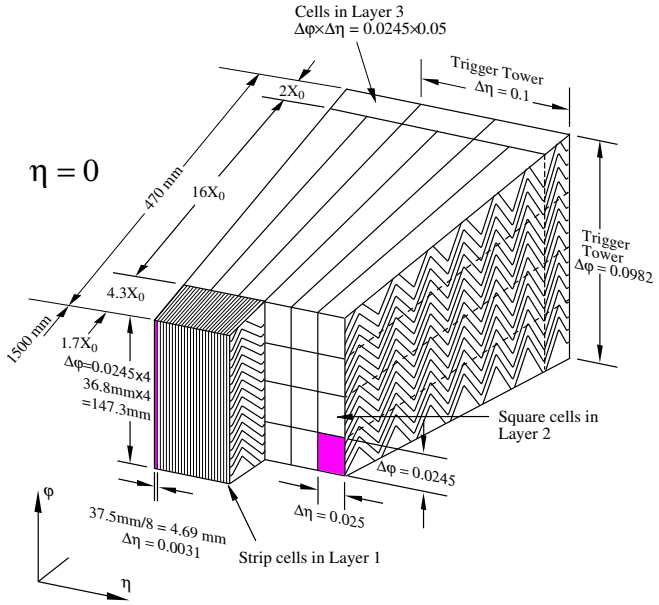

FIGURE 3.5: An example of a LAr calorimeter barrel module. The module is subdivided into three layers: layer one, which has the finest granularity and is read out from the front of the module; layer two, which has an intermediate granularity; and layer three, which has the coarsest granularity. Both layer two and three are read out from the rear of the module. Taken from [55].

This sub-system provides shower shape information to assist in the classification of photons or electrons, and provides measurement of the EM component of hadronic jets.

3.5.2 Hadronic Calorimeters

The hadronic calorimeter sub-system is composed of a tile calorimeter system, implemented in the barrel region, and LAr calorimeters which are implemented in the end-cap regions, similar to the EM calorimeter.

The tile calorimeter (represented as the silver sections in Figure 3.4) is situated outside the EM calorimeter in the barrel region. The central barrel covers $|\eta| < 1.0$ and the extended barrel regions provide additional coverage of $0.8 < |\eta| < 1.7$. Both the

central and extended barrels are split into three layers. The thickness of each layer of the central calorimeter is 1.5, 4.1 and 1.8 λ respectively. The extended tile calorimeter layer thicknesses are 1.5, 2.6 and 3.3 λ.

The hadronic end-cap calorimeters (HEC) are stationed outside the EM end-cap calorimeters, in the same cryogenic system. The HECs use LAr as the active medium and Copper absorbers. Each HEC is composed of two wheels. The total coverage of each wheel is $1.5 < |\eta| < 3.2$, which provides overlap with both the tile calorimeter and the forward calorimeters.

3.5.3 Forward Calorimeters

The forward calorimeters (FCal) are high density LAr calorimeters placed in the far forward regions of the detector. Each FCal is split into three modules. Copper absorbers are used in the first layer to provide EM measurements. The remaining layers use Tungsten absorbers to provide hadronic measurements. The coverage provided by the FCal is $3.1 < |\eta| < 4.9$, with a maximum thickness of 10 λ.

3.6 Muon Spectrometer

The muon sub-system consists of four types of gaseous detectors, with three magnets providing the field required for precision muon identification and p_{T} measurements.

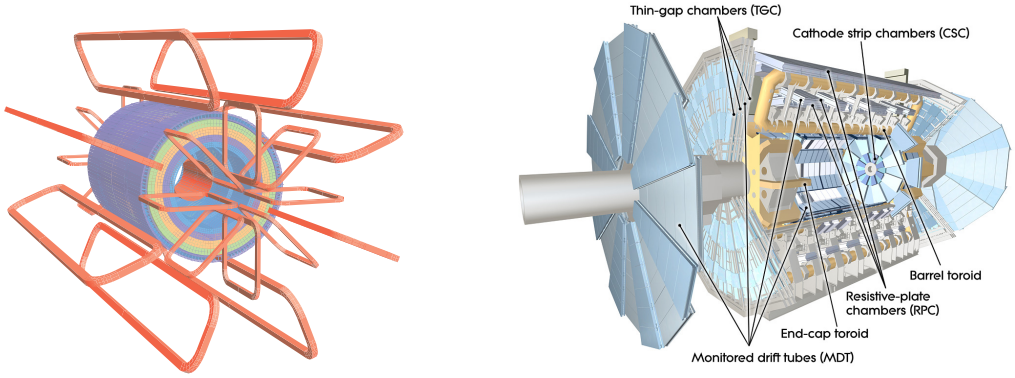

(a) Toroidal magnet system.

(b) Muon detector systems.

FIGURE 3.6: General overview of the muon system. Left: A schematic view of the toroidal magnet system. Right: A general overview of the muon detectors and their location in the detector. Taken from [55].

3.6.1 Toriodal Magnet System

Three air-core toroidal magnets provide the required magnetic field. Each of the toroids is composed of eight coils placed radially and symmetrically around the beam-pipe as shown in Figure 3.6a. One magnet is placed in the barrel region, providing a magnetic field of approximately 0.5 T, exclusively over the range $|\eta| < 1.4$. The two end-cap magnets provide exclusive coverage between $1.6 < |\eta| < 2.7$ with an approximate magnetic field of 1 T. Both of the end-cap magnets and the barrel magnet provide coverage in the range $1.4 < |\eta| < 1.6$, and due to the complicated overlap between the barrel and end-cap magnets in this region, the fields can vary up to $|\delta B| \approx 0.2\,\mathrm{T}$ and are modelled with a dedicated magnetic field simulation package.

3.6.2 Muon detectors

The muon sub-system, Figure 3.6b, consists of four detector technologies. Precision tracking is provided by Monitored Drift Tubes (MDTs) in the barrel region and Cathode Strip Chambers (CSCs) in the end-caps, covering a region of $|\eta| < 2.7$. Resistive Plate Chambers (RPCs) and Thin Gap Chambers (TGCs) are used as triggering chambers in the barrel and end-cap respectively, providing triggering capabilities up to a psuedo-rapidity of $|\eta| < 2.4$.

The MDTs are implemented in three concentric cylinders perpendicular to the beam-pipe. The coverage provided by the innermost layer is $|\eta| < 2.0$, whereas the remaining two layers cover $|\eta| < 2.7$. The number of chambers is 1088, covering a total area of $5500\,\mathrm{m}^2$. Due to the complex geometry of the toroidal magnet system, various designs are used to minimise acceptance losses.

The CSCs are implemented in two disks per end-cap, one small disk and one large disk, which are each segmented into eight chambers. The CSC layers cover the region $2.0 < |\eta| < 2.7$, providing coverage in the region left uncovered by the first layer of MDTs. Each CSC chamber contains four planes, which results in four measurements of η and ϕ for each muon track.

The RPC and TGC triggering chambers are installed in the barrel and end-cap regions respectively. The muon chambers can provide coverage up to $|\eta| < 2.7$ however the triggering sensors only provide triggering capability up to $|\eta| < 2.4$.

3.7 Trigger and DAQ Systems

The dominant process that occurs from the collision of protons is inelastic scattering. The rare physics processes that are targeted by ATLAS occur at a very low rate, and as such need a high luminosity to produce these events in a significance amount. The total integrated luminosity delivered by the LHC during physics data-taking each year from 2011 to 2016 is shown in Figure 3.7.

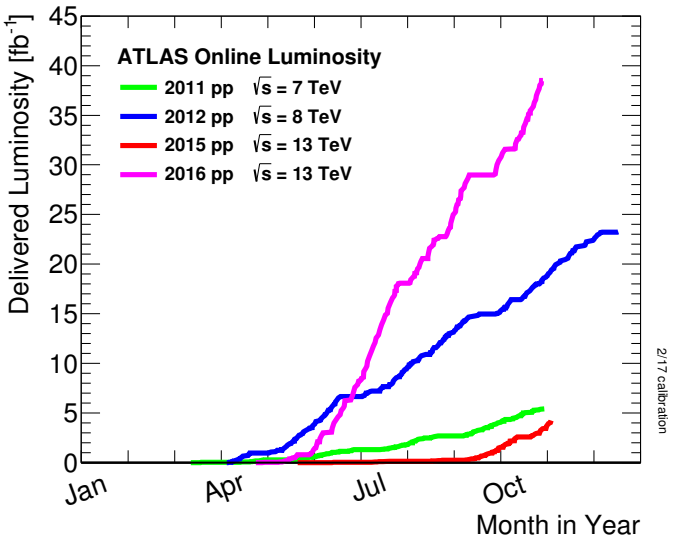

FIGURE 3.7: Luminosity provided by the LHC to the ATLAS detector during Run 1 (2011-2012) and Run 2 to-date (2015-2016). Taken from Ref [61].

A large majority of these events are low p_{T} scattering events that are better studied in short dedicated low luminosity runs. To fully readout these events from the detector and write the events to tape would quickly waste a large amount of storage space and resources. Trigger systems are used to reject events that are copiously produced and instead keep events which contain the rarer physics processes.

The trigger and data-acquisition (TDAQ) system controls the acceptance and rejection of events by ATLAS. A multi-level trigger system, consisting of the Level 1 (L1) hardware trigger and High Level (software) Trigger (HLT) must be passed in order to accept an event. The HLT contains the Level 2 (L2) trigger and event filter (EF). In Run 2 the L2 trigger and EF are combined which provides more efficient event processing than when using two stages. An overview of the ATLAS trigger system is given in Figure 3.8.

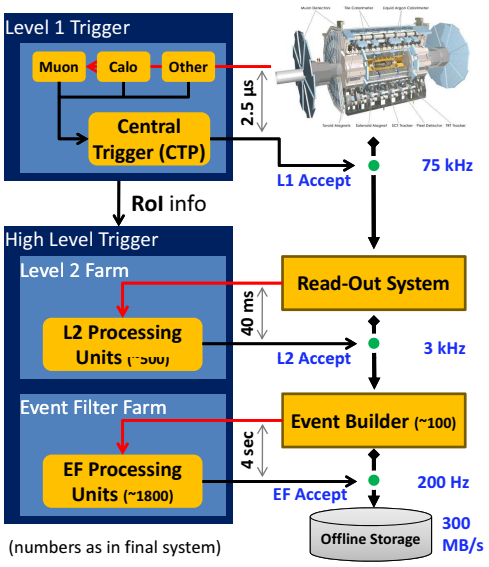

FIGURE 3.8: Schematic of the ATLAS trigger systems, frequencies and time periods correspond to the Run 1 configuration. The final frequency in Run 2 is 1000 Hz. Taken from Ref [62].

The L1 trigger uses calorimeter and muon spectrometer information to measure basic objects such as e, γ, μ, τ and jets, and can detect large $E_{\mathrm{T}}^{\mathrm{miss}}$ or E_{T} based on a reduced detector granularity. The objects measured by the L1 trigger are compared to the trigger menu to check if the objects pass certain thresholds, such as large jet multiplicity or minimum electron p_{T} requirements. In conjunction with this, the L1 trigger defines Regions of Interest (ROIs) which are regions in the detector that are observing hits, for example a deposit in a region of the EM calorimeter. The ROIs are required to coincide with the object that has been triggered upon. This information is used further downstream in the HLT. Prescaling may be applied to the L1 trigger to allow for optimal use of the available bandwidth as instantaneous luminosity increases during data-taking. Prescaling implies that a certain rate is set for the trigger, and if the instantaneous luminosity is too large the trigger will not fire. The L1 trigger decision is made in less than 2.5 μs and if the L1 trigger is passed the L2 trigger subsequently uses the ROI information to investigate the region using the full detector granularity, to further reject or accept events. Finally an event filter is used, processing the events according to ATLAS event reconstruction and analysis. This categorises the events into physics streams for analysis-level usage. The full ATLAS trigger stream has a final rate of 200 Hz (Run 1) or 1000 Hz (Run 2) and each event is 1.3 MB on average.

The trigger system is closely linked with the DAQ system, as the levels of trigger acceptance correspond to different readout stages of the DAQ system. Whilst each sub-detector has its own specific electronics, they all obey a general set of requirements.

The specialised front-end electronics readout the event data from the sub-detector, storing the information in buffers for a time period corresponding to the L1 trigger latency. If the event passes the L1 trigger, then the data is sent further through the DAQ chain. The next stage is the readout drivers (RODs), which format the data in a standard format for usage in ATLAS. The data from the RODs is subsequently stored in readout buffers (ROBs) which store the data for usage by the HLT. If the trigger is passed, the data is subsequently moved to the event filter to reconstruct the event, and then the data is passed to the CERN computer centre for storage and offline reconstruction.

Another important component of the TDAQ system is the ability to feedback to a detector sub-system any errors that may be occurring. For example if a module is reporting a constantly high trigger rate (regardless of the event), then it is possible that the module is experiencing an error. The relevent detector sub-system will be notified of this error, and action can be taken to recover the module.

3.8 SCT DAQ Module Recovery application

As a component of detector work undertaken as part of this thesis, an online module recovery application was developed to recover SCT modules that were experiencing errors due to single event upsets during physics data-taking. This section contains a brief overview of the Run 1 data quality efficiency of the SCT subsystem. A simple description of how a hit is registered in a module is given, with an explanation of how energetic radiation passing through the module can affect the readout. The methods to negate these effects are presented, with the improvements from Run 1 to Run 2 discussed.

During LHC Run 1 the SCT performed exceptionally well achieving an average Data Quality (DQ) efficiency greater than 99%. However, it can be seen in Table 3.3, as Run 1 progressed, the efficiency of the detector decreased. There are several explanations for this decrease in DQ efficiency. One of them is the so-called SCT “hit loss” problem, caused by a desynchronisation of the SCT with the rest of ATLAS. The source of the

desynchronisation was found to be due to the "module recovery" actions which are used to restore the hit threshold of any module that has been affected by a single event upset.

	2010	2011	2012
DQ Efficiency (%)	99.9	99.6	99.1

TABLE 3.3: The data quality efficiency of the SCT subdetector for the three years of Run 1.

The SCT sensors use a binary readout to decide if a charged particle has passed through the sensor. A threshold is set based upon the charge collected in the sensor. If a particle passing through the sensor deposits charge greater than this threshold the module registers a hit. If a highly energetic particle passes through the electronics of a module it can cause a bit-flip, resulting in a change in the hit threshold of the module, this is known as a single event upset (SEU). There are two possible effects of changing the threshold, both of which affect DQ efficiency.

If the threshold is decreased, then a module will report hits which are not true hits, but are due to residual module noise which passes the lowered threshold. Alternatively if the threshold is raised, then the module will not report any hits below the new (increased) threshold, again affecting the DQ efficiency as the module will now not register a hit from a particle that would otherwise register a hit if the original threshold was still in place. Both of the above scenarios affect tracking and reconstruction resulting in a lower DQ efficiency.

There are two types of recovery command that are used: the single module recovery command, which will reset a specific module; and the global recovery command, which resets all SCT modules. Both procedures aim to bring back online modules which may be exhibiting an error due to SEUs.

The single module recovery is used if the threshold of a module has been decreased. In this scenario the module will report a large amount of noise in comparison to the neighbouring modules. The module will be identified as noisy and experiencing an error by the TDAQ system, and can be recovered by a single module reset. Initially a soft-reset command is used to recover the error. If the error still persists after multiple soft-resets, a hard-reset command is sent to the module. If this fails, then a power-cycle command is sent to the module as a last resort to reload the module configuration. If

the module is still in error after this, then it is no longer recovered for the remainder of the physics run.

The global module recovery is used in the scenario where the threshold has increased. These cases cannot be detected as the increased threshold will cause the module to stop reporting hits. As a precaution and to recover modules experiencing this error, the global module recovery command is sent to all modules every 30 minutes of physics running.

It was found that the desynchronisation effect of the global recovery command was caused by the command being queued by the SCT shifter graphical user interface (GUI), instead of being sent immediately.

To prevent this queuing, an independent DAQ application was developed to control both the single and global module recovery commands. In addition to this, the application tracks the number of single module recoveries that have been performed on all modules, reporting this information back to the TDAQ system. The intial iteration of the recovery application was introduced prior to the 2015 *pp* data-taking, which included both the single and global module recovery functionalities.

As the 2015 data-taking progressed, additional functionalities were added to the application, with the introduction of the ability to automatically recover RODs that were experiencing errors. It is possible that during running a ROD itself may experience an error when attempting to format the data readout by the SCT front-end electronics.

When a ROD experiences an error, it is reported to the central TDAQ system. During Run 1 this information was used by the SCT shifter GUI, to request that the shifter recover the ROD. However with the introduction of the module recovery application, it was found to be more beneficial to recover the ROD automatically within the module recovery application. This reduced the time that the ROD would be experiencing an error, due to the speed of the automated recovery, when compared to the manual recovery by a shifter.

	2012	2015	2016
DQ Efficiency (%)	99.1	99.4	99.9

TABLE 3.4: The data quality efficiency of the SCT subdetector for the final year of Run 1 and the two years of Run 2 data-taking.

Table 3.4 presents an overview of the increase in DQ efficiency in Run 2 when compared to the final year of Run 1 data-taking. It can be seen that during Run 2 data taking the DQ efficiency is increased when compared to the final year of Run 1. Further to this, the data taking period in 2016, corresponding to the first full period of data-taking when the module recovery application was fully implemented (including the additional ROD recovery functionality), has an increased DQ efficiency when compared to the 2015 data taking period.

Chapter 4

Modelling of Physics Processes

4.1 Introduction

The Lagrangian formalism introduced in Chapter 2 allows for the calculation of cross sections for SM and BSM processes. For data analysis it is of fundamental importance to use these calculations and convert them to complete simulated events via Monte Carlo (MC) simulation. Dedicated MC samples are used to study possible new physics signals and to aid in the estimate of SM backgrounds in new physics searches. Many considerations must be taken into account when modelling proton-proton collisions. The stages of modelling a proton-proton collision using Monte Carlo generators are discussed in this chapter. General aspects of modelling, and the event definition in terms of the hard scatter process, parton shower, and hadronisation are discussed.

The aspects of MC modelling that may cause uncertainties in the prediction and lead to a systematic uncertainty are introduced, along with the methods to evaluate these uncertainties. Further to this the evaluation of process specific modelling uncertainties are discussed in the context of single-top (Wt-channel) and top-pair ($t\bar{t}$) production. Finally a parameterisation method for evaluating the modelling uncertainties on associated production of W or Z-bosons with jets is presented.

4.1.1 Factorisation Theorem

Protons are not point-like particles, however, they consist of point-like quarks and gluons, which are collectively referred to as "partons". The parton model [63] allows for the calculation of the cross section of the hard scattering process as the incoherent sum

of all partonic cross sections, integrated over the available phase space, an example of which is shown in Equation 4.1:

$$\sigma_{a,b\to n} = \sum_{a,b} \int_0^1 dx_a dx_b f_a^{(P1)}(x_a, \mu_F) f_a^{(P2)}(x_a, \mu_F) d\hat{\sigma}_{ab\to n}(x_a, x_b, s, \mu_F, \mu_R). \quad (4.1)$$

In this equation the $f_i^{(Pi)}(x_i, \mu_F)$ terms correspond to the Parton Distribution Functions (PDFs), which can be considered to be the probability to find a parton (i) with a fraction of the proton's total longitudinal momentum x_i (also known as the Bjorken x), for a given choice of factorisation scale (μ_F).

The factorisation scale is introduced to protect against divergent contributions to the cross section by adding an arbitrary separation. This factorises the hard process which is calculable using perturbative-QCD (pQCD), from the universal parton evolution within the proton. The partonic cross section $\hat{\sigma}(x_a, x_b, s, \mu_F, \mu_R)$ can be calculated in pQCD for the process of interest, and depends on both the factorisation scale, and the renormalisation scale (μ_R), which is the energy scale at which the strong coupling constant is evaluated. Typically $\mu_R = \mu_F$ and is chosen to be a representative energy scale of the process.

Proton PDFs cannot be calculated from first principles and instead need to be determined using experimental inputs. Among these, deep inelastic scattering (DIS) data are most relevant and *ep* data collected by the H1 and ZEUS [64] collaborations with the HERA collider [65] cover the Bjorken x range most relevant to LHC physics. In addition, data on the production of jets, $t\bar{t}$, the electroweak bosons in hadron-hadron collisions are used.

An example PDF set is shown in Figure 4.1, at two different values of Q^2, produced using a combination of the H1 and ZEUS data [66]. The data used in PDF fits cover a wide range of Bjorken x and negative four-momentum-transfer squared (Q^2). The PDFs constrained at low Q^2 can be evolved in Q^2 using pQCD and the Dokshitzer-Gribov-Lipatov-Altarelli-Parisi (DGLAP) equations [67]. When performing an analysis the uncertainty arising from the choice in PDF set is evaluated by calculating an envelope of the uncertainties on the individual partons from the nominal PDF set, and the central values of alternative PDF sets, as recommended by the PDF4LHC working group [68].

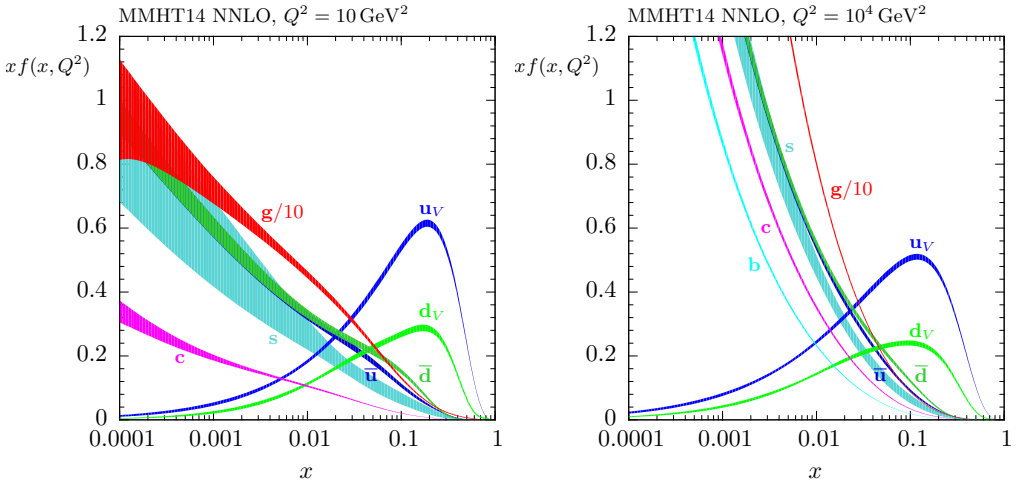

(a) $Q^2 = 10\,\mathrm{GeV}^2$ (b) $Q^2 = 10^4\,\mathrm{GeV}^2$

FIGURE 4.1: Comparison between a PDF set calculated at different Q^2 values. The individual contributions from the quarks and gluons are shown, u_V and d_V correspond to the specific contribution from the valence quarks. Taken from [66].

4.1.2 The hard scattering process

The cross section for a generic $2 \to 1$ scattering process (Equation 4.1) can be rewritten introducing the matrix element (ME), $\hat{\sigma}_{a,b\to n} = \mathcal{M}_{ab\to n}$:

$$\sigma_{ab\to n} = \sum_{a,b} \int_0^1 dx_a dx_b \int d\Phi_n f_a^{(P1)}(x_a,\mu_F) f_b^{(P2)}(x_b,\mu_F) \times \frac{1}{2\hat{s}} |\mathcal{M}_{ab\to n}|^2 (d\Phi;\mu_F,\mu_R), \tag{4.2}$$

This depends upon the final-state phase space momenta available ($d\Phi_n$), the matrix element, the Bjorken x of both particle a (x_a) and particle b (x_b), and the incoming parton flux ($1/2\hat{s} = 1/(2x_a x_b s)$). Generically, the matrix element can be written as the sum over all relevent Feynman diagrams ($\mathcal{F}_{ab\to n}$):

$$\mathcal{M}_{ab\to n} = \sum_i \mathcal{F}_{ab\to n}^{(i)} \tag{4.3}$$

A consequence of this is that the summation over quantum numbers such as helicity and colour can be moved and considered separately to the $|\mathcal{M}|^2$ term. The calculation of the hard process can be performed at various levels of accuracy, depending on the order in QCD coupling of the diagrams. A matrix element calculation at Leading-Order (LO) is nowadays completely automated and fast. Since 2000 huge progress has been made in developing automated Next-to-Leading-Order (NLO) calculations. Improvements in

the algorithms used for the calculations and advances in the understanding of the theory have allowed the majority of processes to be calculated at NLO in an automated way. In the last few years many NNLO (Next-to-Next-to-Leading-Order) calculations exist which are calculated mostly analytically and are used for global corrections rather than in MC simulation.

The matrix element is calculated in multiple ways by various MC generators. These differences are taken into account during an analysis as an uncertainty arising from the choice of generator used. Due to the dependence of $\mathcal{M}$ on both the renormalisation and factorisation scales, it is also possible to vary the choice of scale up and down with respect to the nominal scale choice, to evaluate the hard scattering uncertainty. By convention the scale choices are varied up and down by a factor of two.

4.1.3 Parton shower algorithms

The above discussed fixed order QCD calculations do not produce complete scattering events and specifically only produce a small number of quarks and gluons in the final state, while the experimentally observed final states contain jets of hadrons.

Parton showering algorithms provide a higher order way to generate complete events and to estimate higher order effects, without explicitly calculating the matrix elements. This is a necessary addition to the hard process, to model events beyond inclusive observables and allow the description of exclusive final states. Parton shower algorithms take higher order effects into account, by allowing soft and co-linear QCD emissions from the interacting partons produced in the hard process.

Particles produced in the hard scattering process undergo an evolution in momentum transfer, from the energy scale of the hard scatter itself, down to the hadronisation scale. The evolution of the momentum transfer proceeds via the emission of either quarks or gluons.

For simplicity, consider the $e^+e^- \to q\bar{q}$ process, for which the cross section ($\sigma_{q\bar{q}}$) can be calculated at LO. To expand this process to the next order in accuracy using the parton shower method, requires the emission of a parton, for example a gluon, from one of the quarks, and the calculation of the relevant cross section $\sigma_{q\bar{q}g}$. This can be considered differentially in terms of the opening angle (θ) between the quark and the emitted gluon, and the fraction of the quark's energy (z) that the gluon possesses [69]:

$$\frac{d\sigma_{q\bar{q}g}}{d\cos\theta dz} \approx \sigma_{q\bar{q}}\, C_F\, \frac{\alpha_s}{2\pi}\, \frac{2}{\sin^2\theta}\, \frac{1+(1-z)^2}{z}, \tag{4.4}$$

where C_F is a colour factor that can be thought of as the quark colour charge, squared. The vital component of the above equation is the fact that the differential cross section of the $q\bar{q}g$ process is dependent upon that of the $q\bar{q}$ process. The remaining components of Equation 4.4 can be interpreted as the probability of emission of a gluon differentially in terms of the kinematics of the gluon. While this underpins the basic method behind parton shower algorithms, the divergences in the equation must also be dealt with, before it can be applied. It is seen that if $\theta = 0, \pi$ (co-linear limit) then Equation 4.5 is divergent, additionally if $z = 0$ ("soft" limit) the equation is divergent. In order to prevent these divergences, a "cut-off" must be applied, such that the individual partons from the splitting are required to be resolved. A commonly used, but not the only, resolution variable is the transverse momentum, and a "cut-off" Q_0 is applied, which removes both divergences from θ and z.

Before this method can be fully expanded is useful to rewrite the distribution as the sum of two distributions, one which is divergent when $\theta = 0$, and the other when $\theta = \pi$. The resultant summation (over the partons) is given by:

$$d\sigma_{q\bar{q}g} \approx \sigma_{q\bar{q}} \sum_{\text{partons}} C_F\, \frac{\alpha_s}{2\pi}\, \frac{d\theta^2}{\theta^2}\, dz \frac{1+(1-z)^2}{z}. \tag{4.5}$$

A similar treatment can be applied to the remaining emission processes ($g \to gq$, $g \to g\bar{q}$, $q \to q\bar{q}$). This provides the foundations to perform co-linear splitting and soft emission of the partons from the hard process, which can then be implemented in an algorithm.

The final aspect to be considered to achieve the full implementation of a parton shower algorithm is the point at which to stop showering the partons, which corresponds to the energy at which the partons will no longer be able to emit. This is given by the probability that a parton will no-longer produce resolvable branchings, and is given by the Sudakov form factor [70]:

$$\Delta_i(Q^2, Q_0^2) = \exp\left\{ -\int_{Q_0^2}^{Q^2} \frac{dk^2}{k^2}\, \frac{\alpha_s}{2\pi} \int_{Q_0^2/k^2}^{1-Q_0^2/k^2} dz \mathcal{P}_{ji}(z) \right\}, \tag{4.6}$$

where $\mathcal{P}_{ji}(z)$ are a set of universal, flavour dependent functions [71]. The above equation allows the end point of the algorithm to be defined using the point where there is a zero probability of producing a resolvable branching, with the transverse momentum

(k) running from the lower p_{T} cut off (Q_0) to the input parton p_{T} (Q). It follows that one minus the equation gives the probability of the first emission, which is the starting point of the algorithm. Due to the probabilistic nature of parton shower algorithms and the multiple non-trivial physics choices that can be made when implementing the algorithm, there is a certain arbitrariness when designing the algorithm, therefore it is usual to compare two different but equivalent PS algorithms to assess the uncertainties, for example comparing Pythia6 [72] with Herwig++ [73]. A difference in these algorithms is the variable used to calculate the evolution of the shower (in Equation 4.6 the transverse momentum is used). This is a choice that is made when designing the algorithm, for example Pythia6 orders the showers based upon the transverse momentum, whereas Herwig++ uses angular-ordering. An alternate method to estimate the uncertainty of a single PS algorithm is to vary the gluon resummation scale up and down with respect to the nominal value.

4.1.4 Matrix element matching

It is clear that the hard scattering calculation and the parton shower method should be used in a complimentary manner, with the hard scatter calculation describing the hard partons produced directly at the matrix element, and the PS method describing the emission of softer gluons and quarks. The hard scattering calculation is useful to describe hard partons that are well separated, whilst the parton shower method can describe co-linear and soft emissions. Combining the two approaches will provide a more complete description of an event. This is simple when considering a LO ME calculation, however, this is non-trivial when considering NLO (or higher) ME calculations. The simple addition of a parton shower to an NLO hard scatter event is not possible as the hard scatter event is generated exclusively in terms of the number of partons, whereas the parton shower is inclusive in parton number. Another issue is possible double-counting of regions of phase space.

Generally there are two methods, matching and merging, that are used to combine the hard scatter and the parton shower. Matching methods seek to correct the hardest emissions from the parton shower, which can also change the NLO cross section. Merging methods introduce a scale dependence (known as the merging scale): above this scale the partons are generated from the matrix element, below the scale from the parton shower.

When performing the matching between the parton shower and the matrix element there are two main effects. Firstly, as previously mentioned, the total cross section changes. Secondly, the shape of distributions related to the hardest emission are modified. Since there is again a certain arbitrariness in the choice of matching scale and other related parameters, which are usually set depending upon the partons produced, systematic uncertainties arise. There are multiple assumptions that can be made when performing the matching between the matrix element and the parton shower. The uncertainty from these assumptions are taken into account by comparing different generators in a similar manner to that of the hard scattering.

When performing the merging method, the uncertainty due to the choice of merging scale is estimated by varying the scale up and down by a factor of two with respect to the nominal. For example, when evaluating the ME matching uncertainty for the signal samples, the parameter used for parton clustering is varied up and down by a factor of two.

4.1.5 Hadronisation

After an event has proceeded via a parton shower algorithm, the remaining partons which are unable to undergo further splitting must then hadronise. The method of proceeding from the unphysical parton state, to the physically observed hadronic state is known as "hadronisation". As the process of hadronisation occurs at the level of non-perturbative QCD, it cannot be calculated from first principles. Primarily two distinct methods exist to model the hadronisation process: the string model [74] and cluster model [75].

The string model is based upon the assumption of linear confinement. For example, a $q\bar{q}$ pair can be considered to be the end-point of a string of colour-flux. The potential energy of the string (V) is proportional to the linear separation of the $q\bar{q}$, with $V(r) = \kappa r$ due to the assumption of confinement. As the $q\bar{q}$ move further apart along the string axis, eventually the energy in the string may be such that a new pair of quarks are formed, $q'\bar{q}'$. This new pair of quarks will create two colour singlet pairs, $q\bar{q}'$ and $q'\bar{q}$, with a region absent of field between them. These new pairs of quarks may themselves split further, until the energy left in the subsequent quark systems is too small to create further pairs. In the case where gluons are also present, they can be considered to be "kinks" in the string, however the principle of the string-splitting remains the same.

The cluster model is based upon an inherent property of parton shower algorithms, known as the "preconfinement property". The preconfinement property states that at any scale (Q) of a parton shower algorithm, the colour structure of a shower is such that colour singlet combinations of partons can be formed with a universal asymptotic invariant mass distribution. In this case universal means dependent upon only Q_0 (the shower resolution scale) and the hadronisation scale (Λ). Asymptotic refers to the requirement that $Q \gg Q_0$. If it is further required that $Q_0 \gg \Lambda$, then the mass distribution can be calculated perturbatively. Hadronisation models based on preconfinement use non-perturbative splitting of gluons at the resolution scale. Adjacent colour lines then become $q\bar{q}$ pairs and can form clusters which are mesons. This method leads to a natural link between the partons from the cut-off scale, and those from the hadronisation process. The splitting of the gluon into quarks is non-trivial and introduces caveats, such as the choice of momentum for the resultant quarks and the flavour distributions. Another available choice is the method of how the clusters proceed to the final state baryons and mesons. Generally, this proceeds via a two-body decay to lighter states according to the relevant branching ratios etc, however the kinematics in this region surpresses heavy flavour/strangeness and baryon production.

Both models have their drawbacks. A drawback of the string model is that there are many unknown parameters related to flavour properties, that must be determined directly from data. A problem with the cluster model is that it produces clusters at low mass, but there is a high mass tail from events with only a small amount of showering. A comparison between these options reveals that the string model describes data slightly better; however, this is at the cost of requiring many parameters to be "tuned" to data. The cluster model provides acceptable modelling with a minimal set of unknown parameters. A final drawback of both models is that neither model are able to take into account possible collective behaviour of the hadrons such as in a quark-gluon plasma [76]. The uncertainty due to the hadronisation modelling is evaluated by varying the tuning parameters used as an input.

4.2 General overview of Monte Carlo modelling

Due to the substructure of protons and the properties of QCD, modelling proton-proton collisions is a difficult task. Considerations which must be taken into account include the interactions between the quarks and gluons inside the colliding protons, initial and

final state radiation of partons involved in the hard scattering, and the modelling of additional (secondary) interactions in the collision. The modelling of a proton-proton collision event can generally be divided into three main stages, described by Figure 4.2:

- Hard scattering process

  This is the primary interaction of two partons from the protons. The production cross section for a generic $q\bar{q}, qq', gq, qq, gg \rightarrow X$ process is calculable at using pQCD as discussed in 4.1.1. In Figure 4.2 the hard process considered is the interaction between two gluons (blue) from the incoming protons, producing a top pair in association with a Higgs boson at the large red circle. Each particle in the $t\bar{t}H$ system subsequently decays at the smaller red circles.

- Parton Shower (PS)

  Later in the event is the shower evolution (PS), where any strongly-interacting particles can radiate either gluons and quarks. The PS stage is represented by the red particles in the figure.

- Hadronisation

  The final step in an event is the hadronisation stage (green objects). In this stage the strongly-interacting particles from the hard scatter and PS stages have lost energy and are at a low momentum. In this regime perturbative QCD breaks down. At this stage the strongly-interacting particles are grouped together to form colourless hadrons, which are measured in the detector. In MC the hadronisation stage is modelled using data as hadronisation cannot be analytically predicted.

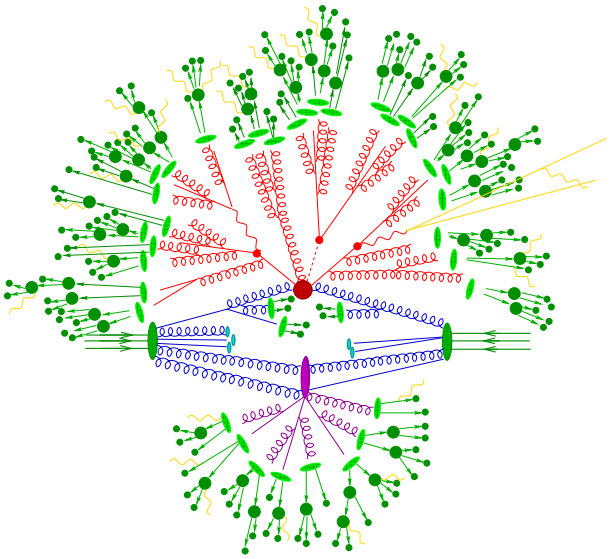

FIGURE 4.2: An example of the stages involved in a generic proton-proton event. Gluons and quarks from the initial protons are shown in blue. The hard scatter process (in this case $t\bar{t}H$ production) is the large red circle, with the subsequent decays and QCD radiation, forming the PS, in red. The hadronisation stage is in green. Yellow objects denote QED radiation. An additional (pile up) interaction is shown in purple. Figure taken from [77]

Further to the stages described above, charged particles may emit EM radiation at any point in the event (yellow objects). It is also possible that an additional interaction (purple) occurs in a collision which arises from the partons in the interacting proton, this is commonly referred to as a multiple parton interaction (MPI) or underlying event (UE). These interactions are of limited physics interest but can occur in a collision and must be modelled.

In addition to MPI interactions, it is possible that collisions occur between other protons in the colliding bunch. These collisions are referred to as "pile-up" interactions. The average number of pile-up interactions in an event, $\langle\mu\rangle$, is dependent upon the centre of mass energy of the collision, the bunch spacing configuration used in the LHC and other accelerator parameters. For the Run 1 data, $\langle\mu\rangle \approx 20$. The collision data collected at the beginning of Run 2 (2015) used a 50 ns bunch spacing which was subsequently reduced to 25 ns, resulting in $\langle\mu\rangle \approx 14$. During 2016, a bunch spacing of 25 ns was used throughout data taking, resulting in $\langle\mu\rangle \approx 24$.

4.2.1 MC Generators Used

The most used generators for the studies presented in this thesis are listed below with a brief overview of the usage of the generator and its properties. The number of expected

events for a given process using a MC generator is calculated using Equation 4.7:

$$N_{\text{Expected Events}} = \frac{\mathcal{L}_{\text{data}} \cdot sf \cdot \sigma_{\text{process}} \cdot \epsilon \cdot k}{\mathcal{L}_{\text{generated}}} \cdot N_{\text{Raw Events}}. \tag{4.7}$$

For a given analysis selection the number of expected events is dependent upon: the total luminosity collected by the detector ($\mathcal{L}_{\text{data}}$), which the MC is being compared to; the cross section of the process under consideration (σ_{process}); scale factors (sf) that need to be applied to the MC, as discussed in Section 5.1, to correctly model the response of the detector; the efficiency (ϵ) of any filters used during the generation of the sample; the k-factor (k), which is used to scale the cross section from NLO to NNLO if applicable; and the number of unscaled MC events ($N_{\text{Raw Events}}$) passing the selection.

Sherpa

The Sherpa event generator [77] performs ME calculation at NLO for up to two partons, with four additional partons able to be generated at LO using the Comix [78] and OpenLoops [79] matrix element generators. This is interfaced to an internal PS algorithm [80] according to the ME+PS@NLO prescription [81]. Sherpa is used predominantly to model the Z+jets and W+jets processes where a global k-factor is used to scale the NLO ME calculation to NNLO. It is also used to model the γ+jets process at LO. Depending on the version of Sherpa used in the analysis either the CT10 PDF set [82] (for version 2.1) or the NNPDF3.0NNLO PDF set [83] (for versions 2.2 and above) is used.

Powheg

The Powheg [84, 85, 86] generator performs ME calculations at NLO for a variety of processes. In this analysis it is used to generate the $t\bar{t}$ and single-top processes. This is subsequently interfaced to a PS algorithm. The ME calculation uses the 5 flavour scheme (5FS), with massless $b-$quarks in the intial state using the CT10 PDF set. The top-quark mass is set to 172.5 GeV when generating events.

MadGraph_aMC@NLO

MadGraph_aMC@NLO [87] calculates the ME at LO with the emission of up to two additional partons, and is interfaced with a PS algorithm (usually Pythia8), using the CKKW-L matching prescription [88]. MadGraph is used to generate the BSM signal samples, and also the SM $t\bar{t} + V(V = W/Z)$ processes. The NNPDF2.3LO PDF set is used in the ME calculation.

Pythia

Currently two versions of Pythia are in use, Pythia6 and Pythia8 [89]. Pythia is able to be used as a LO ME generator to generate the SM multi-jet process. More commonly however, Pythia is used exclusively as a PS and hadronisation program, used for showering events that have been generated via a different higher order ME generator (such as Powheg and MadGraph). The PDF set used by Pythia6 is CTEQ6L1 [90], whilst Pythia8 uses the NNPDF2.3LO PDF set.

Herwig++

Herwig++ is able to be used as a NLO ME generator for a variety of processes, however similarly to Pythia, it is predominantly used as a shower and hadronisation algorithm interfaced to other higher order ME generators.

The remainder of this Chapter discusses the studies investigating the MC modelling of dominant processes for the physics analyses presented herein. An overview of the investigation of the modelling of top production processes is presented, seeking to quantify the interference effects between the single-top Wt-process and top-pair production. In addition to this, the production of a parameterisation for the Sherpa V+jets modelling uncertainties are presented.

4.3 Modelling the single-top Wt-process

In addition to the sources of uncertainty that arise due to the choices made when defining the MC setup for a certain process, there are specific physics processes that require the evaluation of additional uncertainties, due to the uncertainty on the treatment of the process itself at the lowest order. An example of this in context of the analyses presented within this thesis is single-top Wt-channel production.

Figure 4.3 compares two Feynman diagrams to present the interference effects between $t\bar{t}$ and single-top Wt generated at NLO. From the hard scattering process it can be seen that both processes may produce a $WWbb$ final state.

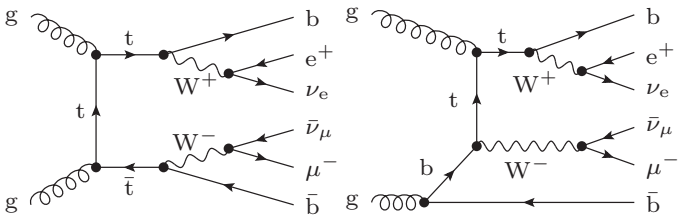

FIGURE 4.3: Feynman diagrams representing $t\bar{t}$ (left) pair production at LO, and single-top Wt-channel production at NLO. Taken from [91].

Difficulties arise when producing the hard scattering processes that correspond to these processes in certain regions of the phase space, most noticably in the region of phase space where the invariant mass of the W-boson and b-quark approaches the top-quark mass [91].

Consider a generic $p_a p_b \to Wt+\delta$ production process, where δ can be considered to be the remaining particles in the process, and denote the amplitude of this process as $\mathcal{A}_{a,b}$. This amplitude can be considered to be the sum of the two processes, $t\bar{t}$ ($\mathcal{A}^{t\bar{t}}_{a,b}$) where the top-quarks produced are doubly-resonant (both top-quarks are on-shell), and single-top Wt ($\mathcal{A}^{Wt}_{a,b}$) where only one top-quark is on-shell (referred to as singly-resonant):

$$\mathcal{A}_{a,b} = \mathcal{A}^{Wt}_{a,b} + \mathcal{A}^{t\bar{t}}_{a,b}. \tag{4.8}$$

The calculation of the matrix element for this process leads to an expression of the form:

$$|\mathcal{A}_{a,b}|^2 = |\mathcal{A}^{Wt}_{a,b}|^2 + |\mathcal{A}^{t\bar{t}}_{a,b}|^2 + 2\Re(\mathcal{A}^{Wt}_{a,b}\mathcal{A}^{t\bar{t}*}_{a,b}), \tag{4.9}$$

which can be rewritten as the sum of three contributions: $\mathcal{S}_{a,b}$, the contribution from the singly-resonant single-top (Wt) process; $\mathcal{D}_{a,b}$, the contribution from the doubly-resonant $t\bar{t}$ process; and $\mathcal{I}_{a,b}$, which is the interference term between the Wt and $t\bar{t}$:

$$|\mathcal{A}_{a,b}|^2 \equiv \mathcal{S}_{a,b} + \mathcal{D}_{a,b} + \mathcal{I}_{a,b}. \tag{4.10}$$

A differential cross section for this process can now be evaluated, taking into account soft/colinear singularities that may arise in the calculation of $\mathcal{S}_{a,b}$, and including the phase space ϕ_3 and beam energy (s). In cross section definition used, $d\hat{\sigma}_{a,b}$, the infrared singularities have been removed from the singly-resonant process (denoted $\hat{\mathcal{S}}_{a,b}$). As the doubly-resonant process does not contain IR singularities, and the infrared singularities

are sub-leading in the interference term, these terms remain unchanged in the cross section definition:

$$d\hat{\sigma}_{a,b} = \frac{1}{2s}(\hat{\mathcal{S}}_{a,b} + \mathcal{I}_{a,b} + \mathcal{D}_{a,b})d\phi_3, \tag{4.11}$$

the resultant production cross section, summing over the initial state particles is:

$$\begin{aligned} d\sigma &= d\sigma^{(2)} + \sum_{a,b} \int dx_1 dx_2 \mathcal{L}_{a,b}\, d\hat{\sigma}_{a,b} \\ &= d\sigma^{(2)} + \sum_{a,b} \int \frac{dx_1 dx_2}{2x_1 x_2 S} \mathcal{L}_{a,b}\, (\hat{\mathcal{S}}_{a,b} + \mathcal{I}_{a,b} + \mathcal{D}_{a,b})d\phi_3. \end{aligned} \tag{4.12}$$

This expression contains the quantity $d\sigma^2$ which includes contributions to the cross section that are not included in Equation 4.11, the parton-parton luminosity ($\mathcal{L}_{a,b}$) and partonic centre of mass energy squared (S).

From this point it is possible to define two approaches to estimate the cross section, the Diagram Removal (DR) scheme and the Diagram Subtraction (DS) scheme, described below.

4.3.1 Diagram Removal Scheme

In the DR scheme the doubly-resonant amplitude ($\mathcal{A}^{t\bar{t}}_{a,b}$) is removed from the matrix element calculation. A consequence of this is the removal of the $\mathcal{I}_{a,b}$ and $\mathcal{D}_{a,b}$ terms in the cross section calculation. The resultant cross section (Equation 4.13 corresponds to the production of an on-shell top quark, a W-boson and a b-quark, where the W-boson and b-quark are produced away from the top-quark mass:

$$d\sigma^{\mathrm{DR}} = d\sigma^{(2)} + \sum_{a,b} \int \frac{dx_1 dx_2}{2x_1 x_2 S} \mathcal{L}_{a,b}\, (\hat{\mathcal{S}}_{a,b})d\phi_3. \tag{4.13}$$

This cross section violates gauge invariance, however, the gauge dependence of the above cross section has been tested and found to be negligible.

4.3.2 Diagram Subtraction Scheme

In the DS scheme, a constant numerical contribution to the cross section, σ^{subt}, is removed from Equation 4.12. This numerical value represents the cross section contribution when both top-quarks are on-shell. This corresponds to:

$$d\sigma^{\mathrm{DS}} = d\sigma - d\sigma^{subt}. \tag{4.14}$$

where the subtraction term is defined as:

$$\begin{aligned} d\sigma^{subt} &= \sum_{a,b} \int dx_1 dx_2 \mathcal{L}_{a,b}\, d\sigma^{subt}_{a,b}, \\ d\sigma^{subt}_{a,b} &= \frac{1}{2s}\tilde{\mathcal{D}}_{a,b}\, d\phi_3. \end{aligned} \tag{4.15}$$

The $\tilde{\mathcal{D}}$ term is related to the doubly-resonant amplitude in a way, such that when the invariant mass of the W-boson and b-quark tends to the top-quark mass, the following equation is satisfied:

$$\mathcal{D}_{a,b} - \tilde{\mathcal{D}}_{a,b} = 0. \tag{4.16}$$

With the expression in Equation 4.15, the cross section for the DS scheme can be rewritten in a similar form to that of the DR scheme:

$$d\sigma^{\mathrm{DS}} = d\sigma^{(2)} + \sum_{a,b} \int \frac{dx_1 dx_2}{2x_1 x_2 S} \mathcal{L}_{a,b} \left(\hat{\mathcal{S}}_{a,b} + \mathcal{I}_{a,b} + \mathcal{D}_{a,b} - \tilde{\mathcal{D}}_{a,b}\right) d\phi_3. \tag{4.17}$$

It is seen by inspection of Equations 4.13 and 4.17 that the cross sections for the DR and DS schemes differ by:

$$d\sigma^{\mathrm{DS}} - d\sigma^{\mathrm{DR}} = \sum_{a,b} \int \frac{dx_1 dx_2}{2x_1 x_2 S} \mathcal{L}_{a,b} \left(\mathcal{I}_{a,b} + \mathcal{D}_{a,b} - \tilde{\mathcal{D}}_{a,b}\right) d\phi_3. \tag{4.18}$$

Whilst both schemes aim to model the singly resonant contribution, the DS scheme attempts to also include the interference term between the singly and doubly-resonant diagrams. When performing tests of the modelling of the above two methods, the authors of Ref. [92] state that the NLO corrections to the single top Wt-channel process are larger than the interference effects and that there can be a large ambiguity in certain regions of phase space between the DR and DS estimates.

For the majority of regions of the analyses presented herein, there is a requirement that the event contains two $b-$quarks. For this selection the interference effects are more relevant and as such a test of the validity of the DR and DS estimates must be performed. Naively it could be assumed that an uncertainty should be applied to the Wt process due to the choice of interference scheme. However, this approach is only

valid if both schemes model the phase space that the analyses targets in an appropriate manner. Applying an uncertainty from a scheme with poor modelling of the phase space would artificially increase the uncertainties.

It may be assumed that the DS method would be a better description of the single-top process as it includes the interference term. However, as previously described, the DS method assumes that the W-boson and b-quark are close to the top-quark mass. If, in the phase space under consideration, the invariant mass of the W-boson and b-quark is away from m_t then using the DS scheme to model the single-top process may no longer be valid.

4.3.3 Validity test of the DR and DS schemes

The validity of the DR and DS schemes is investigated in the context of the sbottom 2015 analysis as presented in Chapter 6. The predictions of the DR and DS samples are compared against data in a single-top Wt-channel enriched region. The MC generator used for these studies is Powheg interfaced with Pythia6 for showering for both $t\bar{t}$ and single-top. The nominal single-top sample uses the DR scheme, which is compared with the alternative Powheg+Pythia6 DS sample. The selections used to define the single-top control region (referred to as bb_CRstA) are fully described in Table 6.12.

Process	Yield
$t\bar{t}$	11.7 ± 0.9
single-top (DR)	28.1 ± 0.7
single-top (DS)	6.4 ± 0.4
Z+jets	0.9 ± 0.2
W+jets	16.7 ± 0.8
Diboson	0.5 ± 0.1
$t\bar{t}$Z	0.08 ± 0.01
$t\bar{t}$W	0.11 ± 0.01
MC Total with DR scheme	58.1 ± 1.5
MC Total with DS scheme	36.4 ± 1.3
Observed data events	56

TABLE 4.1: Data and MC comparison of the main SM background processes in the sbottom bb_CRstA region, with 3.2 fb^{-1}. Only statistical uncertainties are considered.

From Table 4.1 it can be seen that, in the region of phase space considered by the analysis, the DS sample greatly underestimates the data. The MC prediction in this

region, assuming a 20% systematic uncertainty on the background estimate, when using the DR sample is within 0.2σ of the data, whereas the estimate when using the DS scheme underestimates the data in the region by 2.7σ.

A normalisation parameter ($\mu_{\text{single-top}}$) is subsequently calculated, by removing the 30 events corresponding to the non-single-top backgrounds, and evaluating the single-top contributions after rescaling number of remaining data events:

$$\mu_{\text{single-top}} = \frac{N_{\text{data non-singletop}}}{N_{\text{MC singletop}}} \tag{4.19}$$

These calculations result in $\mu_{\text{single-top}} = 4.08$ for the DS scheme compared with $\mu_{\text{single-top}} = 0.92$ using the DR scheme. This drastic difference in DR and DS estimations in the bb_CRstA region suggests that the DS scheme is not appropriate to apply in the phase space targeted by the analysis, as the invariant mass of the W-bosn and b-quark are away from the top-quark mass. Applying this uncertainty would artificially inflate the uncertainty. Further understanding of the differences between the DR and DS methods comes from analysing distributions key analysis variables, using samples without detector simulation, referred to as "truth-level" samples.

The object and variable definitions employed follow closely the definitions which will be reported in Chapter 5. Figures 4.4 and 4.5 show key variables from the sbottom analysis as reported in Chapter 6, and illustrate how these variables differ when not applying any selection and when applying a selection of $n_{\text{b-jets}} = 2$. As the DR scheme is shown to model the data in the bb_CRstA very well, the large differences at truth-level between the DR and DS schemes suggests that applying the relative uncertainty between the schemes artificially inflates the analysis uncertainty.

The results of these tests show that the DS scheme is not a valid method in the phase space targeted by the analysis, and the relative uncertainty should not be applied as an additional systematic uncertainty. In the next section, studies performed investigating an alternative sample, which can shed some light on the interference contributions relevant for the $n_{\text{b-jets}} = 2$ selection, are reported.

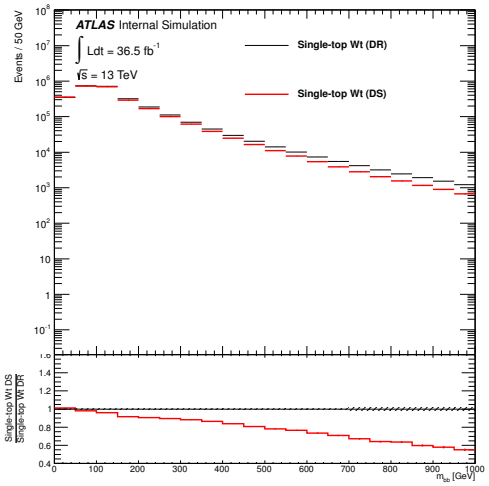

(a) m_{bb}

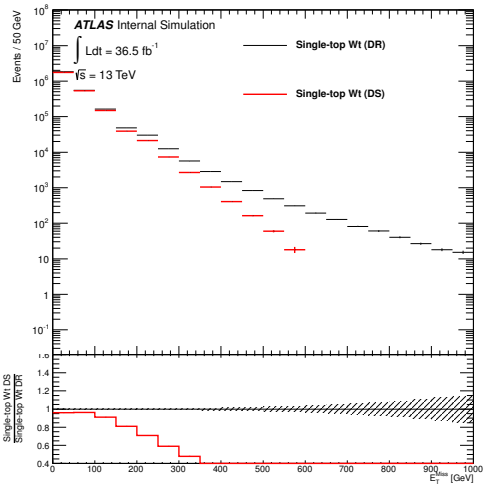

(b) $E_{\mathrm{T}}^{\mathrm{miss}}$

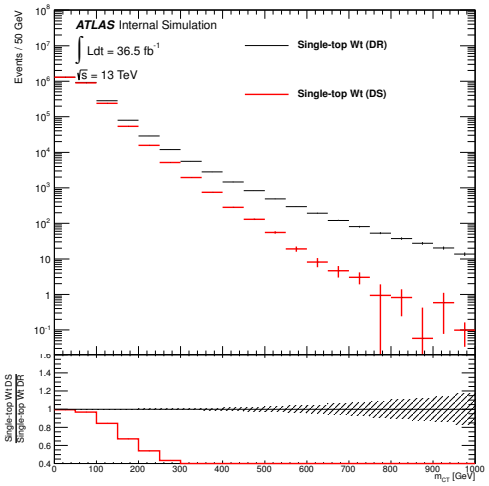

(c) m_{CT}

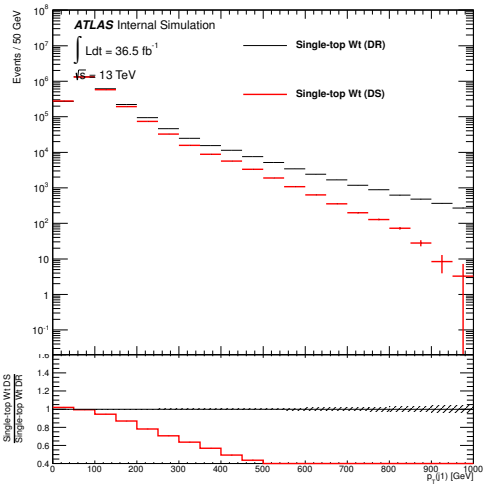

(d) $p_T(j_1)$

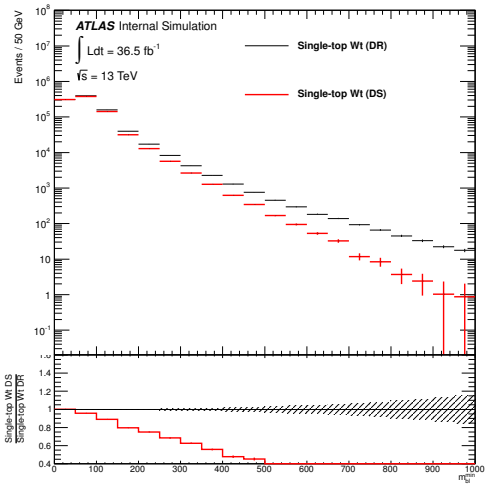

(e) $m_{(b,l)}^{\mathrm{min}}$

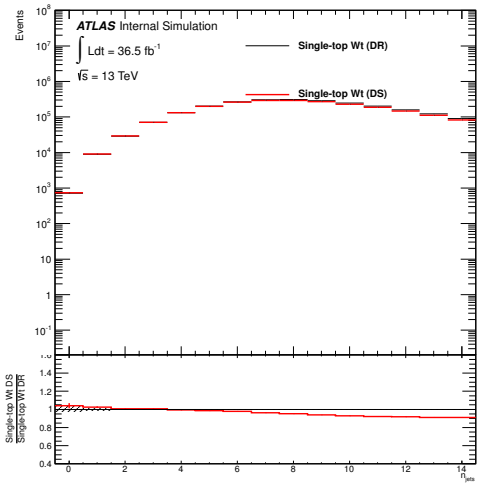

(f) n_{jets}

FIGURE 4.4: Selection of key variables in the bb_CRstA without any selection applied, comparing the DR and DS schemes at truth-level: (a) m_{bb} (b) $E_{\mathrm{T}}^{\mathrm{miss}}$ (c) m_{CT} (d) $p_T(j_1)$ (e) $m_{(b,l)}^{\mathrm{min}}$ (f) n_{jets}. Only the statistical uncertainties on both the DR and DS samples are shown.

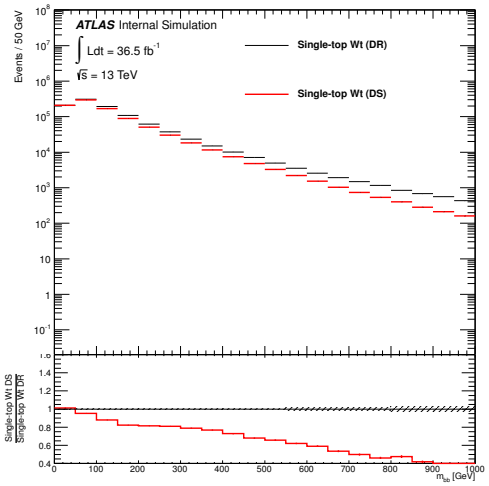

(a) m_{bb}

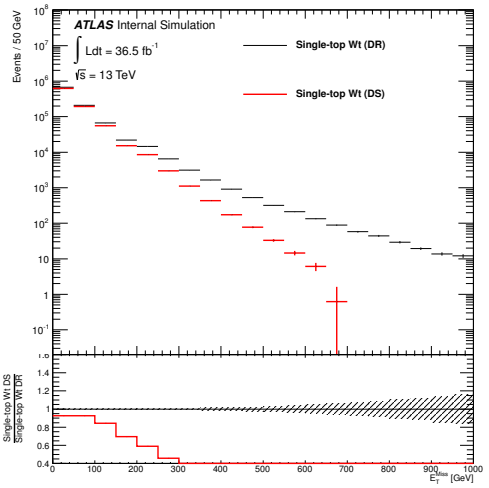

(b) $E_{\mathrm{T}}^{\mathrm{miss}}$

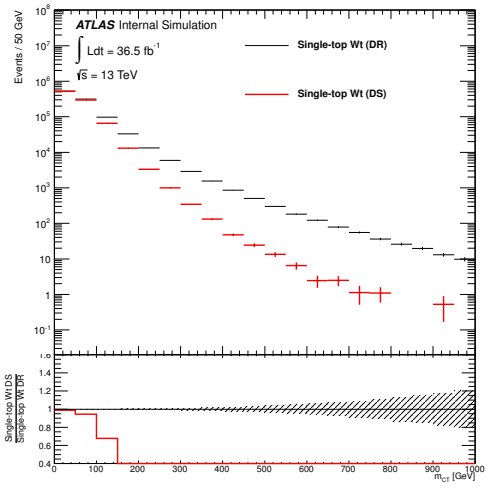

(c) m_{CT}

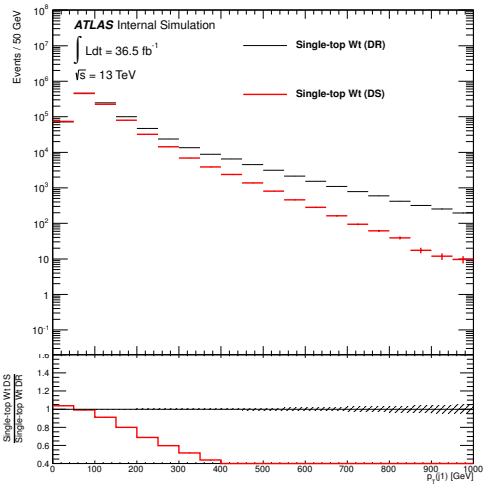

(d) $p_T(j_1)$

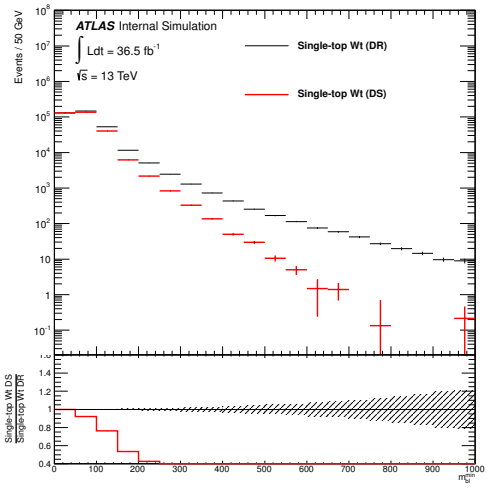

(e) $m_{(b,l)}^{\mathrm{min}}$

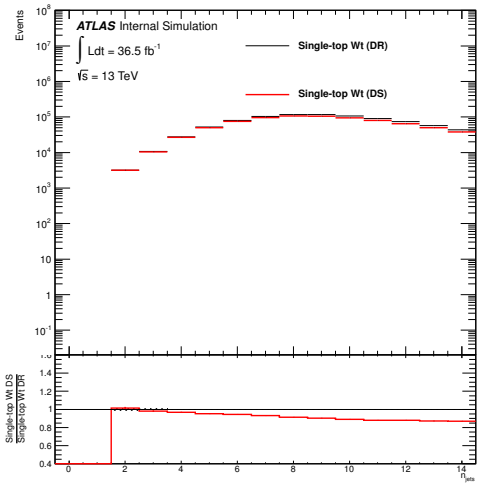

(f) n_{jets}

FIGURE 4.5: Selection of key variables in the bb_CRstA at with an $n_{\mathrm{b-jets}} = 2$ requirement, comparing the DR and DS schemes at truth-level: (a) m_{bb} (b) $E_{\mathrm{T}}^{\mathrm{miss}}$ (c) m_{CT} (d) $p_T(j_1)$ (e) $m_{(b,l)}^{\mathrm{min}}$ (f) n_{jets}. Only the statistical uncertainties on both the DR and DS samples are shown.

4.3.4 Using a dedicated $WWbb$ Sample

Contributions related to the interference effects between the single-top and $t\bar{t}$ processes can be studied by combining the individual $t\bar{t}$ and single-top samples and comparing this to a single sample which fully generates the off-, singly- and doubly-resonant contributions to the $WWbb$ process.

Due to difficulties encountered when generating the $WWbb$ process at NLO [93], the best accuracy achievable when performing these studies is LO using MadGraph for the ME calculation and Pythia8 for the PS. Samples are generated in the so-called 4 Flavour Scheme (4FS) where $b-$quarks are treated as massive and any $b-$quark initiated process begins with $g \to bb$.

A similar method is used as in the previous comparison in the context of the 2015 sbottom analysis. To perform this comparison in the same manner as the DS comparison in the previous section, it is required to combine the contributions of the nominal single-top (DR) method, with the $t\bar{t}$ sample, and then to compare this with the full $WWbb$ sample.

Whilst these studies are performed at truth-level only, any significant differences in the yields of $t\bar{t}$+single-top and $WWbb$ would suggest that a reconstruction-level $WWbb$ sample would not be appropriate to model the regions under consideration, as the nominal $t\bar{t}$ and single-top DR samples describe the data in the bb_CRstA well. The truth-level yields for the bb_CRstA region and a signal region used in the sbottom 2015 analysis (referred to as bb_SRA250 and defined in Table 6.3) are shown in Table 4.2.

Process	bb_CRstA	bb_SRA250
$t\bar{t}$ + single-top (NLO, DR)	64.02	3.443
$WWbb$ (LO)	27.70	1.796

TABLE 4.2: Truth-level yields for the combined $t\bar{t}$ and single-top processes and the $WWbb$ process in the bb_CRstA and bb_SRinA regions.

The large difference between the predicted yield for the nominal $t\bar{t}$ +single-top and the $WWbb$ sample shown in Table 4.2, suggests a global normalisation required for the $WWbb$ sample. However at truth-level there are significant deviations between samples. As the nominal sample is shown to estimate the data well (at reconstruction-level) it is assumed that a $WWbb$ sample, generated at reconstruction-level, would compare poorly with the data due to this large difference in yield at truth-level.

4.3.5 Conclusions

The previous section presented an overview of the methods to model the interference between the single-top (Wt) and $t\bar{t}$ processes when considering events with two $b-$jets in the final state.

The diagram removal method (DR) is used as the nominal method when generating the single-top process. The validity of comparing the DR method with the diagram subtraction (DS) method, to estimate the uncertainty arising from the interference effects, is investigated and a comparison between the yields provided using these methods is shown. It is seen that the DR method models the data well in the single-top enriched region used in the sbottom analysis. The DS method underestimates the data in this region. A truth-level comparison is presented showing the distribution of key variables used in the analysis without any selection applied, and with an $n_{\mathrm{b-jets}} = 2$ selection. The dramatic differences between the yield provided by the DS sample, and the differences in the distributions of the key variables, is indicative of the DS sample being inappropriate to use to estimate the interference uncertainty due to the phase space targeted by the analysis.

A further sample is investigated, referred to as the $WWbb$ sample, which contains the doubly-, singly- and non-resonant terms. To compare the samples on an even footing the $WWbb$ sample must be compared to the prediction from the combined $t\bar{t}$ + single-top samples. Whilst these studies are very preliminary and performed only at truth-level, there is a significant difference between the predictions from the combined $t\bar{t}$ + single-top nominal samples, and the $WWbb$ sample, which suggests that this sample would also be inappropriate to use to estimate the interference uncertainty.

As neither of the two alternative samples provides a reliable alternative method to the nominal, the samples are not used to estimate the effect of the modelling uncertainty in the context of the sbottom 2015 analysis, to prevent artificially inflating the modelling uncertainties of the analysis.

More recent developments in the generation of the $WWbb$ sample has proven more successful at modelling the regions of phase space under consideration using MadGraph5+aMC@NLO. These samples were used to assess the impact of the interference uncertainty for the Sbottom 36.1 fb^{-1} analysis, documented in Chapter 6 and the Run 2 $tb + E_{\mathrm{T}}^{\mathrm{miss}}$ analysis reported in Chapter 7. The uncertainties on the signal region predictions using the MadGraph5+aMC@NLO samples are between 6-16%.

4.4 Modelling the V-jets process uncertainties using a parameterisation

The MC event generator Sherpa (versions 2.1.1, 2.2.0 and 2.2.1) is used by ATLAS to generate samples corresponding to the NLO production of a W/Z boson in association with jets, with the boson decaying leptonically. The events are normalized to the inclusive (4π) NNLO cross sections using an associated k-factor. The W+jets events are normalised to $\sigma_{\text{NNLO}} = 20080\,\text{pb}$. The cross section used for the normalisation of the Z+jets events is dependent upon the invariant mass of the leptons in the event, for the $Z \to \ell\ell$ events, the samples are normalised to $\sigma_{\text{NNLO}} = 2067\,\text{pb}$ for each flavour of lepton ($\ell = e,\, \mu,\, \tau$). The $Z \to \nu\nu$ samples are normalised to $\sigma_{\text{NNLO}} = 11373\,\text{pb}$.

The nominal Sherpa configuration includes four parameters which are setup by the user and that can be varied to evaluate the corresponding uncertainties:

- Matrix element matching scale (CKKW): This is the merging scale taken for the calculation of the overlap between jets from ME and from PS. The nominal value for this parameter is 20 GeV. The up variation increases this to 30 GeV (CKKW30), whilst the down variation decreases the nominal value to 15 GeV (CKKW15).

- Renormalisation scale (Renorm): This is the scale at which the running strong coupling constant (α_S) is calculated for the underlying hard process, the nominal value is calculated at $m_{W/Z}$. The μ_{R} is varied by a factor of 2 (Renorm4) and a factor of $\frac{1}{2}$ (Renorm025) with respect to the nominal.

- Factorisation scale (Fac): This is the factorisation scale (μ_F) used in the PDF and cross section calculations, the nominal value is chosen such that $\mu_F = m_{W/Z}$. The μ_{F} is varied by a factor of 2 (Fac4) and $\frac{1}{2}$ (Fac025) with respect to the nominal.

- Resummation scale (QSF): This is the scale used in the PS algorithmn to begin the process of soft emission, the nominal value is again chosen such that $\mu_{\text{qsf}} = m_{W/Z}$. The μ_{qsf} is varied by 2 (QSF4) and $\frac{1}{2}$ (QSF025) with respect to the nominal.

Due to the large amount of samples and events that would be required to cover the above variations, only a subset of samples, dependent upon the decay of the vector boson ($Z \to \nu\nu$, $Z \to ee$, $W \to e\nu$) are produced with Sherpa version 2.1, as the variations do not depend on the decays of the vector boson and are independent of lepton flavour. Furthermore, dedicated samples for Sherpa v2.2, and v2.2.1 with alternative scales were

not produced: in this case, the applicability of the same relative variations derive from the fact that v2.1 and v2.2/v2.2.1 samples do not differ in QCD order and ME+PS@NLO prescription.

The following studies consider the variations for the $Z \to \nu\nu$, $Z \to \ell\ell$ and $W \to \ell\nu$ samples. The samples are generated in slices corresponding to the transverse momentum of the vector boson, $p_{\mathrm{T}}(V)$: [0,70], [70-140], [140-280], [280-500], [500-700], [700-1000], [1000-2000], [2000-$\mathrm{E_{CMS}}$] GeV, and are also split depending on the flavour of the jet: $b-, c-$, and $l-$jets. For each of the four variations two samples are produced: down variations (referred to as CKKW15, Renorm025, Fac025, QSF025 respectively); and the up variations (referred to as CKKW30, Renorm4, Fac4, QSF4 respectively).

Figures 4.6, 4.7 and 4.8, show kinematic distributions at truth-level of the variations with respect to the nominal, for the $Z \to \nu\nu$, $W \to e\nu$ and $Z \to ee$ samples respectively. It is seen that varying the renormalisation scale produces the largest deviations when compared to the nominal. This is most prevalent in the $p_{\mathrm{T}}(V)$ distributions.

Generally the variations show a dependence upon $p_{\mathrm{T}}(V)$ and the jet multiplicity. Other variables, such as m_{eff} and H_{T} (defined in Section 5.4) also show some sensitivity to the variations, however, not to the same extent as $p_{\mathrm{T}}(V)$ and n_{jets}. Due to this dependency on $p_{\mathrm{T}}(V)$ and n_{jets} a set of weights in two-dimensions was developed to describe the uncertainties.

The following section shows how the parameterisation of the uncertainties based on the afforementioned variables has been developed, and closure tests of the parameterisation are shown. The results of the parameterisation allows a wide range of ATLAS analyses to evaluate the impact of these modelling uncertainties in a much quicker manner than running directly on the alternate samples.

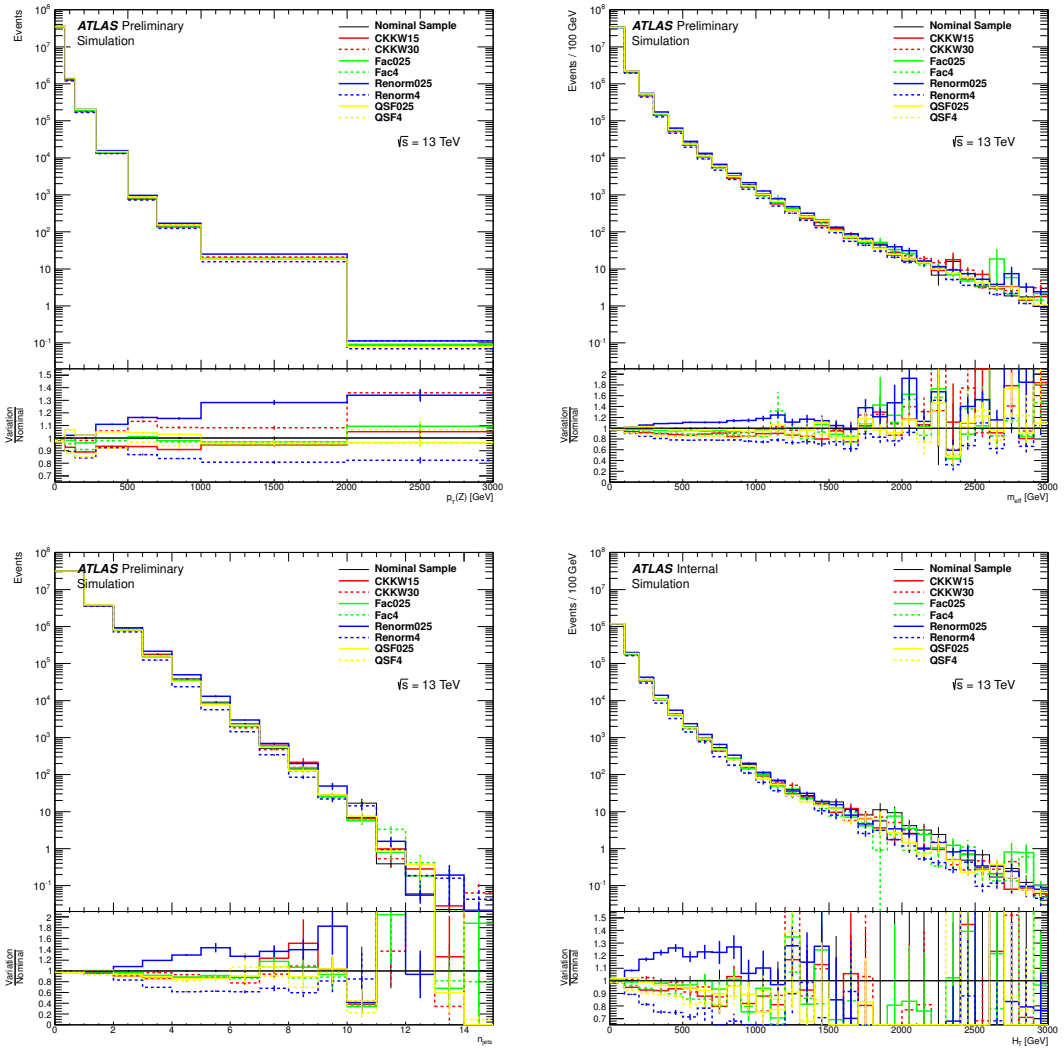

FIGURE 4.6: Key variables for the systematic and nominal $Z \to \nu\nu$ samples. Top row: left $p_{\mathrm{T}}(Z)$; right m_{eff}. Bottom row: left $n_{\mathrm{TruthJets}}$, right $\mathrm{H_T}$. Figures taken from [4].

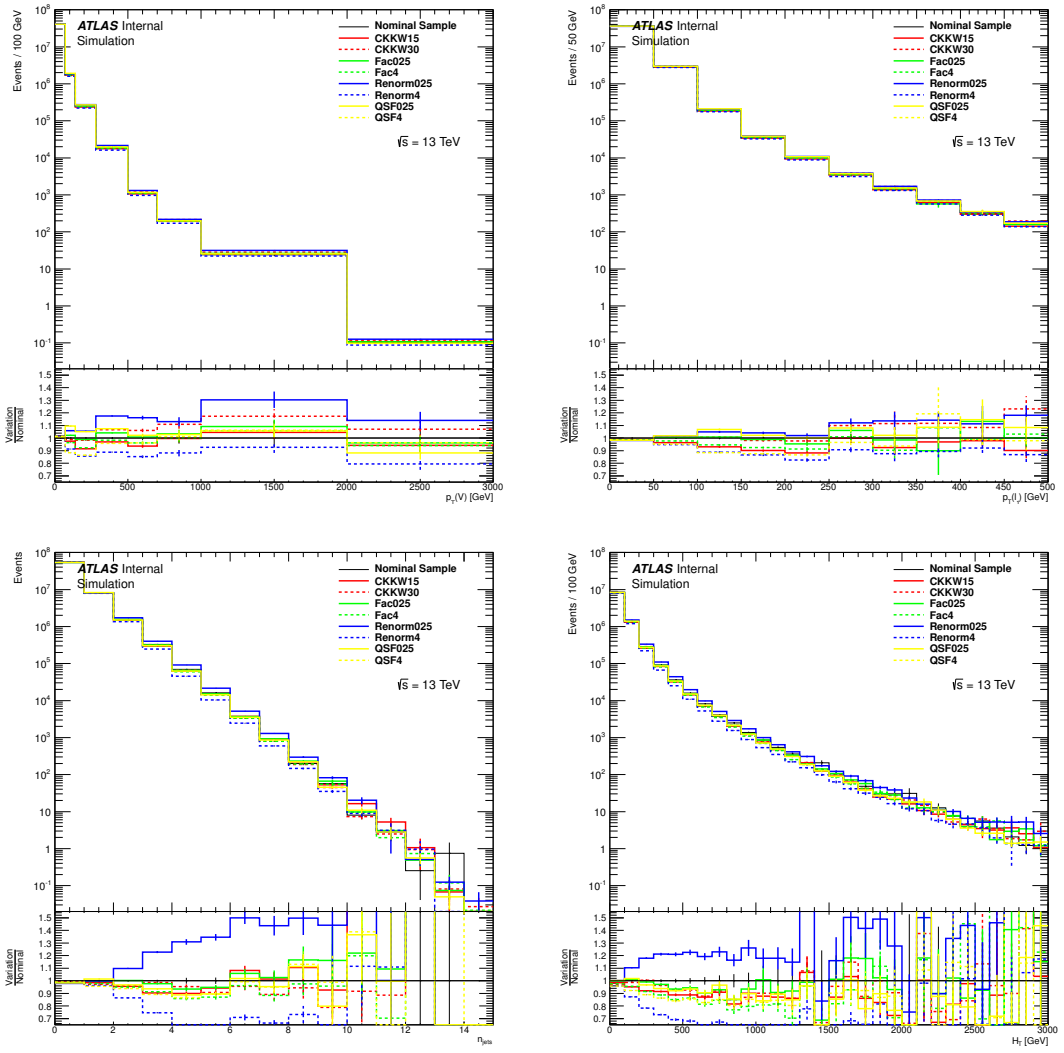

FIGURE 4.7: Key variables for the systematic and nominal $W \to e\nu$ samples. Top row: left $p_{\mathrm{T}}(W)$; right $p_{\mathrm{T}}(e)$. Bottom row: left $n_{\mathrm{TruthJets}}$, right $\mathrm{H_T}$

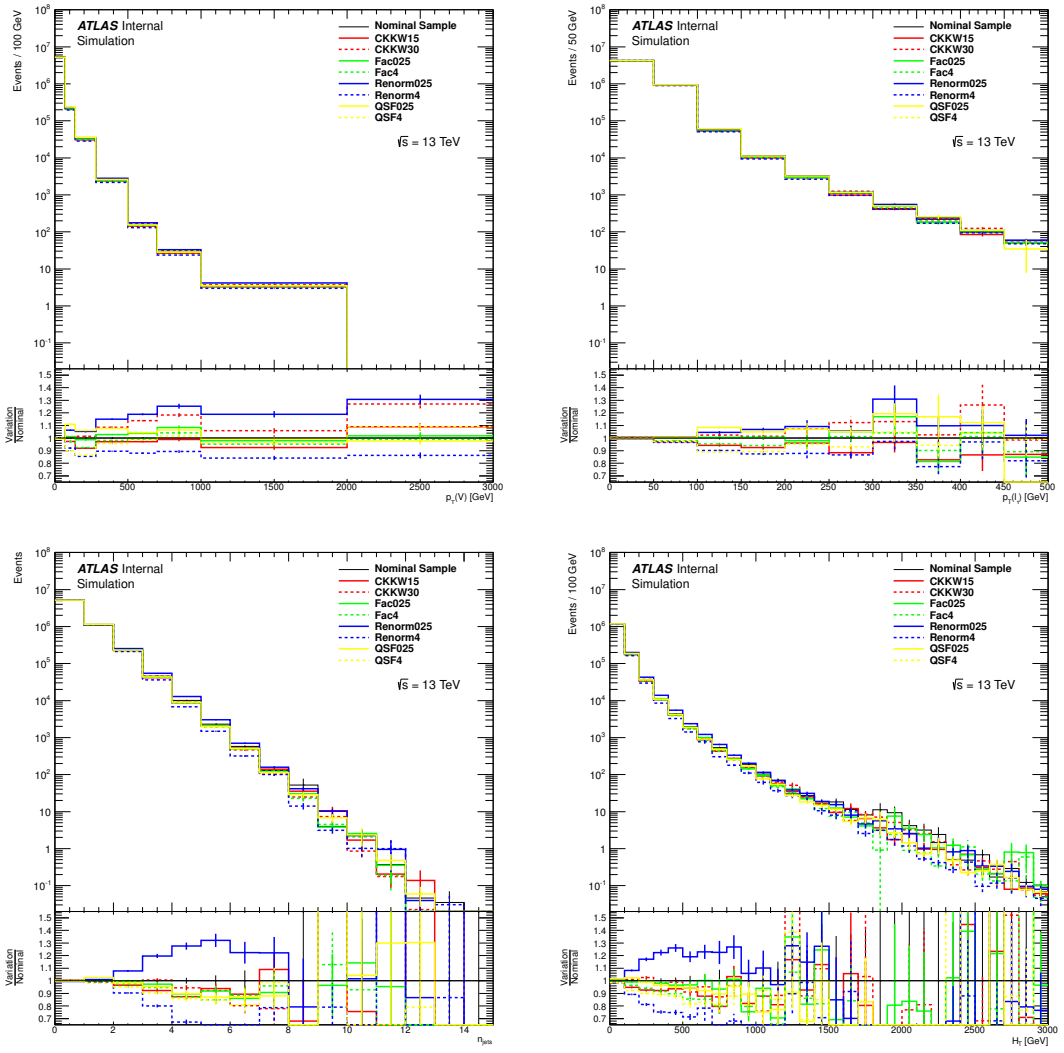

FIGURE 4.8: Key variables for the systematic and nominal $Z \to ee$ samples. Top row: left $p_{\mathrm{T}}(Z)$; right $p_{\mathrm{T}}(e)$. Bottom row: left $n_{\mathrm{TruthJets}}$, right $\mathrm{H_T}$

4.4.1 Parameterisation Method Overview

The first step in parameterising the uncertainties is to identify the appropriate variables. As a first step, weights were derived using a 1-dimensional parameterisation using either $p_{\mathrm{T}}(V)$ or n_{jets} ($p_{\mathrm{T}} > 20\,\mathrm{GeV}$, $|\eta| < 2.8$). For the case where $p_{\mathrm{T}}(V)$ was used for the parameterisation process, properties related to the jets ($\mathrm{H_T}$, $p_{\mathrm{T}}(j_1)$ etc) were not reproduced with the parameterisation, whilst using the jet multiplicity as the basis for the parameterisation caused variables relating to the $E_{\mathrm{T}}^{\mathrm{miss}}$ to be poorly reproduced. This shows that a multidimensional parameterisation must be performed: two variables were found to be sufficient and $p_{\mathrm{T}}(V)$ and n_{jets} are used.

For a given $p_{\mathrm{T}}(V)$ bin (i), and n_{jets} bin (j), the weights are calculated per sample (up and down variations are treated separately) using Eqn 4.20:

$$W_{i,j} = \frac{N_{i,j}^{Syst}}{N_{i,j}^{Nominal}}, \tag{4.20}$$

where the number of events for each sample is normalised to the NNLO cross section.

The choice of $p_{\mathrm{T}}(V)$ bins is guided by the p_{T} slices that are used for the generation of the samples ([0,70], [70-140], [280-500], [500-700], [700-100], [1000-2000], [2000-$\mathrm{E_{CMS}}$]) GeV. The n_{jets} bins correspond to values of the jet multiplicity of $(0, 1, 2...10, >10)$ jets. A cut off point of > 10 is chosen due to low statistics in bins with jet multiplicity > 10 which may lead to unphysical fluctuations. A representation of the bin structure is shown in Fig. 4.9.

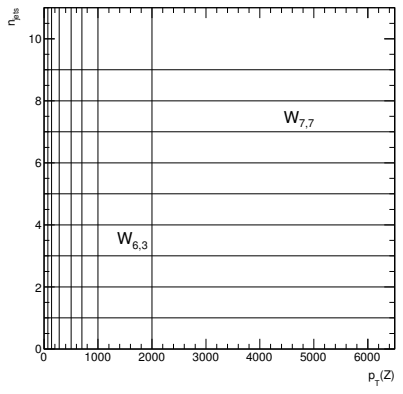

FIGURE 4.9: Representation of the bin structure for a given n_{jets} and $\mathrm{p_T(V)}$ selection. Weights are calculated using Eqn 4.20 on a bin-by-bin basis corresponding $p_{\mathrm{T}}(V)$ (i) and n_{jets} (j).

The weights produced corresponding to the renormalisation scale variations are shown in Figure 4.10, using the $Z \to \nu\nu$ process as an example.

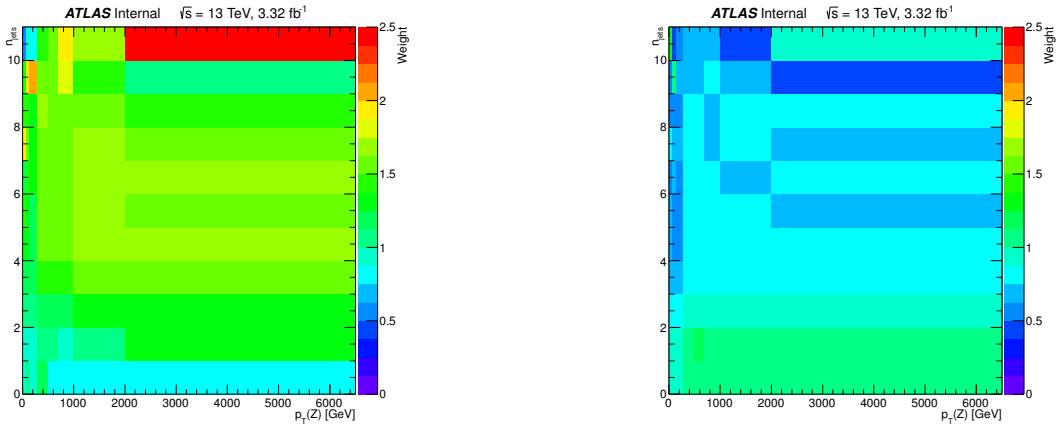

(a) Renorm025 (b) Renorm4

FIGURE 4.10: Examples of the weights produced for the $Z \to \nu\nu$ renormalisation scale variations.

4.4.2 Validation of the Parameterisation Weights

In order to validate the method, a closure test is performed comparing the weighted nominal (i.e. applying the weights from the parameterisation to the nominal sample), and the actual systematic sample, for variables that are used for many SUSY analyses.

By definition, for the variables used for the parameterisation method, the weighted nominal should reproduce exactly the systematic sample. Fig 4.11 shows the distributions corresponding to the parameterisation variables $p_{\mathrm{T}}(V)$ and n_{jets}. The weighted nominal and the systematic variation differ in the high multiplicity bins for the n_{jets} distribution due to the truncation at $n_{\mathrm{jets}} = 10$ used in the parameterisation.

A small subset of observables are shown in Figures 4.12 and 4.13 corresponding to the Renorm025 and Renorm4 variations for the $Z \to \nu\nu$ process, as Figures 4.6, 4.7 and 4.8 show how the uncertainty from these variations are expected to lead to the largest difference from the nominal sample and hence the renormalisation variations have the largest impact on the modelling uncertainty.

The black markers denote the weighted nominal whilst the systematic sample is represented by the black line. Generally good agreement is observed using the weighted method in all variables that are considered.

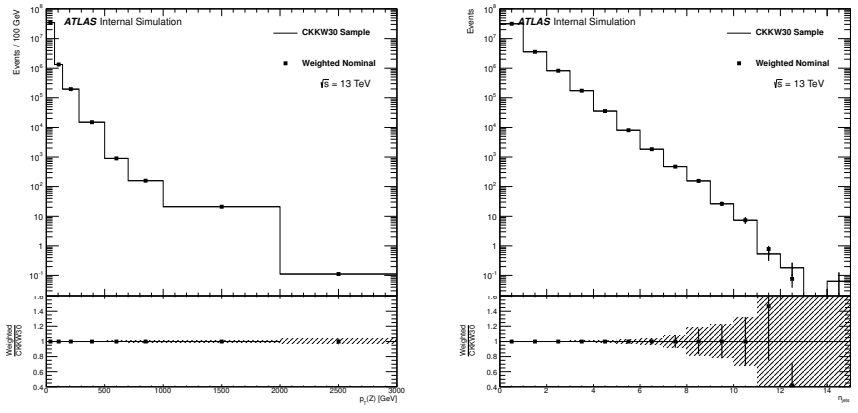

FIGURE 4.11: $p_{\mathrm{T}}(V)$ (left) and n_{jets} (right) distributions for the ckkw30 (ME matching up) $Z \to \nu\nu$ sample. As these variables are used for the parameterisation it would be expected that the weighted method and the actual systematic variation would agree exactly for these variables. This is the case for the $p_{\mathrm{T}}(V)$ distribution (left) however due to the binning used when producing the weights for the high jet multiplicity events this is not the case for the n_{jets} distribution. The statistical uncertainty on both the nominal and variation samples are shown.

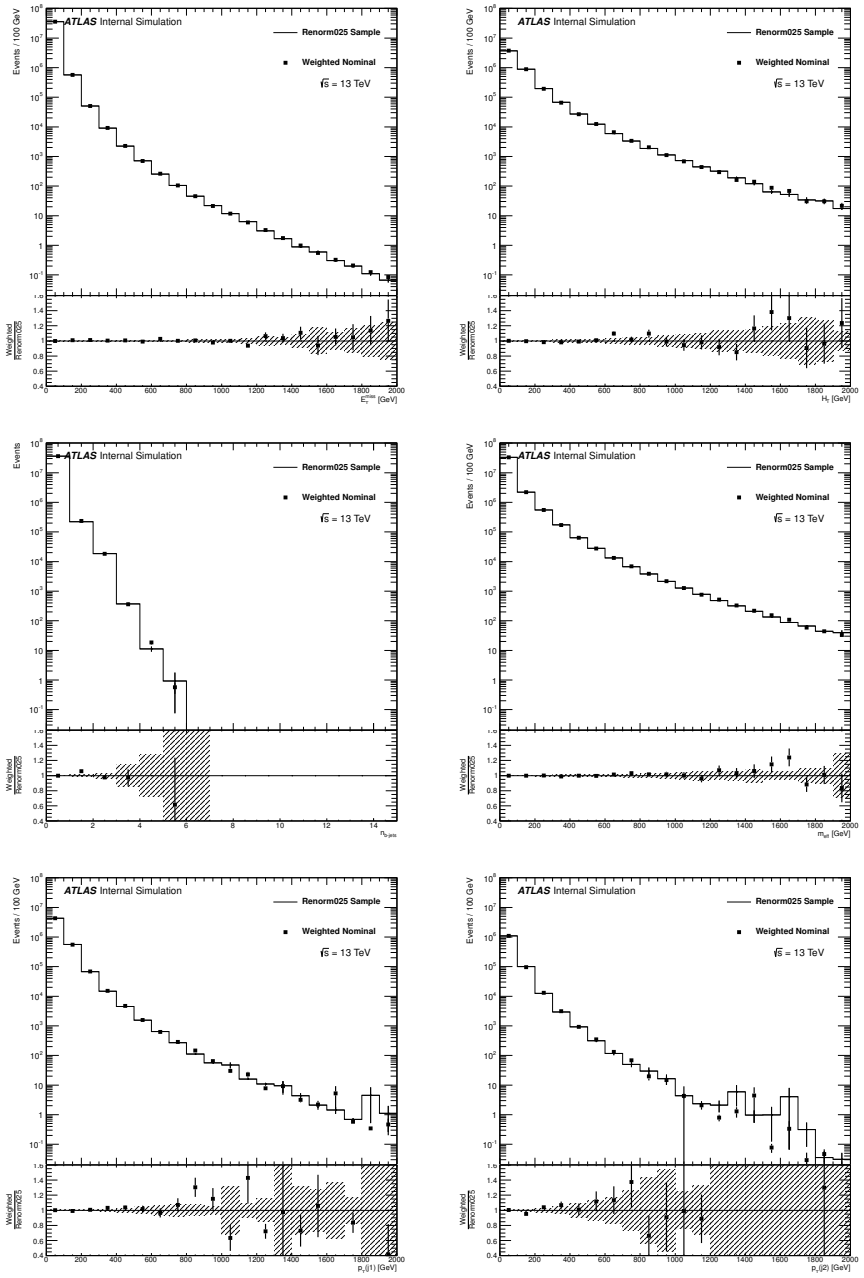

FIGURE 4.12: Distributions of kinematic variables for the $Z \to \nu\nu$ renorm025 sample. Top row: Left $E_{\mathrm{T}}^{\mathrm{miss}}$; right $\mathrm{H_T}$. Middle row: Left $b-$jet multiplicity; right m_{eff}' Bottom row: Left $p_{\mathrm{T}}^{\mathrm{j1}}$; right $p_{\mathrm{T}}^{\mathrm{j2}}$. The statistical uncertainty on both the nominal and variation samples are shown.

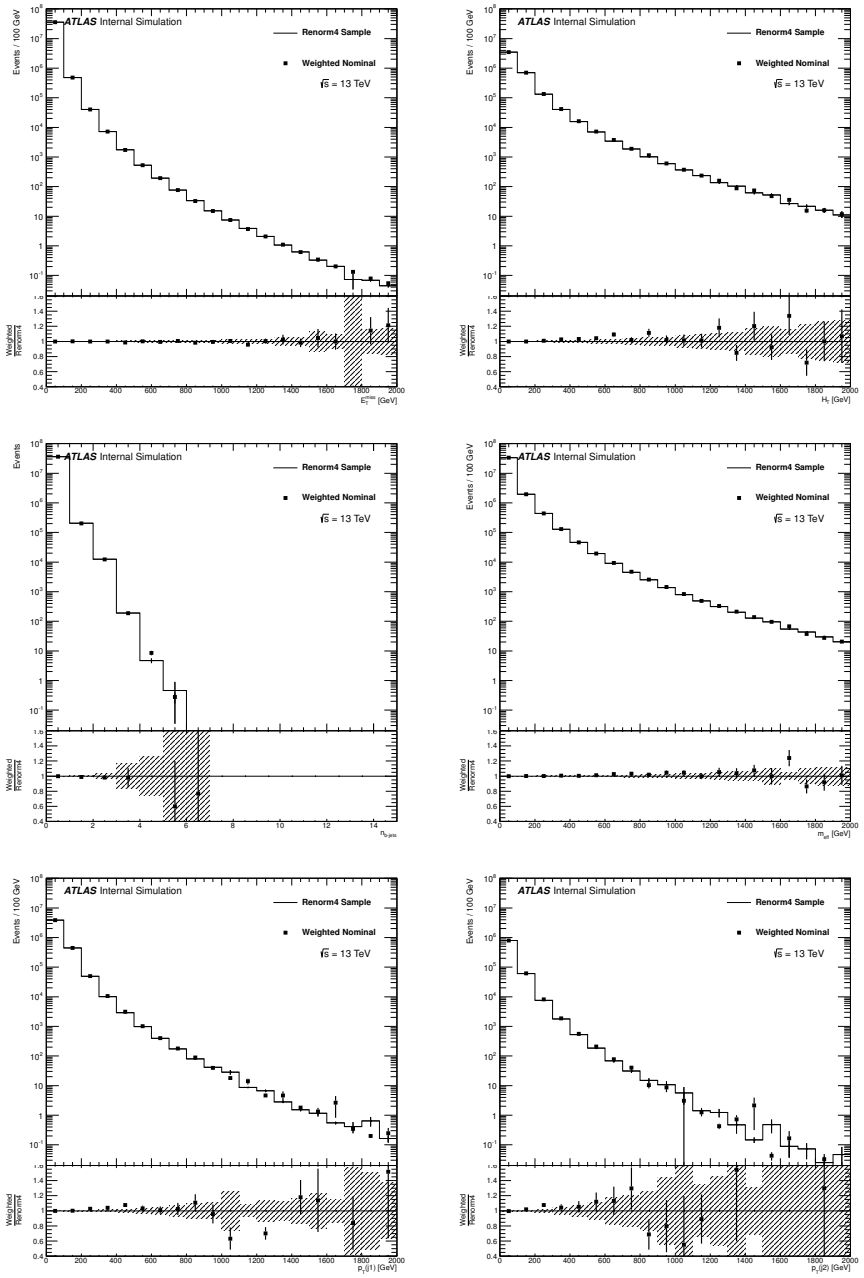

FIGURE 4.13: Distributions of kinematic variables for the $Z \to \nu\nu$ renorm4 sample. Top row: Left $E_{\mathrm{T}}^{\mathrm{miss}}$; right $\mathrm{H_T}$. Middle row: Left $b-$jet multiplicity; right m_{eff}' Bottom row: Left $p_{\mathrm{T}}^{\mathrm{j_1}}$; right $p_{\mathrm{T}}^{\mathrm{j_2}}$. The statistical uncertainty on both the nominal and variation samples are shown.

4.4.3 Parameterisation usage with later versions of Sherpa

During the progression of Run 2 the Sherpa 2.1.1 version used for the generation of the V+Jets processes has been replaced by 2.2.0, and then version 2.2.1.

In doing this the nominal V+Jets samples were regenerated, however the systematic variation samples were not regenerated. Sherpa 2.2.1 presents a new functionality which allows the generation of internal weights on an event-by-event basis, which can be used to quantify the μ_R, μ_F and PDF uncertainties on the ME. On the other hand the matrix element matching and resummation scale variations are not available "on the fly". Hence the parameterisation weights remain a useful method to calculate these uncertainties at the analysis level without dealing with many large samples.

Applicability of the parameterisation to the 2.2 samples has been studied in two ways. The first method is to compare the 2.1 and 2.2 weighted distributions to understand the behaviour of the weights. Figure 4.14 presents a comparison of the weights used with the nominal 2.1 and 2.2 samples. It is seen that the ratio of the nominal (solid line) to the weighted samples (markers) for the Sherpa 2.1 (red) and Sherpa 2.2 (black) are very similar. This implies that the the parameterisation varies the nominal sample in a similar manner for both 2.1 and 2.2, validating the usage of the parameterisation to the Sherpa 2.2 nominal samples.

With regards to Sherpa 2.2.1, the addition of the internal weights for the renormalisation and factorisation uncertainties allows for a more direct manner of validating the parameterisation. Figures 4.15 and 4.16, show a direct comparison between the internal weights, and the parameterisation weights, when applied to a reconstruction level Z-jets sample, for some key variables of interest. There is very good agreement between the internal weights and the parameterisation method for the scale variations that have corresponding internal weights, validating the usage of the parameterisation with these samples.

4.4.4 Conclusions

The previous section contained an overview of the studies performed investigating the modelling uncertainties for the Sherpa V+jets samples, which are used to model key background processes in the analyses presented in this thesis. The effects of varying the parameters corresponding to the renormalisation scale (μ_R), factorisation scale (μ_F), matrix element matching scale (CKKW) and soft gluon resummation scale (μ_{QSF}) are

investigated, with the renormalisation scale variations showing the largest difference with respect to the nominal.

To allow for the efficient calculation of the impact of these uncertainties, a two-dimensional parameterisation was developed, based upon the transverse momentum of the vector boson ($p_{\mathrm{T}}(V)$) and the jet multiplicity (n_{jets}). A closure test was performed using the weights, by comparing distributions produced with the weighted nominal and with the true systematic sample, which resulted in the reproduction of the true systematic sample with the weights, when considering a selection of variables used in analyses.

Finally, the usage of the weights when applied to the updated Sherpa 2.2 samples was presented. Two methods are used to perform this check. The first method compares a selection of distributions using the weights applied to the 2.1 samples, and to the 2.2 samples. The ratio of the weighted distributions to the nominal sample for both 2.1 and 2.2 exhibits similar behaviour, validating the usage of the parameterisation here. The second method is to compare the weights to the internal weights that were included in the updated version. Not all of the uncertainties are available with the internal weights (μ_F, μ_R and PDF uncertainties are provided), so the parameterisation provides a complimentary method to investigate the modelling uncertainties. The validation is performed by comparing distributions in key variables produced using the internal weights applied on an event-by-event basis, to the distributions produced using the parameterisation weights. The comparisons performed are encouraging, with the internal weights and parameterised weights producing similar distributions.

The usage of the weights produced via the parameterisation is currently the SUSY Working Group recommended method to evaluate the modelling uncertainties on the W+jets and Z+jets backgrounds.

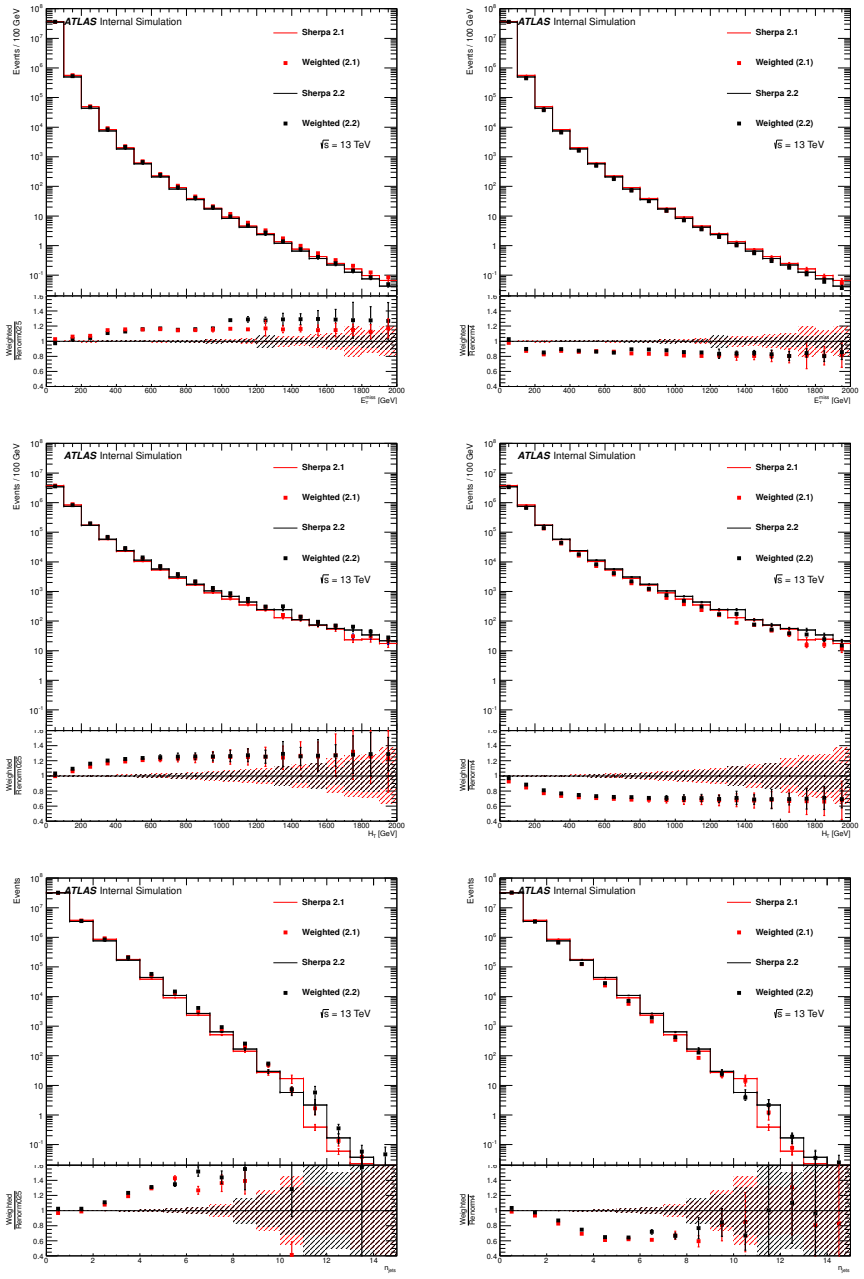

FIGURE 4.14: Comparison between key distributions for the $Z \to \nu\nu$ 2.1 (red) and 2.2 (black) for the renormalisation variation samples. The left plots show the renorm025 (down) variation, and the right plots show the renorm4 (up) variation: Top, $E_{\mathrm{T}}^{\mathrm{miss}}$; Middle, $\mathrm{H_T}$; Bottom: $n_{\mathrm{truthjets}}$.
It can be seen in the ratio plot, that the variation (weighted nominal) effects both 2.1 and 2.2 nominal samples in a similar manner, validating the use of the weighted method when applied to Sherpa 2.2. The statistical uncertainty is shown for both the nominal and weighted samples.

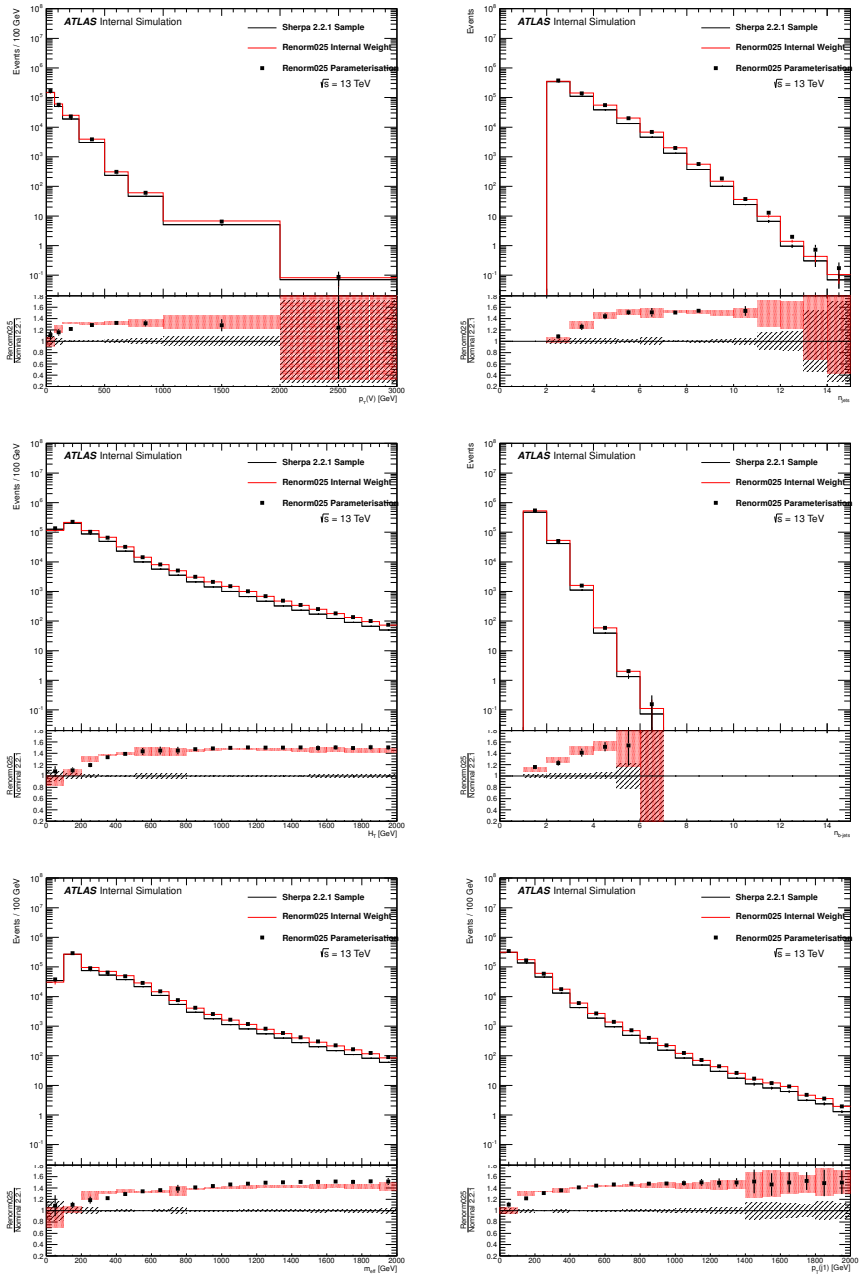

FIGURE 4.15: Comparisons of the renormalisation down variation between the internal weights and parameterisation method for key distributions using a reconstruction level Z-jets sample.
Top: left, $p_{\mathrm{T}}(Z)$; right, n_{jets}. Centre: left H_{T}; right, $n_{\mathrm{b-jets}}$. Bottom: left, m_{eff}; right, $p_{\mathrm{T}}(j_1)$. The statistical uncertainties are shown in the ratio plots for the nominal distribution (grey dashes), the distribution using the internal weights (red dots) and the distribution using the parameterisation weights (black markers).

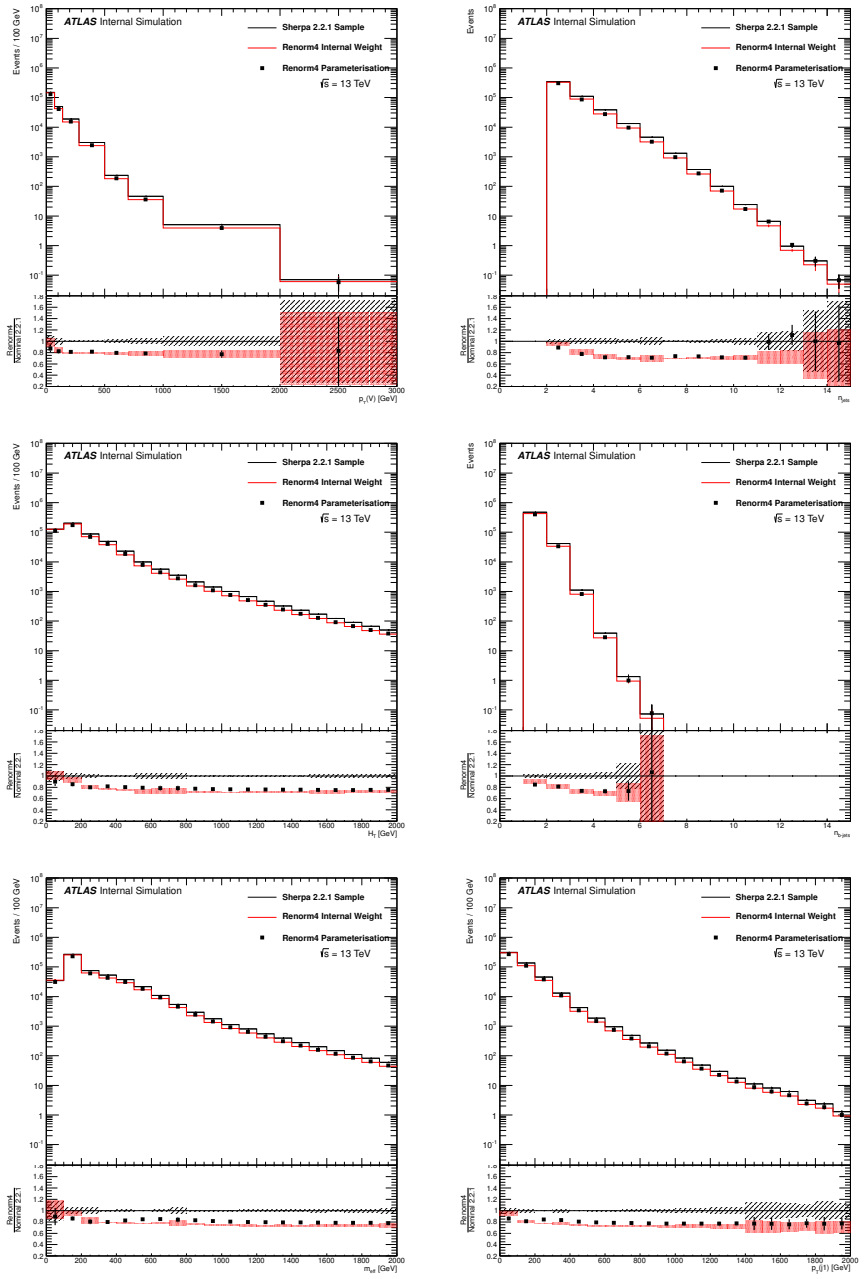

FIGURE 4.16: Comparisons of the renormalisation up variation between the internal weights and parameterisation method for key distributions using a reconstruction level Z-jets sample.
Top: left, $p_{\mathrm{T}}(Z)$; right, n_{jets}. Centre: left $\mathrm{H_T}$; right, $n_{\mathrm{b-jets}}$. Bottom: left, m_{eff}; right, $p_{\mathrm{T}}(j_1)$ .The statistical uncertainties are shown in the ratio plots for the nominal distribution (grey dashes), the distribution using the internal weights (red dots) and the distribution using the parameterisation weights (black markers).

4.5 Conclusion

This chapter presented an overview of the modelling of a generic proton-proton collision, and the tools available to model an array of physics processes of importance to the

analyses presented in this thesis. A brief overview of the MC generators used to model the key physics processes for the analyses is given, with a discussion of the specific methods used by each generator. The modelling of two specific cases were studied in detail.

The interference between the single-top Wt-channel process and the $t\bar{t}$ process was investigated in the context of the sbottom 2015 analysis to ascertain if an additional modelling uncertainty should be placed on the single-top background. It was found that the alternative samples available to model the interference effects provided unsatisfactory modelling and were not used, to avoid inflating the uncertainty due to the poor modelling provided by the alternative samples.

The uncertainties associated with the MC samples used to model the Z+jets and W+jets processes were investigated, with the uncertainty from varying the renormalisation scale the most dominant uncertainty. A 2D parameterisation was produced using the jet multiplicity and vector boson p_{T} as the basis for the parameterisation, to provide an quick method to evaluate these uncertainties. A closure test was performed to ensure that the parameterisation produced similar results to the true variation samples, and additional checks were performed to validate the usage of the parameterisation with the newest available samples used to model the V+jets processes.

Chapter 5

Event Reconstruction

This chapter contains an overview of the physics object definitions, the event cleaning selections and the key discriminating variables used in the analyses contained in this thesis. A brief introduction to the algorithm used for the definition of jets is given, before a list of the key objects required for the analyses is presented. Each object is subsequently discussed to produce the final definition for the objects and in addition to this the differences between the Run 1 and Run 2 definitions are given when appropriate. The event-level cleaning selections applied to the data to ensure that the data used for the analyses is of a good quality are reported. Finally the key kinematic variables that are used in each analysis are discussed, with an explanation of why they are useful to discriminate between signal and background.

In the following section, an overview of the definitions used to reconstruct physical objects such as electrons, muons and jets based upon information received from the detector is presented. The objects to be considered are:

- Charged leptons, (electrons or muons)
- Jets: Clusters of hadrons, formed into a jet using the anti-k_T algorithm [94] with $R = 0.4$
- $b-$jets: Jets which have been further identified as originating from a $b-$quark.
- $E_{\mathrm{T}}^{\mathrm{miss}}$: Unbalanced momentum in the transverse plane when summing all other objects in the detector. $E_{\mathrm{T}}^{\mathrm{miss}}$ is required to conserve momentum in the transverse plane, and suggests a particle escaping detection, such as a neutrino.
- Photons

In an event the above objects will interact in a relatively unique way in the detector, such that an energy deposit or track can be associated uniquely with one of the above objects, as shown in Figure 5.1. However, additional selections are employed to provide more accurate classification of the objects, and to distinguish between scenarios where there is uncertainty in the reconstruction.

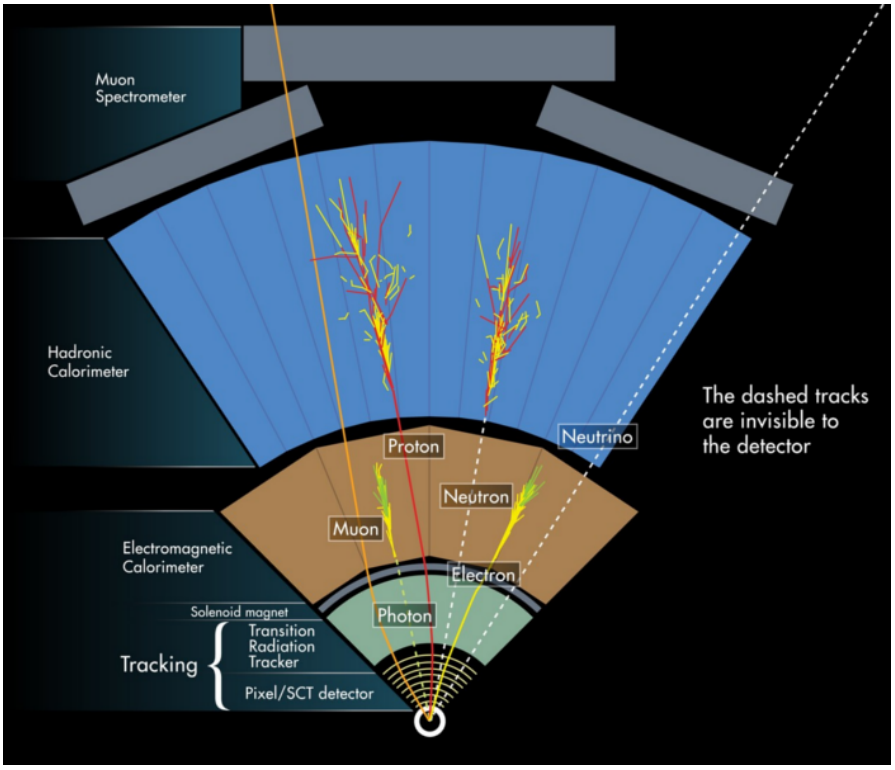

FIGURE 5.1: An overview of how physics objects would interact in the ATLAS detector. Taken from [95].

5.1 Object Reconstruction and Definitions

When reconstructing an event "baseline" objects are initially defined. These are objects that pass a loose set of requirements based upon the p_{T}, η and isolation of the object.

An overlap removal (OR) procedure is then used to avoid possible double counting between physics objects. The overlap removal procedure is defined in Section 5.2. After the overlap removal has been applied to the objects, the remaining baseline objects are checked to see if they pass the "signal" selection, which is a set of more stringent selections used to define signal objects. If the object passes the signal selection, then it is referred to as a signal object.

In order to correctly model the response of the detector when considering MC generated objects, scale factors are applied to the MC objects to correctly reproduce the

detector response in data. These scale factors are produced comparing the MC expectations to data. For example the electron [96] and muon [97] reconstruction efficiencies as a function of p_{T} and η are calculated using Z-boson decays and a tag-and-probe method. The MC expectation is compared to data, producing an reconstruction efficiency for the lepton. A similar method is used to calculate the photon reconstruction efficiency [98].

In the following sub-sections, the definitions are presented for the relevant objects used in each analysis. A generic overview of how the object would present itself in the detector is given, with a more specific overview of the selections used in each analysis to ensure well defined physics objects.

5.1.1 Charged Leptons: Electrons

Electrons are expected to leave tracks in the ID, which point to energy deposits in the EM calorimeter. As such, the selections employed to define electrons are based upon tracking (referred to as track) and calorimeter (cluster) information, including the transverse energy E_{T} and the pseudorapidity of the electron candidate. For example: η^{track} is the pseudorapidity calculated using tracking information from the inner detector; E^{cluster} corresponds to the energy calculated using only clustering information; and so on. Electrons must also pass an isolation requirement ensuring that the energy clusters or tracks are well defined [99]. Scale factors are applied to reconstructed MC electrons, whilst calibration factors are applied to reconstructed data electrons.

Due to improvements in the reconstruction algorithms, the electron object definitions during Run 2 are based upon multivariate analysis (MVA) methods. An overview of the electron object definitions used for each analysis are presented in Table 5.1.

$tb + E_{\mathrm{T}}^{\mathrm{miss}}$ Analysis

Baseline electrons are defined using a set of "medium" quality definitions [100] with $E^{\mathrm{cluster}}/\cosh(\eta) > 7\,\mathrm{GeV}$. If the object has deposited 4 hits in the silicon components of the ID, then η^{track} is used, otherwise η^{cluster} is used. Additionally the baseline electrons require $p_{\mathrm{T}} > 10\,\mathrm{GeV}$ and $\left|\eta^{\mathrm{cluster}}\right| < 2.47$.

Electron candidates that pass the OR procedure, as defined in Section 5.2, are further required to pass a "tight" quality definition and have $E_{\mathrm{T}} > 20\,\mathrm{GeV}$. An isolation requirement is also used, requiring ptCone20$/p_{\mathrm{T}} < 0.1$, where ptCone20 is the sum of all tracks within a radius $R = 0.2$ around the candidate electron, excluding the electron track iself. A transverse impact parameter requirement of $d_0 < 5\,\mathrm{mm}$ is used to ensure

high quality tracks. Finally to ensure that the electrons are in the single-electron trigger plateau, an additional selection of $p_{\mathrm{T}} > 25\,\mathrm{GeV}$ is employed.

Sbottom and Dark Matter $bb + E_{\mathrm{T}}^{\mathrm{miss}}$ Analyses

Electrons are labelled as baseline if they satisfy the likelihood-based LooseAndBLayer-LLH identification criteria [101], and also have $p_{\mathrm{T}} > 10\,\mathrm{GeV}$ with $\left|\eta^{\mathrm{cluster}}\right| < 2.47$. A looser baseline p_{T} selection is used for the dark matter analysis, with a baseline selection of $p_{\mathrm{T}} > 7\,\mathrm{GeV}$ applied.

After passing the OR procedure, signal electrons are selected with $p_{\mathrm{T}} > 26\,\mathrm{GeV}$ to guarantee that the electrons are in the single-electron trigger plateau. The signal electrons are also required to pass impact parameter selections $d_0/\sigma(d_0) < 5$, and $z_0\sin(\theta) < 0.5$, where z_0 is the longitudinal impact parameter. In addition to this, tighter isolation criteria are applied referred to as "GradientLoose" or "LooseTrackOnly" which refer to a general set of selections placed upon isolation variables [102].

Variable	$tb + E_{\mathrm{T}}^{\mathrm{miss}}$	Sbottom $bb + E_{\mathrm{T}}^{\mathrm{miss}}$	DM $bb + E_{\mathrm{T}}^{\mathrm{miss}}$
Baseline			
Acceptance	p_{T} >10 GeV, $\lvert\eta\rvert < 2.47$	p_{T} >10 GeV, $\lvert\eta\rvert < 2.47$	p_{T} >7 GeV, $\lvert\eta\rvert < 2.47$
Quality/ID	Medium	LooseAndBLayerLLH	
Signal			
Acceptance	p_{T} >25 GeV, $\lvert\eta\rvert < 2.47$	p_{T} >26 GeV, $\lvert\eta\rvert < 2.47$	p_{T} >26 GeV, $\lvert\eta\rvert < 2.47$
Quality	Tight	TightLLH	
Isolation	ptCone20/$p_{\mathrm{T}} < 0.1$	GradientLoose	LooseTrackOnly
d_0	< 5	-	
d_0 Significance	-	< 5	
$z_0\sin(\theta)$	–	< 0.5	

TABLE 5.1: Overview of the electron object definitions for both Run 1 and Run 2.

5.1.2 Charged Leptons: Muons

Tracks associated to muons are expected in both the ID and the muon spectrometer. The tracking information from these two sections of the detector are used simultaneously to define "combined" muons [97]. The selections used to define a muon candidate are therefore based upon the tracks in these sections of the detector, the p_{T} and η of the object. The muon object definitions used for the analyses are presented in Table 5.2. Differences between the muon p_{T} spectrum in MC and data are taken into account by applying p_{T} dependent scale factors to the MC muons.

$tb + E_{\mathrm{T}}^{\mathrm{miss}}$ Analysis

Baseline muons are required to pass selections of $p_{\mathrm{T}} > 10\,\mathrm{GeV}$ and $|\eta| < 2.5$. Quality requirements are also applied to the muon tracks left in the ID, referred to as the "loose" selection [103]. These requirements include:

$\geqslant 1$ b-layer hit (when within the b-layer acceptance);

$\geqslant 1$ pixel hit;

$\geqslant 5$ SCT hits;

pixel + SCT holes < 3 (holes referring to missing hits in the subsystem);

if $0.1 < |\eta| < 1.9$: $n_{\mathrm{TRT}} \geqslant 6$ or $n_{\mathrm{TRT}}^{\mathrm{outliers}} < 0.9 n_{\mathrm{TRT}}$;

else if $|\eta| \geqslant 1.9$ and $n_{\mathrm{TRT}} \geqslant 6$: $n_{\mathrm{TRT}}^{\mathrm{outliers}} < 0.9 n_{\mathrm{TRT}}$

(where n_{TRT} refers to the number of hits in the TRT subsystem and $n_{\mathrm{TRT}}^{\mathrm{outliers}}$ refer to high threshold TRT hits)

Further to this, signal muons require $p_{\mathrm{T}} > 25\,\mathrm{GeV}$, to ensure the muon is in the single-muon trigger threshold, and an isolation requirement is applied such that the sum of all tracks within a cone of radius $R = 0.2$ is less than 1.8 GeV. Events where a muon is found to be consistent with a cosmic ray are rejected [104], using impact parameter selections: d_0 significance < 3 and $z_0 \sin(\theta) < 0.5$.

Sbottom and DM $bb + E_{\mathrm{T}}^{\mathrm{miss}}$ Analyses

Baseline muons are required to have $p_{\mathrm{T}} > 10$ GeV and $|\eta| < 2.5$ and to pass a set of selections based upon the quality of the tracks, referred to as the "Medium" requirements [105]. The baseline muon p_{T} is lowered to $> 6\,\mathrm{GeV}$ for the dark matter analysis.

Following the OR, signal muons are selected with $p_{\mathrm{T}} > 26\,\mathrm{GeV}$, to ensure that the muons are in the trigger plateau. The signal muons must also pass the impact parameter selections d_0 significance < 3 and $z_0 \sin(\theta) < 0.5$.

A series of selections based upon isolation variables are applied to the signal muons. For the sbottom analysis, signal muons must pass the GradientLoose isolation criteria, whilst for the DM analysis the LooseTrackOnly requirement is used [105]. Baseline muons that are consistent with originating from a cosmic ray (from the impact parameter information) are vetoed.

Variable	$tb + E_{\mathrm{T}}^{\mathrm{miss}}$	Sbottom $bb + E_{\mathrm{T}}^{\mathrm{miss}}$	DM $bb + E_{\mathrm{T}}^{\mathrm{miss}}$
Baseline			
Acceptance	$p_{\mathrm{T}} > 10\,\mathrm{GeV}$, $\lvert\eta\rvert < 2.5$	$p_{\mathrm{T}} > 10\,\mathrm{GeV}$, $\lvert\eta\rvert < 2.5$	$p_{\mathrm{T}} > 6\,\mathrm{GeV}$, $\lvert\eta\rvert < 2.5$
Quality/ID	Loose	Medium	
Signal			
Acceptance	$p_{\mathrm{T}} > 25\,\mathrm{GeV}$, $\lvert\eta\rvert < 2.5$	$p_{\mathrm{T}} > 26\,\mathrm{GeV}$, $\lvert\eta\rvert < 2.5$	$p_{\mathrm{T}} > 26\,\mathrm{GeV}$, $\lvert\eta\rvert < 2.5$
Quality	Loose	Medium	
Isolation	ptCone20 $< 1.8\,\mathrm{GeV}$	GradientLoose	LooseTrackOnly
d_0 Significance	–	< 3	
$z_0\sin(\theta)$	–	< 0.5	
Cosmic Muon	Veto whole event	Only veto muon	

TABLE 5.2: Overview of the Muon object definitions for Run 1 and Run 2.

5.1.3 Anti-k_T Jets

As alluded to in Section 2.3, partons are not measured directly in the detector and instead hadronise. How to relate the parton-level objects to the hadrons measured in the detector is a vital component of event reconstruction. The flow of collimated hadrons is referred to as a jet. Jet finding can be thought of as trying to recover the original parton from the measured hadrons. There are generally two categories of jet algorithm: cone algorithms and sequential recombination algorithms. For the purposes of this thesis, the anti-k_T sequential recombination algorithm is used.

Sequential recombination algorithms are based upon minimising the distance (ΔR) between hadrons. This is done by iterating over all partons, grouping the closest (based upon a p_{T} weighted distance parameter $d_{i,j}$) pair of hadrons together into one hadron, and iterating until the final set of hadrons are all greater than the desired radius (R) apart. The distance measures for the grouping performed by the anti-k_t algorithm are defined as:

$$\begin{aligned} d_{i,j} &= \min(p_{ti}^{2p}, p_{tj}^{2p})\frac{\Delta R_{ij}^2}{R^2}, \qquad \Delta R_{ij} = \sqrt{(\eta_i - \eta_j)^2 + (\phi_i^2 - \phi_j^2)} \\ d_{iB} &= p_{ti}^{2p} \end{aligned} \tag{5.1}$$

In this case, to take into account beam remnants, an additional distance parameter, $d_{i,B}$, is required which is the distance from the i^{th} particle to the beam. The anti-k_T algorithm uses $p = -1$, which results in clusters being formed around the hardest hadrons in the event and runs according to the following three steps:

- Find the pair of particles with the smallest $d_{i,j}$ in the event and combine these particles into one particle.
- If the smallest value is $d_{i,B}$ then the particle i is combined with the beam.
- Continue the iteration until all particles in the event are separated by $> R$, the required jet radius.

A beneficial aspect of the anti-k_t algorithm is that hard jets produced by the algorithm are approximately circular in the (ϕ, η) plane, in a similar manner to the cone-based algorithms.

The seeds for the jet algorithm originate from topological calorimeter clusters. The jet algorithm builds jets with $|\eta| < 4.5$ which are then calibrated. In addition to this, the $|\eta| < 4.5$ jets are used in the $E_{\mathrm{T}}^{\mathrm{miss}}$ calculation.

The reconstructed jets can be calibrated using different methods to take into account detector response and performance. A jet energy scale (JES) calibration is applied to correct the response of the calorimeters to the true jet energy based upon the p_{T} and η of the jet. The jets are also corrected to take into account pile-up effects, using methods to account for residual detector response effects. Jets which may arise from pile-up events are vetoed using a combination of jet vertex fraction (JVF), minimum jet p_{T} and $|\eta|$ selections [106]. The JVF algorithm associates calorimeter clusters with tracks in the ID and assigns the resultant jet a weight, depending upon how likely the jet is to have originated from the primary vertex. The calculation of the JVF weight is related to the momentum fraction of the tracks associated with the primary vertex [107].

It is possible that "fake" jets can occur in an event, arising in non-collision background events, fake calorimeter signals due to noise or other similar unexpected occurances. Consequently, a jet cleaning selection is applied to the jets in each analysis [108]. In all events, if a "baseline" jet after the OR procedure is labelled as a "bad" or "loose" jet, then the event is vetoed. The full jet definitions for the analyses presented are shown in Table 5.3.

$tb + E_{\mathrm{T}}^{\mathrm{miss}}$ Analysis

The local cluster weighting calibration (LCW) method is used to calibrate the reconstructed jets [109]. In this method the clusters used to build the jets are defined as either electromagnetic or hadronic. These components are then weighted to take into account the difference between electron and pion response in the calorimeters.

The baseline selection requires $p_{\mathrm{T}} > 25\,\mathrm{GeV}$, and $|\eta| < 2.5$ to ensure the jets are in the central region of the detector. No additional acceptance requirements are used to define signal jets, only that the baseline jet passes the overlap removal procedure.

Sbottom and DM $bb + E_{\mathrm{T}}^{\mathrm{miss}}$ Analysis

The EM topo-cluster calibration scheme is used to calibrate the reconstructed jets. In this scheme, the jets are calibrated to the electromagnetic scale using measurements of the calorimeter response to electrons [110].

Baseline jets are required to have $p_{\mathrm{T}} > 20\,\mathrm{GeV}$ and $|\eta| < 2.8$. The pseudorapidity range chosen is such that for anti-k_T jets with $R = 0.4$, the clusters used to create the jet will be within $|\eta| < 3.2$ corresponding to the total coverage provided by the barrel and end-cap calorimeters. Jets which pass the OR requirements have an additional signal acceptance selection of $p_{\mathrm{T}} > 30\,\mathrm{GeV}$ for the sbottom analysis. Due to the relatively low p_{T} jets expected in the DM analysis, this additional requirement is not applied.

An additional Jet Vertex Tagger (JVT) requirement is applied to low p_{T} central jets to protect against jets arising from pile-up interactions. The JVT method is an extension of the previously introduced JVF method. The JVF method is found to decrease the efficiency of correctly identifying jets from the hard-scatter event as the number of pile-up vertices increases. The JVT algorithm introduces additional variables related to the number of vertices in the event and the p_{T} of the tracks in the event. The output weight of the algorithm is found to provide further discrimination between pile-up jets and jets arising from the hard scatter process [111]. The output of the JVT algorithm is required to be > 0.59 for jets with $p_{\mathrm{T}} < 60\,\mathrm{GeV}$, $|\eta| < 2.5$.

Variable	$tb + E_{\mathrm{T}}^{\mathrm{miss}}$	Sbottom $bb + E_{\mathrm{T}}^{\mathrm{miss}}$	DM $bb + E_{\mathrm{T}}^{\mathrm{miss}}$
Baseline			
Acceptance	$p_{\mathrm{T}} > 20\,\mathrm{GeV}$, $\|\eta\| < 2.5$	$p_{\mathrm{T}} > 20\,\mathrm{GeV}$, $\|\eta\| < 2.8$	
Jet Cleaning	Veto event if a bad/loose jet is present		
Signal			
Acceptance	$p_{\mathrm{T}} > 20\,\mathrm{GeV}$, $\|\eta\| < 2.5$	$p_{\mathrm{T}} > 30\,\mathrm{GeV}$, $\|\eta\| < 2.8$	$p_{\mathrm{T}} > 20\,\mathrm{GeV}$, $\|\eta\| < 2.8$
JVT Acceptance	–	> 0.59, if $p_{\mathrm{T}} < 60\,\mathrm{GeV}$, $\|\eta\| < 2.4$	

TABLE 5.3: Overview of the jet object definitions used in Run 1 and Run 2.

5.1.4 $b-$jets

A key component of all of the analyses in this thesis is the presence of $b-$tagged jets (subsequently referred to as $b-$jets) in the final state. Due to the difficulty in recognising if a jet has originated from a $b-$quark, machine learning techniques such as neural networks (NN) are used to identify $b-$jets. These algorithms take advantage of the an important characteristic of $b-$quark production, which is that, after hadronisation, the lifetime of the B-hadron is such that it can travel a distance in the detector, producing a secondary vertex (from which the B-hadron subsequently decays). The average distance travelled by a B-hadron can be roughly calculated, using the average lifetime ($\tau_{\mathrm{B}} = 1.5 \times 10^{-12}\,\mathrm{s}$) of the B-hadron, as $d = \beta\gamma c\tau \approx 3\,\mathrm{mm}$, where $\beta\gamma$ is the relativistic boost taken to be ≈ 6. Figure 5.2 presents an example of a secondary vertex arising due to the decay of a B-hadron.

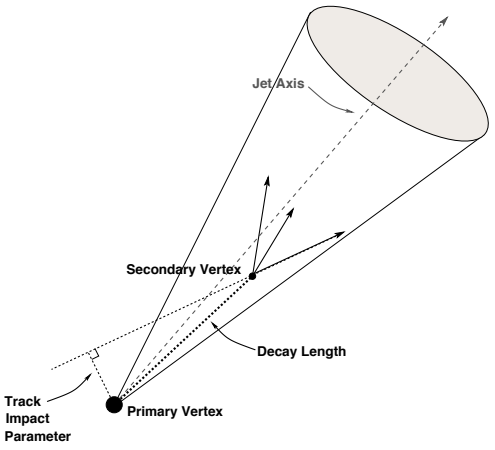

FIGURE 5.2: An example of a secondary vertex due to a $b-$hadron decay. Taken from [112].

The inner workings of these algorithms are discussed elsewhere [112], however generally two levels of algorithms are used. The initial level contains multiple algorithms, each of which uses key discriminating variables to distinguish between $b-$ and non-$b-$tagged jets. The information from the identified secondary vertices is used, such as the impact parameters of the tracks originating from the vertices, the distance travelled by the hadron, and information from the subsequent hadron decay. The Working-Point (WP) of an algorithm is the selection placed on the output score of the algorithm, to ensure a certain $b-$tagging efficiency. Each efficiency also relates to a $b-$tagging "purity", which is the percentage of correctly identified $b-$jets. Scale factors which are p_{T}-dependent

are applied to the resultant $b-$jets corresponding to the ratio between the efficiency of $b-$tagging in data and MC using a $t\bar{t}$ enriched sample [113].

Due to the requirement of tracks and/or secondary vertices, that are subsequently used as an input for the algorithms, a general acceptance requirement for $b-$jets throughout each analysis is that the jet must fall within $|\eta| < 2.5$, to provide tracking information from the ID.

It is noted that in the subsequent $b-$jet definitions the $b-$tagging algorithm differs between Run 1, the first year of data-taking in Run 2 (2015), and the combined 2015+2016 dataset of Run 2. The changes in $b-$tagging algorithms are motivated by improvements made to the algorithms. The MV1 algorithm uses a NN based upon the outputs of multiple algorithms. The two MV2 algorithms improve upon this by using boosted decision trees (BDTs) based upon a set of inputs (the same inputs used for the algorithms which the MV1 method is based upon) [114]. The difference between the MV2_c20 and MV2_c10 is the $c-$jet fraction used in the training of the BDTs. The MV2_c20 uses a $c-$jet fraction of 20%, whilst the MV2_c10 algorithm uses 10% [115].

$tb + E_{\mathrm{T}}^{\mathrm{miss}}$ Analysis

The MV1 algorithm [116] is used to provide the final $b-$tagging discriminant. The 70% $b-$tagging efficiency operating point is used. For this operating point, the rejection factors for non-$b-$jets are 137, 5 and 13 for light-quarks, $c-$quarks and τ leptons respectively.

Sbottom $bb + E_{\mathrm{T}}^{\mathrm{miss}}$ Analysis

Identification of the $b-$jets is performed using the MV2c20 algorithm. The WP used is the 77% efficiency point, The rejection factors for this WP are 6.57, 21.4 and 100.37 for $c-$jets, τ leptons and light-jets respectively.

It is known that the $b-$tagging efficiency is dependent upon the $b-$jet p_{T}. For the high squark masses targeted in this analysis a more preferred option would be to use a "flat efficiency" WP, which provides a constant 77% efficiency regardless of $b-$jet p_{T}. Unfortunately this flat efficiency $b-$tagging was unavailable on the timescale of the analysis.

Dark Matter $bb + E_{\mathrm{T}}^{\mathrm{miss}}$ Analysis

The MV2c10 $b-$tagging algorithm is used to produce the final $b-$tagging discriminant in the analysis. The 60% WP is used, where the rejection factors for light-flavour jets,

$c-$jets and τ leptons are 1538.78, 34.54, 183.98, respectively.

An optimisation was performed considering which $b-$tagging WP to use for this analysis, optimising based upon the signal topology under investigation. The higher purity selection caused by the decreased efficiency WP, was found to increase the background rejection to an extent that compensated for the decreased signal sensitivity.

Variable	$tb + E_{\mathrm{T}}^{\mathrm{miss}}$	Sbottom $bb + E_{\mathrm{T}}^{\mathrm{miss}}$	DM $bb + E_{\mathrm{T}}^{\mathrm{miss}}$
Signal $b-$jet			
Acceptance	p_{T} >25 GeV, $\lvert\eta\rvert < 2.5$	p_{T} >30 GeV, $\lvert\eta\rvert < 2.5$	p_{T} >20 GeV, $\lvert\eta\rvert < 2.5$
Algorithm	MV1	MV2c20	MV2c10
Efficiency WP	70%	77%	60%
$b-$jet purity	92.28%	94.99%	99.00%
Quality	Passes signal jet selection		

TABLE 5.4: Overview of the $b-$jet object definitions used in Run 1 and Run 2.

5.1.5 Photons

Nominally photons are expected to mainly interact in the electromagnetic calorimeter, depositing all of their energy and producing a shower in this section of the detector. If a photon interacted in this manner, the only noticable trace of the photon in the detector would be a shower in the calorimeter.

However as the EM calorimeter is placed outside the ID environment, it is possible that photons can interact with the ID, producing tracks before showering in the calorimeter which, as discussed in Section 5.1.1, is similar to how an electron would be expected to interact with the detector. These two methods of photon interactions in the detector lead to two classifications of the final photon object, referred to as "unconverted" and "converted" photons respectively.

Unconverted photons are photons that interact only with the EM calorimeter and are characterised by the shower information only. An algorithm is used to define a cluster area around the calorimeter cell recording the highest energy, and this is used to calculate the total shower energy, and thus the photon p_{T} and η [117].

Converted photons interact with the ID material to produce e^+e^- pairs which produce tracks in the ID. Converted photons are identified by reconstructing the conversion vertices within the ID and attaching these reconstructed vertices to a shower in the calorimeter, using an algorithm to distinguish converted photons from electrons using the conversion vertices and the track p_{T} as inputs [118].

Photon objects are only relevant for the sbottom $bb + E_{\mathrm{T}}^{\mathrm{miss}}$ analysis, as a photon replacement method is used to validate the nominal $Z-$jets prediction (Section 6.2.4). In this analysis, the baseline photon acceptance selections are $p_{\mathrm{T}} > 125\,\mathrm{GeV}$ and $|\eta| < 2.37$. The η selection used corresponds with the finely segmented regions of the EM calorimeter, which is shown to provide good discrimination between photons and π^0 mesons. The quality selection corresponds to tight cuts on shower-shape variables and leakage of the shower into the hadronic calorimeter.

The signal photon requirements include $p_{\mathrm{T}} > 130\,\mathrm{GeV}$ to ensure that the photon is in the single-photon trigger plateau. The isolation requirement of "FixedCutTight" implies $p_{\mathrm{T}}(\gamma)$ dependent selections on both the calorimeter and track isolation [119]. For the calorimeter isolation, a selection based upon the energy in a topological cone of $R = 0.4$ around the photon object is used, requiring $E(\mathrm{topoEtcone40}) < 0.022 p_{\mathrm{T}}(\gamma) + 2.45$. The track isolation requires the p_{T} sum in a cone $R < 0.2$, to satisfy: $\mathrm{ptcone20}/p_{\mathrm{T}} < 0.05$.

Variable	Sbottom $bb + E_{\mathrm{T}}^{\mathrm{miss}}$
Baseline	
Acceptance	p_{T} >25 GeV, $\lvert\eta\rvert < 2.37$
Quality	Tight
Signal	
Acceptance	p_{T} >130 GeV, $\lvert\eta\rvert < 2.37$
Quality	Tight
Isolation	FixedCutTight

TABLE 5.5: Overview of the photon object definitions used in Run 1 and Run 2.

5.1.6 Missing Transverse Momentum

Missing transverse momentum ($\vec{\boldsymbol{p}}_{\mathrm{T}}^{\mathrm{miss}}$ and its modulus $E_{\mathrm{T}}^{\mathrm{miss}}$) is considered to be an object as it can be thought of as attempting to reconstruct particles that do not interact with the detector and thus escape detection.

When considering the SM, neutrinos are the only particles that are not expected to interact with the detector, however, when considering R-parity conserving SUSY, the LSP ($\tilde{\chi}_1^0$) will also exhibit this behaviour, and as such the $\vec{\boldsymbol{p}}_{\mathrm{T}}^{\mathrm{miss}}$ variable is a vital component of SUSY analyses.

The $\vec{\boldsymbol{p}}_{\mathrm{T}}^{\mathrm{miss}}$ definition uses the fact that in the transverse plane, the sum of the momenta of detected particles would be expected to be zero. For example, Equation 5.2 considers an event containing only two measured particles, labelled 1 and 2.

$$0 = \vec{\boldsymbol{p}}_{\mathrm{T}}^{1} + \vec{\boldsymbol{p}}_{\mathrm{T}}^{2} \tag{5.2}$$

If instead, the above equation is not satisfied, and the sum of particle transverse momenta in the event is not equal to zero, then a particle (or particles) must have escaped the detector in order to balance the momenta, denoted by $\vec{\boldsymbol{p}}_{\mathrm{T}}^{\mathrm{miss}}$ as in Equation 5.3. It is the magnitude of the $\vec{\boldsymbol{p}}_{\mathrm{T}}^{\mathrm{miss}}$ vector which is used as the definition of the $E_{\mathrm{T}}^{\mathrm{miss}}$.

$$0 = \vec{\boldsymbol{p}}_{\mathrm{T}}^{1} + \vec{\boldsymbol{p}}_{\mathrm{T}}^{2} + \vec{\boldsymbol{p}}_{\mathrm{T}}^{\mathrm{miss}} \tag{5.3}$$

Due to the busy enviroment of a pp collision, the reconstruction of the $\vec{\boldsymbol{p}}_{\mathrm{T}}^{\mathrm{miss}}$ vector must take into account all energy deposits within the detector that could have arisen from the hard scattering process. This is done using algorithms which take into account baseline objects that are measured in the event (electrons, muons, jets, etc), using a $E_{\mathrm{T}}^{\mathrm{miss}}$ specific overlap removal. There is also the ability to include calorimeter clusters that are not associated with any object, and tracks in the ID that are also not associated with any object, in the $E_{\mathrm{T}}^{\mathrm{miss}}$ calculation.

$tb + E_{\mathrm{T}}^{\mathrm{miss}}$ Analysis

The $E_{\mathrm{T}}^{\mathrm{miss}}$ definition used for this analysis includes the transverse momenta of objects such as jets, photons, muons and electron, after calibration but before any acceptance selection has been employed. In addition, it includes the momenta from topological clusters in the calorimeter that are not associated with a reconstructed object. This term is referred to as the "soft" $E_{\mathrm{T}}^{\mathrm{miss}}$ term ($\vec{\boldsymbol{p}}_{\mathrm{T}}^{\mathrm{miss}}{}_{\mathrm{Cellout}}$), as it is calculated from the remaining energy deposits in the detector, that do not belong to a "hard" or well-defined object [120].

$$\vec{\boldsymbol{p}}_{\mathrm{T}}^{\mathrm{miss}} = \vec{\boldsymbol{p}}_{\mathrm{T}}^{\mathrm{miss}}{}_{\mathrm{Jet}} + \vec{\boldsymbol{p}}_{\mathrm{T}}^{\mathrm{miss}}{}_{\mathrm{Gamma}} + \vec{\boldsymbol{p}}_{\mathrm{T}}^{\mathrm{miss}}{}_{\mathrm{Muon}} + \vec{\boldsymbol{p}}_{\mathrm{T}}^{\mathrm{miss}}{}_{\mathrm{Ele}} + \vec{\boldsymbol{p}}_{\mathrm{T}}^{\mathrm{miss}}{}_{\mathrm{Cellout}} \tag{5.4}$$

Sbottom and DM $bb + E_{\mathrm{T}}^{\mathrm{miss}}$ Analyses

The $E_{\mathrm{T}}^{\mathrm{miss}}$ definition used in these analyses is similar to the previous definition, including the electron, photon, muon and jet terms, however, the soft $E_{\mathrm{T}}^{\mathrm{miss}}$ term is replaced with the Track Soft Term (TST), $\vec{\boldsymbol{p}}_{\mathrm{T}}^{\mathrm{miss}}{}_{\mathrm{TST}}$. The TST arises from tracks in the ID that are not associated with any reconstructed object, but are associated with the primary vertex. Quality selections are applied to the tracks that enter into the TST term [121]. The use of the TST term reduces the pile-up dependence of the $E_{\mathrm{T}}^{\mathrm{miss}}$ [122].

$$\vec{\boldsymbol{p}}_{\mathrm{T}}^{\,\mathrm{miss}} = \vec{\boldsymbol{p}}_{\mathrm{T}}^{\,\mathrm{miss}}{}_{\mathrm{Jet}} + \vec{\boldsymbol{p}}_{\mathrm{T}}^{\,\mathrm{miss}}{}_{\mathrm{Gamma}} + \vec{\boldsymbol{p}}_{\mathrm{T}}^{\,\mathrm{miss}}{}_{\mathrm{Muon}} + \vec{\boldsymbol{p}}_{\mathrm{T}}^{\,\mathrm{miss}}{}_{\mathrm{Ele}} + \vec{\boldsymbol{p}}_{\mathrm{T}}^{\,\mathrm{miss}}{}_{\mathrm{TST}} \tag{5.5}$$

5.2 Overlapping Physics Objects

After defining the baseline object selections it is possible that the objects have been reconstructed using the same regions of interest within the detector. For example: the behaviour of an isolated electron in the detector can be reconstructed as both an electron and a jet. A removal procedure is applied to all baseline physics objects, in order to resolve overlaps and to correctly associate regions of interest in the detector to the correct physics object.

The overlap removal is applied based upon the separation (ΔR) in the (η, ϕ) plane, between the electrons, jets, muons and photons, with the value of the separation in this plane used to discard one of the candidate objects, whilst keeping the other.

$tb + E_{\mathrm{T}}^{\mathrm{miss}}$ Analysis

The overlap removal used in this analysis is defined to remove leptons overlapping with jets, and is applied as follows:

- If $\Delta R(e, j) < 0.2$, the jet is rejected, the electron is kept.
- If $0.2 < \Delta R(j, e) < 0.4$, the electron is rejected, the jet is kept.
- If $\Delta R(\mu, j) < 0.4$, the muon is rejected, the jet is kept.

Sbottom and DM $bb + E_{\mathrm{T}}^{\mathrm{miss}}$ Analyses

A more sophisticated overlap removal was introduced during Run 2, in order to exploit $b-$tagging information when deciding if an object should be rejected. It is expected that when a $b-$quark is produced and subsequently hadronises, then it may decay leptonically. If this is the case, then the previous overlap removal method would assign the $b-$jet as a lepton, leading to an incorrect characterisation of the event. In order to maximise the capability of correctly assigning a $b-$jet object, instead of a lepton object, the efficiency WP for the $b-$jets entering into the OR calculation is increased to 80% (85% for the DM $bb + E_{\mathrm{T}}^{\mathrm{miss}}$ analysis), resulting in a higher $b-$tagging efficiency, but also causing a decrease in the purity of the $b-$jets entering the OR calculation.

Further to this, due to the installation of the IBL prior to Run 2, additional track information is used to distinguish if an object is a jet or a muon. The overlap removal is applied as follows:

- If $\Delta R(e, j) < 0.2$, the jet is rejected and the electron is kept, unless the jet is tagged as a $b-$jet using the looser WP, then the (prospective) $b-$jet is kept.
- If $0.2 < \Delta R(j, e) < 0.4$, the electron is rejected and the jet is kept.
- If $\Delta R(\mu, j) < 0.4$, the muon is rejected and the jet is kept. Unless the object has less than three associated tracks with $p_{\mathrm{T}} < 500$ MeV, then the jet is rejected and the muon is kept.

For the sbottom $bb + E_{\mathrm{T}}^{\mathrm{miss}}$ analysis, photons are also included when performing the data-driven background estimation technique. As such an overlap removal which also includes photons is used:

- If $\Delta R(e, \gamma) < 0.4$, the photon is rejected and the electron is kept.
- If $\Delta R(\gamma, j) < 0.4$, the jet is rejected and the photon is kept.
- If $\Delta R(\mu, \gamma) < 0.4$, the photon is rejected and the muon is kept.

The previous sections have discussed the definition of the physics objects used in the analyses, including the baseline selection to initially identify candidate objects, and the signal object selection to firmly classify the candidate as a physics object. Further to this, the overlap removal procedure that prevents the double counting of objects has been explained with the differences between the Run 1 and Run 2 versions of the overlap removal discussed.

Before a physics analysis can be performed using the events with the above object classifications, a stringent set of cleaning selections are applied to the events and to the objects. These selections are discussed in the following section.

5.3 Event Cleaning

To ensure good quality data is used for analyses, a set of cleaning selections are applied to both data and MC [123]. They are used to prevent spurious signals from the detector and poorly measured events from being included in the analysis. There are many similarities

between the event cleaning selections adopted in Run 1 and Run 2 analyses as possible detector issues that will have occurred during Run 1 are also likely be present in Run 2. Due to detector improvements between Run 1 and Run 2, there are event cleaning selections that are applied to the Run 1 data and not the Run 2 data and vice versa. Unless otherwise specified, the following event cleaning requirements are applied to both the Run 1 and Run 2 data.

- **Good Run List (GRL):** Events from luminosity blocks that do not appear on the GRL are rejected. The GRL contains a list of all luminosity blocks, and has been cross-referenced with the status of the detector. Luminosity blocks appearing on the GRL pass a basic set of data quality requirements, such as all components of the detector being fully operational and not experiencing any errors. If an event arises from a luminosity block that does not appear on the GRL it is rejected.

- **Trigger requirements:** The trigger requirements for the regions defined in each analysis (to be discussed in subsequent chapters) are required to be passed. For single lepton triggers (e, μ) this includes a requirement that the lepton in the event is trigger matched, implying that the lepton in the event caused the trigger to fire.

- **Primary vertex selection:** All events are required to contain a primary vertex (PV). The PV in an event is taken to be the vertex containing at least 5 associated tracks (with $p_{\mathrm{T}} > 0.4\,\mathrm{GeV}$), with the highest $\sum p_{\mathrm{T}}^2(\mathrm{track})$.

- **LAr and Tile calorimeter cleaning:** During physics running it is possible that the LAr calorimeters undergo a noise burst corrupting the data. It is also possible that events from the Tile calorimeter are corrupted in a similar manner due to high voltage trips. As such, events where either the LAr or Tile calorimeter are reporting data corruption are vetoed.

- **Incomplete events:** When a section of the detector is reporting errors during running, a possible resolution to the error is to perform a Timing, Trigger and Control (TTC) restart. This will restart the section of the detector, causing incomplete events as the data is not completely written to the buffers. Events which have data loss due to a TTC restart are vetoed. In addition to this, events affected by the SCT single event upset recovery procedure are removed in the Run 2 data.

- **Jet Cleaning:** Clusters in calorimeters that appear to represent a jet, but are not caused by a jet (referred to as "fake" jets) can arise in multiple ways, such as

from non-collision background events, cosmic muon events with unexpected muon energy loss in the calorimeters, or from calorimeter noise. A set of selections are applied in order to reject such events containing fake jets, whilst maintaining an efficiency of close to 100% for signal jets [108]. This selection criteria is designed based upon the quality of fit on calorimeter pulse shape, the jet energy and jet charged energy fraction, as measured in the ID. Events are rejected if, after overlap removal, they contain at least one baseline jet which fails the loose cleaning cuts.

- **Tile negative energy cleaning:** Another possible outcome of data corruption in the Tile calorimeter is the appearance of large negative energy in calorimeter cells, causing topological clusters to be built with negative energy. These topoclusters cause events to have a large amount of fake $E_{\mathrm{T}}^{\mathrm{miss}}$ as the noisy cells are not clustered in a jet, and are attributed to the $\vec{\boldsymbol{p}}_{\mathrm{T}}^{\,\mathrm{miss}}{}_{\mathrm{Cellout}}$ term in the calculation. To reject these events, the significance of the $\vec{\boldsymbol{p}}_{\mathrm{T}}^{\,\mathrm{miss}}{}_{\mathrm{Cellout}}$ term in the $E_{\mathrm{T}}^{\mathrm{miss}}$ calculation is estimated, and if a significant amount of $E_{\mathrm{T}}^{\mathrm{miss}}$ in the event arises from the Cellout term the event is vetoed.

- **Jet timing Selection:** Events with a mean jet time $|\langle t \rangle| < 5\,\mathrm{ns}$ (where $|\langle t \rangle|$ is the energy weighted mean), pass the timing selection, as events are expected to be reconstructed with an average time of a few ns. Events which are outside of this window are considered to come from non-collision background events and are rejected.

- **Tile hot cells:** During Run 1 data taking, in some data taking periods a noisy tile calorimeter cell was not properly excluded (masked) in the event reconstruction. Events which contain a jet pointing to the region in (η, ϕ) close to the affected module and with the largest energy deposit in the second tile layer, were rejected.

- **Dead Tile cells:** Again during Run 1, there were some non-operational cells in the tile calorimeter. These non-functional cells affect the jet reconstruction and energy response, and also the $E_{\mathrm{T}}^{\mathrm{miss}}$ calculation. Events that are affected by these non-operational tile cells are rejected by vetoing events containing any jet with $p_{\mathrm{T}}^{\mathrm{miss}} > 40\,\mathrm{GeV}$, $B_{\mathrm{jet}}^{\mathrm{corr}} > 0.05$ (this is a measure of the fraction of energy in the reconstructed jet, that arises from a correction applied to the non-operational cell, from the average of the neighbouring cells) and $\Delta\phi(j, E_{\mathrm{T}}^{\mathrm{miss}}) < 0.3$. This selection

is also efficient at removing events in which the $E_{\mathrm{T}}^{\mathrm{miss}}$ arises from the hole in the hadronic calorimeter end-cap.

- **Bad muon veto:** In order to ensure a high quality of reconstructed muons, events are rejected if they contain a baseline muon with $\frac{\sigma(q/p)}{|q/p|} > 0.2$.

The efficiency of the above data-quality selections corresponds to a rejection of $\approx 10\%$ of the data. The remaining data is of a high quality and is subsequently used for the analyses. The remainder of this Chapter concerns global event variables, which are used to select a specific event topology.

5.4 Global event variables

When targeting BSM signal topologies, the likely final state objects are initially considered when designing the analysis. For example, in the $bb + E_{\mathrm{T}}^{\mathrm{miss}}$ analysis, the signal topology targeted is that of sbottom pair production, with each leg of the decay proceeding via the decay $\tilde{b} \rightarrow b\tilde{\chi}_1^0$, hence the final state would contain zero leptons, 2 $b-$jets and $E_{\mathrm{T}}^{\mathrm{miss}}$. However, searching for a SUSY signal in all events containing zero leptons, 2 $b-$jets and $E_{\mathrm{T}}^{\mathrm{miss}}$ would be extremely difficult, due to the large amount of SM background that is also expected.

In order to attempt to isolate the signal on top of the large amount of SM backgrounds, kinematic variables are employed to further discriminate between expected signal events and background. The aim of a variable definition is to combine the final state objects from the signal topology under investigation in a way that produces a useful variable to reject the SM backgrounds, whilst maintaining a relatively high signal efficiency.

In the following section, general analysis variables are defined, that are used throughout each analysis presented herein. A brief explanation of why the variables are generally useful to target a generic third generation SUSY signal is given.

Further to this, the key kinematic variables that are used for the specific signal topologies targeted by each analysis are defined. For these variables a slightly more in-depth explanation of why they are useful is presented.

5.4.1 Common global event variables

Throughout the analyses presented within this thesis, a similar set of baseline kinematic variables are used due to their general discriminating power to remove SM backgrounds and enhance SUSY signals.

$\min \Delta\phi(j, E_{\mathrm{T}}^{\mathrm{miss}})$: The minimum azimuthal distance between the jets and the $E_{\mathrm{T}}^{\mathrm{miss}}$ is a useful variable to discriminate between multi-jet backgrounds with a large amount of $E_{\mathrm{T}}^{\mathrm{miss}}$ due to mismeasured jets. Studies performed using data-driven QCD estimation methods indicate that a selection of $\min \Delta\phi(j, E_{\mathrm{T}}^{\mathrm{miss}}) > 0.4$ is sufficient to reduce the QCD background to a negligible amount.

The QCD background is estimated using a data-driven method referred to as the "jet smearing" method. The $E_{\mathrm{T}}^{\mathrm{miss}}$ arising in QCD events is due to mismeasurement of the jet p_{T} and neutrinos arising from heavy flavour decays. In order to model this background, a selection of seed events containing well measured jets are "smeared", by smearing the 4-momenta of the jets. These smeared events are then used to predict the QCD contribution in the regions used for the analysis.

H_{T} [GeV]: The H_{T} variable is defined as the scalar sum of the p_{T} of all signal jets in an event. For SUSY signals with high p_{T} jets it would be expected to peak at a larger value than the SM backgrounds:

$$H_{\mathrm{T}} = \sum_{i=0}^{n_{\mathrm{jets}}} p_{\mathrm{T}}(j_i), \tag{5.6}$$

alternative definitions of H_{T} may be used, based upon including different numbers of jets in the calculation, or using different jet p_{T} or $|\eta|$ thresholds.

m_{eff} [GeV]: The effective mass of an event, m_{eff}, is taken to be the scalar p_{T} sum of the hadronic activity in the detector (the previously defined H_{T}) and the $E_{\mathrm{T}}^{\mathrm{miss}}$. Generally the definition of m_{eff} is:

$$\begin{aligned} m_{\mathrm{eff}} &= \sum_{i=0}^{n_{\mathrm{jets}}} p_{\mathrm{T}}(j_i) + E_{\mathrm{T}}^{\mathrm{miss}}, \\ &= H_{\mathrm{T}} + E_{\mathrm{T}}^{\mathrm{miss}}. \end{aligned} \tag{5.7}$$

For signal samples, the m_{eff} peaks at a larger value than for SM backgrounds, as can be seen in Figure 5.4(d). For sparticle pair production the peak of the m_{eff} distribution is correlated with $2m_{\tilde{\mathrm{p}}}$. Hence, a selection for large values of m_{eff} can improve the ratio of

signal to background. Similar to the H_{T}, alternative definitions of the m_{eff} may be used, with different jet multiplicities or acceptance selections. For example in the sbottom analysis, only the two highest p_{T} jets enter the m_{eff} calculation.

$E_{\mathrm{T}}^{\mathrm{miss}}$ significance [$\mathrm{GeV}^{1/2}$]: The $E_{\mathrm{T}}^{\mathrm{miss}}$ significance is a measure of the contribution of the $E_{\mathrm{T}}^{\mathrm{miss}}$ to the total activity in an event.

$$E_{\mathrm{T}}^{\mathrm{miss}}\,\text{significance} = \frac{E_{\mathrm{T}}^{\mathrm{miss}}}{\sqrt{H_{\mathrm{T}}}}. \tag{5.8}$$

For signal events, large $E_{\mathrm{T}}^{\mathrm{miss}}$ and H_{T} are expected, and as such the $E_{\mathrm{T}}^{\mathrm{miss}}$ significance is expected to be large. As the $E_{\mathrm{T}}^{\mathrm{miss}}$ significance is constructed from the same variables as the m_{eff}, these two variables are highly correlated. A selection on $E_{\mathrm{T}}^{\mathrm{miss}}$ significance is effective at removing the multi-jet background with fake $E_{\mathrm{T}}^{\mathrm{miss}}$.

$E_{\mathrm{T}}^{\mathrm{miss}}/m_{\mathrm{eff}}$: Another variable used to reject multi-jet background is the ratio of $E_{\mathrm{T}}^{\mathrm{miss}}$ to m_{eff}. This variable gives a measure of the total contribution of the $E_{\mathrm{T}}^{\mathrm{miss}}$ to the event. Due to similar studies as performed above for the $\min\Delta\phi(j, E_{\mathrm{T}}^{\mathrm{miss}})$ variable, it is found that selections of $E_{\mathrm{T}}^{\mathrm{miss}}/m_{\mathrm{eff}} > 0.25$ remove the majority of the QCD background.

m_{T} [GeV]: The transverse mass m_{T} is used to reconstruct the mass of a particle that undergoes a decay, to a detectable particle, usually a lepton ($p_{\mathrm{T}}(\ell)$), and an invisible particle (represented by the $E_{\mathrm{T}}^{\mathrm{miss}}$):

$$\begin{aligned} m_{\mathrm{T}} &= \sqrt{2(p_{\mathrm{T}}(l)E_{\mathrm{T}}^{\mathrm{miss}} - \vec{\mathbf{p}}_{\mathrm{T}}(l)\cdot\vec{\mathbf{E}}_{\mathrm{T}}^{\mathrm{miss}})}, \\ &= \sqrt{2p_{\mathrm{T}}(l)E_{\mathrm{T}}^{\mathrm{miss}}(1-\cos(\Delta\phi(\ell, E_{\mathrm{T}}^{\mathrm{miss}})))}. \end{aligned} \tag{5.9}$$

In regions containing one lepton, m_{T} is used mainly to discriminate between SM processes containing a $W-$boson decay and SUSY signals. For $W-$boson decays the endpoint of the m_{T} distribution is expected to be at m_{W}, as in this case the $E_{\mathrm{T}}^{\mathrm{miss}}$ in the event will arise from the neutrino from the W decay. In SUSY scenarios the main contribution to the $E_{\mathrm{T}}^{\mathrm{miss}}$ is from the neutralinos in the event. As such the endpoint of the m_{T} distribution is not the same as for the SM processes. Usually a selection is placed on $m_{\mathrm{T}} > 90-120\,\mathrm{GeV}$ to remove the $W+$jets background, taking into account detector resolution effects. A comparison between the m_{T} distributions for a signal process and the main background processes is presented in Figure 5.4(c), the signal distribution can be seen to peak at larger values of m_{T} when compared to the background.

m_{bb} [GeV]: When considering searches for the production of third generation quarks, it is common that either top- or bottom-quarks will be produced in the decay chain. Due to this, a standard background for most third generation analyses is $t\bar{t}$ pair production. The invariant mass of the two $b-$quarks from the $t\bar{t}$ decay generally peaks at around 200 GeV as in this case the $b-$quarks are each coming from a top-quark produced at rest. For SUSY signals, the $b-$quarks will be produced from the decay of a more massive particle, and generally the m_{bb} distribution peaks at larger values of m_{bb}.

$\mathcal{I}(j_1, j_2)$ or $\mathcal{A}$: The jet imbalance ($\mathcal{I}(j_1, j_2)$) (also referred to as the p_{T} asymmetry, $\mathcal{A}$) is a variable that is used to discriminate between jets that originate from gluon splitting (such as the HF jets produced in association with a Z-boson), and the jets produced from signal events when targeting events containing Initial State Radiation (ISR):

$$\mathcal{I}(j_1, j_2) = \frac{p_{\mathrm{T}}(j_1) - p_{\mathrm{T}}(j_2)}{p_{\mathrm{T}}(j_1) + p_{\mathrm{T}}(j_2)}. \tag{5.10}$$

For jets produced via gluon splitting, $\mathcal{I}(j_1, j_2)$ is expected to be low, as the jets would be expected to be produced with similar p_{T} as they arise from the same parent particle. For the jets produced in signal events, this is not be the case as the $b-$jets in the event are not produced at the same decay vertex.

5.4.2 Dedicated complex variables for the $tb + E_{\mathrm{T}}^{\mathrm{miss}}$ analysis

The signal topology under investigation for the $tb + E_{\mathrm{T}}^{\mathrm{miss}}$ analysis results in a final state containing a top-quark, a $b-$quark and $E_{\mathrm{T}}^{\mathrm{miss}}$, as shown in Figure 1.1(b). The top-quark will subsequently decay via a W and another $b-$quark. The channel under investigation is the one lepton (e, μ) channel, hence the W will decay leptonically, giving a final state containing: one lepton, two $b-$tagged jets, and $E_{\mathrm{T}}^{\mathrm{miss}}$. For this final state a variety of kinematic variables can be employed to enhance the signal and reject SM processes.

$\min \Delta\phi(b-\mathrm{jets}, E_{\mathrm{T}}^{\mathrm{miss}})$: Angular selections between the $E_{\mathrm{T}}^{\mathrm{miss}}$ and jets are useful to remove QCD multi-jet backgrounds from poorly measured jets. The $\min \Delta\phi(b-\mathrm{jets}, E_{\mathrm{T}}^{\mathrm{miss}})$ variable is defined as the minimum azimuthal distance between the $b-$jets and the $E_{\mathrm{T}}^{\mathrm{miss}}$:

$$\min \Delta\phi(b-\mathrm{jets}, E_{\mathrm{T}}^{\mathrm{miss}}) = \min(\left|\phi(\mathrm{b}_1) - \phi(E_{\mathrm{T}}^{\mathrm{miss}})\right|, \left|\phi(\mathrm{b}_2) - \phi(E_{\mathrm{T}}^{\mathrm{miss}})\right|). \tag{5.11}$$

Poorly reconstructed multi-jet events tend to have a jet and the $E_{\mathrm{T}}^{\mathrm{miss}}$ close together in the azimuthal plane, hence a selection on $\min \Delta\phi(b-\mathrm{jets}, E_{\mathrm{T}}^{\mathrm{miss}})$ is used to remove these events.

H_{T} [GeV]: In this analysis, the definition of the H_{T} is changed to include only the $b-$jets and the leading non-$b-$tagged jet, as it is expected that the signals will contain a low jet multiplicity.

$$H_{\mathrm{T}} = \sum_{i=1}^{2} p_{\mathrm{T}}(b_i) + p_{\mathrm{T}}(j_1). \tag{5.12}$$

For the previously defined variables that use the H_{T} variable (such as m_{eff} and $E_{\mathrm{T}}^{\mathrm{miss}}$ significance), this version of H_{T} is used in all calculations.

$n_{\mathrm{extra-jets}}$: The number of "extra" jets in the event is used in the $tb + E_{\mathrm{T}}^{\mathrm{miss}}$ analysis to reject events with large numbers of high p_{T} non-$b-$tagged jets. In the simplified model scenarios considered in the analysis there is expected to be a small amount of additional hadronic activity. As such $n_{\mathrm{extra-jets}}$ is defined as the number of non-$b-$tagged jets in an event with $p_{\mathrm{T}} > 50\,\mathrm{GeV}$.

am_{T2} [GeV]: The asymmetric transverse mass am_{T2} [124], is a generalisation of the M_{T2} variable [125], used to measure the masses of semi-invisibly decaying particles, which in itself is a generalisation of the previously discussed m_{T} variable.

In order to adequately discuss the am_{T2} variable, a brief discussion of the M_{T2} variable is required. The following closely follows the derivation presented in [125].

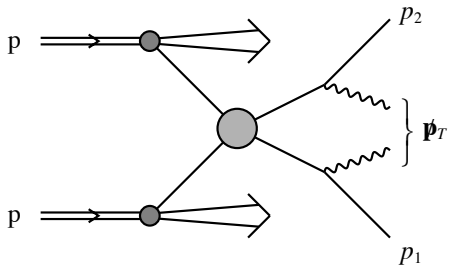

FIGURE 5.3: An overview of the generic sparticle production process that is considered for the M_{T2} calculation.
Taken from [125].

Consider the process in Figure 5.3, where the interaction between two protons produces a pair of identical particles, each one of these particles subsequently decaying to a

visible particle and an invisible particle. The visible particles are detected and measured (referred to as p_1 and p_2), whilst the invisible particles both contribute to the missing transverse energy $E_{\mathrm{T}}^{\mathrm{miss}}$, or in the figure, $\not{p}_{\mathrm{T}}$.

If one considers a scenario where only one leg of this process occurs, a singly produced particle denoted by $\tilde{\alpha}$ decays into the visible particle α (measurable in the detector) and the invisible particle $\tilde{\chi}$ (perceived in the detector as $E_{\mathrm{T}}^{\mathrm{miss}}$) then the decay can be written as: $\tilde{\alpha} \to \alpha\tilde{\chi}$. In this case the invariant mass of the parent particle can be reconstructed using the masses and 4-momenta of the two particles:

$$m(\tilde{\alpha})^2 = m(\alpha)^2 + m(\tilde{\chi})^2 + 2(E_{\mathrm{T}}(\alpha)E_{\mathrm{T}}(\tilde{\chi})\cosh(\Delta\eta) - \vec{\mathbf{p}}_{\mathrm{T}}(\alpha)\cdot\vec{\mathbf{p}}_{\mathrm{T}}(\tilde{\chi})). \tag{5.13}$$

As the condition $\cosh(\Delta\eta) > 1$ must be satisfied ($\Delta\eta > 0$), the equation can be written:

$$m(\tilde{\alpha})^2 \geq m_{\mathrm{T}}^2(\vec{\mathbf{p}}_{\mathrm{T}}(\alpha), \vec{\mathbf{p}}_{\mathrm{T}}(\tilde{\chi})) \equiv m(\alpha)^2 + m(\tilde{\chi})^2 + 2(E_{\mathrm{T}}(\alpha)E_{\mathrm{T}}(\tilde{\chi}) - \vec{\mathbf{p}}_{\mathrm{T}}(\alpha)\cdot\vec{\mathbf{p}}_{\mathrm{T}}(\tilde{\chi})), \tag{5.14}$$

which is a generalised version of the m_{T} that was introduced in the previous section, now including the daughter particle masses. The previously introduced m_{T} definition neglects these, as the m_{T} previously introduced is used to discriminate between leptonic W-boson decays, and as such the masses of the leptons (e, μ) and neutrinos are treated as negligible.

Generalising the above argument to the case where pair-produced particles are both decaying semi-invisibly is unfortunately not possible as the above derivation is based upon the capability to measure two decay products, which for the scenario pictured in 5.3 is not possible for both legs of the decay. However, the vector sum of the two invisible particles corresponds to the $E_{\mathrm{T}}^{\mathrm{miss}}$. Referring to the two invisible particles as $\tilde{\chi}_1$ and $\tilde{\chi}_2$ respectively, then the $\vec{\boldsymbol{p}}_{\mathrm{T}}^{\mathrm{miss}}$ can be written as:

$$\vec{\boldsymbol{p}}_{\mathrm{T}}^{\mathrm{miss}} = \vec{\mathbf{p}}_{\mathrm{T}}(\tilde{\chi}_1) + \vec{\mathbf{p}}_{\mathrm{T}}(\tilde{\chi}_2). \tag{5.15}$$

If it was possible to measure $\tilde{\chi}_1$ and $\tilde{\chi}_2$, the parent particle mass could be reconstructed by calculating two transverse masses (with visible particles α_1 and α_2), and taking the maximum of these two values:

$$m(\tilde{\alpha})^2 \geq \max[m_{\mathrm{T}}^2(\vec{\mathbf{p}}_{\mathrm{T}}(\alpha_1), \vec{\mathbf{p}}_{\mathrm{T}}(\tilde{\chi}_1))\,,\, m_{\mathrm{T}}^2(\vec{\mathbf{p}}_{\mathrm{T}}(\alpha_2), \vec{\mathbf{p}}_{\mathrm{T}}(\tilde{\chi}_2))]. \tag{5.16}$$

Using Equation 5.15 it is possible to perform a minimisation over all the possible 2-momenta that could construct the measured $\vec{\boldsymbol{p}}_{\mathrm{T}}^{\mathrm{miss}}$, and using these two vectors as the input to the m_{T} calculation:

$$m(\tilde{\alpha})^2 \geq M_{T2}^2 \equiv \min_{\vec{\boldsymbol{p}}_{\mathrm{T}}^{\mathrm{miss}}=\vec{\mathbf{p}}_{\mathrm{T}}(\tilde{\chi}_1)+\vec{\mathbf{p}}_{\mathrm{T}}(\tilde{\chi}_2)} \Big\{ \max[m_{\mathrm{T}}^2(\vec{\mathbf{p}}_{\mathrm{T}}(\alpha_1), \vec{\mathbf{p}}_{\mathrm{T}}(\tilde{\chi}_1)) \, , \, m_{\mathrm{T}}^2(\vec{\mathbf{p}}_{\mathrm{T}}(\alpha_2), \vec{\mathbf{p}}_{\mathrm{T}}(\tilde{\chi}_2))] \Big\}. \tag{5.17}$$

The above minimisation procedure, performed over the possible vector components of the $\vec{\boldsymbol{p}}_{\mathrm{T}}^{\mathrm{miss}}$ to calculate the parent particle mass, is the definition of the M_{T2} variable.

There is a requirement in the above derivation that the topologies are symmetric, and hence the derivation of the M_{T2} variable is dependent upon pair produced particles decaying symmetrically to the same invisible and visible particles. For the $tb + E_{\mathrm{T}}^{\mathrm{miss}}$ decay scenario this is not the case, and as such the asymmetric transverse mass is used.

If one considers the input parameters of the M_{T2} as described in Equation 5.14, the variable can be written as a function of properties related to the visible particles (m_α, $p_{\mathrm{T}}(\alpha_1)$, $p_{\mathrm{T}}(\alpha_2)$), and the invisible particles ($m_{\tilde{\chi}}$, $p_{\mathrm{T}}(\tilde{\chi}_1)$, $p_{\mathrm{T}}(\tilde{\chi}_2)$). However, as previously discussed, the invisible particles cannot be reconstructed, and instead a minimisation is performed over using the missing momentum vector ($\vec{\boldsymbol{p}}_{\mathrm{T}}^{\mathrm{miss}}$), allowing M_{T2} to be written as a function of properties of the visible particles, $\vec{\boldsymbol{p}}_{\mathrm{T}}^{\mathrm{miss}}$ and $m_{\tilde{\chi}}$:

$$M_{T2} = M_{T2}(m_\alpha, m_{\tilde{\chi}}, \vec{p}_{\mathrm{T}}(\alpha_1), \vec{p}_{\mathrm{T}}(\alpha_2), \vec{\boldsymbol{p}}_{\mathrm{T}}^{\mathrm{miss}}). \tag{5.18}$$

It is with the above formalism that it is simplest to generalise the symmetric case (using M_{T2}) to the asymmetric case (am_{T2}), by relaxing the mass constraints on both the visible and invisible particles. This can be done by introducing two more mass parameters into the calculation, one mass parameter corresponding to the relaxed requirement of identical visible particles being produced in the decays, and the other corresponding to relaxing the requirement on identical invisible particles being produced.

Identifying again the pair-production of two identical particles, however allowing one leg to decay via a visible particle (α) and invisible particle ($\tilde{\chi}$) such that $\tilde{\alpha} \to \alpha\tilde{\chi}$, and the other leg decays via a different visible particle (β) and a different invisible particle ($\tilde{\kappa}$) such that $\tilde{\alpha} \to \beta\tilde{\kappa}$, the am_{T2} in this case is then written as a function of 7 parameters:

$$am_{\mathrm{T2}} = am_{\mathrm{T2}}(m_\alpha, m_\beta, m_{\tilde{\chi}}, m_{\tilde{\kappa}}, \vec{p}_{\mathrm{T}}(\alpha_1), \vec{p}_{\mathrm{T}}(\alpha_2), \vec{\boldsymbol{p}}_{\mathrm{T}}^{\mathrm{miss}}). \tag{5.19}$$

Working through this argument in a similar manner to the M_{T2}, again requires two m_{T} calculations corresponding to calculating the m_{T} for both legs of the decay, however in contrast to Equation 5.14, the input particles to the m_{T} calculation are different on each leg of the decay.

$$m_{\mathrm{T}}^2(\vec{\mathbf{p}}_{\mathrm{T}}(\alpha), \vec{\mathbf{p}}_{\mathrm{T}}(\tilde{\chi})) \equiv m(\alpha)^2 + m(\tilde{\chi})^2 + 2(E_{\mathrm{T}}(\alpha)E_{\mathrm{T}}(\tilde{\chi}) - \vec{\mathbf{p}}_{\mathrm{T}}(\alpha) \cdot \vec{\mathbf{p}}_{\mathrm{T}}(\tilde{\chi})). \tag{5.20}$$

$$m_{\mathrm{T}}^2(\vec{\mathbf{p}}_{\mathrm{T}}(\beta), \vec{\mathbf{p}}_{\mathrm{T}}(\tilde{\kappa})) \equiv m(\beta)^2 + m(\tilde{\kappa})^2 + 2(E_{\mathrm{T}}(\beta)E_{\mathrm{T}}(\tilde{\kappa}) - \vec{\mathbf{p}}_{\mathrm{T}}(\beta) \cdot \vec{\mathbf{p}}_{\mathrm{T}}(\tilde{\kappa})). \tag{5.21}$$

The minimisation procedure (the asymmetric equivalent to Equation 5.17) in this scenario becomes:

$$m(\tilde{\alpha})^2 \geq am_{\mathrm{T2}}^2 \equiv \min_{\vec{\boldsymbol{p}}_{\mathrm{T}}^{\mathrm{miss}} = \vec{\mathbf{p}}_{\mathrm{T}}(\tilde{\chi}) + \vec{\mathbf{p}}_{\mathrm{T}}(\tilde{\kappa})} \Big\{ \max[m_{\mathrm{T}}^2(\vec{\mathbf{p}}_{\mathrm{T}}(\alpha), \vec{\mathbf{p}}_{\mathrm{T}}(\tilde{\chi})) \,,\, m_{\mathrm{T}}^2(\vec{\mathbf{p}}_{\mathrm{T}}(\beta), \vec{\mathbf{p}}_{\mathrm{T}}(\tilde{\kappa}))] \Big\}. \tag{5.22}$$

Whilst the above definitions of both M_{T2} and am_{T2} were originally intended to be used to characterise possible BSM signals, the variables are used in the analysis to reject SM backgrounds and in particular $t\bar{t}$.

The am_{T2} is used in the $tb + E_{\mathrm{T}}^{\mathrm{miss}}$ analysis to reject $t\bar{t}$ pair production where one top quark decays semi-leptonically. For the $t\bar{t}$ process, am_{T2} can be calculated as a function of 5 parameters. The visible particles in the decay are the two $b-$quarks ($b-$jets) and the lepton (e, μ), reducing the number of mass parameters by one (in this scenario, as in the standard m_{T} calculation, the lepton mass is neglected). There is only one invisible particle expected in the decay, the neutrino from the leptonic decay of the W-boson, hence the masses of the invisible particles are taken to be 0.

In the case for $t\bar{t}$, the am_{T2} function becomes:

$$am_{\mathrm{T2}} = am_{\mathrm{T2}}(m_b, \vec{p}_{\mathrm{T}}(b_1), \vec{p}_{\mathrm{T}}(b_2), \vec{p}_{\mathrm{T}}(\ell), \vec{\boldsymbol{p}}_{\mathrm{T}}^{\mathrm{miss}}). \tag{5.23}$$

The introduction of the lepton in this scenario requires an additional step to be performed before the am_{T2} can be calculated. The lepton in the decay can be paired with either of the $b-$jets in the event (as it is unknown to which leg of the decay the lepton belongs). The minimum invariant mass of the lepton with each of the $b-$jets is calculated, referred to as $m_{b,l}$. If $m_{b,l} < 170\,\mathrm{GeV}$, then the lepton and the $b-$jet are compatible with a top-quark, and hence can be used for the am_{T2} calculation.

The inputs used to calculate am_{T2} are based upon both of the calculated values of $m_{b,l}$. The prescription for the calculation is the following:

- If $m_{b,l}\ (b_1, \ell) < 170$ and $m_{b,l}\ (b_2, \ell) > 170$, the am_{T2} is constructed by pairing the lepton with the first $b-$jet:

$$am_{\mathrm{T2}}^2 = \min_{\vec{\boldsymbol{p}}_{\mathrm{T}}^{\mathrm{miss}} = \vec{\mathbf{p}}_{\mathrm{T}}(\tilde{\chi_1}) + \vec{\mathbf{p}}_{\mathrm{T}}(\tilde{\chi_2})} \Big\{ \max[m_{\mathrm{T}}^2(\vec{\mathbf{p}}_{\mathrm{T}}(b_1 + \ell), \vec{\mathbf{p}}_{\mathrm{T}}(\tilde{\chi}))\,,\, m_{\mathrm{T}}^2(\vec{\mathbf{p}}_{\mathrm{T}}(b_2), \vec{\mathbf{p}}_{\mathrm{T}}(\tilde{\chi}))] \Big\} \tag{5.24}$$

- If $m_{b,l}\ (b_1, \ell) > 170$ and $m_{b,l}\ (b_2, \ell) < 170$, the am_{T2} is constructed by pairing the lepton with the second $b-$jet:

$$am_{\mathrm{T2}}^2 = \min_{\vec{\boldsymbol{p}}_{\mathrm{T}}^{\mathrm{miss}} = \vec{\mathbf{p}}_{\mathrm{T}}(\tilde{\chi_1}) + \vec{\mathbf{p}}_{\mathrm{T}}(\tilde{\chi_2})} \Big\{ \max[m_{\mathrm{T}}^2(\vec{\mathbf{p}}_{\mathrm{T}}(b_1), \vec{\mathbf{p}}_{\mathrm{T}}(\tilde{\chi}))\,,\, m_{\mathrm{T}}^2(\vec{\mathbf{p}}_{\mathrm{T}}(b_2 + \ell), \vec{\mathbf{p}}_{\mathrm{T}}(\tilde{\chi}))] \Big\} \tag{5.25}$$

- If both $m_{b,l}\ (b_1, \ell) < 170$ and $m_{b,l}\ (b_2, \ell) < 170$, the am_{T2} is calculated for both scenarios, as both are compatible with the lepton and $b-$jet arising from a top-quark decay. In this case, the minimum value of am_{T2} for the two scenarios is used.

$$\begin{aligned} am_{\mathrm{T2}}(1)^2 &= \min_{\vec{\boldsymbol{p}}_{\mathrm{T}}^{\mathrm{miss}} = \vec{\mathbf{p}}_{\mathrm{T}}(\tilde{\chi_1}) + \vec{\mathbf{p}}_{\mathrm{T}}(\tilde{\chi_2})} \Big\{ \max[m_{\mathrm{T}}^2(\vec{\mathbf{p}}_{\mathrm{T}}(b_1 + \ell), \vec{\mathbf{p}}_{\mathrm{T}}(\tilde{\chi}))\,,\, m_{\mathrm{T}}^2(\vec{\mathbf{p}}_{\mathrm{T}}(b_2), \vec{\mathbf{p}}_{\mathrm{T}}(\tilde{\chi}))] \Big\} \\ am_{\mathrm{T2}}(2)^2 &= \min_{\vec{\boldsymbol{p}}_{\mathrm{T}}^{\mathrm{miss}} = \vec{\mathbf{p}}_{\mathrm{T}}(\tilde{\chi_1}) + \vec{\mathbf{p}}_{\mathrm{T}}(\tilde{\chi_2})} \Big\{ \max[m_{\mathrm{T}}^2(\vec{\mathbf{p}}_{\mathrm{T}}(b_1), \vec{\mathbf{p}}_{\mathrm{T}}(\tilde{\chi}))\,,\, m_{\mathrm{T}}^2(\vec{\mathbf{p}}_{\mathrm{T}}(b_2 + \ell), \vec{\mathbf{p}}_{\mathrm{T}}(\tilde{\chi}))] \Big\} \\ am_{\mathrm{T2}} &= \min(am_{\mathrm{T2}}(1), am_{\mathrm{T2}}(2)) \end{aligned} \tag{5.26}$$

- If neither $m_{b,l}\ (b_1, \ell)$ or $m_{b,l}\ (b_2, \ell)$, value is compatible with arising from a top-quark (both values are $> 170\,\mathrm{GeV}$), the am_{T2} is not calculated, and is set to an overflow value.

As can be seen in Equation 5.22, the maximum value of am_{T2} for $t\bar{t}$ pair production would fall at the top-quark mass. Thus a selection of $am_{\mathrm{T2}} > 175\,\mathrm{GeV}$ can be used to reject $t\bar{t}$ background. Tighter selections on am_{T2} may be employed to further reject $t\bar{t}$, taking into account resolution effects. Figure 5.4(a) compares the distributions of the am_{T2} variable for signal and background. The end-point for the $t\bar{t}$ background is clearly visible, whilst the signal sample is seen to peak at larger values of am_{T2}.

5.4.3 Dedicated complex variables for the sbottom $bb + E_{\mathrm{T}}^{\mathrm{miss}}$ analysis

The sbottom pair production topology under investigation for the $bb + E_{\mathrm{T}}^{\mathrm{miss}}$ analysis results in a relatively simple final state containing only two $b-$jets and $E_{\mathrm{T}}^{\mathrm{miss}}$. Additional high-$p_{\mathrm{T}}$ jets may from initial and final state radiation (ISR, FSR) and events with an ISR jet are used to target compressed scenarios.

Due to the sparse amount of objects in the final state, the main discriminating variables for this analysis are based upon the $b-$jets and $E_{\mathrm{T}}^{\mathrm{miss}}$. As this analysis has zero leptons in the final state, angular selections between the jets and $E_{\mathrm{T}}^{\mathrm{miss}}$ are employed to ensure the removal of QCD multi-jet backgrounds. Angular selections are also used to target events where the sbottom system recoils against an ISR jet.

$\Delta\phi(j_1, E_{\mathrm{T}}^{\mathrm{miss}})$: When targeting scenarios with small mass splitting between the sbottom and neutralino, it is likely that low p_{T} $b-$jets will be present in the detector. In this scenario the $E_{\mathrm{T}}^{\mathrm{miss}}$ will be small. For these scenarios is advantageous to target events containing a high p_{T} ISR jet, which the sbottom system recoils against.

As the sbottom system is recoiling against the jet (which is assumed to be the highest p_{T} jet in the event), a large separation is expected in the azimuthal plane. Hence a selection on $\Delta\phi(j_1, E_{\mathrm{T}}^{\mathrm{miss}}) > 2$ is used to select these events, where j_1 is the highest p_{T} jet in the event, taken to be the ISR jet.

m_{CT} [GeV]: The contransverse mass m_{CT} [126], is a variable very similar to the previously introduced M_{T2}, in that it seeks to reconstruct a mass-like property of pair produced semi-invisibly decaying particles. Unlike the M_{T2} or am_{T2} however, the m_{CT} does not require information about the missing energy in the event, and instead uses Lorentz invariance to derive a variable related to the parent particle mass.

Consider again a symmetric decay of a similar form as considered for the M_{T2} derivation, but writing both legs of the decay:

$$\tilde{\alpha_1}\tilde{\alpha_2} \rightarrow \alpha_1\tilde{\chi}_1 + \alpha_2\tilde{\chi}_2. \tag{5.27}$$

The following derivation, and subsequent definition of m_{CT}, focuses on the two visible particles α_1 and α_2, with mass and 4-momenta $m(\alpha_1)$, $p(\alpha_1)$ and $\mathrm{m}(\alpha_2)$, $p(\alpha_2)$ respectively. The mass obtained from $p(\alpha_1)+p(\alpha_2)$ is known to be a Lorentz invariant quantity, such that in any reference frame Equation 5.28 is unchanged:

$$\begin{aligned} m^2(\alpha_1,\alpha_2) &= [E(\alpha_1)+E(\alpha_2)]^2 - [\vec{\mathbf{p}}(\alpha_1)+\vec{\mathbf{p}}(\alpha_2)]^2, \\ m^2(\alpha_1,\alpha_2) &= m^2(\alpha_1)+m^2(\alpha_2)+2(E(\alpha_1)E(\alpha_2)-\vec{\mathbf{p}}(\alpha_1)\cdot\vec{\mathbf{p}}(\alpha_2)). \end{aligned} \tag{5.28}$$

Another way of interpreting the result, is that if the two particles undergo a co-linear boost of equal magnitude, then the mass is invariant.

If the two particles are boosted by an equal magnitude but in opposite directions (referred to as a contra-linear boost) in the original frame of reference (F_0), such that particle α_1 is in a frame F_{α_1} and particle α_2 is in a frame F_{α_2}, then it is obvious that Equation 5.28 is no longer invariant.

However, one can consider a quantity "M_C", the invariant mass of $p(\alpha_1)+\mathcal{P}(p(\alpha_2))$, where $\mathcal{P}$ is the parity transformation operator, acting on the second particle:

$$\begin{aligned} M_C^2(\alpha_1,\alpha_2) &= [E(\alpha_1)+E(\alpha_2)]^2 - [\vec{\mathbf{p}}(\alpha_1)-\vec{\mathbf{p}}(\alpha_2)]^2, \\ M_C^2(\alpha_1,\alpha_2) &= m^2(\alpha_1)+m^2(\alpha_2)+2(E(\alpha_1)E(\alpha_2)+\vec{\mathbf{p}}(\alpha_1)\cdot\vec{\mathbf{p}}(\alpha_2)). \end{aligned} \tag{5.29}$$

It can be shown that Equation 5.29 is an invariant quantity under contra-linear boosts. The above reasoning can subsequently be applied to the transverse plane, with the resulting definition of the contransverse mass:

$$\begin{aligned} m_{CT}^2(\alpha_1,\alpha_2) &= [E_{\mathrm{T}}(\alpha_1)+E_{\mathrm{T}}(\alpha_2)]^2 - [\vec{\mathbf{p}}_{\mathrm{T}}(\alpha_1)-\vec{\mathbf{p}}_{\mathrm{T}}(\alpha_2)]^2, \\ m_{CT}^2(\alpha_1,\alpha_2) &= m^2(\alpha_1)+m^2(\alpha_2)+2(E_{\mathrm{T}}(\alpha_1)E_{\mathrm{T}}(\alpha_2)+\vec{\mathbf{p}}_{\mathrm{T}}(\alpha_1)\cdot\vec{\mathbf{p}}_{\mathrm{T}}(\alpha_2)). \end{aligned} \tag{5.30}$$

Assuming that particles α_1 and α_2 are massless reduces the m_{CT} to a form which is very similar to the m_{T} variable:

$$\begin{aligned} m_{\mathrm{CT}} &= \sqrt{2(E_{\mathrm{T}}(\alpha_1)E_{\mathrm{T}}(\alpha_2)-\vec{\mathbf{p}}_{\mathrm{T}}(\alpha_1)\cdot\vec{\mathbf{p}}_{\mathrm{T}}(\alpha_2))}, \\ &= \sqrt{2p_{\mathrm{T}}(\alpha_1)p_{\mathrm{T}}(\alpha_2)(1+\cos(\Delta\phi(\alpha_1,\alpha_2)))}. \end{aligned} \tag{5.31}$$

Unlike the m_{T} variable, and the similar am_{T2} and M_{T2} variables, it is more difficult to interpret the m_{CT} variable in terms of a physical quantity. However, the end-point of the variable for a given process can still be calculated, and it is in this way that the m_{CT} is used to reject $t\bar{t}$ background in the analysis.

The end-point of the m_{CT} variable is given by Equation 5.32, for the scenario considered in Equation 5.27:

$$m_{\mathrm{CT}}^{\mathrm{max}} = \frac{m^2(\tilde{\alpha}) - m^2(\tilde{\chi})}{m(\tilde{\alpha})}, \tag{5.32}$$

When this is applied to $t\bar{t}$ pair production, the end-point can be calculated as:

$$m_{\mathrm{CT}}^{\mathrm{max}} = \frac{m^2(t) - m^2(W)}{m(t)} \approx 135\,\mathrm{GeV}. \tag{5.33}$$

As such, a selection of at least $m_{\mathrm{CT}} > 150\,\mathrm{GeV}$ is used to reject $t\bar{t}$ pair production background in this analysis. The use of m_{CT} to reject $t\bar{t}$ was the main motivation to employ this variable as the discriminating variable in the Run 1 analysis. Currently the analysis uses this variable due to the relationship between the sbottom mass and the end-point of the variable, as shown in Equation 5.32. This behaviour is also displayed in Figure 5.4(b), where the shoulder of the m_{CT} distribution can be seen for the $t\bar{t}$ background at around 150 GeV.

$\min m_{\mathrm{T}}(j, E_{\mathrm{T}}^{\mathrm{miss}})$ [GeV]: When targeting 0 lepton events, semi-leptonic $t\bar{t}$ events can pass this selection if the lepton is out of acceptance ("lost") and is reconstructed as missing energy. The minimum transverse mass between all jets in the event and the $E_{\mathrm{T}}^{\mathrm{miss}}$, $\min m_{\mathrm{T}}(j, E_{\mathrm{T}}^{\mathrm{miss}})$, can be used to discriminate between $t\bar{t}$ events with a "lost" lepton and the sbottom signal events. Generally a selection of $\min m_{\mathrm{T}}(j, E_{\mathrm{T}}^{\mathrm{miss}}) > 150\,\mathrm{GeV}$ can be placed on this variable to reduce the $t\bar{t}$ background. This variable is useful in the intermediate region, where the mass splitting of the sbottom and neutralino result in a similar m_{CT} end-point for both signal and $t\bar{t}$.

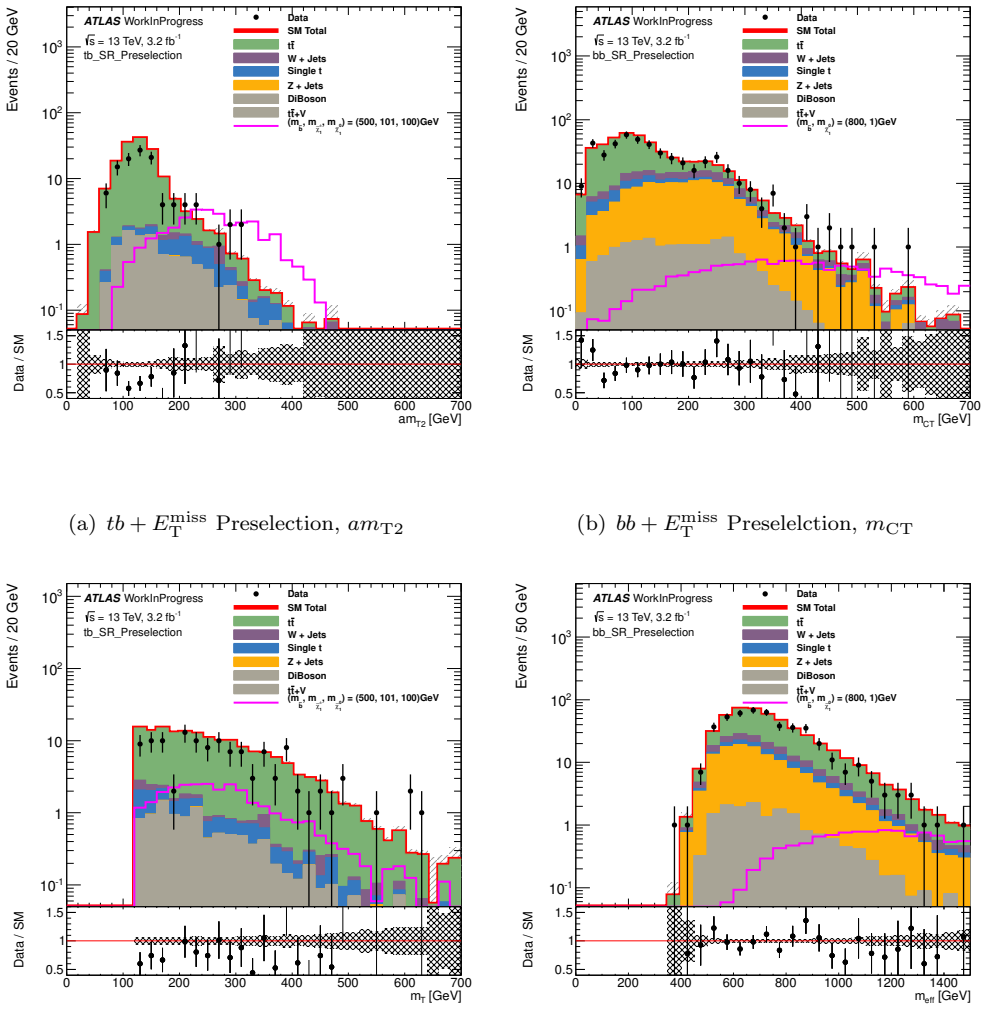

(a) $tb + E_{\mathrm{T}}^{\mathrm{miss}}$ Preselection, am_{T2}

(b) $bb + E_{\mathrm{T}}^{\mathrm{miss}}$ Preselelction, m_{CT}

(c) $tb + E_{\mathrm{T}}^{\mathrm{miss}}$ Preselection, m_{T}

(d) $bb + E_{\mathrm{T}}^{\mathrm{miss}}$ Preselelction, m_{eff}

FIGURE 5.4: Comparison between signal and background events for four key discriminating variables used in the analyses to discriminate between signal and background events: (a) am_{T2}, (b) m_{CT}, (c) m_{T}, (d) m_{eff}.

5.4.4 Dedicated complex variables for the Dark Matter $bb + E_{\mathrm{T}}^{\mathrm{miss}}$ analysis

Similarly to the sbottom search, the signals under investigation in the search for direct dark matter production lead to events containing 0 leptons, two $b-$quarks and $E_{\mathrm{T}}^{\mathrm{miss}}$. The main background in this search is Z-boson production in association with heavy flavour (HF) jets with the Z decaying to neutrinos.

The signal event topology is such that there is a large separation between the $b-$jets in the (ϕ, η) phase-space, whereas for the background the $b-$jets are expected to be

relatively close as the jets originate from gluon splitting. Another method to distinguish the signal is take advantage of the p_{T} spectra of jets produced via gluon splitting, to further reject this background. Three variables are considered for the analysis and are listed below.

$\Delta R(b,b)$: The separation of the $b-$jets in the (ϕ, η) space, $\Delta R(b,b)$, is used to distinguish between $b-$jets that result from gluon splitting and jets from signal events.

$$\Delta R(b_1, b_2) = \sqrt{\Delta\phi(b_1, b_2)^2 + \Delta\eta(b_1, b_2)^2}. \tag{5.34}$$

For the Z-jets background it is expected that $\Delta R(b,b)$ would peak at smaller values due to the common origin of the $b-$jets when compared to the signal events.

$\Delta\eta(b,b)$: The separation in pseudorapidity itself, $\Delta\eta(b,b)$, is also used to discriminate between the signal and background as the $\Delta\eta(b,b)$ distribution is dependent upon the spin properties of the decaying particle. The difference in spin of the mediator ($s = 0$) for the signal, and the Z-boson ($s = 1$) produces different pseudorapidity distributions, which can be used to discriminate between signal and background.

5.5 Conclusion

Presented in this chapter was an overview of the basic tools required to design the regions used in the analyses presented in the remaining chapters of this thesis.

Initially an overview of the definitions required to classify objects as measured in the detector to the corresponding physical particle were presented, with the definitions used for both the Run 1 and Run 2 analyses given. A description of the overlap removal procedure used to avoid double-counting objects was also discussed.

The data quality selections applied to the data collected by the detector are listed. The application of these requirements ensures the data used for physics analyses is of a high quality, to provide certainty in the results presented. After the application of the data quality requirements approximately 10% of collected data is discarded.

Finally, the complex global event variables used to define specific regions of interest for the analyses are presented. Some of the variables take into account the mass properties of the SUSY particles under investigation for to allow for discrimination between the SM and BSM physics, others take into account differences in angular distributions expected between the SM and the BSM processes. These global variables allow the definition of

analysis regions enhanced in either the signal under investigation (signal regions), or a SM process which must be constrained (control regions), enabling complex statistical methods to be employed in the attempt to discover BSM physics, as discussed in the subsequent chapters.

Chapter 6

Search for direct bottom squark pair production in the bb+$E_{\mathrm{T}}^{\mathrm{miss}}$ final state

The following chapter contains an overview of the searches for direct sbottom pair production in the $bb + E_{\mathrm{T}}^{\mathrm{miss}}$ final state performed with ATLAS during Run 2. The analysis was originally performed using the 2015 data-set with a total luminosity of $3.2\,\mathrm{fb}^{-1}$ resulting in, at the time of publication, world-leading limits on the $\tilde{b} \to b + \tilde{\chi}_1^0$ decay. Further to this the analysis was updated and improved upon with the addition of the 2016 dataset adding a luminosity of $32.9\,\mathrm{fb}^{-1}$, resulting in a total luminosity of $36.1\,\mathrm{fb}^{-1}$.

This chapter is split into three components. The first component, "Analysis Motivation" considers the results of the previous ATLAS sbottom analysis, performed with the 2012, $\sqrt{s} = 8\,\mathrm{TeV}$ data. An overview of the signal phenomenology and the results of a preliminary sensitivity study are presented which is used to guide the subsequent analysis. To conclude this section the results of a Run 2 sensitivity study based on the Run 1 analysis are presented.

The second component consists of the 2015 analysis. An overview of the optimisation studies performed to define the signal regions is presented and the definition of control regions to constrain the SM backgrounds is discussed. An overview of the data-driven γ+jets background estimation technique that was developed for the analysis is given. Finally the statistical interpretations of the results are documented.

The final component is comprised of the update to the analysis using the full $36.1\,\mathrm{fb}^{-1}$ 2015+2016 dataset. In addition to the inclusion of the 2016 data, the analysis is also

improved with the redefinition of the earlier SRs and the inclusion of an additional category of signal region. Control and validation regions are defined for the new regions. The data-driven γ+jets method is also updated. To conclude this section the latest results of the search for sbottom pair production are presented.

The author's contribution to the $3.2\,\text{fb}^{-1}$ analysis consisted of the development of the single-top CR, the evaluation of the modelling uncertainties, the implementation of the "γ + jets replacement method". The contribution to the $36.1\,\text{fb}^{-1}$ analysis consisted of updating the definitions of the A-type control and validation regions, the updates to the "γ + jets" data driven method and the evaluation of the modelling uncertainties.

6.1 Analysis Motivation

Searches for the superpartners of the third generation quarks ($\tilde{t}$, $\tilde{b}$) are of great interest due to the naturalness considerations first introduced in Section 2.7.5. In brief, to satisfy naturalness requirements, the mass eigenstates of the third generation squarks must be light, and would be expected to be at around the TeV scale. If this is the case then squarks should be produced with a relatively high cross-section at the LHC.

A search was performed by ATLAS using the Run 1, $\sqrt{s} = 8\,\text{TeV}$ dataset [127], which set limits at the 95% Confidence Level (CL) on simplified sbottom models which assume that the sbottom is the lightest coloured sparticle and decays via a bottom-quark and a neutralino ($\tilde{b} \to b + \tilde{\chi}_1^0$), as shown in Figure 6.1.

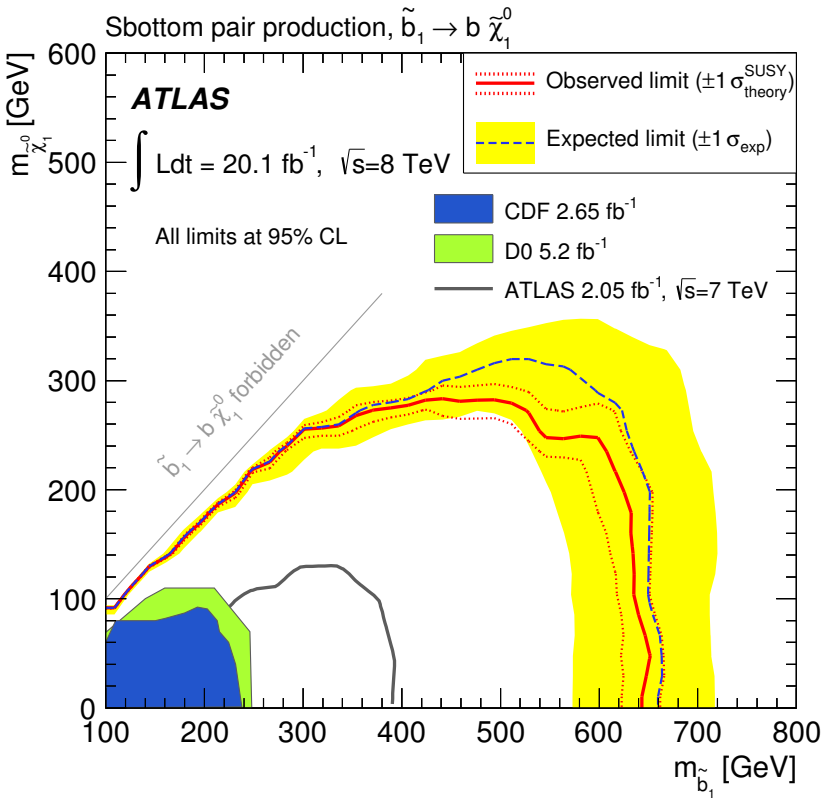

FIGURE 6.1: ATLAS $\sqrt{s} = 8\,\text{TeV}$ limits placed on the simplified $\tilde{b} \rightarrow b + \tilde{\chi}_1^0$ decay scenario, excluding sbottom quarks of masses of up to 640 GeV for massless neutralinos. Taken from citeSbottom:Run1.

Whilst the concept of naturalness can guide the SUSY mass spectrum and the requirement of R-parity can suggest the decays that are available, there are no specific guidelines to decide on the Branching Ratios (BRs) for sparticle decays, aside from kinematic constraints. In order to search in an agnostic manner without any dependence upon a specific signal model, simplified model scenarios are investigated with a simple direct decay usually considered, a representative diagram of this decay mode is shown in Figure 6.2.

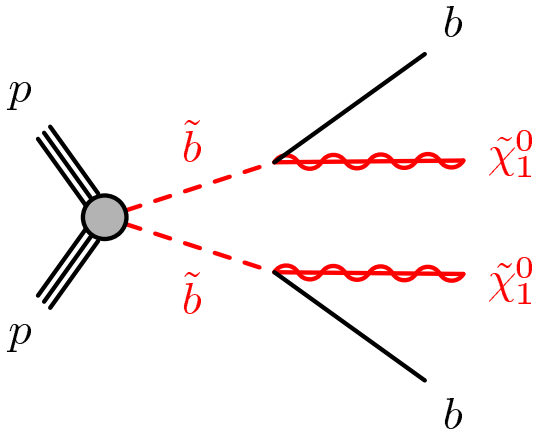

FIGURE 6.2: Representative diagram of the simplified model scenario $\tilde{b} \rightarrow b + \tilde{\chi}_1^0$ considered in this analysis.

6.1.1 Signal Phenomenology

The decay $\tilde{b} \rightarrow b + \tilde{\chi}_1^0$ leads to a relatively simple final state consisting of 0 leptons, two $b-$jets and $E_{\mathrm{T}}^{\mathrm{miss}}$. There are only two options to trigger on these events, either using an $E_{\mathrm{T}}^{\mathrm{miss}}$-based trigger, or a $b-$jet-based trigger. In order to enable $b-$jet efficiency studies, and also to enable a switch to the flat efficiency $b-$tagging algorithms in the future, a trigger strategy independent of jets identified as $b-$jets is preferred and the $E_{\mathrm{T}}^{\mathrm{miss}}$ trigger is used. This guides the analysis strategy as all signal regions must be defined with $E_{\mathrm{T}}^{\mathrm{miss}}$ requirements such that the $E_{\mathrm{T}}^{\mathrm{miss}}$ trigger is fully efficient. The online trigger thresholds differ between the 2015 and 2016 analysis. The 2015 analysis uses an online threshold of 70 GeV, whilst the 2016 analysis uses a threshold of either 100 or 110 GeV. The $E_{\mathrm{T}}^{\mathrm{miss}}$ trigger is fully efficient with an offline $E_{\mathrm{T}}^{\mathrm{miss}}$ selection of > 200 GeV.

There are several SM background processes that must be considered when analysing the 0 lepton, 2 $b-$jets and $E_{\mathrm{T}}^{\mathrm{miss}}$ final state: $t\bar{t}$ pair production; single-top Wt-channel production; $t\bar{t}$ production in association with a vector boson ($t\bar{t}$+V); W-boson production in association with heavy-flavour (HF) jets, referred to as W+jets; Z-boson production in association with HF jets (Z+jets); diboson production; and finally multi-jet production.

As the signal topology leads to a relatively low expected jet multiplicity and high $E_{\mathrm{T}}^{\mathrm{miss}}$, fully-hadronic $t\bar{t}$ is not a significant contribution to the analysis, and instead the main $t\bar{t}$ background arises from semi-leptonic $t\bar{t}$ decays, where either, the lepton in the event is a τ-lepton, which subsequently decays hadronically or the lepton (e, μ) from the

$t\bar{t}$ decay is lost (out of acceptance) or not reconstructed as a lepton. A similar scenario is expected to occur in the case of single-top production.

The W+jets background may contribute to this final state in a similar manner as the semi-leptonic $t\bar{t}$ background, where the W decays via $W \to \tau\nu_\tau$, which subsequently decays hadronically, or the W decays via $W \to \ell\nu_\ell$, and the lepton (e, μ) is lost or is not reconstructed. The $b-$jets arise in this process due to gluon splitting $g \to b\bar{b}$.

The Z+jets background is expected to be the most prevalent SM process in the final state considered. If the Z-boson is produced in association with two $b-$jets, the Z can subsequently decay via $Z \to \nu\nu$, leading to the final state considered.

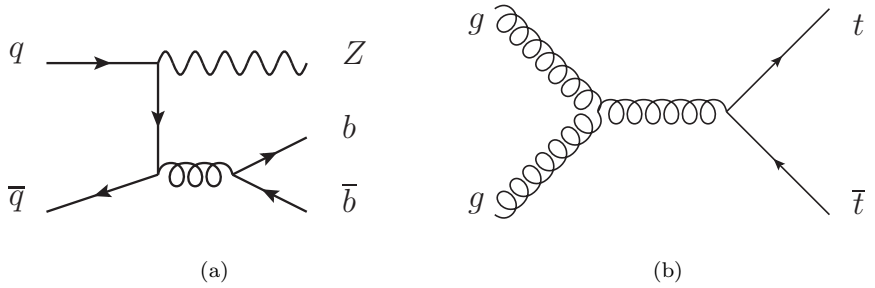

FIGURE 6.3: Example Feynman diagrams for two of the dominant SM processes in the analysis. (a) Z+jets production taken from [128], (b) $t\bar{t}$ pair production, taken from [129].

The diboson and $t\bar{t}$+V ($V = W, Z$) backgrounds are expected to be small when compared to the other backgrounds in the analysis. When considering diboson production, (eg ZZ, WZ, WW), these are rare processes in the SM and are expected to contribute only a small amount to the number of events with the targeted final state. The majority of the $t\bar{t}$+V background is expected to consist of mainly $t\bar{t} + Z$ production with the Z decay proceeding via $Z \to \nu\nu$, and the $t\bar{t}$ decaying in a similar manner to the top-pair production scenario described above. Contributions may also arise from the all hadronic $t\bar{t}$ decay, as the decay of the Z boson can provide the required $E_{\mathrm{T}}^{\mathrm{miss}}$ in the event.

The multi-jet background must be considered in any analysis targeting a final state containing 0 leptons. This background arises from the mis-reconstruction of a jet which produces "fake" $E_{\mathrm{T}}^{\mathrm{miss}}$ in an event. Selections on certain variables can be applied, as discussed in Section 5.4.3, that are shown to reduce the contribution from this background to a negligible amount.

6.1.2 Run 2 Sensitivity Study

In preparation for the beginning of Run 2, a preliminary sensitivity study was performed based upon the Run 1 analysis [130]. The analysis strategy introduced in the 8 TeV analysis defined two categories of Signal Region (SRs): a set of A-type SRs, and a single B-type SR. The A-type SRs were based upon sequential selections on the m_{CT} variable, and were used to target the region in $m(\tilde{b}, \tilde{\chi}_1^0)$ where there is a large mass splitting between the sbottom and neutralino, referred to as the "bulk" region. The B-type SR was used to target the "compressed" region, where the sbottom and neutralino are almost mass degenerate. In this region an ISR-like selection is required, in order to detect the low-p_{T} particles from the sbottom decay which recoil against the ISR jet.

The studies performed are based very closely on the Run 1 A-type regions, by defining a selection with a tighter m_{CT} requirement than the one used in the Run 1 analysis. As discussed more in-detail in Ref [130], only the main backgrounds are considered, which are the top-quark backgrounds, $t\bar{t}$, single-top, and $t\bar{t}+V$, and the V+jets backgrounds, W+jets, and Z+jets.

In addition to the tighter m_{CT} selection, the SR defined for these studies uses a selection of $E_{\mathrm{T}}^{\mathrm{miss}} > 250\,\mathrm{GeV}$ to take into account the tighter $E_{\mathrm{T}}^{\mathrm{miss}}$ trigger thresholds foreseen for the Run 2 $E_{\mathrm{T}}^{\mathrm{miss}}$ trigger. Figure 6.4 shows the m_{CT} distribution in the A-type SR used for the studies, without the selection placed on the m_{CT} variable itself (henceforth referred to as an N-1 distribution).

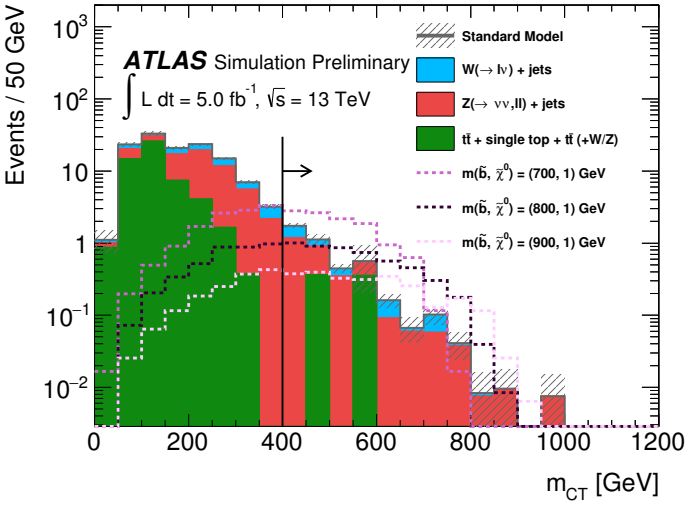

FIGURE 6.4: m_{CT} N-1 distribution in the SR used in the sensitivity studies. The arrow represents the selection of $m_{\mathrm{CT}} > 400\,\mathrm{GeV}$ applied in this region. Taken from [130].

The possible discovery potential for four $(\tilde{b},\, \tilde{\chi}_1^0)$ mass scenarios in the bulk region, are shown in Figure 6.5, assuming a total systematic uncertainty of 20% on the background estimate, which is an approximation of the systematic uncertainty in the 8 TeV analysis. The mass points considered are chosen such that $m_{\tilde{\chi}_1^0} = 1\,\mathrm{GeV}$, in order to study in a simple manner the possible discovery of sbottoms with masses ranging from 700 to 1000 GeV. The smallest sbottom mass considered (700 GeV) is chosen based on the 8 TeV exclusion limit, which is represented in the figure by the grey band.

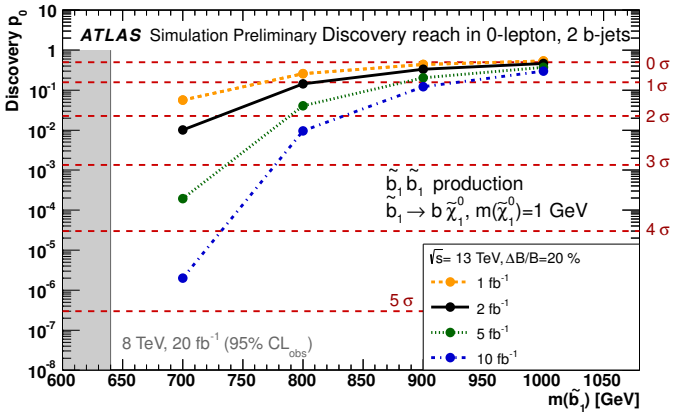

FIGURE 6.5: Discovery sensitivity projections for four $(\tilde{b},\, \tilde{\chi}_1^0)$ mass scenarios: (700, 1) GeV, (800, 1) GeV, (900, 1) GeV and (1000, 1) GeV, assuming a total overall systematic uncertainty on the background estimate of 20%. The exclusion limits from the 8 TeV analysis can be seen as the grey band in the left of the figure. Taken from [130].

It is seen that with the assumption of $L = 5\,\text{fb}^{-1}$ there would be $3\,\sigma$ evidence for the existence of the sbottom with $m_{\tilde{b}} = 700\,\text{GeV}$, decaying to a $b-$jet and a neutralino of mass $m_{\tilde{\chi}_1^0} = 1\,\text{GeV}$.

This gain in sensitivity for a small luminosity when compared to the 8 TeV analysis, can be explained by the increase in cross-section for sbottom pair production when increasing the centre of mass energy from 8 TeV to 13 TeV. Figure 6.6 compares the cross-sections for sbottom masses in the range 100 GeV to 2 TeV for the two cases. It can be seen that for the masses investigated in the sensitivity study, the cross-section increases by a factor of ≈ 10, when moving from $\sqrt{s} = 8$ to 13 TeV.

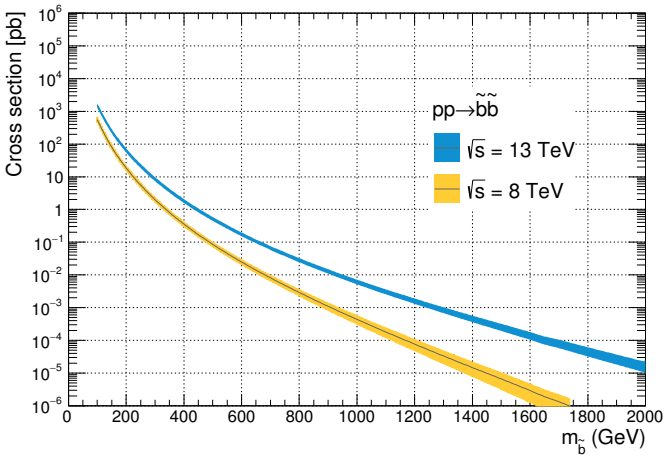

FIGURE 6.6: Comparison of the cross-sections for sbottom pair production, when moving from 8 to 13 TeV.

Comparatively, the cross-section of the main SM background processes in the analysis, $Z+$jets and $t\bar{t}$ increase by factors of ≈ 3 and 5 respectively. As the $Z+$jets process is a quark initiated EW process, the change in centre of mass energy results in a smaller increase in cross section due to the proton PDF. Hence there is a significant gain in sensitivity for the analysis moving from Run 1 to Run 2, even with the smaller expected luminosity of the 2015 dataset.

6.2 Sbottom 2015 Analysis

The 2015 analysis builds further on the sensitivity studies performed in the in the previous section using the SR defined for the sensitivity studies as a baseline SR on which to proceed with an optimisation. In addition to this, the B-type SR from the 8 TeV analysis is used as a baseline region to perform an optimisation targeting the compressed-region.

In the following sections, an overview of the signal region optimisation studies are presented for both the A-type and B-type regions. The dominant background processes in these regions are considered, and an overview is presented of the Control Region (CR) selections that are used to constrain the main SM backgrounds. A data-driven photon replacement method, referred to as "γ replacement" is used to estimate the Z+jets background is explained and the results are subsequently used to validate the nominal prediction for the Z+jets background. The description of the Validation Regions (VRs) used to validate the modelling of the main backgrounds are discussed.

An overview of the systematic uncertainties taken into consideration are discussed and the impact of the main uncertainties are quantified. Finally the fit results are presented with an overview of the statistical methods used to perform the fit procedure. The statistical interpretation of the fit is presented, and the resultant model-independent and model-dependent limits are shown.

6.2.1 Signal Kinematic Studies

Following the optimisation studies performed, and the analysis strategy used for the Run 1 result, there are two distinct regions of the $(\tilde{b},\ \tilde{\chi}_1^0)$ mass plane which produce different event topologies. These distinct topologies require different kinematic selections to enhance sensitivity to the mass scenario under consideration.

The "bulk" region, where the mass different between the sbottom and the neutralino is large ($\Delta m(\tilde{b}, \tilde{\chi}_1^0) = 100\,\text{GeV}$) leads to events with large $E_{\text{T}}^{\text{miss}}$, two high p_{T} $b-$jets and zero leptons in the final state. The optimisation is performed to maximise the discovery potential of the $(m_{\tilde{b}},\ m_{\tilde{\chi}_1^0}) = (800,\ 1)\,\text{GeV}$ point. This point is chosen as it is just beyond the exclusion contour in the bulk region of the Run 1 analysis.

The "compressed" region is defined as the region where the mass splitting between the sbottom and the neutralino is relatively small ($\Delta m(\tilde{b}, \tilde{\chi}_1^0) < 100\,\text{GeV}$). In these scenarios the $b-$jets from the sbottom decay have very low momenta and are difficult to detect. A selection targetting the cases when a sbottom system is produced in association with a high p_{T} ISR jet is used. In these events the sbottom system recoils from the ISR jet leading to slightly harder decay products and high $E_{\text{T}}^{\text{miss}}$ recoiling from the ISR jet. The specific focus of the compressed region optimisation is to maximise the discovery potential of the $(m_{\tilde{b}},\ m_{\tilde{\chi}_1^0}) = (400,\ 300)\,\text{GeV}$ point, which is chosen as it was just beyond the Run 1 exclusion contour in the compressed region.

Prior to the proper definition of a Signal Region, a preliminary set of selections are applied, referred to as a "Preselection", based upon similarities in the expected signal topology for both the bulk and compressed regions. This selection also takes into account any detector related constraints related to the trigger or reconstruction.

All events are required to pass the Run 2 Event Cleaning, as previously discussed in Chapter 5. The object definitions presented in Chapter 5 are used to define electrons, muons, jets, $b-$jets and photons. Events are selected with exclusively two $b-$tagged jets and 0 baseline leptons (e, μ). In order to be in the trigger plateau, a selection of $E_{\mathrm{T}}^{\mathrm{miss}}$ $> 250\,\mathrm{GeV}$ is applied. Due to the signal topology, a small jet multiplicity is expected; as such, events are selected requiring $n_{\mathrm{jets}} = 2, 3, 4$. The two leading jets in the event are expected to have $p_{\mathrm{T}} > 50\,\mathrm{GeV}$, be labelled as signal jets according to Table 5.3. As any additional jets beyond the two jets from the $\tilde{b}$ decay would be expected to be relatively soft, events are also rejected if the fourth jet in the event possesses $p_{\mathrm{T}} > 50\,\mathrm{GeV}$. The contribution from multi-jet events can be reduced to a negligible level by selecting events with $\min \Delta\phi(j, E_{\mathrm{T}}^{\mathrm{miss}}) > 0.4$ and $E_{\mathrm{T}}^{\mathrm{miss}}/m_{\mathrm{eff}} > 0.25$ as explained in Section 5.4.1.

The selection defined in Table 6.1 is the preselection applied to all regions of the 2015 analysis. Such baseline selections underpin the definition of all Control, Validation and Signal Regions.

Variable	Selection
Event cleaning selections	✔
Trigger	Passed either of the single lepton (e, μ) triggers, or the $E_{\mathrm{T}}^{\mathrm{miss}}$ trigger
$n_{b-\mathrm{jets}}$	2
n_{jets}	2, 3, 4
p_{T} (j_1), p_{T} (j_2)	$> 50\,\mathrm{GeV}$
p_{T} (j_4)	$< 50\,\mathrm{GeV}$ (or $n_{\mathrm{jets}} = 2, 3$)
$\min \Delta\phi(j, E_{\mathrm{T}}^{\mathrm{miss}})$	> 0.4
$E_{\mathrm{T}}^{\mathrm{miss}}/m_{\mathrm{eff}}$	> 0.25
$E_{\mathrm{T}}^{\mathrm{miss}}$	$> 100\,\mathrm{GeV}$ ($250\,\mathrm{GeV}$ for $n_{\mathrm{leptons}} = 0$)

TABLE 6.1: Sbottom 2015 analysis, preselection definition used as a baseline selection for all regions in the analysis.

Background Process	Number of Events
$t\bar{t}$	600.71 ± 2.75
Diboson	14.30 ± 0.50
Z+jets	120.25 ± 1.41
W+jets	80.62 ± 1.63
$t\bar{t}V$	19.62 ± 0.83
Single-top	60.75 ± 1.13
SM	896.28 ± 3.81
$m_{\tilde{b}} = 800\,\text{GeV}$, $m_{\tilde{\chi}_1^0} = 1\,\text{GeV}$	17.68 ± 4.21

TABLE 6.2: Expected event yield at the preselection level. Only statistical uncertainties are considered.

To perform the SR optimisation additional selections are applied to the preselection in Table 6.1. The requirement that there are no baseline leptons and $E_{\text{T}}^{\text{miss}} > 250\,\text{GeV}$ are required by the final state and trigger requirements. The expected yields of SM processes with the 0 lepton preselection are shown in Table 6.2. It can be seen that the main backgrounds are $t\bar{t}$, Z+jets, single-top and W+jets. Figure 6.7 presents distributions with the preselection and zero lepton requirements, referred to as bb_SR_Preselection, applied for a selection of key kinematic variables. It is these variables that are subsequently used to design the SRs targeting the bulk region.

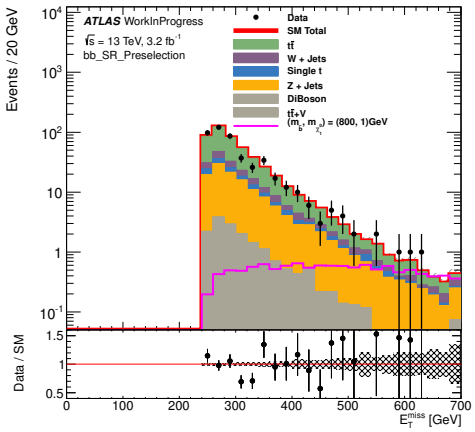

(a) $E_{\mathrm{T}}^{\mathrm{miss}}$

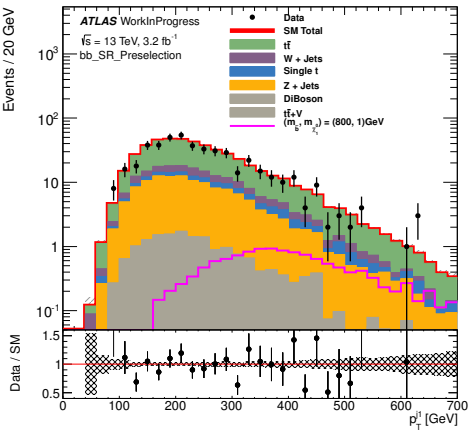

(b) $p_{\mathrm{T}}(j_1)$

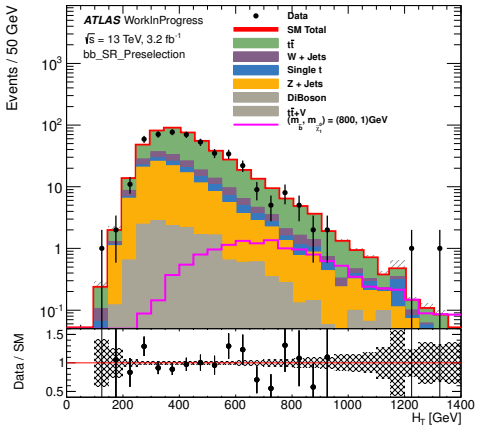

(c) H_{T}

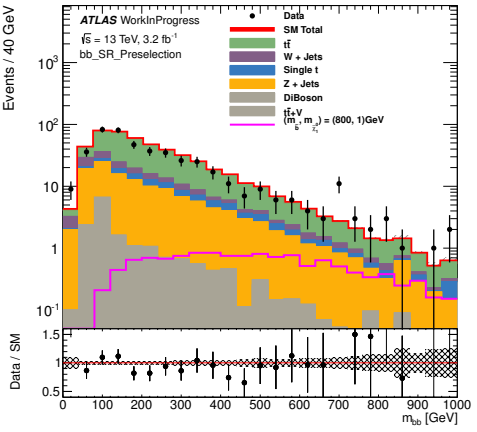

(d) m_{bb}

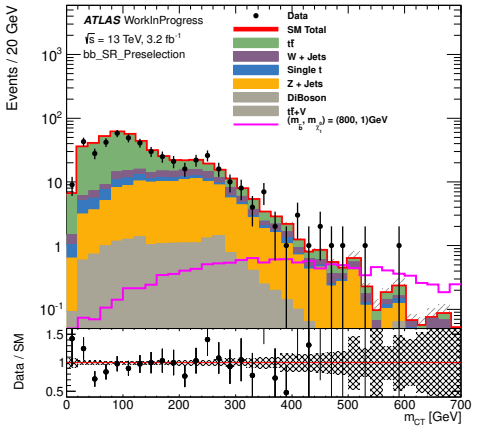

(e) m_{CT}

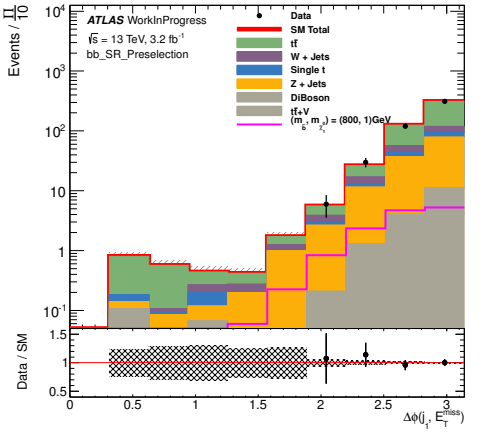

(f) $\Delta\phi(j_1, E_{\mathrm{T}}^{\mathrm{miss}})$

FIGURE 6.7: Sbottom 2015 preselection distributions with the benchmark signal point $(m_{\tilde{b}}, m_{\tilde{\chi}_1^0}) = (800,1)$ GeV.

6.2.2 Signal Region Definitions

As expected following the analysis strategy originally used for the Run 1 analysis, the m_{CT} is the most useful variable to remove the dominant $t\bar{t}$ background when considering the bulk event topology. For the compressed topology this is not the case, as the kinematic end-point for the $(m_{\tilde{b}}, m_{\tilde{\chi}_1^0}) = (400, 300)$ GeV scenario is 175 GeV, compared to the kinematic end-point of the $t\bar{t}$ background which is $\approx$ 140 GeV (from Equation 5.33). The differences between the two topologies can also be seen in Figure 6.8, where a selection of $m_{\mathrm{CT}} > 150$ GeV would reduce a significant amount of the signal for the compressed scenario (right) whilst for the bulk scenario the selection can even be tightened to reduce the background further.

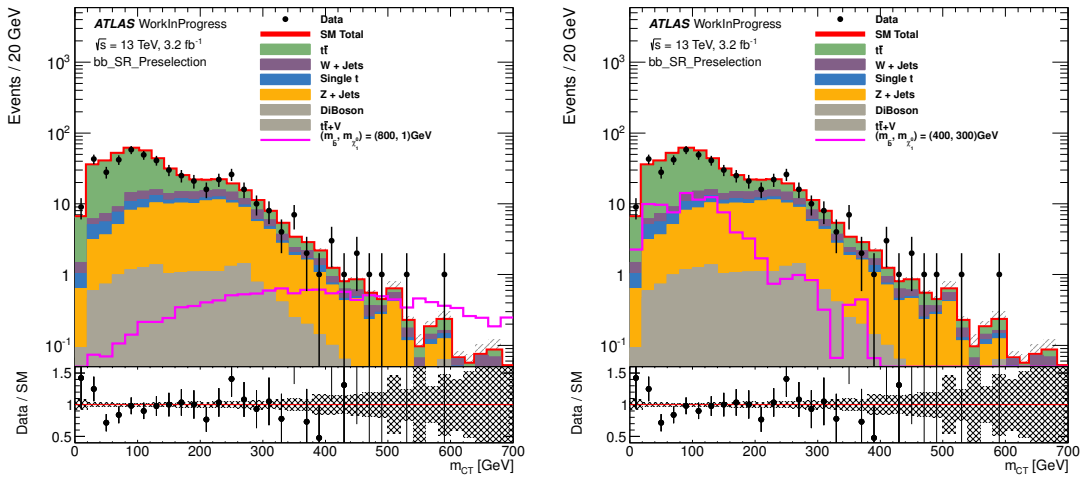

FIGURE 6.8: Sbottom 2015 m_{CT} distributions comparing the two benchmark signal points: left, $(m_{\tilde{b}}, m_{\tilde{\chi}_1^0}) = (800,1)$ GeV; right, $(m_{\tilde{b}}, m_{\tilde{\chi}_1^0}) = (400,300)$ GeV.

It is at this point that the kinematic selections for the bulk and compressed regions diverge. The selections targeting the bulk scenario are heavily based upon selections on the m_{CT} variable. The signal regions defined with an m_{CT} selection are referred to as the "A-type" regions. The selection targeting the compressed scenario instead requires a high p_{T} non-$b-$tagged ISR jet to reject the $t\bar{t}$ background, and is referred to as the "B-type" region.

The optimisation procedure performed to produce a final SR definition for both SR types follow the same strategy of attempting to maximise the discovery significance (S), defined in Equation 6.1:

$$S = \frac{N_{\text{sig}}}{\sqrt{N_{\text{bkg}} + (0.2 \cdot N_{\text{bkg}} + 1)^2}} \tag{6.1}$$

The discovery significance can be thought of as a measure of the ability to claim evidence for a specific SUSY signal scenario, given the number of expected signal events (N_{sig}) and number of expected background events (N_{bkg}) for a specific selection. The squared term in the equation takes into account the expected systematic uncertainty on the modelling of the background, in this case it is taken to be 20%, and the "+1" term is added by hand to prevent unnaturally large significances in the case where there are very few (< 1) predicted background events. A significance of 3 can be thought of as the minimum value for which a model can be excluded.

To define the A- and B-type regions, a variety of selections are placed on the key discriminating variables and the significance is calculated for the signal point under investigation. The final set of selections are chosen such that the significance is maximised.

After performing the optimisation for the bulk region, it is found that the best sensitivity is acquired using three SRs with overlapping m_{CT} selections, such that the three SRA regions are defined with $m_{\text{CT}} > 250$, > 350 and $> 450\,\text{GeV}$ respectively. For the compressed region a single SR is defined, requiring a high p_{T} ISR jet which is back-to-back with the $E_{\text{T}}^{\text{miss}}$ in the event. The full selection criteria for the A- and B-type SRs are shown in Tables 6.3 and 6.4, respectively.

Variable	SRA250	SRA350	SRA450
Preselection		✔	
$n_{\text{baseline leptons}}$		0	
Leading two jets (p_{T} ordered) are $b-$tagged		✔	
p_{T} (j_1)		$> 130\,\text{GeV}$	
m_{bb}		$>200\,\text{GeV}$	
$E_{\text{T}}^{\text{miss}}$		$>250\,\text{GeV}$	
m_{CT}	$>250\,\text{GeV}$	$>350\,\text{GeV}$	$>450\,\text{GeV}$

TABLE 6.3: Sbottom 2015 analysis, A-type SR definitions.

Variable	SRB
Preselection	✔
$n_{\text{baseline leptons}}$	0
Leading jet non-$b-$tagged	✔
p_{T} (j_1)	$> 300\,\text{GeV}$
Sub-leading jet $b-$tagged	✔
$\Delta\phi(j_1, E_{\text{T}}^{\text{miss}})$	> 2.5
$E_{\text{T}}^{\text{miss}}$	$> 400\,\text{GeV}$

TABLE 6.4: Sbottom 2015 analysis, B-type SR definition.

Figures 6.9 and 6.10 present the expected discovery significance for both A- and B-type SRs, with a luminosity corresponding to $3.2\,\text{fb}^{-1}$. Concerning the bulk region, it is seen that a tighter selection on m_{CT} targets the highest sbottom masses, whereas the selection of $m_{\text{CT}} > 250\,\text{GeV}$ targets the sbottom masses in the region tending towards more compressed scenarios.

	Number of Events			
Process	SRA250	SRA350	SRA450	SRB
$t\bar{t}$	1.1 ± 0.11	0.18 ± 0.04	0.044 ± 0.02	5.57 ± 0.21
Diboson	0.21 ± 0.08	0.065 ± 0.04	0.016 ± 0.016	0.19 ± 0.07
Z+jets	16.09 ± 0.37	3.70 ± 0.12	1.001 ± 0.04	2.81 ± 0.10
W+jets	3.60 ± 0.21	0.98 ± 0.09	0.25 ± 0.02	1.11 ± 0.08
$t\bar{t}V$	0.23 ± 0.01	0.62 ± 0.08	0.022 ± 0.005	0.12 ± 0.003
Single-top	2.18 ± 0.12	0.64 ± 0.05	0.15 ± 0.02	0.99 ± 0.13
SM Total	23.41 ± 0.46	5.63 ± 0.17	1.48 ± 0.06	10.8 ± 0.31

TABLE 6.5: Sbottom 2015 analysis, expected SM background yields (pre-fit) for all SRs.

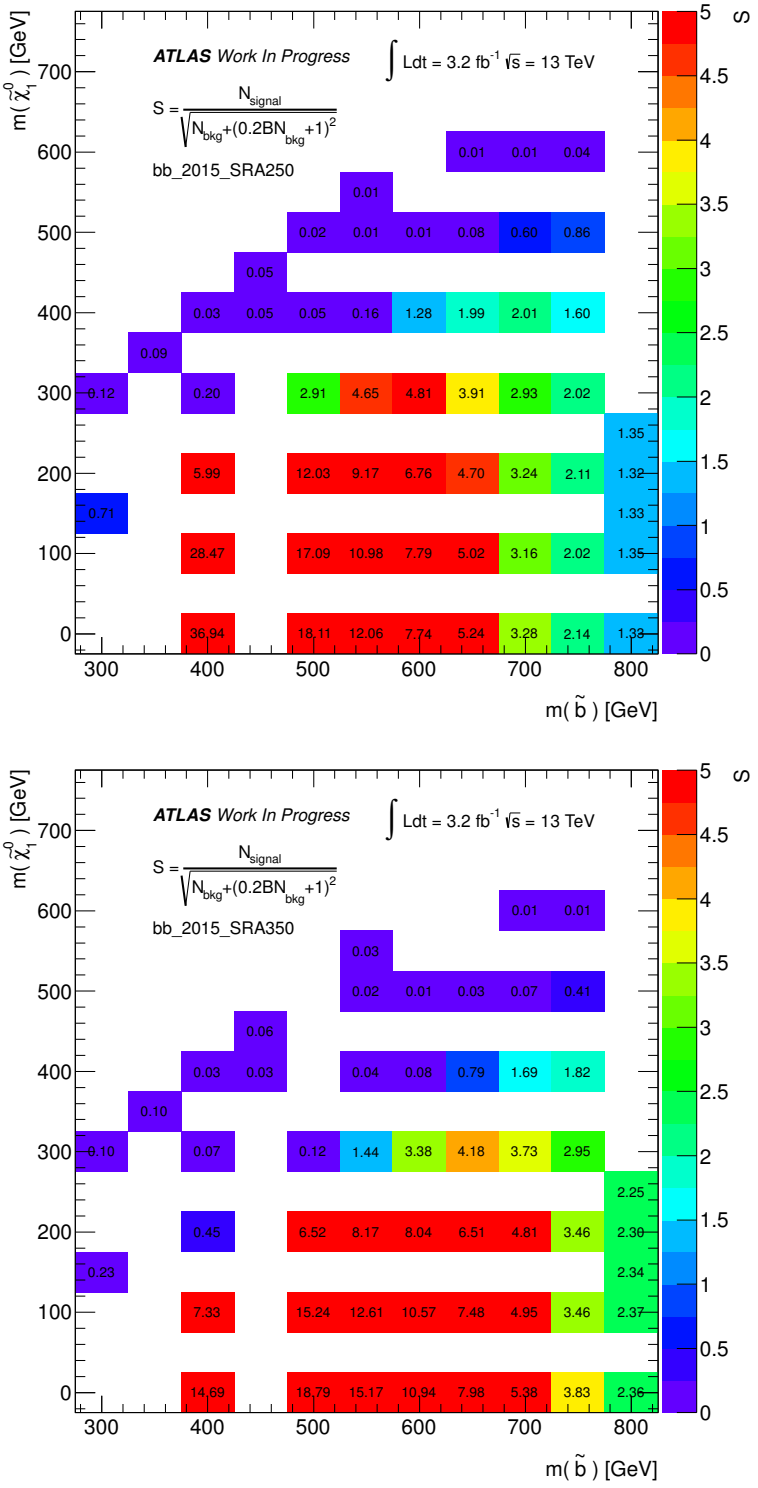

FIGURE 6.9: Expected significance plots for the 2015 sbottom SR definitions. Top: SRA250. Bottom: SRA350.

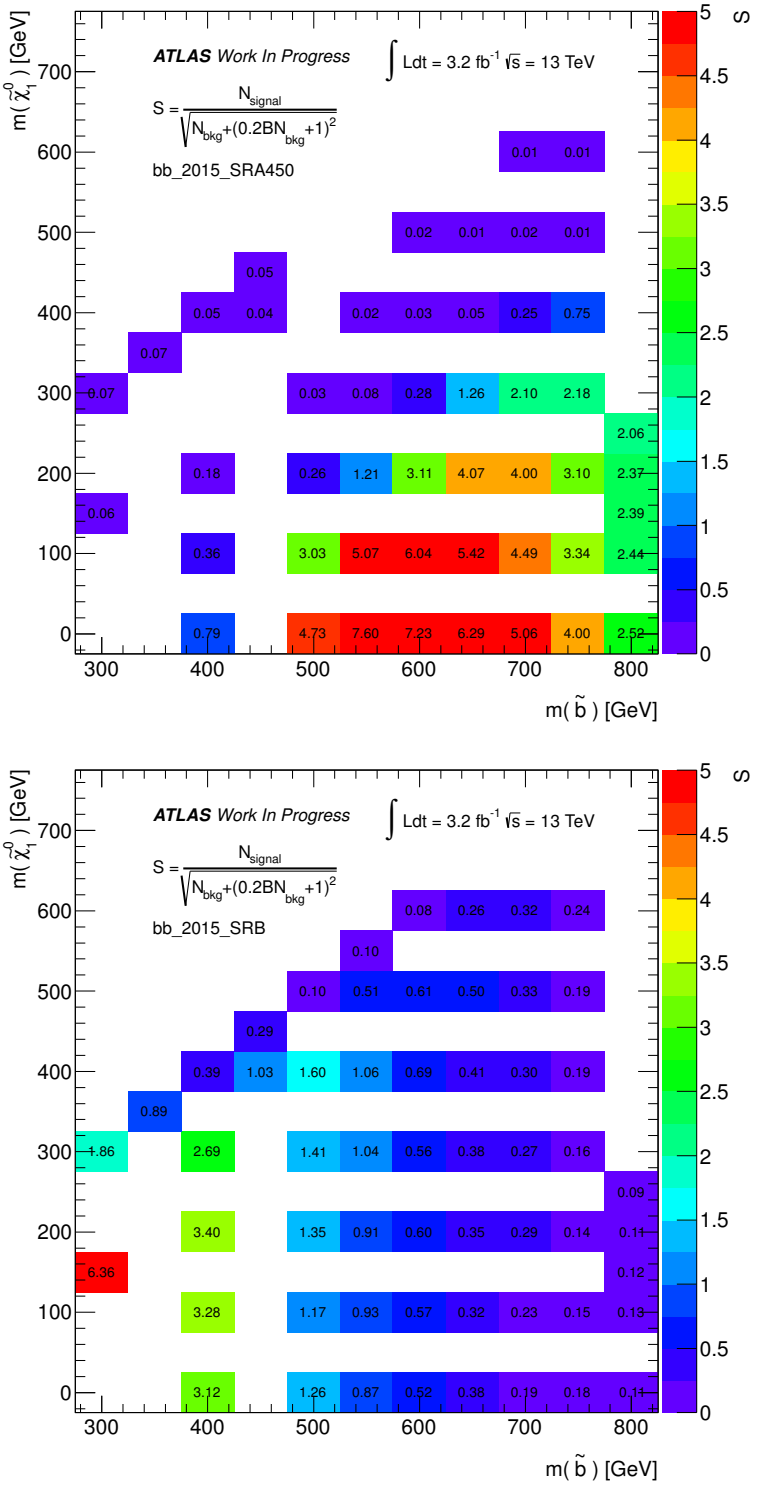

FIGURE 6.10: Expected significance plots for the 2015 sbottom SR definitions. Top: SRA450. Bottom: SRB.

6.2.3 Control Region Definitions

In order to constrain the main background processes in the SRs, control regions (CRs) are defined. CRs are defined for each of the main backgrounds of a specific SR. The regions are designed such that they are enhanced in the SM events of interest with kinematics close to that of the SR whilst remaining orthogonal. The number of expected background events and the observed number of events in each CR enter a log likelihood fit, to obtain normalisation parameters to be applied to the MC prediction for that specific background. The fit procedure will be further discussed in Section 6.2.7.

Due to the different kinematic selections of the A-type and B-type regions, two different CR strategies are required. When considering the regions defined for the Z+jets background, to attempt to mimic the $Z \to \nu\nu$ decay, which would be the dominant Z decay mode in either of the SRs, the leptons in this region are vectorally added to the reconstructed $E_{\mathrm{T}}^{\mathrm{miss}}$ in the event. The lepton corrected $E_{\mathrm{T}}^{\mathrm{miss}}$ is referred to as $E_{\mathrm{T}}^{\mathrm{miss}\prime}$. To more closely model the SR kinematics, the SR selection placed on the $E_{\mathrm{T}}^{\mathrm{miss}}$, is placed on the $E_{\mathrm{T}}^{\mathrm{miss}\prime}$ in these two lepton regions.

For the A-type regions, a common set of four CRs are defined for the $t\bar{t}$, single-top, W+jets and Z+jets backgrounds respectively. The normalisation parameters obtained from these regions are then applied to all three SRs. Orthogonality of these regions with the SR is ensured by the presence of at least one signal lepton in the event. The CR defined for the Z+jets process (CRzA) requires two same-flavour (SF) leptons (e, μ) with invariant mass ($m_{\ell\ell}$) in the Z-mass window (76-106 GeV). One lepton CRs are defined for the remaining backgrounds. The CR defined for the W+jets process (CRwA) is orthogonal to the other one lepton regions, as it requires exclusively one $b-$tagged jet. The CRs defined for the $t\bar{t}$ (CRttA) and single-top (CRstA) regions are orthogonal thanks to the requirement on m_{bb}. A full overview of the A-type CR definitions are presented in Table 6.12. As it can be seen in the Table, additional selections are also employed to enhance the contribution of the background under consideration (such as m_{T} in the CRW), and to further mimic the kinematics in the SR (such as the leading $b-$jet requirements). Table 6.7 presents the MC predictions for each SM background and the data. Each of the CRs is clearly dominated by the SM process under scrutiny, with the exception of CRstA which also includes a large fraction of $t\bar{t}$ and W+jets events.

Variable	CRzA	CRttA	CRwA	CRstA
Preselection	✔	✔	✔ (one $b-$jet)	✔
$n_{\text{signal leptons}}$	2 (SF)	1	1	1
p_{T} (ℓ)	$> 90, 20$ GeV	> 26 GeV	> 26 GeV	> 26 GeV
Leading two jets are $b-$tagged	✔	✔	✔ (primary $b-$jet)	✔
$E_{\text{T}}^{\text{miss}}$	< 100 GeV	> 100 GeV	> 100 GeV	> 100 GeV
$E_{\text{T}}^{\text{miss}\,\prime}$	> 100 GeV	-	-	-
m_{CT}	-	> 150 GeV	> 150 GeV	> 150 GeV
p_{T} (j_1)	> 50 GeV	> 130 GeV	> 130 GeV	> 50 GeV
$m_{\ell\ell}$	[76 - 106] GeV	-	-	-
m_{T}	-	-	> 30 GeV	-
m_{bb}	> 200 GeV	< 200 GeV	> 200 GeV ($m_{b,j}$)	> 200 GeV
$m_{b,l}^{\text{min}}$	-	-	-	> 170 GeV

TABLE 6.6: Sbottom 2015 analysis, A-type CR definitions.

	Number of Events			
Process	CRzA	CRttA	CRwA	CRstA
$t\bar{t}$	8.1 ± 0.8	200.0 ± 3.6	160.6 ± 3.2	11.7 ± 0.9
Diboson	0.3 ± 0.1	4.7 ± 0.3	7.0 ± 0.5	0.5 ± 0.1
Z+jets	49.6 ± 2.0	0.9 ± 0.2	4.8 ± 1.0	0.9 ± 0.2
W+jets	0.0 ± 0.0	37.0 ± 1.0	268 ± 6	16.7 ± 0.8
$t\bar{t}V$	0.62 ± 0.01	0.87 ± 0.02	1.13 ± 0.02	0.184 ± 0.007
Single-top	1.1 ± 0.2	33.8 ± 0.8	61.0 ± 1.0	28.1 ± 0.7
SM Total	59.7 ± 2.2	268.0 ± 4.0	510.0 ± 6.7	58.1 ± 1.5
Observed Data	79	260	543	56

TABLE 6.7: Sbottom 2015 analysis, expected pre-fit CR yields for all A-type regions, including the observed number of data events.

For the B-type region two CRs are defined, one each for the $t\bar{t}$ and Z+jets backgrounds. These regions are othogonal to the SRB region due to the requirement of either one lepton, for the $t\bar{t}$ CR (CRttB), or two same-flavour leptons, for the Z+jets CR (CRzB). This also ensures that the CRs are mutually orthogonal. Additional selections are placed on the CRs to reproduce the SR kinematics more closely. The full selections for the B-type CRs are defined in Table 6.8, Table 6.9 contains the data and MC yields in the B-type CRs. In this case CRzB also contains a large contamination of $t\bar{t}$.

Variable	CRttB	CRzB
Preselection	✔	✔
$n_{\text{baseline leptons}}$	1	2 (SF)
p_{T} (ℓ)	$> 26\,\text{GeV}$	$> 26, 20\,\text{GeV}$
Leading jet non-$b-$tagged	✔	✔
p_{T} (j_1)	$> 130\,\text{GeV}$	$> 50\,\text{GeV}$
Sub-leading jet $b-$tagged	✔	✔
$\Delta\phi(j_1, E_{\text{T}}^{\text{miss}})$	> 2.5	> 2.0
$E_{\text{T}}^{\text{miss}}$	$> 100\,\text{GeV}$	$< 100\,\text{GeV}$
$E_{\text{T}}^{\text{miss}\,\prime}$	-	$> 100\,\text{GeV}$
$m_{\ell\ell}$	-	[76-106] GeV

TABLE 6.8: Sbottom 2015 analysis, B-type CR definitions.

	Number of Events	
Process	CRzB	CRttB
$t\bar{t}$	15.2 ± 1.1	158.4 ± 2.0
Diboson	0.8 ± 0.2	1.2 ± 0.2
Z+jets	30.0 ± 2.0	0.18 ± 0.03
W+jets	0.0 ± 0.0	13.3 ± 0.5
$t\bar{t}V$	0.78 ± 0.01	0.7 ± 0.02
Single-top	0.5 ± 0.1	16.7 ± 1.4
SM Total	47.6 ± 2.3	190.6 ± 2.1
Observed Data	59	188

TABLE 6.9: Sbottom 2015 analysis, expected pre-fit CR yields for all B-type regions, including the observed number of data events.

The results of the simultaneous fit procedure are presented in 6.2.7.1. The $\mu_{Z+\text{jets}}$ value is found to be significantly higher than 1, suggesting a poor modelling of the Z+jets process. Due to the prevalence of the Z+jets process in both types of SR, and this noticable pre-fit discrepancy in both CRzA and CRzB regions between the expected Z+jets from MC and the observed data, alternative data-driven methods are investigated to validate the modelling of the Z+jets process in the SRs.

6.2.4 Data-driven replacement methods

There are two alternative data driven methods used and the underlying strategy for both methods is relatively similar, in that the methods require the replacement of one branch of the Z+jets process, either replacing the Z boson with a photon (referred to as

the "γ+jets replacement method"), or replacing the $b-$jets in the final state, with light jets (referred to as the "Z from light" method). As the main component of the author's work was implementing the "γ+jets replacement" method, the "Z from light" method will only be discussed briefly.

The "Z from light" method allows for an alternative estimate of the $Z \to \nu\nu$ in the A-type SRs. This method requires the assumption that the shape of the m_{CT} variable in the SRs is similar for Z + light jet events, and for $Z + b-$jet events. As the method explicitly depends upon the m_{CT} variable, it cannot be used to provide an estimate in the B-type SR. A high statistics two lepton CR is defined to select events with $Z \to \ell\ell$ + light jets. The m_{CT} distribution in this region is then used to estimate the m_{CT} shape for the Z+jets process. The normalisation of the estimate from this method is calculated based on the ratio of $Z \to \ell\ell$ events with zero $b-$tagged jets, to a $Z \to \ell\ell$ events with two $b-$tagged jets. The main advantage of this method is that it allows for the use of a very high statistics region dominated by the Z+jets background, to perform the extrapolation to the SR.

The γ+jets replacement method exploits the similarity between the production mechanisms of the Z+jets and γ+jets processes. When considering the differences between the production of a γ or Z at a $q, \bar{q}$ vertex, the primary difference is the mass contribution in the propagator term:

$$\mathcal{M} \propto \frac{1}{q^2 - m^2} \tag{6.2}$$

For the γ+jets process, Equation 6.2 reduces to $1/q^2$, whereas for the Z+jets process the mass term does not disappear. However if the momentum of the Z boson is much larger than its mass, ($q^2 >> m_Z^2$) then the propagator term for the Z+jets process can be approximated as $1/q^2$, similar to the γ+jets process. In the 0 leptons final state, the $p_{\mathrm{T}}(Z)$ is very closely related to the $E_{\mathrm{T}}^{\mathrm{miss}}$. The $E_{\mathrm{T}}^{\mathrm{miss}}$ selection requirements in both types of SR almost fufil the requirement that $p_{\mathrm{T}}(Z) >> m_Z$. To correct for any remaining differences that may arise due to the mass term and additional kinematic differences, a $p_{\mathrm{T}}(Z)$-based reweighting procedure is used. The usage of the p_{T}-based reweighting procedure also mitigates the second difference between the γ and Z vertices, that is the difference in the coupling term between the electromagnetic and weak forces. At the Z vertex, the coupling term is related to $g_W \sin(\theta_W)$, whereas at the γ vertex, the coupling is related to e. These differences are taken into account implicitly in the p_{T}

(Z) reweighting procedure. The overall method is as follows:

- A γ+jets CR (CRγ) is defined, matching the SR selection but dropping the requirement on $E_{\mathrm{T}}^{\mathrm{miss}}$ and instead requiring one photon with $p_{\mathrm{T}} > 130\,\mathrm{GeV}$ to satisfy trigger requirements. The photon 4-vector is added vectorally to the reconstructed $E_{\mathrm{T}}^{\mathrm{miss}}$, to produce a photon-corrected variant referred to as $E_{\mathrm{T}}^{\mathrm{miss},\gamma}$. The $E_{\mathrm{T}}^{\mathrm{miss}}$ selection is then applied to the photon-corrected $E_{\mathrm{T}}^{\mathrm{miss},\gamma}$.

- Events passing the above requirement lead to a very high purity γ+jets region, however some non-γ backgrounds still remain. Those are subtracted from the data using estimates from MC. In this scenario the shape of any given distribution can be expressed as $f_{\mathrm{CR}\gamma}^{\mathrm{data}} - f_{\mathrm{CR}\gamma}^{\mathrm{non}\gamma-\mathrm{MC}}$. The non-$\gamma$ MC contributes less than 1% in the regions of interest.

- The reweighting factor, $R(Z,\gamma)$, is defined as the ratio of Z+jets to γ+jets events binned in p_{T} and it is calculated using the $Z \to \nu\nu + bb$ events in the SR, and the $\gamma + bb$ events passing the CRγ selection. This gives:

$$R(V)dp_{\mathrm{T}}(V) = \frac{f_{\mathrm{SR}}^{Z\to\nu\nu}dp_{\mathrm{T}}(Z^{\mathrm{truth}})}{f_{\mathrm{CR}\gamma}^{\gamma+bb}dp_{\mathrm{T}}(\gamma^{\mathrm{reco}})}. \tag{6.3}$$

  The reweighting procedure is performed using the truth-level Z-boson p_{T}. As the above ratio includes $p_{\mathrm{T}}(\gamma)$ at reconstruction level acceptance effects are implicitly taken into account. The available γ+jets samples are generated at LO, whereas the nominal Z+jets sample is at NLO. Figure 6.11 presents the differences in reweighting the γ+jets to NLO and LO Z+jets, as seen in the figure there is no significant difference between the ratio produced from the NLO and LO samples for the selection used in this analysis.

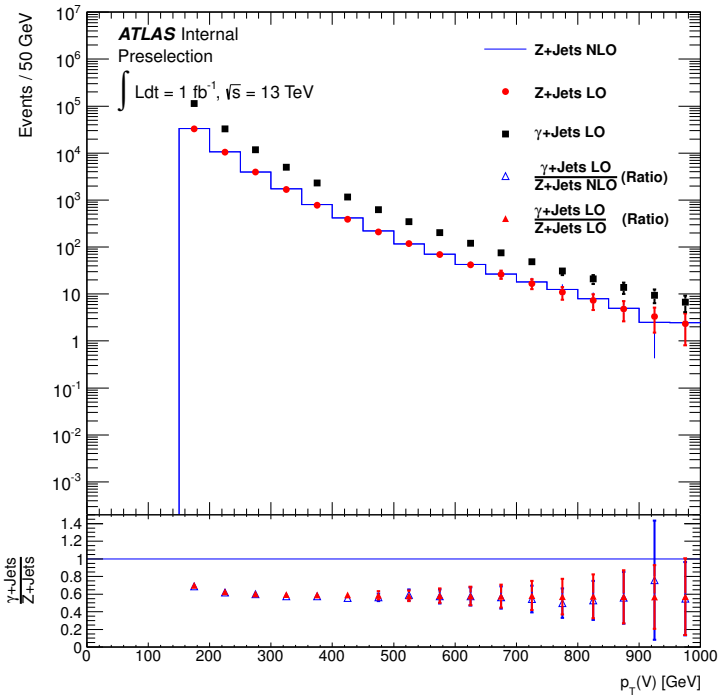

FIGURE 6.11: Truth-level p_{T} ratio for γ+jets and Z+jets processes. No significant differences are found between reweighting the LO γ+jets to the NLO Z+jets, when compared to the LO Z+jets.

- An additional normalisation parameter, κ, is also introduced to take into account the differences between the cross sections the Z+jets and γ+jets processes. This requires the introduction of two additional regions referred to as "loose". These regions are designed as loose as they are defined by relaxing the selections when compared to the standard region definitions. These regions are referred to as CRγ^{loose} and CRZ^{loose}. The κ factor is defined as the ratio of the normalisation parameters $\mu_{\gamma}^{\mathrm{loose}}$ and μ_{Z}^{loose}, normalising the MC prediction of the γ+jets and Z+jets in the CRγ^{loose} and CRZ^{loose} to the observed data. This factor is used to reconcile the known differences between the observed γ+jets process and the MC expectations, using a relaxed selection.

$$\begin{aligned}\kappa &= \frac{\mu_{\gamma}^{\mathrm{loose}}}{\mu_{Z}^{\mathrm{loose}}} \\ &= \frac{N_{\mathrm{CR}\gamma^{\mathrm{loose}}}^{\mathrm{data}} - N_{\mathrm{CR}\gamma^{\mathrm{loose}}}^{\mathrm{non-}\gamma\mathrm{+jets\,MC}}}{N_{\mathrm{CR}\gamma^{\mathrm{loose}}}^{\gamma\mathrm{+jets\,MC}}} \cdot \frac{N_{\mathrm{CR}Z^{\mathrm{loose}}}^{\mathrm{Z+jets\,MC}}}{N_{\mathrm{CR}Z^{\mathrm{loose}}}^{\mathrm{data}} - N_{\mathrm{CR}Z^{\mathrm{loose}}}^{\mathrm{non-Z+jets\,MC}}} \\ &= \frac{N_{\mathrm{CR}\gamma^{\mathrm{loose}}}^{\mathrm{data}} - N_{\mathrm{CR}\gamma^{\mathrm{loose}}}^{\mathrm{non-}\gamma\mathrm{+jets\,MC}}}{N_{\mathrm{CR}Z^{\mathrm{loose}}}^{\mathrm{data}} - N_{\mathrm{CR}Z^{\mathrm{loose}}}^{\mathrm{non-Z+jets\,MC}}} \cdot \frac{N_{\mathrm{CR}Z^{\mathrm{loose}}}^{\mathrm{Z+jets\,MC}}}{N_{\mathrm{CR}\gamma^{\mathrm{loose}}}^{\gamma\mathrm{+jets\,MC}}}\end{aligned} \tag{6.4}$$

- Using the contributions from the above steps the expected number of $Z \to \nu\nu$ + $b-$jets events in a SR can be calculated for a selection, x, on a given variable, in this case m_{CT} using:

$$N_{\mathrm{SR}}^{Z\to\nu\nu} = \int_{x}^{\infty} (f_{\mathrm{CR}\gamma}^{\mathrm{data}} - f_{\mathrm{CR}\gamma}^{\mathrm{non}\gamma-\mathrm{MC}}) \cdot \frac{1}{\kappa} \cdot R(V) dp_{\mathrm{T}}(V) dm_{\mathrm{CT}} \tag{6.5}$$

The extra CRs that are defined for the γ+jets replacement method are presented in Table 6.10. The predicted number of events in the "loose" and tighter regions are presented in Table 6.11. Using the looser region yields from Table 6.11 allows for the calculation of the κ factor to be performed, resulting in a value of $\kappa = 1.27 \pm 0.27$. This value is consistent with the SM γ+jets measurement. The final predicted number of events using the method are shown in Tables 6.16 and 6.19, where they are compared to the nominal fit procedure, and also the prediction from the "Z from light" method. The predictions using the alternative data-driven methods are consistent with the nominal fit procedure, providing further confidence in the modelling of the Z+jets process.

Variable	CRγA	CRγB	CRγ^{loose}	CRZ$^{\mathrm{loose}}$
Preselection	✔	✔	✔	✔
$n_{\mathrm{signal\,leptons}}$	0	0	0	2 (SF)
$n_{\mathrm{signal\,photons}}$	1	1	1	0
p_{T} (ℓ)	-	-	-	$> 26, 20$ GeV
p_{T} (γ)	> 130 GeV	> 130 GeV	> 130 GeV	-
Leading jet is $b-$tagged	✔	✗	-	-
Sub-leading jet is $b-$tagged	✔	✔	-	-
p_{T} (j_1)	> 130 GeV	> 300 GeV	> 50 GeV	> 50 GeV
$E_{\mathrm{T}}^{\mathrm{miss}}$	-	-	-	< 100 GeV
$E_{\mathrm{T}}^{\mathrm{miss}\,\prime}$	-	-	-	> 250 GeV
$E_{\mathrm{T}}^{\mathrm{miss},\gamma}$	> 250 GeV	> 400 GeV	> 250 GeV	-
m_{CT}	$> 250, 350, 450$	-	-	-
$m_{\ell\ell}$	-	-	-	[76 - 106] GeV
m_{bb}	> 200 GeV	-	-	-

TABLE 6.10: Sbottom 2015 analysis, additional CR definitions used in the implementation of the γ+jets replacement method.

	CRγ^{loose}	CRZ$^{\text{loose}}$	CRγA250	CRγA350	CRγA450	CRγB
Observed Data	381 ± 19.52	31.00 ± 5.57	40.00 ± 6.32	8.00 ± 2.83	4.00 ± 2.00	6.00 ± 2.45
MC Total	248.76 ± 5.06	26.14 ± 1.49	26.50 ± 1.40	5.87 ± 0.55	1.66 ± 0.25	6.26 ± 0.59
W + jets	0.62 ± 0.09	0.00 ± 0.00	0.10 ± 0.03	0.02 ± 0.01	0.01 ± 0.00	0.03 ± 0.01
Z + jets	0.08 ± 0.02	23.15 ± 0.83	0.01 ± 0.01	0.00 ± 0.00	0.00 ± 0.00	0.00 ± 0.00
Other	$0.12\pm$	2.58 ± 0.47	0.00 ± 0.00	0.00 ± 0.00	0.00 ± 0.00	0.00 ± 0.00
SingleTop	0.49 ± 0.09	0.18 ± 0.06	0.03 ± 0.01	0.02 ± 0.01	0.01 ± 0.00	0.02 ± 0.01
$t\bar{t}$	2.28 ± 0.4	0.022 ± 0.13	0.00 ± 0.00	0.00 ± 0.00	0.00 ± 0.00	0.14 ± 0.07
γ + jets	245.17 ± 5.04	0.0 ± 0.0	26.33 ± 1.33	5.81 ± 0.52	1.63 ± 0.22	6.08 ± 0.50

TABLE 6.11: Expected yields of the SM background processes and observed events with $3.2\,\text{fb}^{-1}$ in the regions defined for the γ+jets alternative data driven method.

6.2.5 Validation Region Definitions

To validate the normalisation of the backgrounds, VRs are defined for both the A- and B-type SRs. The VRs are chosen such that they are orthogonal to both of the relevant SRs and CRs, and are selected to be kinematically close to the SR. As all of the CRs that have previously been defined require leptons in the final state, whilst the SRs contain no leptons, a sensible requirement is to design VRs such that they also contain zero leptons. A simple method to ensure othogonality between the SRs and the VRs is to select a key kinematic variable used in the SR (for example, m_{CT}) and to invert the SR selection that is placed on this variable. It is also possible to select a "window" on this variable (after inverting the SR selection), to attempt to keep the kinematics of the VR close to that of the SR. This is done taking into account that the signal contamination must be as minimal as possible.

Two VRs are associated with the set of A-type SRs, defined by either inverting the m_{bb} selection (VRmbbA), or the m_{CT} selection (VRmctA). For the VRmctA region, the upper bound on the m_{CT} selection is chosen to be 150 GeV, reducing signal contamination, this region validates the modelling of the Z+jets background. The VRAmbb region is used to validate the modelling of the $t\bar{t}$ background.

A single VR is designed to validate the background prediction in the B-type SRs, defined by inverting both the selection on the leading jet p_{T} and the selection on $E_{\text{T}}^{\text{miss}}$. Lower bounds are placed on both of these inverted selections, to ensure similar kinematics to those expected in the SR, creating a region dominated by the $t\bar{t}$ process.

Variable	VRmctA	VRmbbA	VRB
Preselection	✔	✔	✔
$n_{\text{baseline leptons}}$	0	0	0
Primary jet is $b-$tagged	✔	✔	✗
Secondary jet is $b-$tagged	✔	✔	✔
p_{T} (j_1)	$> 130\,\text{GeV}$	$> 130\,\text{GeV}$	$[100, 300]\,\text{GeV}$
m_{bb}	$<200\,\text{GeV}$	$>200\,\text{GeV}$	-
$E_{\text{T}}^{\text{miss}}$	$>250\,\text{GeV}$	$>250\,\text{GeV}$	$[250, 300]\,\text{GeV}$
m_{CT}	$>150\,\text{GeV}$	$<150\,\text{GeV}$	-
$\Delta\phi(j_1, E_{\text{T}}^{\text{miss}})$	-	-	> 2.5

TABLE 6.12: Sbottom 2015 analysis, VR definitions for both A- and B-type regions.

The fitted background events for the A- and B-type validation regions are presented in Tables 6.15 and 6.18. It is found that the observed data in the VRs is modelled well by the results of the background only fit.

6.2.6 Systematic Uncertainties

There are two possible sources of systematic uncertainty that can affect the results of the analysis: systematic uncertainties arising from the detector, known as "Detector Uncertainties", which apply on the signal and background; or uncertainties arising from the choice in MC generator, known as "Modelling Uncertainties". Systematics to the theoretical predictions are also considered on the signal.

6.2.6.1 Detector Uncertainties

As discussed in Chapter 5, the definition of physics objects in the analysis is dependent upon both p_{T} and η of the object as reconstructed using the information collected by the detector. There are many sources of uncertainty that can arise from the modelling of the detector in MC, including uncertainties from the calibrations used, uncertainties applied to MC objects to reproduce the detector efficiency and uncertainty from the luminosity delivered by the LHC machine. These uncertainties must be taken into account when performing the analysis, as they can affect the number of events passing a given selection. This subsequently changes the expected number of events in the SRs and CRs, affecting the fit results and the statistical intepretations of the results. The individual sources of detector uncertainty considered in the analysis are:

Luminosity: The luminosity uncertainty is the uncertainty arising from the measurement of the total luminosity (via a Van Der Meer scan [131]) performed in June 2015. The total measured luminosity is $3.2\,\text{fb}^{-1}$ with an associated uncertainty of 5%.

Jet Energy Scale (JES): Initially, reconstructed jets are calibrated at the electromagnetic scale which is established for the EM calorimeter using test beam measurements. The EM scale accounts correctly for photons and electrons, however it does not account for detector effects, inefficiencies in calorimeter clustering or jet reconstruction. For hadronic jets the measured energy is less than the actual jet energy. A JES calibration must be applied which takes into account the non-compensating nature of the calorimeter to correct the hadronic jet activity. The JES uncertainty is the uncertainty that arises from the choices made when developing the JES calibration from both data and MC [132]. In total there are 67 parameters which must be varied in order to produce the JES uncertainty, however a reduced set of parameters (4 sets of 3 parameters each) were produced to provide a more efficient way to estimate the effect of the JES uncertainty [133].

Dedicated calibrations are used to determine the JES uncertainty arising from light jets and heavy-flavour jets, as heavy-flavour jets have additional contributions to the final JES uncertainty calculation [134].

Jet Energy Resolution (JER): The jet energy resolution is the uncertainty on the central value measured for the energy of a jet. Varying the jet energy resolution can result in a change to the jet multiplicity as varying the JER can change the measured p_{T} of a given jet, which can result in the jet no-longer passing the jet p_{T} requirements (or vice-versa) [135].

Jet Vertex Tagger (JVT). The JVT method used to reject central jets that arising from pile-up events, applies p_{T} dependant scale factors in MC to match the observed efficiency of the JVT in data events. The JVT uncertainty arises from varying these scale factors [136].

$E_{\text{T}}^{\text{miss}}$ **and** $E_{\text{T}}^{\text{miss}}$ **soft term**: The uncertainty on the $E_{\text{T}}^{\text{miss}}$ arises arises as a consequence of the changes from other variations (for example the JER and JES systematics) which affect the objects that enter the $E_{\text{T}}^{\text{miss}}$ calculation. The uncertainty on the reconstructed $E_{\text{T}}^{\text{miss}}$ can also be affected by the $E_{\text{T}}^{\text{miss}}$ soft term. There are three associated uncertainties related to the soft term: the scale term, which varies the offset of the soft term along the $E_{\text{T}}^{\text{miss}}$ axis; and the parallel and perpendicular resolution terms, which vary the resolution of the soft term either parallel to, or perpendicular to, the $E_{\text{T}}^{\text{miss}}$

axis. These uncertainties are varied orthogonally to provide the total uncertainty on the $E_{\mathrm{T}}^{\mathrm{miss}}$ soft term.

$b-$**tagging**: The uncertainties arising from the $b-$tagging algorithm are taken into account by varying the p_{T}, η and flavour-dependent scale factors that are applied to the jets [112]. The variations are applied in an orthogonal manner (as the uncertainties are flavour dependent, so correspond individually to $b-$jets, $c-$jets and light-jets). A final variation is considered to estimate the uncertainty arising from the extrapolation required to perform $b-$tagging for high p_{T} jets, as the method for calculating the efficiency of the $b-$tagging algorithms is dependent upon a sample of $t\bar{t}$ events. An extrapolation is required for the calibration of high p_{T} due to a lack of statistics.

Lepton energy scale and resolution: Uncertainties from the calibration of the lepton energy scale and resolution are estimated in a similar manner to the JES and JER uncertainties, as similar to that of the JER/JES uncertainties, varying the lepton energy scale/resolution may change the lepton multiplicity in an event, changing the number of events that pass a lepton multiplicity selection.

Lepton efficiency: The uncertainty on the scale factors applied to MC to match the reconstruction, identification, isolation and trigger efficiencies in data are taken into account by varying the scale factors within their uncertainties.

PileUp: A scale-factor is applied to the MC simulations to better describe the minimum-bias vertex data related to the number of pile-up interactions. The uncertainty on the scale-factor applied is evaluated by varying the scale-factor within its uncertainties.

The most relevant detector uncertainties for the analysis are the uncertainties related to the jets, the JER, JES and $b-$tagging uncertainties. The uncertainties arising from the leptons and $E_{\mathrm{T}}^{\mathrm{miss}}$ are relatively unimportant in the analysis and only contribute a small ($< 1\%$) amount to the overall total uncertainty.

6.2.6.2 Modelling Uncertainties

The uncertainties arising due to non-arbitrary choices made when constructing a MC generator to model a physics process have previously been discussed in Chapter 4. For the four main backgrounds in the analysis ($t\bar{t}$, single-top, Z+jets and W+jets), the effects of the modelling uncertainties are evaluated.

As previously introduced in Section 4.1.1 the uncertainty due to the choice in PDF set is evaluated by comparing the nominal PDF set for each sample with alternative PDF sets. For every analysis presented herein the uncertainty arising from the choice in PDF set is found to be negligible.

For the $t\bar{t}$ and single-top backgrounds, the nominal MC generator setup used for both samples is Powheg for the hard-scatter process, with showering performed by Pythia6. There are four sources of modelling uncertainty when using Powheg+Pythia6 as the nominal sample:

- Hard scatter generation: A comparison is performed between the results produced by Powheg+Herwig++ to an alternative generator (using the same PS algorithm), in this case MC@NLO+Herwig++. This is motivated by the fact that MC@NLO cannot be interfaced to Pythia6.

- Parton shower algorithm/Hadronisation uncertainty: The nominal setup is compared to a sample generated with the same ME calculation but with using a different parton shower algorithm, in this case Powheg+Herwig++.

- Factorisation scale, renormalisation scale and shower radiation uncertainties: The uncertainties arising from μ_R, μ_F and the shower radiation are estimated by comparing the nominal predictions to those of two alternative PowhegPythia samples which use different parameters for the values of μ_R, μ_F and the hdamp parameter, which is used as a cut-off to change the amount of hard radiation produced by the generator. The samples chosen produce an envelope around the nominal sample with respect to the μ_R, μ_F and hdamp parameters chosen.

The above comparisons are made to evaluate the $t\bar{t}$ and single-top modelling uncertainties. However, as also discussed in Section 4.3 an additional source of uncertainty arises in the modelling of the single-top process, arising from the interference between the single-top and $t\bar{t}$ processes. As more thoroughly described in Section 4.3, the two alternative methods that can be used to estimate the interference uncertainty (the DS scheme and the $WWbb$ sample) do not provide sensible results when compared to the modelling provided by the nominal DR sample. As such no specific uncertainty is associated to the interference term, to prevent artificially inflating the systematics.

The prescription for the V+jets processes is slightly different, as the effects of the modelling uncertainties are all evaluated using the nominal generator (Sherpa) with differing

scale choices, although there is no available method to evaluate the uncertainty on the hadronisation model. Alternative samples were generated with different scale choices (either twice or half the nominal value chosen) for the factorisation scale (μ_F), the renormalisation scale (μ_R) and the soft gluon resummation scale (μ_{QSF}). The matrix element matching scale (ckkw), used to distinguish the p_{T} of jets that should arise from the showering algorithm and the jets that arise from the hard-scatter is also varied from the nominal value of 20 GeV, with the up variation increasing the ckkw scale to 30 GeV, and the down variation decreasing this parameter to 15 GeV.

The work performed calculating a parameterisation to allow for easier calculation of the effect of the modelling uncertainties for the V+jets processes, documented in Section 4.4, is used to calculate the effects of these uncertainties.

The modelling uncertainties arising from the rare backgrounds, $t\bar{t}+V$ and diboson are estimated by varying the cross-section values up and down within the recommended values.

The overall uncertainties that are applied due to the modelling of a given process are calculated as percentage uncertainties on the transfer factor when moving from the CR (defined for the process under consideration) to the SR, as shown in Equation 6.6.

$$\mathrm{TF}_{\mathrm{Proc}} = \frac{N_{\mathrm{Proc}}(\mathrm{SR},\mathrm{MC})}{N_{\mathrm{Proc}}(\mathrm{CR},\mathrm{MC})} \tag{6.6}$$

For a given uncertainty, the error on the transfer factor is given by:

$$\Delta\mathrm{TF}^{\mathrm{variation}}_{\mathrm{Process}} = \frac{\mathrm{TF}^{\mathrm{variation}}_{\mathrm{process}} - \mathrm{TF}^{\mathrm{nominal}}_{\mathrm{process}}}{\mathrm{TF}^{\mathrm{nominal}}_{\mathrm{process}}} \tag{6.7}$$

The total uncertainty is given by the sum in quadrature of the average of the two uncertainties related to the μ_F, μ_R (referred to as RadHi and RadLo), with the generator and PS uncertainties:

$$\Delta\mathrm{TF} = \sqrt{(\Delta\mathrm{TF}^{\mathrm{generator}})^2 + (\Delta\mathrm{TF}^{\mathrm{PS}})^2 + (\frac{\Delta\mathrm{TF}^{\mathrm{RadHi}} + \Delta\mathrm{TF}^{\mathrm{RadHi}}}{2})^2} \tag{6.8}$$

The V+jets uncertainties for the A-type regions are calculated in a similar manner, taking the average uncertainty on the TF for each variation considered:

$$\Delta\mathrm{TF} = \sqrt{(\Delta\mathrm{TF}^{\mathrm{ckkw}}_{\mathrm{avg}})^2 + (\Delta\mathrm{TF}^{\mathrm{fac}}_{\mathrm{avg}})^2 + (\Delta\mathrm{TF}^{\mathrm{renorm}}_{\mathrm{avg}})^2 + (\Delta\mathrm{TF}^{\mathrm{qsf}}_{\mathrm{avg}})^2} \tag{6.9}$$

For the W+jets sample, an additional uncertainty is applied which arises from the

uncertainty in the heavy-flavour component of the jets produced in association with the W. This must be applied due to the differences in $b-$jet multiplicity when moving from the 1 $b-$jet CR to the 2 $b-$jet SR. In order to evaluate this uncertainty, the heavy-flavour fraction of the W+jets samples is varied by 40%, following the measurement in [137], which is a conservative estimate based on the uncertainties of the W+jets flavour composition in this Run 1 measurement.

For the samples (diboson and $t\bar{t}V$) which do not have an associated CR, uncertainties on the total production cross-section are considered for the samples.

With respect to the B-type regions, the same calculation is performed to ascertain the modelling uncertainties for the $t\bar{t}$ and Z+jets processes, as these processes have a B-type CR defined. For the W+jets and single-top processes the uncertainty on the absolute yield in the SRs is calculated.

Source of uncertainty	SRAs	SRB
Detector uncertainties		
JES	15 - 30%	25%
JER	20 - 35%	$< 10\%$
$b-$tagging	25 - 40%	15%
Modelling uncertainties		
Z+jets	25 - 35%	12%
W+jets	20 - 22%	27%
Top production	15 - 20%	70%
Total background systematic (% of expected background)	16 - 21%	21%

TABLE 6.13: Overview of the dominant detector and modelling uncertainties present in the 2015 sbottom analysis. Due to the similarities between the SRA regions, and the fact that they are defined such that they overlap, a range of values are given for the uncertainties in this region. The size of the total systematic uncertainty (as a % of the background expectation) is also given. As the uncertainties considered may be correlated, the total uncertainty may not simply be the sum in quadrature of the uncertainties.

Table 6.13 presents the dominant systematic uncertainties for the analysis. The dominant detector systematic uncertainties arise due to uncertainties on the JES and JER, and also on the $b-$tagging, which is expected when investigating a signal consisting of $b-$jets and missing energy. The dominant modelling uncertainty in the A-type regions is the uncertainty on the Z+jets background, which is expected as the Z+jets process is dominant in the A-type SRs. The uncertainty on the modelling of top production processes (both $t\bar{t}$ and single-top) in the B-type SR is shown to be relatively large, this uncertainty is driven by the difficult region of phase space targeted by the B-type SR.

The uncertainties arising from the choices made when producing the signal MC (such as the hard scatter processes, the PS algorithm and the shower radiation) are estimated when performing the model-dependent fit procedure and account for a total systematic uncertainty on the signal of approximately 10% for each signal point.

6.2.7 Fitting Procedure

The fitting procedure used in the analysis is implemented using the HistFitter [138] framework. This framework performs a log likelihood fit with three types of input: the number of expected MC events for each process, in each CR and SR; the number of data events in each region, and the errors on the number of expected MC events arising from the systematic uncertainties.

The number of expected and observed events in a given region, is used to calculate the transfer factors (TFs) of each normalised background between each CR and SR, which then allows the observed number of events in the CRs to be converted to an estimation of the background in the SRs, using Equation 6.10.

$$N_{proc}(\mathrm{SR},\mathrm{exp}) = N_{\mathrm{proc}}(\mathrm{CR},\mathrm{obs}) \cdot \frac{N_{\mathrm{Proc}}(\mathrm{SR})}{N_{\mathrm{Proc}}(\mathrm{CR})} = \mu_p \cdot N_{\mathrm{Proc}}(\mathrm{SR}) \tag{6.10}$$

In this equation, the number of expected SR events for a given process ($N_{proc}(\mathrm{SR},\mathrm{exp})$) is calculated using the number of observed events in the CR defined for the process ($N_{proc}(\mathrm{CR},\mathrm{obs})$), and the transfer factor for the process as introduced in Equation 6.6. This equation can be rewritten using the normalisation parameter, (μ_p), which is the ratio of observed data events to the MC expected events, for the process in the CR multiplied by the number of expected SR events for the process.

When performing the fit, a likelihood function (L) is built using the products of the Poisson distributions of the number of events (MC and observed) in each of the SRs (P_{SR}) and CRs (P_{CR}), and additional distributions to implement the systematic uncertainties (C_{syst}):

$$\begin{aligned} L(n,\theta^0|\mu_{sig},b,\theta) &= P_{\mathrm{SR}} \times P_{\mathrm{CR}} \times C_{\mathrm{syst}} \\ &= P(n_S|\lambda_S(\mu_{\mathrm{sig}},b,\theta)) \times \prod_{i\in CR} P(n_i|\lambda_i(\mu_{\mathrm{sig}},b,\theta)) \times C_{\mathrm{syst}}(\theta^0,\theta) \end{aligned} \tag{6.11}$$

To break this down further, when viewing the longer form of the equation, the first terms (containing n_S and n_i) are the Poisson measurements of the number of observed events in the SR and each CR, λ_S and λ_i representing the Poisson prediction for the number of events in the SR/CRs given the background prediction (b) for the processes (implicitly contained here are the normalisation parameters μ_p), the nuisance parameters containing the systematic uncertainties, and also the signal strength parameter μ_{sig}, which can be set to 0, to remove the signal component as in the background-only fit procedure, or 1, to set it to the nominal value of the signal model under consideration as in the model-dependent fit procedure.

The systematic term, $C_{\text{syst}}(\theta^0, \theta)$, is a probability density function built upon the product of Gaussians for each systematic variation (Equation 6.12), using the central values (θ^0) of the variations, around which θ (the nominal value) can be varied when performing the maximum likelihood procedure.

$$C_{\text{syst}}(\theta^0, \theta) = \prod_{j \in Systs} G(\theta_j^0 - \theta_j) \tag{6.12}$$

After the creation of the likelihood function, there are three statistical interpretations that can be performed with this information, known as a background-only fit, a model-dependent signal fit and a model-independent fit. Each of these fit types are performed in the process of an analysis.

6.2.7.1 Background-only fit

The background-only fit is performed to produce the normalisation parameters (μ_p) for each of the backgrounds that have associated CRs. The purpose of the background only fit is to produce an estimate of the total background expectation in the SRs (and VRs) without making any assumptions on the signal model under consideration ($\mu_{\text{sig}} = 0$).

The method to perform the background only fit is to produce the likelihood function as in Equation 6.11, but to remove the information in the fit from the VRs and SRs, producing normalisation parameters calculated only using information from the CRs. These normalisation parameters are then introduced into a different likelihood function, containing information from the CRs, VRs and SRs, to produce estimates of the background rates in the SRs and VRs. The results of the background-only fit procedure are reported without applying any rounding to the output.

6.2.7.2 Model-dependent fit

The model dependent fit, also known as an "exclusion" fit, is a frequentist fit performed intending to study a specific signal model. This fit is also known as an exclusion fit, as if there is no significant excess of events in the SRs (which is known by previously performing the background-only fit), then exclusion limits can be placed on a specific signal model considered. In the case of an excess, then the model-dependent fit can be used to measure the signal strength of the model.

In this scenario, the likelihood function is built and the signal model under investigation is included in the fit for all CRs and SRs. From this the normalisation parameter/signal strength (μ_{sig}) is calculated for the signal model. Usually when performing an exclusion fit a grid of signal samples with different mass assumptions are used in the fit (with a fit performed on each signal sample in the grid). The results of the exclusion fit when taking into account all of the signal mass scenarios allow an exclusion contour to be placed in the mass plane considered (for this analysis, in the $\tilde{b}, \tilde{\chi}_1^0$ mass plane).

To construct an exclusion contour, a signal model hypothesis test is used. The signal strength is used as the parameter of interest in the test. The model can be considered to be excluded at the 95% Confidence Level (CL), if the results of the hypothesis test return a p-value of > 0.05. In these scenarios the p-value is the probability of rejecting the background-only hypothesis. By performing the hypothesis test on the full signal grid an exclusion contour can be produced.

6.2.7.3 Model-Independent fit

The so-called "discovery" fit provides a model-independent limit on any additional number of events in the SRs beyond the expected number of background events. This enables the results of the analysis to be interpreted in the context of any generic model (not specifically SUSY), which would expect to contribute to the expected number of events in the SRs.

The procedure for this fit proceeds generally in the same manner as the model-dependent fit, however a "dummy" signal is inserted instead of using an actual signal model. In this scenario no signal contamination is taken into account in the CRs ($\mu_{\text{sig}} = 0$). The number of observed events in the SR is added to the fit to enable the signal strength (of the dummy signal) to be investigated. The value of the signal strength where the CLs value falls below the 5% level (corresponding to a p-value of 0.05) is

finally evaluated, that can then be converted into an upper limit on the visible cross-section of a generic BSM production mechanism, σ_{vis}, which is defined as the product of the cross-section for the process, the selection efficiency and the detector acceptance.

6.2.8 Background-only Fit Results

The background-only fit results for the A-type CRs, VRs and SRs are shown in Tables 6.15 and 6.16, respectively. The estimates of the two data driven methods are also presented. Generally a good overall agreement is found between the MC prediction and the observed data within uncertainties, with some slight overestimates of the number of background events, at the level of less than 1 σ.

The normalisation factors for the A-type fit are shown in Table 6.14. The normalisation factor for the Z+jets background ($\mu_{Z+\text{jets}}$) is large (with a value of 1.3) however it is seen that this estimate is consistent with the data-driven estimates, shown in Table 6.16. The nominal background-only fit and the data-driven methods are consistent to within 1σ in each of the regions, providing further confidence in the nominal background-only fit procedure. There is a relatively large uncertainty (44.6%) on the normalisation of the single-top background, which is driven by the relatively small number of events in the CRstA and the associated statistical uncertainty.

Normalisation	Value
$\mu_{\text{single-top}}$	0.83 ± 0.37
$\mu_{t\bar{t}}$	0.95 ± 0.13
$\mu_{W+\text{jets}}$	1.21 ± 0.18
$\mu_{Z+\text{jets}}$	1.34 ± 0.18

TABLE 6.14: Normalisation factors for the main backgrounds in the A-type regions using the background-only fit with 3.2 fb^{-1}.

Figure 6.12 shows a selection of key kinematic variables in the A-type CRs after applying the normalisation factors. Generally acceptable modelling is found throughout the key variables.

A-type CRs & VRs	CRzA	CRwA	CRttA	CRstA	VRmctA	VRmbbA
Observed events	78	543	260	56	41	68
Fitted bkg events	78.01 ± 8.82	542.99 ± 23.29	260.11 ± 16.12	55.89 ± 7.42	54.23 ± 7.44	75.60 ± 7.48
Fitted Z+jets events	67.40 ± 8.98	3.75 ± 0.64	1.38 ± 0.23	0.94 ± 0.17	10.74 ± 3.34	35.22 ± 6.29
Fitted W+jets events	0.00 ± 0.00	327.51 ± 43.48	45.04 ± 14.19	20.24 ± 5.71	2.94 ± 0.84	11.35 ± 4.04
Fitted $t\bar{t}$ events	9.00 ± 1.63	153.58 ± 26.17	180.82 ± 22.66	11.14 ± 2.09	35.56 ± 6.88	20.74 ± 3.82
Fitted single-top events	0.75 ± 0.36	49.99 ± 22.43	27.18 ± 12.19	23.02 ± 10.22	4.65 ± 2.12	2.60 ± 1.20
Fitted diboson events	0.27 ± 0.06	7.02 ± 1.11	4.84 ± 0.62	0.37 ± 0.08	0.18 ± 0.06	5.29 ± 0.59
Fitted $t\bar{t} + Z$ events	0.57 ± 0.06	0.75 ± 0.06	0.59 ± 0.06	0.08 ± 0.01	0.14 ± 0.02	0.36 ± 0.04
Fitted $t\bar{t} + W$ events	0.01 ± 0.00	0.39 ± 0.03	0.26 ± 0.03	0.10 ± 0.01	0.03 ± 0.00	0.03 ± 0.01
MC exp. SM events	61.66	503.18	266.75	57.49	53.77	66.35
MC exp. Z+jets events	50.45	2.81	1.03	0.70	8.04	26.35
MC exp. W+jets events	0.00	270.54	37.20	16.72	2.43	9.38
MC exp. $t\bar{t}$ events	9.45	161.22	189.94	11.69	37.34	21.78
MC exp. single-top events	0.91	60.45	32.88	27.83	5.62	3.15
MC exp. diboson events	0.27	7.03	4.85	0.37	0.18	5.29
MC exp. $t\bar{t} + Z$ events	0.57	0.75	0.59	0.08	0.14	0.36
MC exp. $t\bar{t} + W$ events	0.01	0.39	0.26	0.10	0.03	0.03

TABLE 6.15: Fit results in the CRs and VRs defined for the A-type SRs with an integrated luminosity of $3.2\,\text{fb}^{-1}$ The results are obtained using the background only fit procedure. The errors contain both statistical and systematic uncertainties.

A-Type SRs	SRA250	SRA350	SRA450
Observed events	23	6	1
Fitted bkg events	29.16 ± 4.71	6.96 ± 1.23	1.84 ± 0.39
Fitted Z+jets events	21.50 ± 4.29	4.94 ± 1.08	1.34 ± 0.35
Z+jets events (using "γ+jets replacement" method)	18.24 ± 4.93	3.69 ± 1.54	1.84 ± 1.01
Z+jets events (using "Z from light" method)	25.22 ± 6.63	6.28 ± 1.68	1.80 ± 0.54
Fitted W+jets events	4.36 ± 1.33	1.19 ± 0.41	0.30 ± 0.12
Fitted $t\bar{t}$ events	1.04 ± 0.45	0.17 ± 0.08	0.04 ± 0.02
Fitted single-top events	1.80 ± 1.01	0.53 ± 0.30	0.13 ± 0.07
Fitted diboson events	0.21 ± 0.05	0.07 ± 0.04	$0.02^{+0.02}_{-0.02}$
Fitted $t\bar{t} + Z$ events	0.22 ± 0.03	0.06 ± 0.01	0.02 ± 0.00
Fitted $t\bar{t} + W$ events	0.02 ± 0.00	0.01 ± 0.00	0.00 ± 0.00
MC exp. SM events	23.41	5.63	1.48
MC exp. Z+jets events	16.09	3.70	1.00
MC exp. W+jets events	3.60	0.98	0.25
MC exp. $t\bar{t}$ events	1.10	0.18	0.04
MC exp. single-top events	2.18	0.64	0.15
MC exp. diboson events	0.21	0.07	0.02
MC exp. $t\bar{t} + Z$ events	0.22	0.06	0.02
MC exp. $t\bar{t} + W$ events	0.02	0.01	0.00

TABLE 6.16: Fit results in A-type SRs with an integrated luminosity of $3.2\,\text{fb}^{-1}$. The results are obtained using the background-only fit procedure. The uncertaintes shown contain only the systematic uncertainties on the background prediction.

The background-only fit results for the B-type CRs, VRs and SRs are shown in Tables 6.18 and 6.19 respectively. The number of fitted background events is consistent with the number of observed data events in the VRB region, whilst in the SRB region there is an overestimate of the expected number of background events

Normalisation	Value
$\mu_{t\bar{t}}$	0.98 ± 0.10
$\mu_{Z+\text{jets}}$	1.46 ± 0.27

TABLE 6.17: Normalisation factors for the main backgrounds in the B-type regions using the background-only fit with $3.2\,\text{fb}^{-1}$.

The normalisation factors for the B-type fit are shown in Table 6.17. Similarly to the A-type fit, the normalisation factor for the Z+jets background (μ_Z+jets) for the B-type regions is large with a large uncertainty due to the small number of events in the CRzB region. The alternative data-driven "γ+jets replacement" method provides additional validation of the Z+jets normalisation, as it can be seen in Table 6.19 that the predictions from the nominal background-only fit procedure and the alternative method are within 1.2σ.

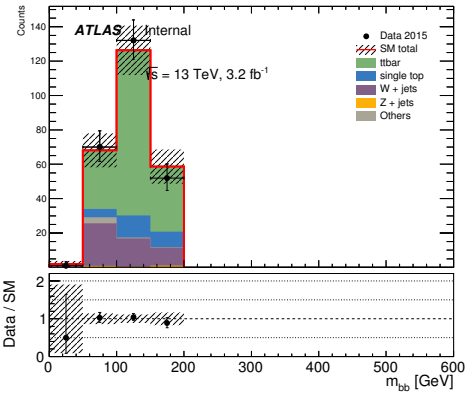

(a) CRttA m_{bb}

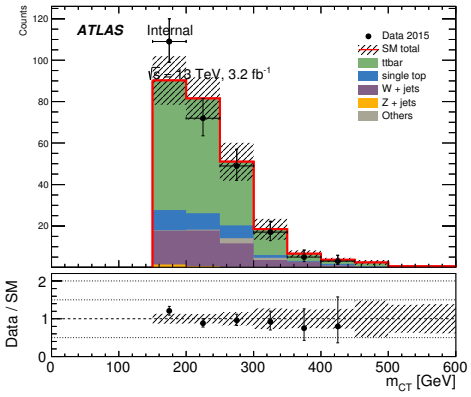

(b) CRttA m_{CT}

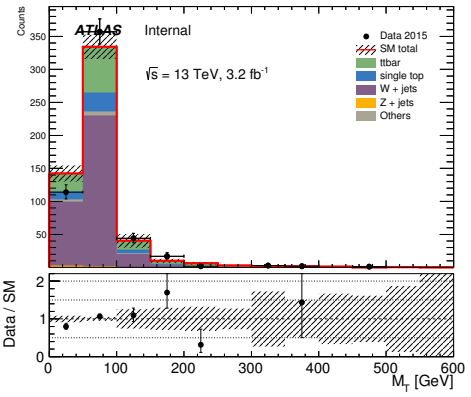

(c) CRwA m_{T}

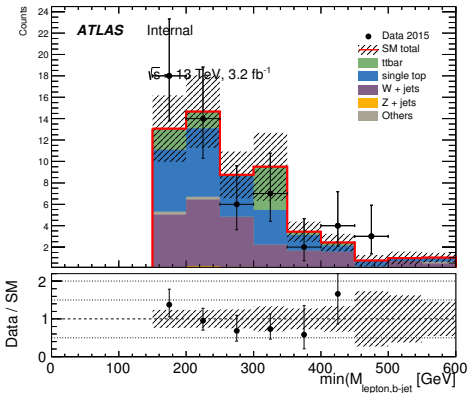

(d) CRstA $m_{b,l}^{\mathrm{min}}$

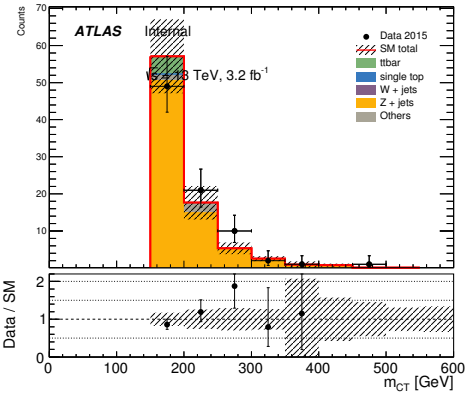

(e) CRzA m_{CT}

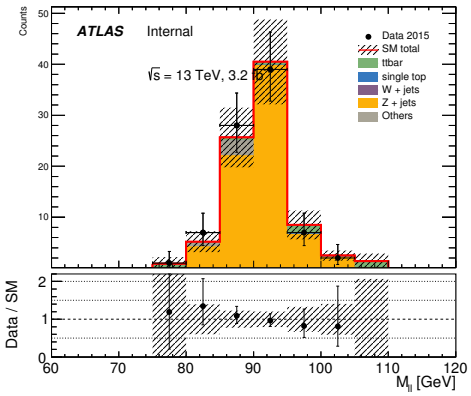

(f) CRzA $m_{\ell\ell}$

FIGURE 6.12: Post-fit distributions for key variables in the A-type CRs.

Figure 6.13 displays post-fit plots for key kinematic variables in the B-type CRs. Generally acceptable modelling is found for the key variables used in the analysis.

B-type CRs & VR	CRzB	CRtopB	VRB
Observed events	59	188	76
Fitted bkg events	58.99 ± 7.66	188.01 ± 13.71	71.71 ± 6.71
Fitted Z+jets events	42.78 ± 7.87	0.30 ± 0.12	13.86 ± 3.16
Fitted W+jets events	0.00 ± 0.00	12.91 ± 4.74	6.42 ± 3.42
Fitted $t\bar{t}$ events	14.23 ± 1.95	155.86 ± 14.98	46.61 ± 5.95
Fitted single-top events	0.42 ± 0.07	16.62 ± 2.13	3.95 ± 0.61
Fitted diboson events	0.83 ± 0.36	1.31 ± 0.20	0.50 ± 0.16
Fitted $t\bar{t} + Z$ events	0.70 ± 0.08	0.69 ± 0.06	0.32 ± 0.04
Fitted $t\bar{t} + W$ events	0.03 ± 0.01	0.31 ± 0.03	0.05 ± 0.01
MC exp. SM events	45.38	191.04	68.14
MC exp. Z+jets events	28.88	0.20	9.36
MC exp. W+jets events	0.00	12.92	6.43
MC exp. $t\bar{t}$ events	14.52	158.97	47.53
MC exp. single-top events	0.42	16.63	3.95
MC exp. diboson events	0.83	1.31	0.50
MC exp. $t\bar{t} + Z$ events	0.70	0.69	0.32
MC exp. $t\bar{t} + W$ events	0.03	0.31	0.05

TABLE 6.18: Fit results in the CRs and VR associated with the B-type SR for an integrated luminosity of $3.2\,\text{fb}^{-1}$, using the background-only fit procedure. The uncertainties shown contain both the systematic and statistical uncertainties.

B-type SR	SRB
Observed events	6
Fitted bkg events	12.03 ± 2.49
Fitted Z+jets events	4.16 ± 1.29
Z+jets events (using "γ+jets replacement method")	2.22 ± 1.04
Fitted W+jets events	1.11 ± 0.57
Fitted $t\bar{t}$ events	5.46 ± 2.03
Fitted single-top events	0.99 ± 0.36
Fitted diboson events	0.19 ± 0.05
Fitted $t\bar{t} + Z$ events	0.10 ± 0.01
Fitted $t\bar{t} + W$ events	0.01 ± 0.00
MC exp. SM events	10.79
MC exp. Z+jets events	2.81
MC exp. W+jets events	1.11
MC exp. $t\bar{t}$ events	5.57
MC exp. single-top events	0.99
MC exp. diboson events	0.19
MC exp. $t\bar{t} + Z$ events	0.10
MC exp. $t\bar{t} + W$ events	0.01

TABLE 6.19: Fit results in SRB for an integrated luminosity of $3.2\,\text{fb}^{-1}$. The results are obtained using the background-only fit procedure. The errors shown contain only the systematic uncertainties on the background estimate.

6.2.9 Interpretation of the results

As no significant deviations from the SM expectations are found in any of the signal regions, exclusion limits are placed on a generic BSM signal hypothesis, using the model-independent fit procedure outlined in Section 6.2.7.3. The results of the model-independent fit-procedure are shown in Table 6.20, which contains the observed (S^{95}_{obs}) and expected (S^{95}_{exp}) 95% CL limits on the number of BSM events. This corresponds to a visible cross section upper limit on a generic BSM process ($\sigma_{\text{vis}} = \epsilon \cdot A \cdot \sigma_{BSM}$), where ϵ is the selection efficiency of a BSM signal, A is the detector acceptance and σ_{BSM} is the BSM production cross section.

Signal Region	σ_{vis} [fb]	S^{95}_{obs}	S^{95}_{exp}
SRA250	3.42	11.0	$13.8^{+6.0}_{-3.2}$
SRA350	1.93	6.2	$6.6^{+3.1}_{-1.1}$
SRA450	1.23	3.9	$4.1^{+1.9}_{-0.6}$
SRB	1.89	6.1	$8.7^{+3.1}_{-2.5}$

TABLE 6.20: 95% CL upper limits on the visible cross section of a generic BSM process (σ_{vis}), the number of expected signal events (S^{95}_{obs}) and the limit on the number of expected signal events, taking into account the expected number of background events (S^{95}_{exp}).

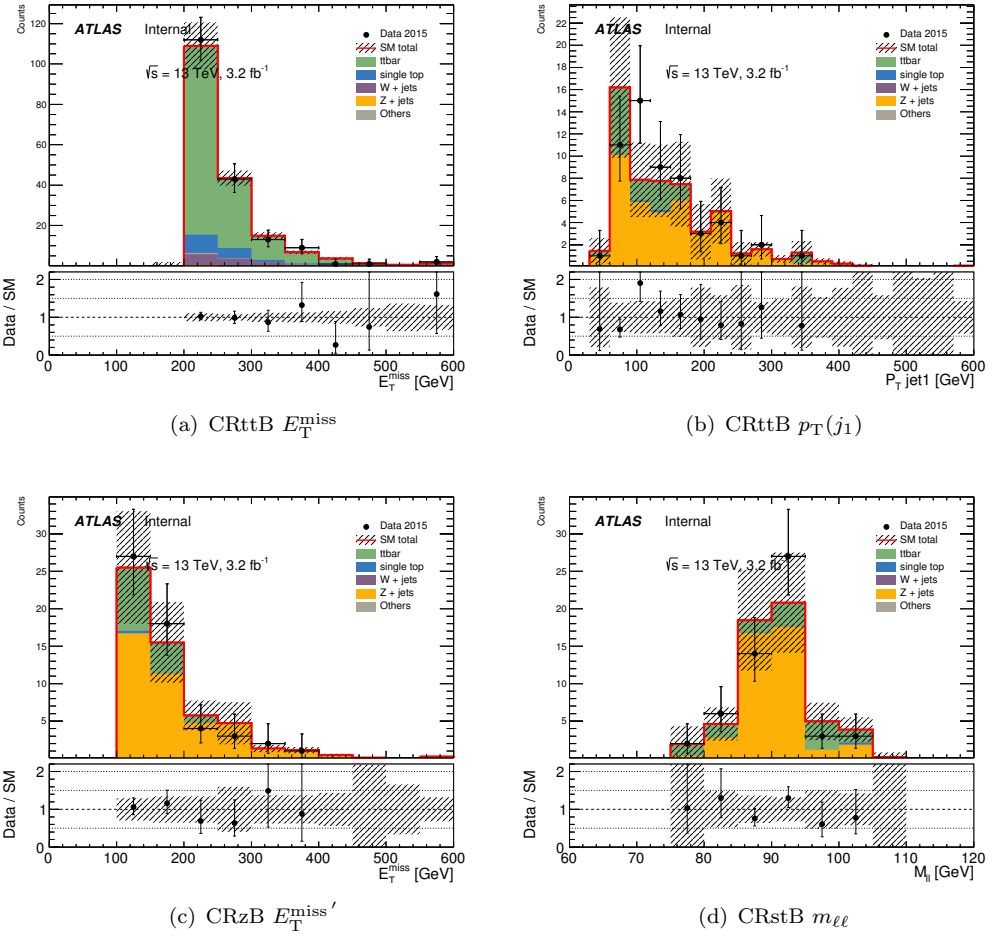

(a) CRttB $E_{\mathrm{T}}^{\mathrm{miss}}$

(b) CRttB $p_{\mathrm{T}}(j_1)$

(c) CRzB $E_{\mathrm{T}}^{\mathrm{miss}\,\prime}$

(d) CRstB $m_{\ell\ell}$

FIGURE 6.13: Post-fit distributions for key variables in the B-type CRs.

Figure 6.18 shows N-1 plots of some key kinematic distributions in the A- and B-type SRs. The arrows on the plots denote where the SR selection on the variable is applied. Acceptable modelling is found in all regions with no significant features in any of the key distributions for the analysis. Additionally Figure 6.15 presents m_{CT} distributions in the SRA250 region, when the Z+jets background is estimated using the data-driven methods. Both methods provide comparable modelling when compared to the nominal Z+jets estimate.

Exclusion limits are also placed in the sbottom-neutralino mass plane, assuming sbottom pair production, subsequently decaying via $\tilde{b} \to b + \tilde{\chi}_1^0$, with a branching ratio of 100%, using the model-dependent fit procedure described in Section 6.2.7.2.

Figure 6.16, shows the exclusion contour obtained using the best expected SR for a given ($\tilde{b}$, $\tilde{\chi}_1^0$) mass scenario. Experimental systematic uncertainties on the signal yields are taken into account in the fit procedure, and are assumed to be fully correlated with

the uncertainties placed on the background estimate. The exclusion contour produced using the best expected SR, shows a significant increase in exclusion when compared to the Run 1 analysis, with $m_{\tilde{b}} = 840\,\text{GeV}$ excluded for massless neutralinos. The high m_{CT} signal region (SRA450) is the region which contributes the most to the exclusion in the bulk scenario, as can be seen in the limit for the SRA450 region in the bottom left of the figure. The regions with a looser selection on m_{CT} (SRA250 and SRA350) provide exclusion in the intermediate mass range where the mass splitting between the sbottom and neutralino is not so large. As expected, the SRB region (bottom right of Figure 6.16) provides the best exclusion in the compressed scenarios.

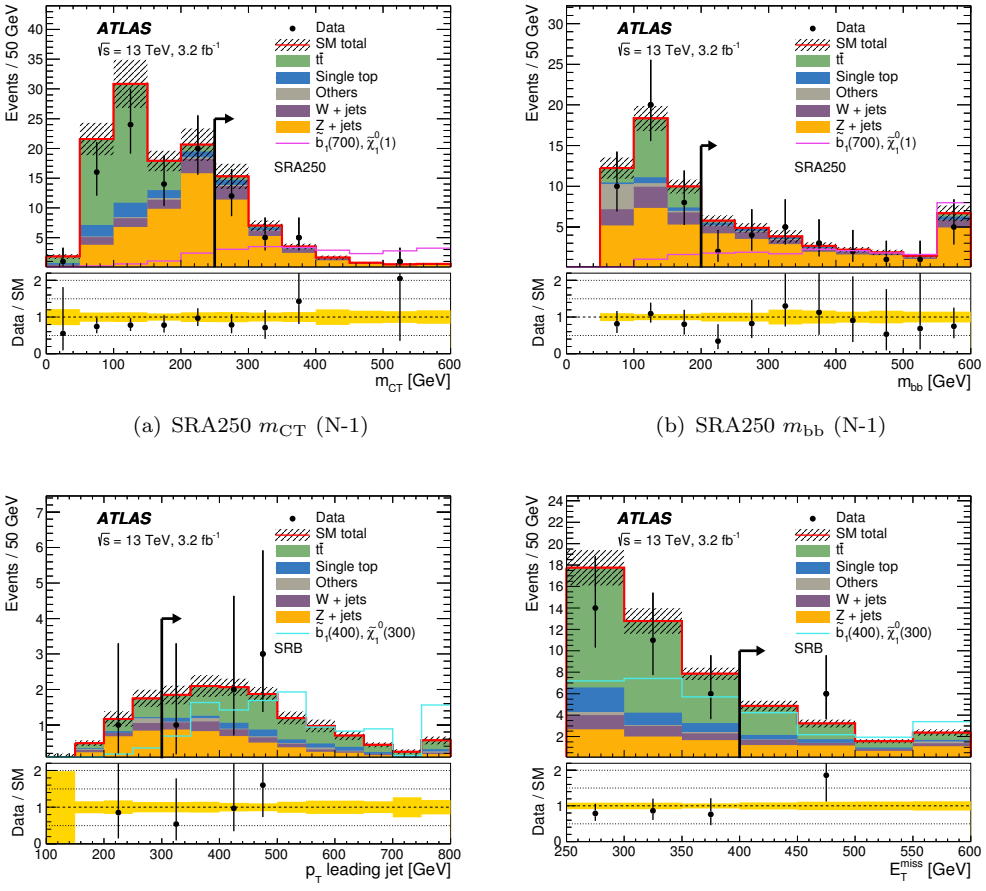

(a) SRA250 m_{CT} (N-1)

(b) SRA250 m_{bb} (N-1)

(c) SRB $p_{\text{T}}(j_1)$ (N-1)

(d) SRB $E_{\text{T}}^{\text{miss}}$ (N-1)

FIGURE 6.14: N-1 distributions of key variables in the SRA and SRB regions. The arrow on the plot denotes where the SR selection is applied.

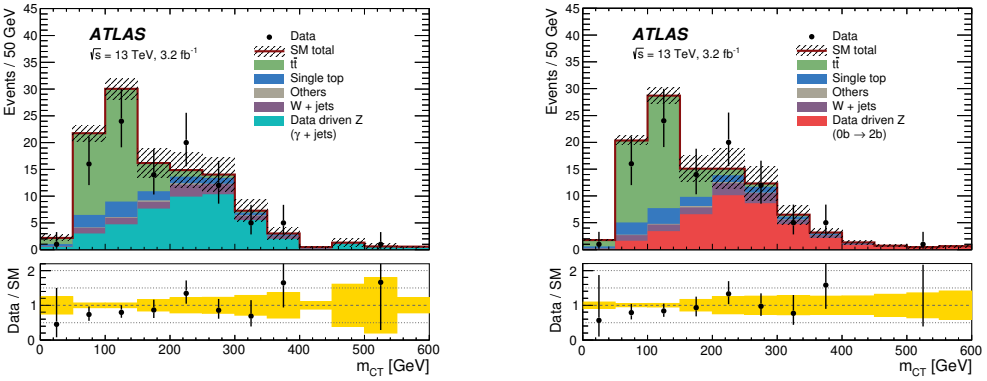

(a) Z+jets estimated using "γ+jets replacement" method

(b) Z estimated using "Z from light" method

FIGURE 6.15: N-1 distributions of the m_{CT} distribution in SRA250, with the Z+jets background estimated using the data-driven methods.

6.3 Sbottom 2016 Analysis

Limits produced using the $3.2\,\mathrm{fb}^{-1}$ collected by ATLAS during 2015 operations provided a significant increase on the exclusion in the $(\tilde{b},\ \tilde{\chi}_1^0)$ mass plane when compared to the Run 1 analysis. An additional extension to the sensitivity was expected with the data collected in 2016. To exploit this the analysis performed during 2016 carried improvements driven by the increased luminosity.

The following sections contain an overview of the updates to the sbottom analysis performed with the combined 2015 and 2016 data corresponding to a total luminosity of $36.1\,\mathrm{fb}^{-1}$. An overview of the improved SRs is given, with an additional type of SR defined to target the intermediate $\Delta m(\tilde{\chi}_1^{\pm}, \tilde{\chi}_1^0)$ scenarios. The dominant background processes are considered and CRs are defined to estimate the backgrounds in the SRs. An update to the γ+jets replacement method is presented, using a 2-dimensional ratio to more accurately model the differences between the Z and γ processes. Updated VRs are presented, which are tighter than the previous version of the analysis. Finally the results of the background-only, model-dependent and model-independent fits are presented, with limits placed in the $(\tilde{b},\ \tilde{\chi}_1^0)$ mass plane and in a model-independent manner.

The analysis is also sensitive to more complex sbottom decay scenarios. The interpretation of the analysis with regards to these models is presented in Section 7.4.

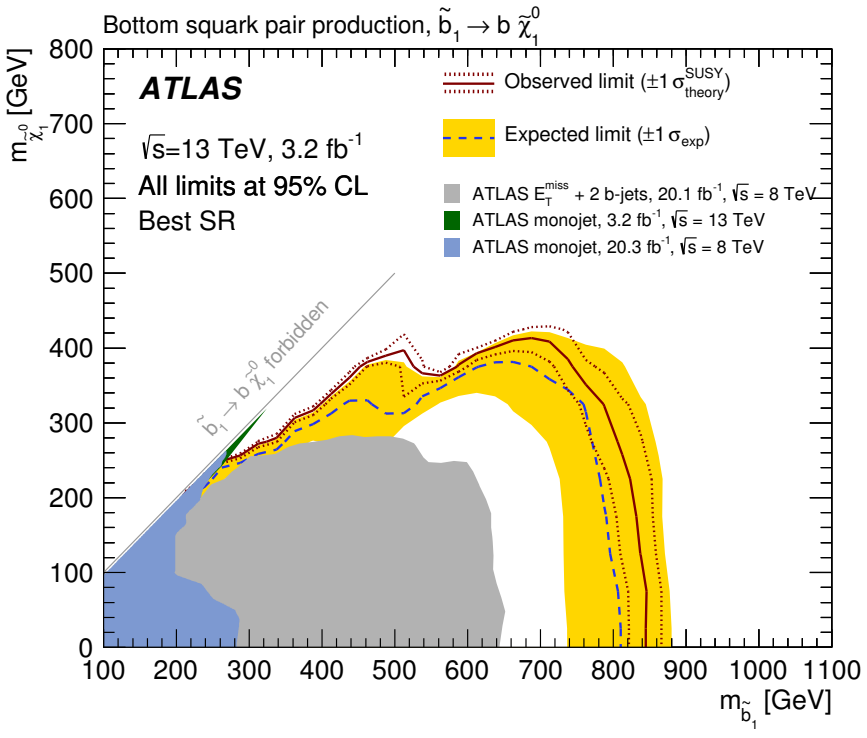

(a) Best expected exclusion contour. Taken from [1]

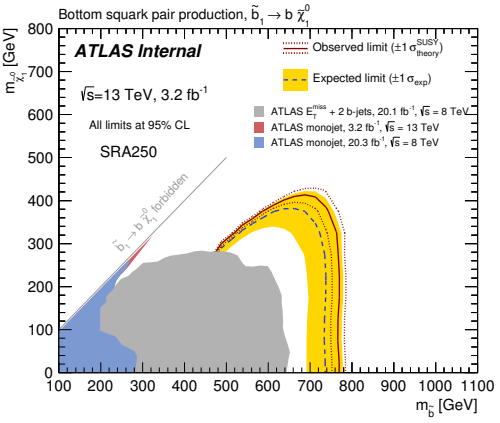

(b) SRA250 exclusion

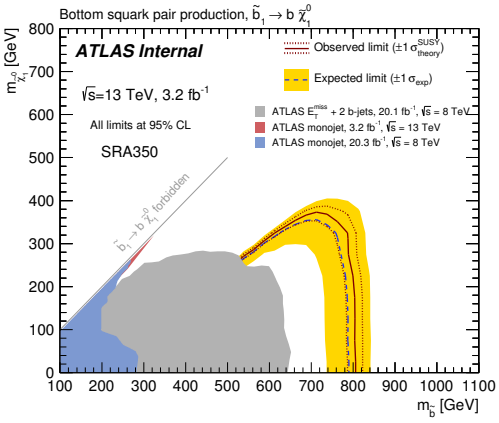

(c) SRA350 exclusion

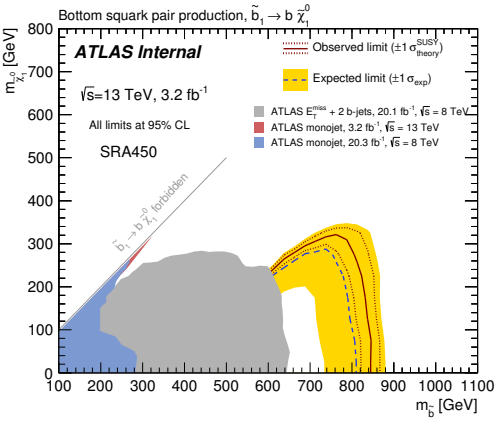

(d) SRA450 exclusion

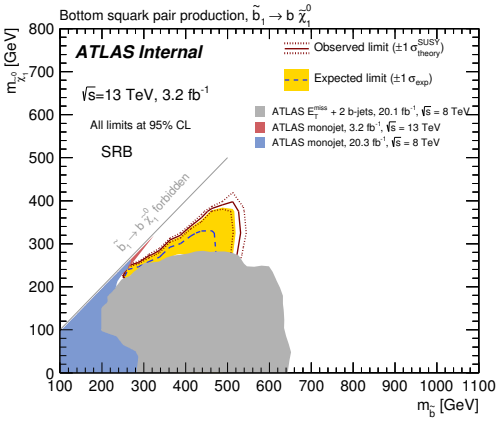

(e) SRB exclusion

FIGURE 6.16: Combined expected and observed exclusion limits at 95% CL in the $(m_{\tilde{b}}, m_{\tilde{\chi}_1^0})$ plane. The dashed black and solid red lines show the 95% CL expected and observed limits respectively, including all uncertainties except the 1σ uncertainty on the signal cross sections, which are represented by the thin red dotted lines. The yellow bands present the experimental uncertainties. The limits from the Run 1 Sbottom analysis [127] are shown for reference.

6.3.1 Signal Region Definitions

Generally the analysis strategy follows closely the 2015 analysis, and as such the preselection applied to the 2015 analysis is still used as the preselection for the 2016 iteration. A set of SRs are defined using m_{CT} as the main discriminating variable defined to target the bulk region of the ($\tilde{b}$, $\tilde{\chi}_1^0$) mass plane, referred to as the A-type regions. The increased luminosity allows for tighter selections to be placed on the m_{CT}, and as such the SRA250 region from the 2015 analysis is dropped, and is replaced with a region requiring $m_{\mathrm{CT}} > 550\,\mathrm{GeV}$. Other than this change, the regions are the same as the 2015 iteration of the analysis. The A-type SR selections are presented in Table 6.21.

Variable	SRA350	SRA450	SRA550
Preselection		✔	
$n_{\text{baseline leptons}}$		0	
Leading two jets (p_{T} ordered) are $b-$tagged		✔	
p_{T} (j_1)		$> 130\,\mathrm{GeV}$	
m_{bb}		$>200\,\mathrm{GeV}$	
$E_{\mathrm{T}}^{\mathrm{miss}}$		$>250\,\mathrm{GeV}$	
m_{CT}	$>350\,\mathrm{GeV}$	$>450\,\mathrm{GeV}$	$>550\,\mathrm{GeV}$

TABLE 6.21: Sbottom 2016 analysis, A-type SR definitions.

As seen previously, the m_{CT} variable is not appropriate to target intermediate and small splitting between the sbottom and neutralino masses. However, an ISR-like selection is also not appropriate to target this region. This can be seen in the best expected exclusion contour in Figure 6.16. For example, if a mass scenario of $(m_{\tilde{b}}, m_{\tilde{\chi}_1^0}) = (550, 350)\,\mathrm{GeV}$ is considered, it can be seen that there is a "bump" in the contour, corresponding to a region where neither the m_{CT}-based or ISR-based analyses are sensitive.

If the kinematics of such a region are considered, then the lack of sensitivity of an m_{CT}-based analysis is understandable due to the expected end-point of the m_{CT} variable. However it is found that the minimum transverse mass between the jets and the $E_{\mathrm{T}}^{\mathrm{miss}}$ ($\min m_{\mathrm{T}}(j, E_{\mathrm{T}}^{\mathrm{miss}})$) provide discrimination in the intermediate region to reject the $t\bar{t}$ background. After a selection on $\min m_{\mathrm{T}}(j, E_{\mathrm{T}}^{\mathrm{miss}})$, the main background is again the Z+jets process. Further consideration of the topology of the signal events suggests that a selection on both $\Delta\phi(b_1, E_{\mathrm{T}}^{\mathrm{miss}})$ and $\Delta\phi(b_2, E_{\mathrm{T}}^{\mathrm{miss}})$ can be used to increase sensitivity. For the signals the angle between the $b-$jets and the $E_{\mathrm{T}}^{\mathrm{miss}}$ would generally be expected to be around $\pi/3$, resulting in a "Mercedes"-like topology, with one of the legs being

constructed of the $E_{\mathrm{T}}^{\mathrm{miss}}$. For the Z+jets background however, the angles would be expected to be around $\pi/2$, as the $b-$jets originate from gluon splitting with gluon being produced back-to-back with the Z boson and leading to a large angular separation between the $E_{\mathrm{T}}^{\mathrm{miss}}$ and the $b-$jets. The region defined based upon the $\min m_{\mathrm{T}}(j, E_{\mathrm{T}}^{\mathrm{miss}})$, $\Delta\phi(b_1, E_{\mathrm{T}}^{\mathrm{miss}})$ and $\Delta\phi(b_2, E_{\mathrm{T}}^{\mathrm{miss}})$ variables is defined as the B-type region. The selections for the B-type SR are presented in Table 6.22. Figure 6.17 (c) and (d) show the discrimination of the $\Delta\phi(b_1, E_{\mathrm{T}}^{\mathrm{miss}})$ and $\min m_{\mathrm{T}}(j, E_{\mathrm{T}}^{\mathrm{miss}})$ variables respectively. It is seen that in this intermediate region a selection of $\min m_{\mathrm{T}}(j, E_{\mathrm{T}}^{\mathrm{miss}}) > 250\,\mathrm{GeV}$ can reduce the $t\bar{t}$ background effectively.

Variable	SRB
Preselection	✔
$n_{\text{baseline leptons}}$	0
p_{T} (j_1), p_{T} (j_2)	$> 50\,\mathrm{GeV}$
m_{jj}	$> 200\,\mathrm{GeV}$
$\Delta\phi(b_1, E_{\mathrm{T}}^{\mathrm{miss}})$	< 2.0
$\Delta\phi(b_2, E_{\mathrm{T}}^{\mathrm{miss}})$	< 2.5
$\min m_{\mathrm{T}}(j, E_{\mathrm{T}}^{\mathrm{miss}})$	$> 250\,\mathrm{GeV}$
$E_{\mathrm{T}}^{\mathrm{miss}}$	$> 250\,\mathrm{GeV}$

TABLE 6.22: Sbottom 2016 analysis, B-type SR definition.

The region designed to target compressed scenarios (referred to as the B-type region in the 2015 analysis) requires an ISR-like selection and is referred to as the C-type region in this analysis. The ISR-like selection is specifically optimised to target smaller mass splitting between the sbottom and neutralino ($\Delta m(\tilde{b}, \tilde{\chi}_1^0) = 20\,\mathrm{GeV}$). The topology of these highly compressed signals contains very soft $b-$jets, and a high p_{T} non-$b-$tagged jet. The p_{T} asymmetry of the leading (non-$b-$tagged) jet and the leading $b-$jet provides excellent discrimination between the signal and backgrounds for this type of selection. A very important difference between the C-type region and the other regions, is that due to the low p_{T} expected from the $b-$jets in the event, the jet p_{T} requirements are lowered to be $p_{\mathrm{T}} > 20\,\mathrm{GeV}$. Lowering the jet p_{T} requirement is found to significantly increase the significance of the selection when targeting the compressed region.

The final important difference for the C-type region, is that the selection on $\min \Delta\phi(j, E_{\mathrm{T}}^{\mathrm{miss}})$ is loosened to > 0.2. Whilst lowering the selection on $\min \Delta\phi(j, E_{\mathrm{T}}^{\mathrm{miss}})$ may allow a significant amount of multi-jet background to be introduced, checks performed using a data driven method to evaluate the multi-jet background suggest a negligible amount

entering the region when applying the full SR selection. The C-type SR selections are presented in Table 6.23. In contrast to the other regions in the analysis, the C-type regions are not required to pass all preselection requirements, where this is the case, the variable with a selection different to the nominal preselection is also presented in the table.

Variable	SRC
Preselection	✔ (unless otherwise stated below)
$n_{\text{baseline leptons}}$	0
n_{jets}	2-5 ($p_{\text{T}} > 20\,\text{GeV}$)
$\min \Delta\phi(j_{1,2}, E_{\text{T}}^{\text{miss}})$	> 0.2
leading jet non-$b-$tagged	✔
sub-leading jet $b-$tagged	✔
p_{T} (j_1)	$> 500\,\text{GeV}$
m_{jj}	$> 200\,\text{GeV}$
m_{eff}	$> 1.3\,\text{TeV}$
$E_{\text{T}}^{\text{miss}}$	$> 500\,\text{GeV}$
$\Delta\phi(j_1 E_{\text{T}}^{\text{miss}})$	> 2.5
$\mathcal{A}$	> 0.8
$H_{\text{T 4}}$	$< 70\,\text{GeV}$

TABLE 6.23: Sbottom 2016 analysis, C-type SR definition. The usage of the $H_{\text{T 4}}$ variable implies the sum for the H_{T} calculation begins with the fourth jet.

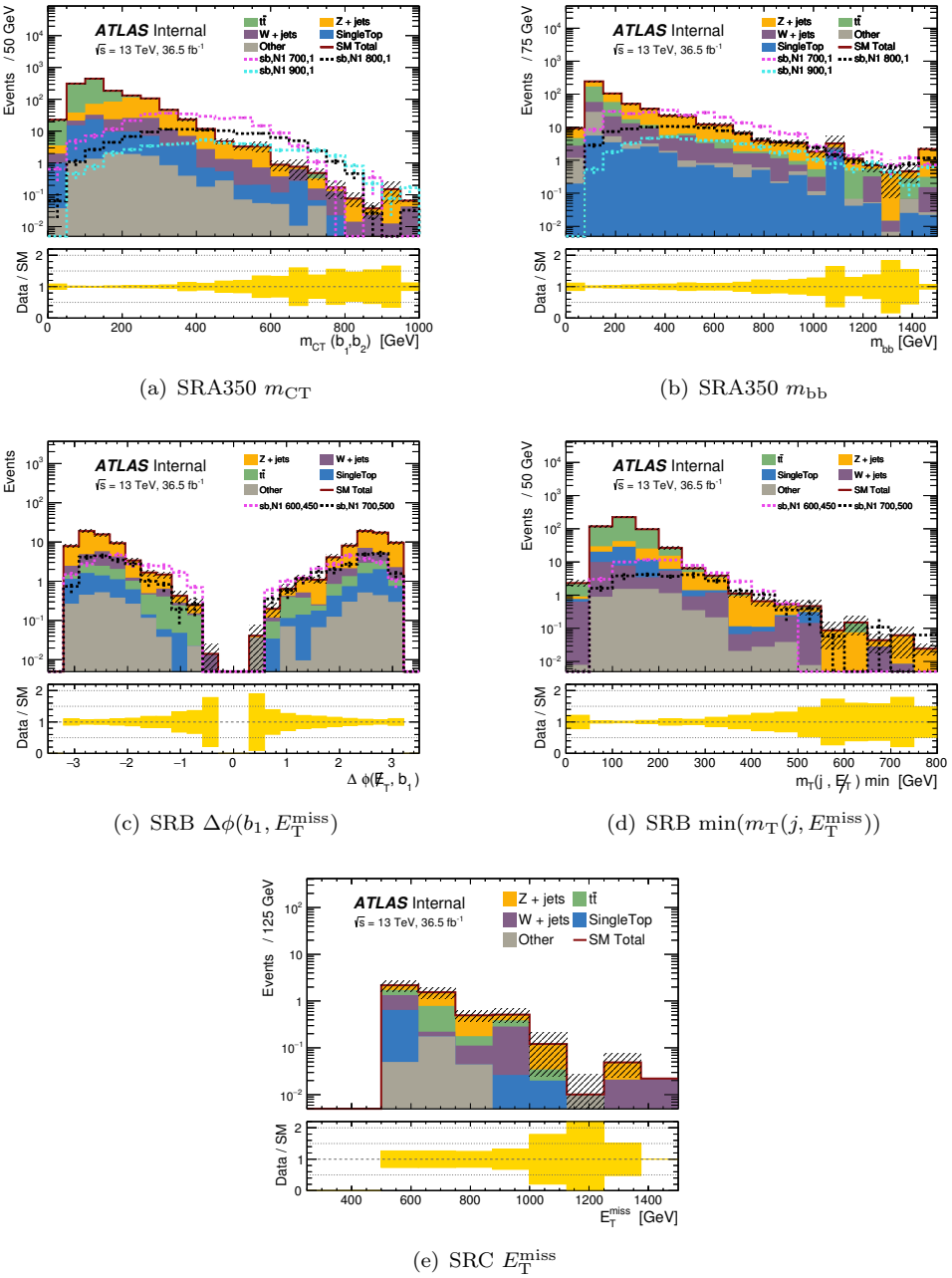

(a) SRA350 m_{CT}

(b) SRA350 m_{bb}

(c) SRB $\Delta\phi(b_1, E_{\mathrm{T}}^{\mathrm{miss}})$

(d) SRB $\min(m_{\mathrm{T}}(j, E_{\mathrm{T}}^{\mathrm{miss}}))$

(e) SRC $E_{\mathrm{T}}^{\mathrm{miss}}$

FIGURE 6.17: Pre-fit N-1 distributions for key variables in the A-, B- and C-type signal regions.

6.3.2 Control Region Definitions

The main SM background process for the A-, B- and C-type SRs is the Z+jets process, with $Z \to \nu\nu$. Due to the similarity of the A-type SRs to the 2015 analysis, the CR strategy is very similar, with CRs defined for the $t\bar{t}$, single-top, Z+jets and W+jets backgrounds using the 2015 regions as a baseline. The additional luminosity provided by the 2016 dataset allows the regions to be tightened to more closely represent the

kinematics in the SRs. Tighter selections are placed on the $E_{\mathrm{T}}^{\mathrm{miss}}$ in the CRttA, CRwA and CRstA regions. The m_{CT} selection is tightened to $> 250\,\mathrm{GeV}$ in all regions. Table 6.24 contains the full selections employed for the A-type CRs.

Variable	CRzA	CRttA	CRwA	CRstA
Preselection	✔	✔	✔ (one $b-$jet)	✔
$n_{\text{signal leptons}}$	2 (SF)	1	1	1
p_{T} (ℓ)	$> 90, 20\,\mathrm{GeV}$	$> 27\,\mathrm{GeV}$	$> 27\,\mathrm{GeV}$	$> 27\,\mathrm{GeV}$
Leading two jets are $b-$tagged	✔	✔	✔ (primary $b-$jet)	✔
$E_{\mathrm{T}}^{\mathrm{miss}}$	$< 100\,\mathrm{GeV}$	$> 200\,\mathrm{GeV}$	$> 200\,\mathrm{GeV}$	$> 200\,\mathrm{GeV}$
$E_{\mathrm{T}}^{\mathrm{miss}\,\prime}$	$> 100\,\mathrm{GeV}$	-	-	-
m_{CT}	$> 250\,\mathrm{GeV}$	$> 250\,\mathrm{GeV}$	$> 250\,\mathrm{GeV}$	$> 250\,\mathrm{GeV}$
p_{T} (j_1)	-	$> 130\,\mathrm{GeV}$	$> 130\,\mathrm{GeV}$	$> 50\,\mathrm{GeV}$
p_{T} (j_2)	-	$> 50\,\mathrm{GeV}$	$> 50\,\mathrm{GeV}$	$> 50\,\mathrm{GeV}$
$m_{\ell\ell}$	[76 - 106] GeV	-	-	-
m_{T}	-	-	$> 30\,\mathrm{GeV}$	-
m_{bb}	$> 200\,\mathrm{GeV}$	$< 200\,\mathrm{GeV}$	$> 200\,\mathrm{GeV}$ $(m_{b,j})$	$> 200\,\mathrm{GeV}$
$m_{b,l}^{\mathrm{min}}$	-	-	-	$> 170\,\mathrm{GeV}$

TABLE 6.24: Sbottom 2016 analysis, A-type CR definitions.

For the B-type regions, three CRs are defined for the Z+jets, $t\bar{t}$ and W+jets backgrounds, presented in Table 6.25. These regions are defined with similar lepton multiplicity selections as the corresponding A-type CR. In all regions, a selection is placed on $\min m_{\mathrm{T}}(j, E_{\mathrm{T}}^{\mathrm{miss}})$, the main discriminating variable in the B-type SR, to ensure the regions are kinematically similar to the SR. In addition to this, in the CRttB and CRwB regions (associated to the $t\bar{t}$ and W+jets processes), the SR selections on $\Delta\phi(b_1, E_{\mathrm{T}}^{\mathrm{miss}})$ and $\Delta\phi(b_2, E_{\mathrm{T}}^{\mathrm{miss}})$ are also used. For the CRwB region events are selected containing one $b-$tagged jet, to ensure a relatively high purity of W+jets events.

Variable	CRttB	CRzB	CRwB
Preselection	✔	✔	✔(one $b-$jet)
$n_{\text{baseline leptons}}$	1	2 (SF)	1
p_{T} (j_1), p_{T} (j_2)	$> 50\,\text{GeV}$	$> 50\,\text{GeV}$	$> 50\,\text{GeV}$
p_{T} (ℓ)	$> 27\,\text{GeV}$	$> 27, 20\,\text{GeV}$	$> 27\,\text{GeV}$
$m_{\ell\ell}$	-	[76-106] GeV	-
$E_{\text{T}}^{\text{miss}}$	$< 100\,\text{GeV}$	$> 100\,\text{GeV}$	$> 100\,\text{GeV}$
$E_{\text{T}}^{\text{miss}\,\prime}$	-	$> 200\,\text{GeV}$	-
m_{T}	-	$> 30\,\text{GeV}$	$> 30\,\text{GeV}$
$\Delta\phi(b_1, E_{\text{T}}^{\text{miss}})$	< 2.0	-	< 2.0
$\Delta\phi(b_2, E_{\text{T}}^{\text{miss}})$	< 2.5	-	< 2.5
$\min m_{\text{T}}(j, E_{\text{T}}^{\text{miss}})$	$> 200\,\text{GeV}$	$> 200\,\text{GeV}$	$> 250\,\text{GeV}$

TABLE 6.25: Sbottom 2016 analysis, B-type CR definitions.

The background strategy of the C-type SR is similar to that of the B-type strategy, with CRs defined for the $t\bar{t}$, W+jets and Z+jets backgrounds. Selections are employed on the leading jet p_{T}, jet asymmetry and $\Delta\phi(j_1, E_{\text{T}}^{\text{miss}})$ to ensure similar kinematics to the SR. As for all the previously defined CRs targeting the W+jets process, the CRwC selects events containing exclusively 1 $b-$tagged jet. Table 6.26 contains the full CR selections for the C-type regions. A slightly adjusted preselection is required to be passed, with the jet multiplicity calculated with $p_{\text{T}} > 20\,\text{GeV}$ jets and $\min\Delta\phi(j, E_{\text{T}}^{\text{miss}})$ selections differing to the usual preselection.

Variable	CRttC	CRzC	CRwC
Preselection (unless otherwise stated below)	✔	✔	✔(one $b-$jet)
n_{jets} ($p_{\text{T}} > 20\,\text{GeV}$)	2-5	2-5	2-5
$n_{\text{baseline leptons}}$	1	2 (SF)	1
p_{T} (j_1)	$> 500\,\text{GeV}$	$> 250\,\text{GeV}$	$> 500\,\text{GeV}$
leading jet non-$b-$tagged	✔	✔	✔
secondary jet $b-$tagged	✔	✔	✔
p_{T} (ℓ)	$> 27\,\text{GeV}$	$> 27, 20\,\text{GeV}$	$> 27\,\text{GeV}$
$m_{\ell\ell}$	-	[76-106] GeV	-
$E_{\text{T}}^{\text{miss}}$	$< 100\,\text{GeV}$	$> 100\,\text{GeV}$	$> 100\,\text{GeV}$
$E_{\text{T}}^{\text{miss}\,\prime}$	-	$> 200\,\text{GeV}$	-
m_{jj}	$> 200\,\text{GeV}$	$> 200\,\text{GeV}$	$> 200\,\text{GeV}$
m_{T}	$> 30\,\text{GeV}$	-	[30-120] GeV
$H_{\text{T 4}}$	$< 70\,\text{GeV}$	$< 70\,\text{GeV}$	$< 70\,\text{GeV}$
$\mathcal{A}$	> 0.5	> 0.5	> 0.8
$\Delta\phi(j_1, E_{\text{T}}^{\text{miss}})$	> 2.5	> 2.5	> 2.5
$\min \Delta\phi(j_{1,2}, E_{\text{T}}^{\text{miss}})$	> 0.2	> 0.2	> 0.2

TABLE 6.26: Sbottom 2016 analysis, C-type CR definitions.

6.3.3 Data-driven γ replacement method

The γ+jets replacement method implemented in the 2015 analysis for the prediction of the Z+jets background in the SRs was extremely useful to provide confidence in the nominal Z+jets prediction using the background-only fit procedure. As such it is also implemented in the 2016 analysis to provide an alternative estimate for the Z+jets backgrounds. The "Z from light" method is also implemented for the A-type SRs, however there are no significant changes to the method from the 2015 analysis, other than the increase in statistics from the additional luminosity.

The main improvement in the γ+jets replacement method arises from the use of a 2-dimensional (2D) reweighting factor, when compared to Equation 6.3. The 2D reweighting is performed using truth-level information for Z and γ for both p_{T} and η. The reweighting factor is given by:

$$R(V)dp_{\text{T}}(V)d\eta(V) = \frac{f_{\text{SR}}^{Z\to\nu\nu}dp_{\text{T}}(Z^{\text{truth}})d\eta(Z^{\text{truth}})}{f_{\text{CR}\gamma}^{\gamma+bb}dp_{\text{T}}(\gamma^{\text{truth}})d\eta(\gamma^{\text{truth}})}. \tag{6.13}$$

This requires the explicit introduction of the acceptance and efficiency for the γ into the final calculation of the number of expected events:

$$N_{\mathrm{SR}}^{Z\to\nu\nu} = \int_{x}^{\infty} (f_{\mathrm{CR}\gamma}^{\mathrm{data}} - f_{\mathrm{CR}\gamma}^{\mathrm{non}\gamma-\mathrm{MC}}) \cdot \frac{1}{\kappa} \cdot R(V) \cdot \epsilon(p_{\mathrm{T}}, \eta) \cdot A_{\mathrm{in}}(p_{\mathrm{T}}, \eta) \cdot A_{\mathrm{out}}(p_{\mathrm{T}}, \eta) dp_{\mathrm{T}}(V) dm_{\mathrm{CT}}. \tag{6.14}$$

These updates to the γ+jets data driven method aim to further take into account the differences between the γ+jets and Z+jets process. This leads to a more valid extrapolation from the γ+jets process to the Z+jets process.

Consistency between the predicted SR yields of Z+jets using the background-only method and the γ+jets method provides further confidence in the modelling of the dominant Z+jets background in the analysis. The results of the background-only fit procedure and the two data-driven methods are presented in Tables 6.32, 6.35 and 6.38. The nominal background-only prediction is found to be consistent with the data-driven methods providing additional confidence in the modelling of the Z+jets background in each region.

6.3.4 Validation Regions

Zero lepton VRs are defined associated with either the A-, B- or C-type SRs. Due to the introduction of a SR targeting the intermediate region which is not explicitly required to be orthogonal to the A-type SRs (and vice-versa), additional care must be taken to ensure that the VR associated with the B-type SR is not overlapping with any of the A-type SRs. A similar situation occurs when attempting to define B-type VRs to ensure that the region does not overlap with SRC, as there is no specific requirement ensuring orthogonality between these regions either.

Due to this difficulty the VR cannot be defined by simply reversing a selection on the key kinematic variables in a given region, and instead must be made to model the SR kinematics.

Table 6.27 presents the full selections applied to define each validation region. The SRs are also presented to allow for easier cross-referencing of the orthogonality of the regions.

Two VRs are defined associated with the SRA regions. Primarily these regions are defined by inverting either the m_{CT} or m_{bb} selections, and introducing a lower bound on each variable. For the VRmctA region a window in m_{CT} is chosen of [150, 250] GeV to allow for relatively similar kinematics to the SR, but to minimise possible signal contamination. For the VRmbbA region, a window in m_{bb} is used of [100, 200] GeV,

which again attempts to closely model the SR kinematics. Finally to ensure othogonality with the B-type SRs, a selection on $\min m_{\mathrm{T}}(j, E_{\mathrm{T}}^{\mathrm{miss}}) < 250\,\mathrm{GeV}$ is applied.

There are two VRs defined associated with the B-type SR, using windows in $\min m_{\mathrm{T}}(j, E_{\mathrm{T}}^{\mathrm{miss}})$ to create VRs enhanced in either Z+jets or $t\bar{t}$, to validate the modelling of these two processes. The VRzB is defined with a selection on $\min m_{\mathrm{T}}(j, E_{\mathrm{T}}^{\mathrm{miss}})$ between 200 and 250 GeV. The selections on the angular separation between the $b-$jets and $E_{\mathrm{T}}^{\mathrm{miss}}$ are dropped in this case to enhance the Z+jets contribution in the region. The VRttB is defined with a window of [150, 200] in $\min m_{\mathrm{T}}(j, E_{\mathrm{T}}^{\mathrm{miss}})$ to enhance the $t\bar{t}$ background. To avoid any overlap with the A-type SRs, an additional selection of $m_{\mathrm{CT}} < 250\,\mathrm{GeV}$ is employed. Further to this, orthogonality with the SRC region is ensured by using a selection on the p_{T} asymmetry, with both VRs requiring $\mathcal{A} < 0.8$.

Finally, a single VR associated with the SRC region is employed to validate the modelling of the $t\bar{t}$ background. The region is defined by inverting the SR selection on the p_{T} asymmetry and introducing a lower bound, such that $0.6 < A < 0.8$. A selection is placed of $m_{\mathrm{CT}} < 250\,\mathrm{GeV}$ to further enhance the $t\bar{t}$ contribution in the region. To ensure orthogonality with the B-type SRs, a selection of $\min m_{\mathrm{T}}(j, E_{\mathrm{T}}^{\mathrm{miss}}) < 250\,\mathrm{GeV}$ is also required.

		A			B			C	
Variable	Units	SRAx	VRmctA	VRmbbA	SRB	VRzB	VRttB	SRC	VRttC
$N_{\mathrm{jets}}(p_T > 35)$			2-4			2-4			-
$N_{\mathrm{jets}}(p_T > 20)$			-			-			$2-5$
Leading jet p_{T}	[GeV]		> 130			> 50			> 500
Sub-leading jetp_{T}	[GeV]		> 50			> 50			> 20
4th jet veto	[GeV]		< 50			-			-
$H_{T;4:5}$	[GeV]		-			-			< 70
$N_{\text{b-jets}}$			2			2			2
Leading jet b-tagged			✓			-			✗
Sub-leading jet b-tagged			✓			-			✓
$E_{\mathrm{T}}^{\mathrm{miss}}$	[GeV]		> 250			> 250			> 500
m_{eff}	[TeV]		-			-			> 1.3
m_{jj}	[GeV]		> 200	$[100, 200]$		-			> 200
m_{CT}	[GeV]	>x	$[150, 250]$	> 250	-	< 250	< 250	-	< 250
$\min[m_{\mathrm{T}}(\mathrm{jet}_{1-4}, E_{\mathrm{T}}^{\mathrm{miss}})]$	[GeV]	-	<250		> 250	$[200,250]$	$[150, 200]$	-	<250
$\Delta\phi(b_1, E_{\mathrm{T}}^{\mathrm{miss}})$			-		< 2.0	-	< 2.0		-
$\Delta\phi(b_2, E_{\mathrm{T}}^{\mathrm{miss}})$			-		< 2.5	-	< 2.5		-
$\Delta\phi(j_1, E_{\mathrm{T}}^{\mathrm{miss}})$			-			-			> 2.5
$\mathcal{A}$			-		-	< 0.8	< 0.8	> 0.8	$[0.6,0.8]$
$E_{\mathrm{T}}^{\mathrm{miss}}/m_{\mathrm{eff}}$			> 0.25			-			-
$\min \Delta\phi(j, E_{\mathrm{T}}^{\mathrm{miss}})$			> 0.4			> 0.4			-
$\min \Delta\phi(j_{1,2}, E_{\mathrm{T}}^{\mathrm{miss}})$			-			-			> 0.2

TABLE 6.27: Overview of the sbottom 2016 VR and SR definitions for each type of SR. In the first column, SRAx refers to the m_{CT} selection used for the 3 A-type SRs (either 350, 450, or 550 GeV).

6.3.5 Systematic Uncertainties

The detector uncertainties that are considered for the 2016 iteration of the analysis are the same as those that were taken into account in the 2015 version. The modelling uncertainties considered are also consistent with the 2015 version of the analysis, including the methods used to calculate the uncertainty. An extra modelling uncertainty is evaluated to assess the interference between the single-top and $t\bar{t}$ processes as reported in Chapter 4.3.5. The effect of the interference is evaluated comparing the alternative samples generated using MadGraph5+aMC@NLO to the nominal sample in a similar manner to the other single-top uncertainties and contributes between 6-16% depending on the SR under consideration.

A more comprehensive overview of all uncertainties considered in the analysis can be found in Section 6.2.6.

Table 6.28 presents the dominant uncertainties in the analysis, the dominant detector uncertainties are due to the JES, JER and the $b-$tagging uncertainties, as in the 2015 analysis. Compared to the 2015 analysis the detector uncertainties are generally a smaller contribution to the total background systematic uncertainty, due to the experience gathered during the 2015 data-taking. This smaller contribution from the detector systematics causes an increase in the relative contribution of the modelling uncertainties, most noticably the uncertainty from the Z+jets process. Whilst the contribution to the total systematic uncertainty is relatively large (70%), the error on the transfer factor (used to calculate the Z+jets uncertainty) is relatively consistent ($\approx 20\%$) in the 2015 and 2016 analyses, hence the large contribution is not necessarily a cause for concern with regards to the modelling of the Z+jets process.

6.3.6 Background-only fit results

The results of the background-only fit procedure for the A-type CRs, VRs and SRs are presented in Tables 6.30, 6.31 and 6.32. The SR estimates provided by the data-driven methods are also presented for comparison, showing a good agreement between the Z+jets prediction using the nominal fit procedure and the data-driven methods.

Generally there are slight excesses in the SRs, which are correlated due to the overlapping nature of the region definitions. The excesses have a significance of $< 1\sigma$ and as such cannot be considered to be significant, and are covered by the statistical and systematic uncertainties.

Source of uncertainty	SRAs	SRB	SRC
Detector uncertainties			
JES	13 - 19%	30%	19%
JER	4 - 15%	11%	42%
$b-$tagging	14 - 20%	28%	35%
Theory uncertainties			
Z+jets	33 - 73%	72%	44%
W+jets	13 - 25%	25%	30%
Top production	11 - 21%	31%	15%
Total background systematic (% of total background)	14 - 19%	19%	25%

TABLE 6.28: Overview of the dominant detector and modelling uncertainties present in the 2016 sbottom analysis. Due to the similarities between the SRA regions, and the fact that they are defined such that they overlap, a range of values are given for the uncertainties in this region. The size of the total systematic uncertainty (as a % of the background expectation) is also given. As the uncertainties considered may be correlated, the total uncertainty may not simply be the sum in quadrature of the uncertainties.

The normalisation factors for the main backgrounds are shown in Table 6.14. The normalisation of the main backgrounds is consistent with the previous iteration of the analysis. Again the uncertainty on the $\mu_{\text{single-top}}$ normalisation is large, which is caused by the relatively small amount of statistics in the CRstA region, but also by the purity of the region, which (pre-fit) contains relatively similar yields of both single-top and W+jets.

Normalisation	Value
$\mu_{\text{single-top}}$	0.82 ± 0.35
$\mu_{t\bar{t}}$	1.04 ± 0.19
$\mu_{W+\text{jets}}$	1.24 ± 0.15
$\mu_{Z+\text{jets}}$	1.32 ± 0.19

TABLE 6.29: Normalisation factors for the main backgrounds in the A-type SRs, using the background-only fit with $36.1\,\text{fb}^{-1}$.

Tables 6.34 and 6.35 present the results of the background-only fit procedure for the B-type regions, with Table 6.33 displaying the normalisation parameters calculated in the fit. The normalisation for the Z+jets background is large in this region ($\mu_{Z+\text{jets}} = 1.5$). There is confidence in the final predicted number of events in the SR, and hence the large normalisation, due to the alternative data-driven γ+jets method. The value predicted by the nominal fit method and by the data-driven method are consistent to within 0.2σ. As with the A-type SRs, there is a slight excess in the SRB region, at the significance level of $\approx 1\sigma$, however as in the A-type regions this excess is not significant.

A-type CRs	CRzA	CRwA	CRttA	CRstA
Observed events	53	1026	381	118
Fitted bkg events	53.04 ± 7.28	1026.13 ± 32.06	381.04 ± 19.53	117.95 ± 10.79
Fitted $t\bar{t}$ events	0.00 ± 0.00	197.31 ± 62.66	242.86 ± 28.44	17.89 ± 3.86
Fitted single-top events	$0.20^{+0.21}_{-0.20}$	69.37 ± 30.67	25.27 ± 10.58	37.95 ± 15.93
Fitted W+jets events	0.00 ± 0.00	731.73 ± 84.14	96.47 ± 20.71	58.81 ± 11.38
Fitted Z+jets events	51.46 ± 7.29	5.71 ± 1.25	2.59 ± 0.42	1.65 ± 0.25
Fitted $t\bar{t} + V$ events	0.32 ± 0.03	2.53 ± 0.19	1.65 ± 0.26	0.46 ± 0.09
Fitted diboson events	1.05 ± 0.24	19.48 ± 3.68	12.20 ± 1.33	1.19 ± 0.52
MC exp. SM events	40.60	889.77	358.59	113.65
MC exp. $t\bar{t}$ events	0.00	189.67	234.31	17.22
MC exp. single-top events	0.25	84.35	30.79	46.16
MC exp. W+jets events	0.00	589.40	77.67	47.37
MC exp. Z+jets events	38.97	4.32	1.96	1.25
MC exp. $t\bar{t} + V$ events	0.32	2.53	1.65	0.46
MC exp. diboson events	1.05	19.50	12.20	1.20

TABLE 6.30: Background-only fit results for the A-type CRs of the sbottom 2016 analysis with an integrated luminosity of $36.1\,\text{fb}^{-1}$. The uncertainties shown contain both systematic and statistical uncertainties.

A-Type VRs	VRmbbA	VRmctA
Observed events	142	257
Fitted bkg events	138.93 ± 22.11	271.87 ± 42.66
Fitted $t\bar{t}$ events	53.60 ± 16.27	77.27 ± 29.75
Fitted single-top events	4.57 ± 2.54	12.73 ± 9.46
Fitted W+jets events	17.82 ± 3.94	29.03 ± 6.70
Fitted Z+jets events	60.13 ± 13.41	148.48 ± 29.09
Fitted $t\bar{t} + V$ events	1.09 ± 0.13	2.01 ± 0.19
Fitted diboson events	1.73 ± 0.67	2.33 ± 0.76
MC exp. SM events	119.87	229.92
MC exp. $t\bar{t}$ events	51.62	74.26
MC exp. single-top events	5.57	15.49
MC exp. W+jets events	14.33	23.36
MC exp. Z+jets events	45.53	112.47
MC exp. $t\bar{t} + V$ events	1.09	2.01
MC exp. diboson events	1.72	2.34

TABLE 6.31: Background-only fit results for the A-type VRs of the sbottom 2016 analysis with an integrated luminosity of $36.1\,\text{fb}^{-1}$. The uncertainties shown contain both systematic and statistical uncertainties.

A-type SRs	SRA350	SRA450	SRA550
Observed events	81	24	10
Fitted bkg events	69.42 ± 11.93	20.00 ± 2.81	7.35 ± 1.37
Fitted $t\bar{t}$ events	2.05 ± 0.66	0.55 ± 0.20	0.19 ± 0.08
Fitted single-top events	2.99 ± 1.79	0.94 ± 0.68	0.49 ± 0.27
Fitted W+jets events	15.14 ± 3.56	5.18 ± 1.17	2.43 ± 0.68
Fitted Z+jets events	47.31 ± 11.42	12.71 ± 2.33	3.98 ± 1.04
Z+jets using "γ+jets" method	43.12 ± 4.13	13.29 ± 2.35	3.13 ± 1.11
Z+jets using "Z from light" method	50.46 ± 9.47	14.48 ± 3.64	4.28 ± 1.42
Fitted $t\bar{t} + V$ events	0.51 ± 0.08	0.22 ± 0.05	0.07 ± 0.02
Fitted diboson events	1.41 ± 0.54	0.40 ± 0.18	0.19 ± 0.16
MC exp. SM events	55.58	16.08	6.01
MC exp. $t\bar{t}$ events	1.98	0.53	0.19
MC exp. single-top events	3.64	1.14	0.60
MC exp. W+jets events	12.21	4.17	1.95
MC exp. Z+jets events	35.84	9.63	3.01
MC exp. $t\bar{t} + V$ events	0.51	0.22	0.07
MC exp. diboson events	1.41	0.40	0.19

TABLE 6.32: Background-only fit results for the A-type SRs with 36.1 fb^{-1}. The uncertainties shown contain both the statistical and systematic uncertainties.

Normalisation	Value
$\mu_{t\bar{t}}$	1.32 ± 0.19
$\mu_{W+\text{jets}}$	1.40 ± 0.12
$\mu_{Z+\text{jets}}$	1.50 ± 0.07

TABLE 6.33: Normalisation factors for the main backgrounds in the B-type SRs, using the background-only fit with 36.1 fb^{-1}.

The results of the background-only fit for the C-type regions are presented in Tables 6.37 and 6.38, with the associated normalisation parameters presented in Table 6.36. The observed and fitted number of events agree well in the SRC region. The normalisation for the $t\bar{t}$ background ($\mu_{t\bar{t}}$) is shifted down when compared to the A- and B-type regions, which had normalisation parameters of ≈ 1.0. This behaviour is expected in the C-type regions due to the ISR-like selection and the known behaviour of the nominal MC used to model $t\bar{t}$ when considering a selection requiring large values of m_{eff}.

Figure 6.18 presents distributions of key variables in the SRA, SRB and SRC regions. The observed data and post-fit background expectation is generally in agreement for the variables considered.

6.3.7 Interpretation of results

The slight discrepancies between the observed and expected number of events in the SRAs and the SRB are not significant and are well within the uncertainties. Limits on the cross section of a generic BSM process are placed using the model-independent fit procedure, the results of which are presented in Table 6.39 which contains the observed and expected 95% CL limits on the number of additional BSM events, corresponding to a visible cross section upper limit.

Exclusion limits are placed in the sbottom-neutralino mass plane, assuming the sbottom decay proceeding via $\tilde{b} \to b + \tilde{\chi}_1^0$ with a BR = 100% using the model-dependent fit procedure. The exclusion contours produced for each individual SR are shown in Figure 6.19. The exclusion contour produced using the best expected SR is shown in Figure 6.20. The A-type SRs targeting the bulk region of the mass plane provide exclusion approaching 1 TeV, in sbottom mass for massless neutralinos. The B-type SR provides exclusion in the intermediate region between the compressed and bulk regions of the phase space, whilst the C-type SR provides exclusion close to the kinematic diagonal of the $\tilde{b} \to b + \tilde{\chi}_1^0$ decay. The inclusion of the region targeting the intermediate mass region provides additional exclusion when comparing the limits to the 2015 analysis, where there was a noticable "bump" between the ISR-like and bulk selections. The general

B-type CRs	CRzB	CRwB	CRttB
Observed events	516	737	232
Fitted bkg events	516.09 ± 22.72	736.77 ± 27.13	232.05 ± 15.21
Fitted $t\bar{t}$ events	7.16 ± 2.21	162.31 ± 33.05	173.34 ± 18.85
Fitted single-top events	3.12 ± 0.87	45.99 ± 3.75	18.90 ± 4.56
Fitted W+jets events	0.00 ± 0.00	508.90 ± 41.92	36.00 ± 6.58
Fitted Z+jets events	479.57 ± 23.05	5.30 ± 0.74	0.37 ± 0.22
Fitted $t\bar{t} + V$ events	5.09 ± 0.43	2.53 ± 0.17	2.43 ± 0.26
Fitted diboson events	21.15 ± 2.10	11.74 ± 1.88	1.01 ± 0.14
MC exp. SM events	354.92	548.85	179.55
MC exp. $t\bar{t}$ events	5.42	123.03	131.36
MC exp. single-top events	3.11	45.98	18.88
MC exp. W+jets events	0.00	362.06	25.62
MC exp. Z+jets events	320.17	3.54	0.25
MC exp. $t\bar{t} + V$ events	5.09	2.52	2.43
MC exp. diboson events	21.14	11.72	1.01

TABLE 6.34: Background-only fit results for the B-type control regions, with an integrated luminosity of 36.1 fb^{-1}. The errors shown contain both the systematic and statistical uncertainty.

B-type VRs & SR	VRzB	VRttB	SRB
Observed events	924	184	45
Fitted bkg events	955.52 ± 165.98	189.29 ± 51.40	35.79 ± 6.92
Fitted $t\bar{t}$ events	240.97 ± 108.93	113.53 ± 50.02	5.19 ± 2.53
Fitted single-top events	32.68 ± 3.94	9.12 ± 1.51	1.47 ± 0.57
Fitted W+jets events	162.58 ± 46.41	22.01 ± 5.61	6.42 ± 2.08
Fitted Z+jets events	488.87 ± 121.84	42.05 ± 10.37	21.36 ± 5.37
Z+jets events using "γ+jets" method	-	-	19.92 ± 2.78
Fitted $t\bar{t} + V$ events	10.29 ± 0.83	1.06 ± 0.18	0.59 ± 0.21
Fitted diboson events	20.14 ± 3.14	1.52 ± 0.29	0.76 ± 0.22
MC exp. SM events	687.55	141.43	25.59
MC exp. $t\bar{t}$ events	182.45	85.99	3.93
MC exp. single-top events	32.67	9.12	1.48
MC exp. W+jets events	115.68	15.65	4.57
MC exp. Z+jets events	326.35	28.08	14.26
MC exp. $t\bar{t} + V$ events	10.29	1.06	0.59
MC exp. diboson events	20.11	1.52	0.76

TABLE 6.35: Background-only fit results for the B-type validation and signal regions, corresponding to an integrated luminosity of $36.1\,\text{fb}^{-1}$. The errors shown contain both the systematic and statistical uncertainty.

Normalisation	Value
$\mu_{t\bar{t}}$	0.72 ± 0.17
$\mu_{W+\text{jets}}$	1.11 ± 0.19
$\mu_{Z+\text{jets}}$	1.12 ± 0.18

TABLE 6.36: Normalisation factors for the main backgrounds in the C-type regions, using the background-only fit with $36.1\,\text{fb}^{-1}$.

1σ discrepancy in the A- and B-type regions is noticable when comparing the observed to the expected limits, however this discrepancy is well within the expected systematic uncertainties.

C-type CRs	CRzC	CRwC	CRttC
Observed events	54	132	43
Fitted bkg events	53.98 ± 7.34	131.96 ± 11.47	43.03 ± 6.55
Fitted $t\bar{t}$ events	5.89 ± 1.74	30.49 ± 7.90	31.06 ± 7.15
Fitted single-top events	0.00 ± 0.00	12.88 ± 1.29	5.78 ± 0.50
Fitted W+jets events	0.00 ± 0.00	86.39 ± 14.64	5.31 ± 1.28
Fitted Z+jets events	46.59 ± 7.55	0.00 ± 0.00	0.15 ± 0.07
Fitted $t\bar{t} + V$ events	0.17 ± 0.04	0.08 ± 0.03	0.25 ± 0.05
Fitted diboson events	1.33 ± 0.16	2.12 ± 1.41	0.47 ± 0.43
MC exp. SM events	51.20	135.62	54.71
MC exp. $t\bar{t}$ events	8.21	42.49	43.27
MC exp. single-top events	0.00	12.89	5.78
MC exp. W+jets events	0.00	78.05	4.80
MC exp. Z+jets events	41.49	0.00	0.13
MC exp. $t\bar{t} + V$ events	0.17	0.08	0.25
MC exp. diboson events	1.33	2.12	0.48

TABLE 6.37: Background only fit results for the control regions associated with the SRC region. All uncertainties include both statistical and systematic uncertainty.

C-type VR & SR	VRttC	SRC
Observed events	37	7
Fitted bkg events	31.71 ± 4.40	6.29 ± 1.54
Fitted $t\bar{t}$ events	15.64 ± 3.88	0.95 ± 0.36
Fitted single-top events	2.81 ± 0.38	0.80 ± 0.21
Fitted W+jets events	5.61 ± 1.74	1.61 ± 0.88
Fitted Z+jets events	6.66 ± 1.33	2.42 ± 0.86
Z+jets events using "γ+jets" method	-	2.16 ± 0.97
Fitted $t\bar{t} + V$ events	0.17 ± 0.03	0.07 ± 0.02
Fitted diboson events	0.81 ± 0.39	0.43 ± 0.18
MC exp. SM events	36.60	6.24
MC exp. $t\bar{t}$ events	21.80	1.32
MC exp. single-top events	2.81	0.80
MC exp. W+jets events	5.07	1.46
MC exp. Z+jets events	5.93	2.16
MC exp. $t\bar{t} + V$ events	0.17	0.07
MC exp. diboson events	0.81	0.43

TABLE 6.38: Background only fit results for the VR and SR associated with the SRC region. All uncertainties include both statistical and systematic uncertainty.

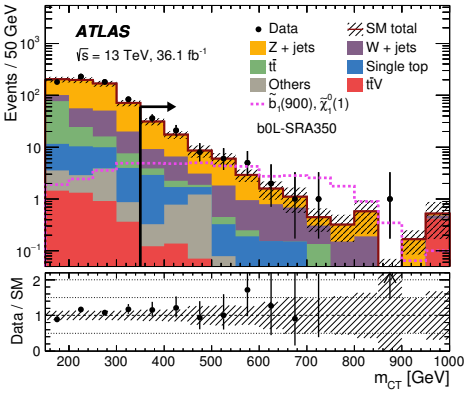

(a) SRA350 m_{CT} (N-1)

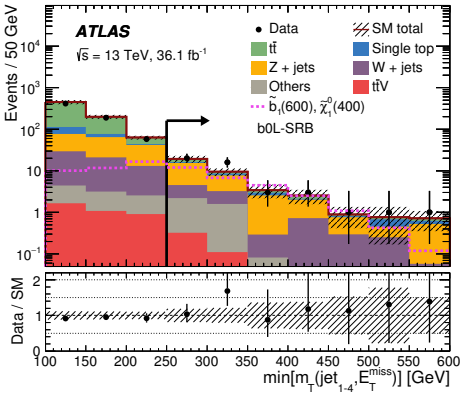

(b) SRB $\min m_{\mathrm{T}}(j, E_{\mathrm{T}}^{\mathrm{miss}})$ (N-1)

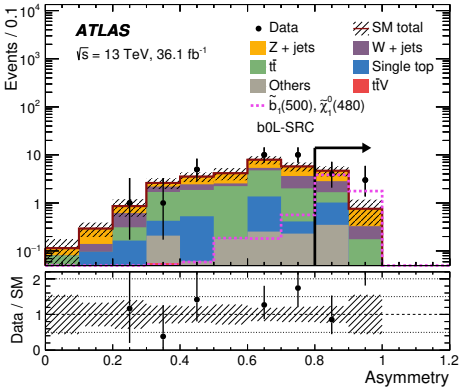

(c) SRC $\mathcal{A}$ (N-1)

FIGURE 6.18: N-1 distributions of key variables in the SRA, SRB and SRC regions. The arrow on the plot denotes where the SR selection is applied. The error bars include both statistical and systematic uncertainties.

Signal Region	σ_{vis} [fb]	S_{obs}^{95}	S_{exp}^{95}
SRA350	1.06	38.2	$30.9^{+11.3}_{-8.4}$
SRA450	0.43	15.6	$13.9^{+5.6}_{-3.8}$
SRA550	0.3	10.7	$7.8^{+3.7}_{-1.6}$
SRB	0.72	26.1	$19.9^{+8.3}_{-5.4}$
SRC	0.24	8.7	$6.8^{+3.3}_{-1.3}$

TABLE 6.39: 95% CL upper limits on the visible cross section of a generic BSM process (σ_{vis}), the number of expected signal events (S_{obs}^{95}) and the limit on the number of expected signal events, taking into account the expected number of background events (S_{exp}^{95}).

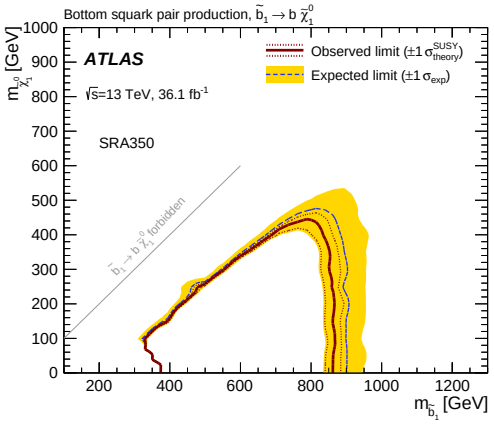

(a) SRA350

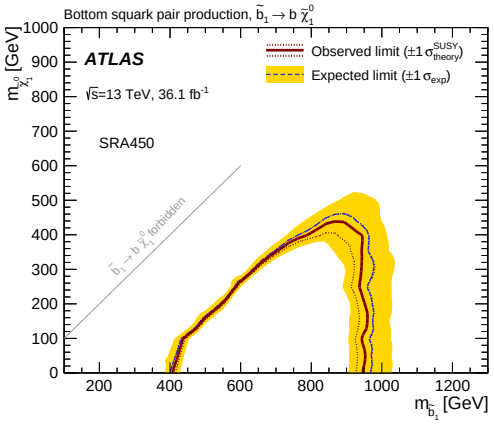

(b) SRA450

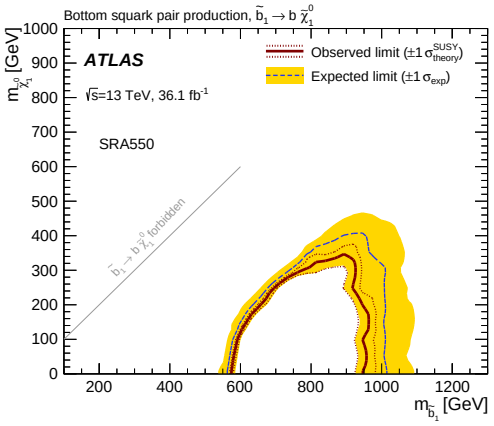

(c) SRA550

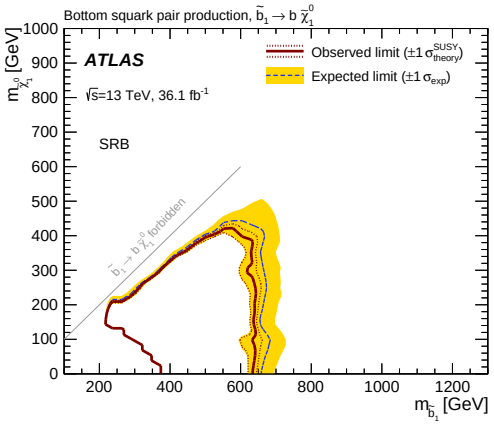

(d) SRB

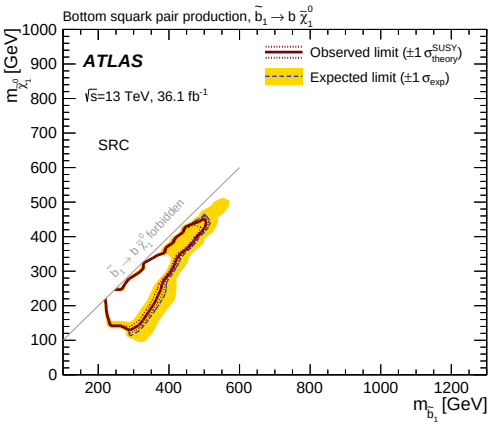

(e) SRC

FIGURE 6.19: Combined expected and observed exclusion limits at 95% CL in the $(m_{\tilde{b}}, m_{\tilde{\chi}_1^0})$ plane. The dashed black and solid red lines show the 95% CL expected and observed limits respectively, including all uncertainties except the 1σ uncertainty on the signal cross sections. The yellow bands present the experimental uncertainties.

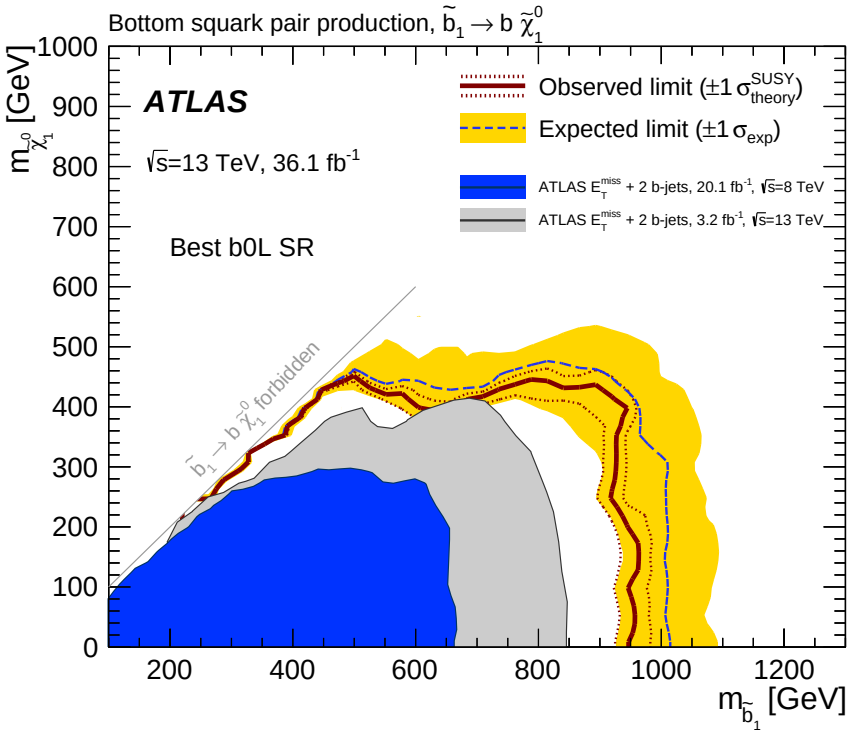

FIGURE 6.20: Combined expected and observed exclusion limits at 95% CL in the $(m_{\tilde{b}}, m_{\tilde{\chi}_1^0})$ plane. The dashed black and solid red lines show the 95% CL expected and observed limits respectively, including all uncertainties except the 1σ uncertainty on the signal cross sections, which are represented by the thin red dotted lines. The signal region providing the best expected exclusion is chosen to produce the final limit contour.

6.4 Conclusions

Presented in this chapter are the most recent results for the search for direct sbottom pair production using the ATLAS detector. The initial search using the 2015 dataset corresponding to a luminosity of $3.2\,\text{fb}^{-1}$ provided world leading limits on sbottom pair production, decaying via the $\tilde{b} \to b + \tilde{\chi}_1^0$ decay mode, when the results were published. This greatly increased the limits when compared to the Run 1 analysis. For massless neutralinos sbottom masses of up to 840 GeV are excluded at the 95% CL. This analysis was heavily based upon the original Run 1 analysis, and was primarily performed to take advantage of the increase in E_{CMS} when moving from Run 1 to Run 2, to use the small luminosity to attempt to discover the sbottom assuming a mass scenario which was just beyond the Run 1 limits.

The search performed utilising the full 2015+2016 dataset comprising of a total luminosity of $36.1\,\text{fb}^{-1}$ further extended these limits by generally improving the analysis strategy, background modelling, and taking advantage of the increased luminosity during 2016 operations. In the bulk region of phase space sbottom masses of up to 950 GeV are excluded for massless neutralinos, up to neutralino masses of 400 GeV. The inclusion of a dedicated SR to target the intermediate region of the phase space, where neither an ISR-like or an m_{CT}-based search are appropriate provides a bridge between the two analysis and resolves the "bump" feature present in the 2015 limits. Finally the lower p_{T} threshold applied to the jets in the ISR-like region allows for signals very close to the kinematic diagonal to be targeted.

Chapter 7

Searches for third generation squarks in the $tb + E_{\mathrm{T}}^{\mathrm{miss}}$ final state

This chapter presents an overview of the searches performed in final state events characterised by the presence of a top quark, a bottom quark and $E_{\mathrm{T}}^{\mathrm{miss}}$ (referred to as the $tb + E_{\mathrm{T}}^{\mathrm{miss}}$ final state) using both Run 1 and Run 2 data with the ATLAS detector. The top quark in the event is considered to decay leptonically. The analysis was originally performed at the end of Run 1, using $20\,\mathrm{fb}^{-1}$ of data collected by ATLAS at $\sqrt{s} = 8\,\mathrm{TeV}$. The aim of the analysis was to target more "complex" decay scenarios than the simplified model cases previously considered. Specifically, the analysis targeted the so-called "mixed" decay scenario, where the pair produced squarks may decay via different decay modes. The mixed-decay scenario was an uncovered signature in Run 1 and this analysis was designed to fully exploit the Run 1 dataset. During Run 2 the $tb + E_{\mathrm{T}}^{\mathrm{miss}}$ analysis was performed using the Run 1 analysis as a baseline but with reoptimised SRs and an updated analysis strategy to more suitably reflect the dominant backgrounds in the signal regions.

The chapter contains three components. The first component, "Analysis Motivation", contains an overview of the signal phenomenology used to guide the design of the signal regions, for both the Run 1 and Run 2 analyses.

Following from the above, the Run 1 analysis is presented. An overview of the studies performed to design the SRs is given, culminating in the definition of the signal, control and validation regions defined in the analysis. The results of the fitting procedure and exclusion limits are discussed.

The Run 2 analysis is also presented. The updates to the SRs defined in the previous

iteration of the analysis are documented, as is the introduction of an additional SR to target compressed scenarios. The new control and validation regions implemented for the analysis are given, and the results of the fitting procedure and limits are presented.

The author's contribution to the Run 1 analysis consisted of the development of the exclusive SR (SRexA) and the associated control and validation regions. The contribution to the Run 2 analysis consisted of the updates to the SR definitions, the updated background estimation strategy, the evaluation of the modelling uncertainties and the fit results.

7.1 Analysis motivation

Approaching the end of Run 1, many possible final states had been investigated when performing searches for the pair production of top and bottom squarks, assuming a 100% Branching Ratio (BR) for the decay of the squark to the lightest neutralino: $\tilde{t} \to t + \tilde{\chi}_1^0$ and $\tilde{b} \to b + \tilde{\chi}_1^0$ [139, 140, 127].

If the BR for the decay scenario considered is not 100%, for example, when the decay of the squark can proceed via a chargino, then the constraints from the previous analyses are less stringent. If the $\tilde{t} \to t + \tilde{\chi}_1^0$ and $\tilde{t} \to b + \tilde{\chi}_1^\pm$ decays are equally probable, approximately half of the events are expected to proceed as in Figure 7.1. If the W boson is off-shell, the decay products of the W are not detected and the signature contains a top-quark, a bottom-quark and $E_{\mathrm{T}}^{\mathrm{miss}}$.

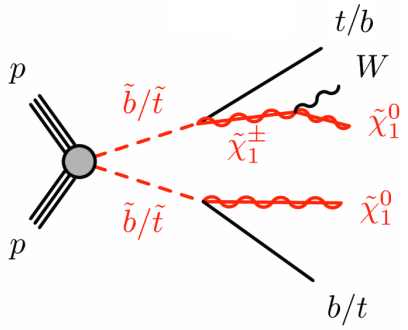

FIGURE 7.1: Diagram of of the asymmetric $tb + E_{\mathrm{T}}^{\mathrm{miss}}$ decay scenario.

The assumption for the W boson to be highly off-shell results from considering SUSY scenarios characterised by a small mass splitting between the gauginos. This is suggested by the constraints on the measured dark matter relic density in the universe.

Constraints placed by LEP [141] on direct chargino production provide a lower limit on the chargino mass of 110 GeV, which in these scenarios also constrains the neutralino masses considered, dependent upon the mass splitting chosen.

If the BR for $\tilde{t} \to t + \tilde{\chi}_1^0$ or $\tilde{b} \to b + \tilde{\chi}_1^0$ is 50%, then 50% of the decays will proceed via the asymmetric decay mode and 25% of decays will proceed with both legs decaying symmetrically. Figure 7.2 contains the processes required to create the physical decay (for both sbottom and stop production) and Equation 7.1 contains the total number of expected events when considering the contributions from each decay scenario, with k taken to be the branching ratio of the $\tilde{t} \to t + \tilde{\chi}_1^0 / \tilde{b} \to b + \tilde{\chi}_1^0$ decay.

$$N_{\mathrm{Total}} = k^2 N_{tt/bb+\tilde{\chi}_1^0\tilde{\chi}_1^0} + 2k(1-k) N_{tb+\tilde{\chi}_1^0\tilde{\chi}_1^\pm} + (1-k)^2 N_{bb/tt+\tilde{\chi}_1^\pm\tilde{\chi}_1^\pm} \tag{7.1}$$

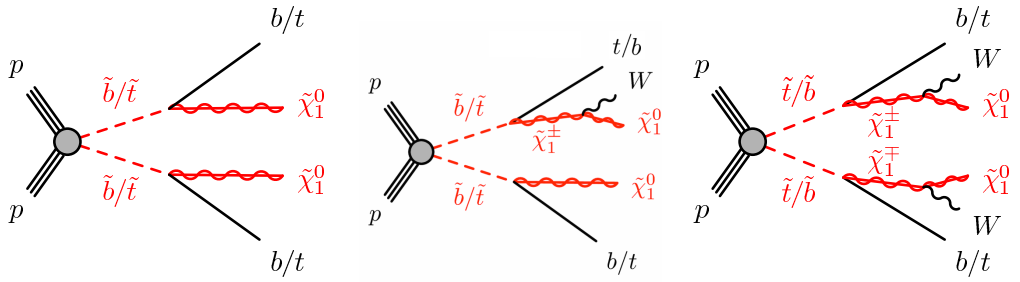

(a) $\tilde{t}\tilde{t}/\tilde{b}\tilde{b} \to tt/bb + \tilde{\chi}_1^0\tilde{\chi}_1^0$ (b) $\tilde{t}\tilde{t}/\tilde{b}\tilde{b} \to tb\tilde{\chi}_1^0\tilde{\chi}_1^\pm$ (c) $\tilde{t}\tilde{t}/\tilde{b}\tilde{b} \to bb/tt + \tilde{\chi}_1^\pm\tilde{\chi}_1^\pm$

FIGURE 7.2: Example of the three decay scenarios required to make the physical decay process for the $tb + E_{\mathrm{T}}^{\mathrm{miss}}$ analysis.

In Run 1 stop production was targeted. In Run 2 the results are reported as part of the search for bottom squarks. The sensitivity to the production of both squarks is the same provided the W decay is invisible. An additional set of SUSY models based upon pMSSM scenarios (as introduced in Section 2.7.7) are also considered for the Run 1 analysis.

7.1.1 Signal phenomenology

The optimisation studies to achieve the best selection are performed by maximising the efficiency to extract the mixed signals from the SM background. It is found that selecting events containing a leptonically decaying top quark is the most optimal to extract the signal.

For this final state, the main SM processes which must be considered as background are: $t\bar{t}$, single-top, W+jets, diboson and $t\bar{t} + V$. The dominant background is expected

to be semi-leptonic $t\bar{t}$ which, due to the expected signal topology, will look very similar to the signal process under investigation. Single-top Wt-channel production will also be expected to contribute significantly to the one lepton final state due to the leptonic decay of either W boson in the event. Additionally a large contribution is expected from the W+jets process, with the W boson decaying via either an electron or a muon, it is also possible that this process can contribute to this final state with the W decaying via a tau-lepton, and the tau subsequently decaying leptonically.

The contributions from the rare diboson and $t\bar{t} + V$ are expected to provide a minor contribution to the final state, due to the small cross sections for these processes at 8 TeV.

7.2 $tb + E_{\mathrm{T}}^{\mathrm{miss}}$ Run 1 Analysis

An overview of the studies performed investigating two signal scenarios is presented, including the optimisation performed to target a more realistic pMSSM-like scenario and a simplified model scenario. Two types of SR are designed, one set of three SRs with an inclusive jet multiplicity selection, targeting the pMSSM models, and a single SR with an exclusive jet selection, targeting the simplified model scenarios. The control regions designed to constrain the main backgrounds in the analysis ($t\bar{t}$ and W+jets) are presented, as are the validation regions used to provide confidence in the fit results and the most relevant systematic uncertainties. The background-only fit results are presented, with the statistical interpretation of the fit given in both model-dependent and independent scenarios.

7.2.1 Signal kinematic studies

The analysis is optimised considering two distinct signal scenarios which both result in the $tb + E_{\mathrm{T}}^{\mathrm{miss}}$ final state.

The first targets realistic pMSSM models, containing the pair production of both stops and sbottoms, which decay asymmetrically as in Figure 7.1. The mass hierarchy of the sparticles in these scenarios is driven by the common third generation mass parameter, m_{QL3}, for the squarks, and the higgsino mass parameter, μ, for the gauginos. The parameters varied in these scenarios are not directly the physical mass of the $\tilde{b}$ and $\tilde{t}$ but are the m_{QL3} and μ parameters. These parameters are chosen such that the mass splitting of $\tilde{\chi}_1^{\pm}$, $\tilde{\chi}_1^0$ is below 10 GeV across all models and both decay modes

are kinematically open for the $\tilde{t}/\tilde{b}$ and are equivalently probable. For example, for the $(m_{QL3}, \mu) = (400, 110)\,\mathrm{GeV}$ scenario, the percentage of events proceeding asymmetrically is 49%.

In contrast to the above models, the second signal scenario is the simplified model scenario containing solely the pair production of top-squarks which decay asymmetrically as shown before. Two mass splitting scenarios are considered for the chargino neutralino of either 5 or 20 GeV.

Due to the similarities between the above models a general preselection is applied shown in Table 7.1, on top of which the optimisation studies are based. All events are required to pass the Run 1 event cleaning, as discussed in Chapter 5. According to the final state requirements, events are selected consisting of one signal lepton and two $b-$tagged jets. A selection of $E_{\mathrm{T}}^{\mathrm{miss}} > 100\,\mathrm{GeV}$ is used to target the neutralinos in the signal whilst also reducing the $t\bar{t}$ contribution. As the analysis aims to use the am_{T2} variable, a requirement placed on all regions is $m_{b,l}^{\mathrm{min}} < 170\,\mathrm{GeV}$, which ensures that the am_{T2} is calculated. Finally selections on $\min \Delta\phi(b - \mathrm{jets}, E_{\mathrm{T}}^{\mathrm{miss}})$ and $E_{\mathrm{T}}^{\mathrm{miss}}$ significance reduce the multi-jet background to negligible levels.

Preselection	
Variable	Selection
Event cleaning selections	✔
$n_{b-\mathrm{jets}}$	2
n_{leptons}	1
$E_{\mathrm{T}}^{\mathrm{miss}}$	$> 100\,\mathrm{GeV}$
$\min \Delta\phi(b - \mathrm{jets}, E_{\mathrm{T}}^{\mathrm{miss}})$	> 0.4
$m_{b,l}^{\mathrm{min}}$	$< 170\,\mathrm{GeV}$
$E_{\mathrm{T}}^{\mathrm{miss}}$ significance	$> 5\,\mathrm{GeV}^{1/2}$

TABLE 7.1: $tb+E_{\mathrm{T}}^{\mathrm{miss}}$ Run 1 analysis, preselection definition used as a baseline selection for all regions in the analysis.

The optimisation of all SRs, VRs and CRs are based upon the preselection requirements described in Table 7.1.

7.2.2 Signal Region definitions

The most discriminating variables used to define the SR selections are am_{T2} and m_{T}, effective to reduce $t\bar{t}$ and $W+$jets backgrounds respectively. Additional selections on

m_{eff}, $E_{\mathrm{T}}^{\mathrm{miss}}$ and $E_{\mathrm{T}}^{\mathrm{miss}}$ significance, the latter two with tighter selections than in the preselection, are used to target specific regions of phase space for both models.

The main difference between the pMSSM models and the simplified models is the number of extra-jets (defined as jets with $p_{\mathrm{T}} > 50\,\mathrm{GeV}$) expected in the event. Since in pMSSM models it is possible for the stops and sbottoms to decay via the second lightest neutralino ($\tilde{\chi}_2^0$), for example $\tilde{t} \to t + \tilde{\chi}_2^0$, with the subsequent decay $\tilde{\chi}_2^0 \to h + \tilde{\chi}_1^0$ or $\tilde{\chi}_2^0 \to Z^0 + \tilde{\chi}_1^0$. These extra decay modes can lead to many extra jets in the pMSSM events. This is in contrast to the simplified model scenarios which consist of only the $\tilde{t} \to t + \tilde{\chi}_1^0$ and $\tilde{t} \to b + \tilde{\chi}_1^{\pm}$ decays. With the small mass difference between the $\tilde{\chi}_1^{\pm}$ and $\tilde{\chi}_1^0$, these scenarios lead to events with a small amount of extra jet activity.

The set of three SRs targeting the pMSSM scenarios are inclusive with respect to the jet multiplicity. The optimisation is performed to maximise the discovery significance (Equation 6.1) targeting three benchmark scenarios in the pMSSM mass plane : (m_{QL3}, μ) = (400, 110) GeV, (500, 210) GeV and (700, 110) GeV. The full selections of the SRs defined to target these regions are reported in Table 7.2. Generally, the m_{eff} selection is increased to target the higher masses with some tuning of the $E_{\mathrm{T}}^{\mathrm{miss}}$ and $E_{\mathrm{T}}^{\mathrm{miss}}$ significance selections. The yields in the inclusive SR defined are shown in Table 7.3.

For the $m_{QL3} = 400\,\mathrm{GeV}$ scenario, a selection of $m_{\mathrm{eff}} > 300\,\mathrm{GeV}$ is employed to further reduce the $t\bar{t}$ background after the am_{T2} selection. In addition to this, the $E_{\mathrm{T}}^{\mathrm{miss}}$ and $E_{\mathrm{T}}^{\mathrm{miss}}$ significance selections are tightened to enhance the signal. This selection is referred to as SRinA. The intermediate scenario (m_{QL3}, μ) = (500, 210) GeV) is targeted by tightening the m_{eff} selection with respect to the SRinA selection. This selection, referred to as SRinB, targets both higher squark and neutralino masses, and requires $E_{\mathrm{T}}^{\mathrm{miss}}$ significance $> 12\,\mathrm{GeV}^{1/2}$. The region defined to target the largest squark mass scenario ($m_{QL3} = 700\,\mathrm{GeV}$) uses the tightest m_{eff} selection of $> 650\,\mathrm{GeV}$ and $E_{\mathrm{T}}^{\mathrm{miss}}$ $> 220\,\mathrm{GeV}$.

Variable	SRinA	SRinB	SRinC
Event cleaning	✔		
Trigger	Single lepton (e, μ) $p_{\mathrm{T}} > 25\,\mathrm{GeV}$		
$n_{b-\mathrm{jets}}$	2		
n_{lepton}	1		
$E_{\mathrm{T}}^{\mathrm{miss}}$	$> 200\,\mathrm{GeV}$	$> 120\,\mathrm{GeV}$	$> 220\,\mathrm{GeV}$
m_{T}	$> 140\,\mathrm{GeV}$		$> 180\,\mathrm{GeV}$
m_{eff}	$> 300\,\mathrm{GeV}$	$> 450\,\mathrm{GeV}$	$> 650\,\mathrm{GeV}$
$E_{\mathrm{T}}^{\mathrm{miss}}$ significance	$> 8\,\mathrm{GeV}^{1/2}$	$> 12\,\mathrm{GeV}^{1/2}$	$> 5\,\mathrm{GeV}^{1/2}$
am_{T2}	> 180 GeV	$> 200\,\mathrm{GeV}$	$> 180\,\mathrm{GeV}$
$m_{b,l}^{\mathrm{min}}$	$< 170\,\mathrm{GeV}$		
$\min \Delta\phi(b-\mathrm{jets}, E_{\mathrm{T}}^{\mathrm{miss}})$	> 0.4		

TABLE 7.2: $tb + E_{\mathrm{T}}^{\mathrm{miss}}$ Run 1 inclusive SR definitions.

Expected Yield	SRinA	SRinB	SRinC
$t\bar{t}$	10.08 ± 3.77	4.44 ± 2.20	2.17 ± 1.56
W+jets	3.41 ± 2.00	1.99 ± 1.53	0.60 ± 0.80
Z+jets	0.08 ± 0.28	0.05 ± 0.23	0.03 ± 0.17
single-top	8.66 ± 3.19	5.12 ± 2.37	3.06 ± 1.83
Other	3.42 ± 2.99	2.19 ± 2.08	1.0 ± 1.12
Background Total	25.67 ± 6.12	13.78 ± 4.14	6.92 ± 2.77
$(m_{QL3},\, \mu) = (400,\, 110)\,\mathrm{GeV}$	71.90 ± 8.48	–	–
$(m_{QL3},\, \mu) = (500,\, 210)\,\mathrm{GeV}$	–	35.63 ± 5.06	–
$(m_{QL3},\, \mu) = (700,\, 110)\,\mathrm{GeV}$	–	–	7.48 ± 2.74

TABLE 7.3: Expected yield values for the inclusive SRs, with the signal point the SRs were optimised for presented for comparison.

A fourth region, defined in Table 7.4, is used to target signal models with low extra jet activity, such as in the simplified models. Relatively loose selections on both m_{eff} and $E_{\mathrm{T}}^{\mathrm{miss}}$ are used with respect to the previous regions, however the main difference is the selection on the extra-jet multiplicity, with either zero or one extra jet expected in the events. Table 7.5 shows the number of expected events for the SM processes, and a representative signal scenario.

Variable	SRexA
Event cleaning	✔
Trigger	Single lepton (e, μ) $p_{\mathrm{T}} > 25\,\mathrm{GeV}$
$n_{b-\mathrm{jets}}$	2
n_{lepton}	1
$E_{\mathrm{T}}^{\mathrm{miss}}$	> 160 GeV
m_{T}	> 120 GeV
m_{eff}	> 300 GeV
am_{T2}	> 180 GeV
$m_{b,l}^{\mathrm{min}}$	< 170 GeV
$E_{\mathrm{T}}^{\mathrm{miss}}$ significance	> 10 GeV$^{1/2}$
$\min \Delta\phi(b-\mathrm{jets}, E_{\mathrm{T}}^{\mathrm{miss}})$	> 0.4
$n_{\mathrm{extrajets}}$, $(p_{\mathrm{T}} > 50$ GeV)	< 2

TABLE 7.4: $tb + E_{\mathrm{T}}^{\mathrm{miss}}$ Run 1 exclusive SR definition.

Expected Yield	SRexA
$t\bar{t}$	12.43 ± 4.78
W+jets	3.87 ± 2.14
Z+jets	0.05 ± 0.25
single-top	9.55 ± 3.35
Other	3.02 ± 3.73
Background Total	28.95 ± 7.25
$(m_{\tilde{t}}, m_{\tilde{\chi}_1^0}) = (300, 100)\,\mathrm{GeV}$	35.01 ± 5.92

TABLE 7.5: $tb + E_{\mathrm{T}}^{\mathrm{miss}}$ Run 1 exclusive SR yield.

Tables 7.3 and 7.5 show that the dominant background in every SR is $t\bar{t}$, followed by single-top and W+jets. There is also a relatively significant contribution from the "Other" category, which is the sum of the diboson and $t\bar{t} + V$ processes. The dominant contribution in the Other category is $t\bar{t} + Z$, however when considered on its own the contribution from $t\bar{t}+Z$ is less than both of the single-top and W+jets backgrounds. The control region strategy is defined based on the dominant top and W+jets backgrounds.

7.2.3 Control Region definitions

The background estimation strategy for the analysis focuses on the definition of one-lepton CRs enhanced in either $t\bar{t}$ or W+jets. Whilst the yields reported in Tables 7.3 and 7.5 would suggest that the ideal strategy would be to define CRs for $t\bar{t}$, single-top

and W+jets, this is found not to be possible due to the difficulties in isolating a region enhanced in single-top. For each SR in the analysis, two CRs are defined, one for $t\bar{t}$ and another for the W+jets process.

The inclusive $t\bar{t}$ CRs (CRTin) are defined similarly to the SR in terms of the m_{eff} selection but inverting the am_{T2} requirement to $< 160\,\mathrm{GeV}$. This value is used as it is close to the predicted end-point of the am_{T2} distribution for $t\bar{t}$, which is 140 GeV. Additionally either the $E_{\mathrm{T}}^{\mathrm{miss}}$ or $E_{\mathrm{T}}^{\mathrm{miss}}$ significance selections are inverted whilst keeping the lower limit required by the preselection. The exclusive $t\bar{t}$ CR (CRTexA) is defined by inverting both the am_{T2} and $E_{\mathrm{T}}^{\mathrm{miss}}$ significance SR selections and is inclusive in m_{eff}. A full overview of the $t\bar{t}$ CRs is presented in Table 7.6.

Selection	CRTinA	CRTinB	CRTinC	CRTexA
Event cleaning		✔		
Trigger		Single lepton (e, μ) $p_{\mathrm{T}} > 25\,\mathrm{GeV}$		
n_{Lepton}		1		
$n_{b-\mathrm{jets}}$		2		
$E_{\mathrm{T}}^{\mathrm{miss}}$	[100, 200] GeV	$> 120\,\mathrm{GeV}$	[100, 220] GeV	$> 100\,\mathrm{GeV}$
m_{T}	$> 140\,\mathrm{GeV}$		$> 180\,\mathrm{GeV}$	$> 120\,\mathrm{GeV}$
am_{T2}		< 160 GeV		< 180 GeV
m_{eff}	> 300 GeV	$> 450\,\mathrm{GeV}$	$> 650\,\mathrm{GeV}$	-
$E_{\mathrm{T}}^{\mathrm{miss}}$ significance	> 8 GeV$^{1/2}$	[6, 12] GeV$^{1/2}$	> 5 GeV$^{1/2}$	[5-10] GeV$^{1/2}$
$m_{b,l}^{\mathrm{min}}$		$< 170\,\mathrm{GeV}$		
$\min \Delta\phi(b - \mathrm{jets}, E_{\mathrm{T}}^{\mathrm{miss}})$		> 0.4		
$n_{\mathrm{extrajets}}$ $(p_{\mathrm{T}} > 50\,\mathrm{GeV})$	-	-	-	< 2

TABLE 7.6: Summary of the selections used to define the top CRs in the $tb + E_{\mathrm{T}}^{\mathrm{miss}}$ Run 1 analysis.

The inclusive W+jets CRs (CRWin) are defined by inverting the selection on m_{T} and lowering the selection to $< 120\,\mathrm{GeV}$. Similarly to the $t\bar{t}$ CRs, the selections on either $E_{\mathrm{T}}^{\mathrm{miss}}$ or $E_{\mathrm{T}}^{\mathrm{miss}}$ significance are also inverted while maintaining the lower bound as required by the preselection. To further ensure a region enhanced in W+jets, the $b-$jet multiplicity is loosened to allow events containing one or two $b-$jets. The exclusive W+jets region (CRWexA) is defined by inverting the m_{T} selection as in the inclusive regions, and also inverting the $E_{\mathrm{T}}^{\mathrm{miss}}$ significance selection. Similarly to the exclusive $t\bar{t}$ region, an inclusive m_{eff} selection is used.

Selection	CRWinA	CRWinB	CRWinC	CRWexA
Event cleaning	✔			
Trigger	Single lepton (e, μ) $p_{\mathrm{T}} > 25\,\mathrm{GeV}$			
n_{lepton}	1			
$n_{b-\mathrm{jets}}$	1,2			2
$E_{\mathrm{T}}^{\mathrm{miss}}$	[100, 200] GeV	$> 120\,\mathrm{GeV}$	[100, 220] GeV	$> 100\,\mathrm{GeV}$
m_{T}	$< 120\,\mathrm{GeV}$			
am_{T2}	> 180 GeV	$> 200\,\mathrm{GeV}$	$> 180\,\mathrm{GeV}$	
m_{eff}	> 300 GeV	$> 450\,\mathrm{GeV}$	$> 650\,\mathrm{GeV}$	-
$E_{\mathrm{T}}^{\mathrm{miss}}$ significance	$> 8\,\mathrm{GeV}^{1/2}$	[6, 12] $\mathrm{GeV}^{1/2}$	> 5 $\mathrm{GeV}^{1/2}$	[5, 10] $\mathrm{GeV}^{1/2}$
$m_{b,l}^{\mathrm{min}}$	$< 170\,\mathrm{GeV}$			
$\min \Delta\phi(b-\mathrm{jets}, E_{\mathrm{T}}^{\mathrm{miss}})$	> 0.4			
$n_{\mathrm{extrajets}}, (p_{\mathrm{T}} > 50$ GeV)	-			< 2

TABLE 7.7: Summary of the selections used to define the W+jets CRs in the $tb + E_{\mathrm{T}}^{\mathrm{miss}}$ Run 1 analysis.

$tb + E_{\mathrm{T}}^{\mathrm{miss}}$ **Inclusive CRs**	CRTinA	CRWinA	CRTinB	CRWinB	CRTinC	CRWinC
Observed events	1371	4997	429	1946	26	411
Fitted bkg events	1370 ± 37.0	5000 ± 70.8	429 ± 20.7	1950 ± 44.1	25.8 ± 5.05	411 ± 20.2
Fitted $t\bar{t}$ events	1330 ± 38.0	2710 ± 389	416 ± 21.0	1230 ± 179	24.5 ± 5.08	175 ± 48.3
Fitted single-top events	27.4 ± 5.05	392 ± 50.9	8.07 ± 1.63	178 ± 21.0	0.65 ± 0.17	37.5 ± 5.79
Fitted W+jets events	5.84 ± 2.24	1740 ± 381	0.86 ± 0.55	465 ± 179	$0.08^{+0.09}_{-0.08}$	179 ± 51.8
Fitted Z+jets events	0.31 ± 0.10	54.8 ± 7.62	0.28 ± 0.22	23.7 ± 4.07	$0.04^{+0.04}_{-0.04}$	6.15 ± 0.82
Fitted diboson events	0.74 ± 0.20	86.8 ± 9.90	0.37 ± 0.07	39.4 ± 5.17	0.12 ± 0.03	11.3 ± 1.23
Fitted $t\bar{t} + V$ events	7.26 ± 2.30	8.96 ± 2.72	3.70 ± 1.19	7.37 ± 2.31	0.41 ± 0.13	2.34 ± 0.73
MC exp. SM events	1300	4990	385	2120	27.4	436
MC exp. $t\bar{t}$ events	1260	2570	371	1100	26.1	187
MC exp. single-top events	27.4	392	8.06	178	0.65	37.5
MC exp. W+jets events	6.31	1880	1.43	768	0.09	192
MC exp. Z+jets events	0.31	54.8	0.27	23.6	0.04	6.14
MC exp. diboson events	0.74	86.8	0.37	39.3	0.11	11.3
MC exp. $t\bar{t} + V$ events	7.26	8.96	3.70	7.36	0.41	2.34

TABLE 7.8: Background fit results for the inclusive CR regions.

Tables 7.8 and 7.9 present both the pre- and post-fit yields for the CRs corresponding to the inclusive and exclusive SRs respectively. The pre-fit yields show that all regions are dominated by the $t\bar{t}$ process. The pre-fit yields for the $t\bar{t}$ process in the CRT regions show that the $t\bar{t}$ MC generally predicts the data well. The W+jets process is sub-dominant in the CRW regions, due to the difficulty in designing CRs dominated by W+jets while remaining close to the kinematics of the SR.

$tb + E_{\mathrm{T}}^{\mathrm{miss}}$ **Exclusive CRs**	CRTexA	CRWexA
Observed events	2870	337
Fitted bkg events	2870 ± 53.6	337 ± 18.3
Fitted $t\bar{t}$ events	2740 ± 60.0	176 ± 26.4
Fitted single-top events	82.1 ± 15.2	54.4 ± 7.58
Fitted W+jets events	35.8 ± 14.0	96.5 ± 29.3
Fitted Z+jets events	1.30 ± 0.67	3.84 ± 0.70
Fitted diboson events	1.88 ± 0.31	5.24 ± 0.84
Fitted $t\bar{t} + V$ events	9.25 ± 2.91	1.06 ± 0.32
MC exp. SM events	2720	318
MC exp. $t\bar{t}$ events	2590	166
MC exp. single-top events	82.0	54.4
MC exp. W+jets events	32.4	87.4
MC exp. Z+jets events	1.30	3.84
MC exp. diboson events	1.88	5.24
MC exp. $t\bar{t} + V$ events	9.25	1.06

TABLE 7.9: Background fit results for the exclusive CRs.

	Value			
Normalisation	SRinA	SRinB	SRinC	SRexA
$\mu_{t\bar{t}}$	1.06 ± 0.07	1.12 ± 0.09	0.94 ± 0.21	1.06 ± 0.07
$\mu_{W+\mathrm{jets}}$	0.92 ± 0.20	0.61 ± 0.23	0.93 ± 0.27	1.10 ± 0.34

TABLE 7.10: $t\bar{t}$ and W+jets normalisation parameters corresponding to the fit performed for each SR of the $tb + E_{\mathrm{T}}^{\mathrm{miss}}$ Run 1 analysis using 20fb^{-1}.

Table 7.10 contains the normalisation parameters for the $t\bar{t}$ and W+jets backgrounds. The $t\bar{t}$ normalisation parameters are consistently found to be close to 1, again suggesting generally good modelling of the $t\bar{t}$ process by the MC.

The fluctuation in the central values of the normalisation parameters for the W+jets backgrounds is due to the purity of the CR in terms of the W+jets background. The W+jets normalisation parameters for the inclusive regions are consistent to within 1σ.

The normalisation parameters are subsequently validated in a set of validation regions.

7.2.4 Validation Region definitions

Similarly to the definition of the CRs, two VRs are defined for each SR, to validate the modelling of the $t\bar{t}$ and W+jets backgrounds.

The regions are defined for both the inclusive and exclusive selections by maintaining the CR selection on either the am_{T2} (for the $t\bar{t}$ regions) or the m_{T} (for the W+jets

regions) to ensure a region enhanced in the background under consideration. Otherwise the SR selections are required. This ensures the region validates the modelling of both the $t\bar{t}$ and W+jets backgrounds using kinematics similar to the SR.

Variable	VRTinA	VRTinB	VRTinC	VRWinA	VRWinB	VRWinC
Event cleaning	✔					
Trigger	Single lepton (e, μ) $p_{\mathrm{T}} > 25\,\mathrm{GeV}$					
n_{Lepton}	1					
$n_{b-\mathrm{jets}}$	2					
$E_{\mathrm{T}}^{\mathrm{miss}}$	$> 200\,\mathrm{GeV}$	$> 120\,\mathrm{GeV}$	$> 220\,\mathrm{GeV}$	$> 200\,\mathrm{GeV}$	$> 120\,\mathrm{GeV}$	$> 220\,\mathrm{GeV}$
m_{T}	$> 140\,\mathrm{GeV}$		$> 180\,\mathrm{GeV}$		$< 120\,\mathrm{GeV}$	
am_{T2}		< 160 GeV		> 180 GeV	$> 200\,\mathrm{GeV}$	$> 180\,\mathrm{GeV}$
m_{eff}	> 300 GeV	$> 450\,\mathrm{GeV}$	$> 650\,\mathrm{GeV}$	> 300 GeV	$> 450\,\mathrm{GeV}$	$> 650\,\mathrm{GeV}$
$E_{\mathrm{T}}^{\mathrm{miss}}$ significance	> 8 GeV$^{1/2}$	$> 12\,\mathrm{GeV}^{1/2}$	$> 5\,\mathrm{GeV}^{1/2}$	$> 8\,\mathrm{GeV}^{1/2}$	$> 12\,\mathrm{GeV}^{1/2}$	$> 5\,\mathrm{GeV}^{1/2}$
$m_{b,l}^{\mathrm{min}}$	$< 170\,\mathrm{GeV}$					
$\min \Delta\phi(b-\mathrm{jets}, E_{\mathrm{T}}^{\mathrm{miss}})$	> 0.4					

TABLE 7.11: Summary of inclusive $tb + E_{\mathrm{T}}^{\mathrm{miss}}$ VR definitions

Variable	VRTexA	VRWexA
Event cleaning	✔	
Trigger	Single lepton (e, μ) $p_{\mathrm{T}} > 25\,\mathrm{GeV}$	
n_{Lepton}	1	
$n_{b-\mathrm{jets}}$	2	
$E_{\mathrm{T}}^{\mathrm{miss}}$	$> 160\,\mathrm{GeV}$	
m_{T}	> 120 GeV	< 120 GeV
am_{T2}	< 180 GeV	> 180 GeV
$m_{b,l}^{\mathrm{min}}$	< 170 GeV	
$E_{\mathrm{T}}^{\mathrm{miss}}$ significance	> 10 GeV$^{1/2}$	
$\min \Delta\phi(b-\mathrm{jets}, E_{\mathrm{T}}^{\mathrm{miss}})$	> 0.4	
m_{eff}	> 300	
$n_{\mathrm{extrajets}}, (p_{\mathrm{T}} > 50$ GeV)	< 2	

TABLE 7.12: Summary of selections used in the exclusive $tb + E_{\mathrm{T}}^{\mathrm{miss}}$ Run 1 VRs.

The results of the background-only fit performed for the inclusive and exclusive regions is included in Tables 7.13 and 7.14, respectively. Generally it is seen that the regions validating the $t\bar{t}$ process have generally good agreement between the post-fit prediction and the observed data. The regions targeting the W+jets process show again

$tb + E_{\mathrm{T}}^{\mathrm{miss}}$ **Inclusive VRs**	VRTinA	VRWinA	VRTinB	VRWinB	VRTinC	VRWinC
Observed events	237	257	122	138	36	83
Fitted bkg events	251 ± 23.2	265 ± 30.6	134 ± 16.3	134 ± 17.4	31.7 ± 6.61	97.3 ± 13.0
Fitted $t\bar{t}$ events	240 ± 22.9	125 ± 20.6	129 ± 16.2	71.1 ± 11.1	30.3 ± 6.61	34.2 ± 8.93
Fitted single-top events	4.63 ± 1.82	51.5 ± 20.5	2.47 ± 1.20	27.4 ± 10.8	0.73 ± 0.32	23.8 ± 6.65
Fitted W+jets events	2.32 ± 0.98	78.2 ± 26.0	0.20 ± 0.11	29.8 ± 14.0	0.10 ± 0.05	33.9 ± 12.8
Fitted Z+jets events	$0.02^{+0.02}_{-0.02}$	2.01 ± 0.28	$0.00^{+0.01}_{-0.00}$	0.94 ± 0.19	0.00 ± 0.00	0.78 ± 0.12
Fitted diboson events	0.37 ± 0.12	6.28 ± 0.84	$0.15^{+0.20}_{-0.15}$	4.09 ± 0.49	$0.02^{+0.02}_{-0.02}$	3.52 ± 0.63
Fitted $t\bar{t} + V$ events	8.96 ± 2.72	2.83 ± 0.92	1.77 ± 0.59	1.19 ± 0.38	0.58 ± 0.19	1.18 ± 0.38
MC exp. SM events	238	265	120	146	33.6	102
MC exp. $t\bar{t}$ events	228	118	115	63.5	32.2	36.4
MC exp. single-top events	4.63	51.5	2.46	27.3	0.73	23.8
MC exp. W+jets events	2.50	84.6	0.33	49.2	0.11	36.3
MC exp. Z+jets events	0.02	2.01	0.00	0.94	0.00	0.78
MC exp. diboson events	0.37	6.28	0.15	4.08	0.02	3.52
MC exp. $t\bar{t} + V$ events	2.83	2.45	1.77	1.19	0.58	1.18

TABLE 7.13: Background fit results for the inclusive VRs.

$tb + E_{\mathrm{T}}^{\mathrm{miss}}$ **Exclusive VRs**	VRTexA	VRWexA
Observed events	665	280
Fitted bkg events	640 ± 71.9	312 ± 41.6
Fitted $t\bar{t}$ events	613 ± 71.7	142 ± 20.3
Fitted single-top events	16.1 ± 6.58	50.3 ± 20.5
Fitted W+jets events	6.14 ± 2.36	108 ± 35.3
Fitted Z+jets events	0.15 ± 0.07	2.34 ± 0.40
Fitted diboson events	0.84 ± 0.12	8.29 ± 1.01
Fitted $t\bar{t} + V$ events	4.02 ± 1.29	1.26 ± 0.40
MC exp. SM events	606	294
MC exp. $t\bar{t}$ events	579	134
MC exp. single-top events	16.1	50.3
MC exp. W+jets events	5.56	97.4
MC exp. Z+jets events	0.15	2.34
MC exp. diboson events	0.84	8.28
MC exp. $t\bar{t} + V$ events	4.02	1.26

TABLE 7.14: Background-only fit results for the exclusive VRs.

generally good agreement. In the VRWinC and VRexA regions the prediction overestimates the observed data, however this overestimate is at a level of less than 1σ in both regions and is covered by the statistical and systematic uncertainties.

7.2.5 Systematic uncertainties

The systematic uncertainties are evaluated as explained in Section 6.2.6 with regards to both the detector and modelling uncertainties. The dominant detector uncertainties are reported in Table 7.15, the largest contributions are jet-related (JES and JER), and the uncertainty arising from the $b-$tagging. The modelling uncertainties are evaluated in a similar manner to the methods previously discussed but with different MC sets as they follow the Run 1 recommendations.

$t\bar{t}$ uncertainties

The uncertainty on the $t\bar{t}$ modelling due to the choice of generator is investigated by comparing the predictions from a $t\bar{t}$ sample generated with Herwig+Jimmy [142] to a sample generated with MC@NLO-Jimmy. The uncertainty on the TF (using the Herwig+Jimmy sample as the nominal), is applied to the nominal Powheg-Pythia sample. The parton shower uncertainty is estimated comparing the nominal Powheg-Pythia sample with the Powheg-Herwig+Jimmy sample. Finally the ISR and FSR uncertainties are evaluated using $t\bar{t}$ samples generated with AcerMC-Pythia [143]. The uncertainties on the TF are calculated and summed in quadrature, before applying them symmetrically to the nominal Powheg-Pythia sample.

Single-top uncertainties

The uncertainties on the single-top modelling are estimated in a similar manner as described above for the $t\bar{t}$ process, however there is no dedicated CR defined for the single-top background and the uncertainty is calculated with respect to the absolute yield and not the transfer factor. In addition to the above uncertainties, the uncertainty on the interference term between single-top and $t\bar{t}$ is also calculated. The sum of the nominal Powheg-Pythia Wt-channel and $t\bar{t}$ yields is compared with the yield of an inclusive $WWbb$ sample generated at LO using AcerMC+Pythia. The uncertainty on the yield in this scenario is summed in quadrature with the generator, PS and radiation uncertainties, and applied to the nominal single-top Wt-channel process.

W+jets uncertainties

For the Sherpa samples used to model the W+jets process, uncertainties arise from the choice of ME matching scale; renormalisation and factorisation scales; and also the soft gluon resummation scale. These uncertainties are evaluated using a 1D parameterisation based upon the number of truth-jets in an event. Further to this, the uncertainty related to the heavy flavour composition of the samples is estimated by varying the cross sections of the c- and b-filtered slices by 24% [137].

Source of uncertainty	SRinA	SRinB	SRinC	SRexA
Detector uncertainties				
JES	8.4%	15%	5.8%	5.4%
JER	28%	32%	6.8	32%
$b-$tagging	11.1%	15%	9.8%	9.5%
Theory uncertainties				
Top production	82%	43%	64%	33%
Single-top	38%	69%	71%	80%
W+jets	4.9%	8.2%	44%	32.5%
Total background systematic (% of total background)	25%	20%	41%	22%

TABLE 7.15: Overview of the dominant detector and modelling uncertainties present in the Run 1 $tb + E_{\mathrm{T}}^{\mathrm{miss}}$ analysis. The size of the total systematic uncertainty (as a % of the background expectation) is also given. As the uncertainties considered may be correlated, the total uncertainty may not simply be the sum in quadrature of the uncertainties.

Table 7.15 presents the dominant uncertainties for the analysis and the contribution to the total systematic uncertainty of each of the dominant uncertainties. The dominant theory uncertainties are related to the modelling of the top-processes (both $t\bar{t}$ and single-top), which is expected as the $t\bar{t}$ and single-top processes are the dominant processes in the SRs. For the inclusive B and C regions, the uncertainty due to the modelling of the single-top processes is the largest contribution to the total uncertainty. Whilst this is is partly due to the single-top process being dominant in these regions, it is also somewhat due to the arbitrary nature to assigning the interference systematic to a specific sample (when it affects both $t\bar{t}$ and single-top). For the $t\bar{t}$ dominated SRexA, the uncertainty from the single-top is also dominant, which is again due to the interference term.

7.2.6 Interpretation of Results

The background only fit results for all SRs are reported in Table 7.16. A slight excess of events in data with respect to the background predictions is observed in every region which are correlated due to the overlapping nature of the SRs. Table 7.17 estimates the significance of the excesses in each of the SR which are found to be between $0.73\sigma - 1.67\sigma$.

Figure 7.3 presents the am_{T2} distributions in each SR where generally there is good agreement between the data and post-fit background.

Signal Regions	SRinA	SRinB	SRinC	SRexA
Observed events	38	20	10	46
Fitted bkg events	27.0 ± 6.73	14.1 ± 2.84	7.12 ± 2.93	31.3 ± 6.82
Fitted $t\bar{t}$ events	10.7 ± 5.64	4.98 ± 1.40	2.04 ± 1.96	13.2 ± 3.01
Fitted single-top events	9.08 ± 2.88	5.24 ± 2.07	3.22 ± 2.14	9.96 ± 5.34
Fitted W+jets events	3.21 ± 1.24	1.24 ± 0.65	0.56 ± 0.26	4.35 ± 1.65
Fitted Z+jets events	0.09 ± 0.02	0.05 ± 0.01	0.03 ± 0.00	0.07 ± 0.01
Fitted diboson events	1.04 ± 0.18	0.72 ± 0.11	0.29 ± 0.06	1.48 ± 0.29
Fitted $t\bar{t} + V$ events	2.92 ± 0.92	1.88 ± 0.61	0.98 ± 0.32	2.30 ± 0.72
MC exp. SM events	26.7	14.4	7.28	30.2
MC exp. $t\bar{t}$ events	10.1	4.44	2.17	12.4
MC exp. single-top events	9.07	5.24	3.21	9.96
MC exp. W+jets events	3.47	2.04	0.60	3.94
MC exp. Z+jets events	0.09	0.05	0.03	0.07
MC exp. diboson events	1.04	0.72	0.29	1.48
MC exp. $t\bar{t} + V$ events	2.92	1.88	0.98	2.30

TABLE 7.16: Background fit results for all SRs in the $tb + E_{\mathrm{T}}^{\mathrm{miss}}$ Run 1 analysis.

	Value			
Normalisation	SRinA	SRinB	SRinC	SRexA
Observed events	38	20	10	46
Expected Events	27.0 ± 6.73	14.1 ± 2.84	7.12 ± 2.93	31.3 ± 6.82
Significance	1.29σ	1.25σ	0.73σ	1.67σ

TABLE 7.17: Expected and observed yields of the $tb + E_{\mathrm{T}}^{\mathrm{miss}}$ SRs. With the significance of the excesses in each region also presented. As the SRs are overlapping (in m_{eff} selection) the excesses are correlated across the regions.

The model-independent fit procedure is used to produce model-independent limits on a generic BSM signal hypothesis, the results of which are presented in Table 7.18. Due to the excesses, the observed limit on the number of signal events is weaker than the expected limit from the background-only fit.

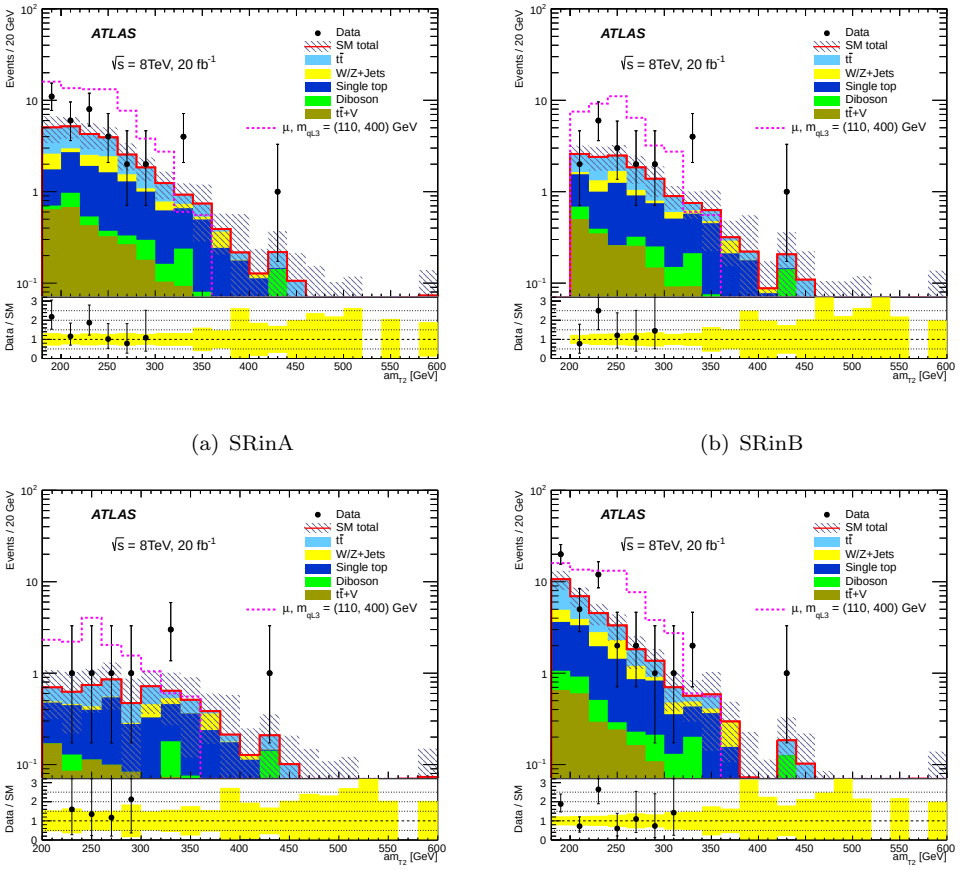

(a) SRinA (b) SRinB

(c) SRinC (d) SRexA

FIGURE 7.3: Post-fit data MC comparisons of the am_{T2} distribution in each SR. Error bands include both statistical and systematic uncertainties.

Signal Region	$\langle \epsilon A \sigma \rangle_{\mathrm{obs}}^{95}$ [fb]	S_{obs}^{95}	S_{exp}^{95}
SRinA	1.41	28.5	$19.3^{+7.0}_{-6.1}$
SRinB	0.81	16.3	$10.7^{+4.5}_{-2.6}$
SRinC	0.58	11.9	$9.8^{+3.3}_{-2.4}$
SRexA	1.58	32.1	$20.3^{+8.0}_{-3.6}$

TABLE 7.18: Breakdown of upper limits. Left to right: 95% CL upper limits on the visible cross section ($\langle \epsilon A \sigma \rangle_{\mathrm{obs}}^{95}$) and on the number of signal events (S_{obs}^{95}). The third column (S_{exp}^{95}) shows the 95% CL upper limit on the number of signal events, given the expected number of background events

Figure 7.4 presents model-dependent exclusion limits for the pMSSM model considered. Plot 7.4(a) presents the limits placed in the (m_{QL3}, μ) mass plane, with limits placed on m_{QL3} from 340 to 680 GeV for $\mu = 110$ GeV. The limits on placed on m_{QL3} and μ can be translated into direct limits on the masses of the sbottom, stop and neutralino in this pMSSM model, which are shown in Figures 7.4(b) and 7.4(c) respectively.

The limits placed directly on the m_{QL3} and μ parameters show interesting behaviour for $m_{QL3} > 700\,\mathrm{GeV}$. This is due to the relationship between m_{QL3} and $m_{\tilde{t}}$: increasing the m_{QL3} parameter beyond 700 GeV leads to scenarios with a significant production of the heavier stop eigenstate, $\tilde{t}_2$; whilst leaving the $\tilde{t}_1$ mass at about 600 GeV. A representation of this behaviour can be seen further in Figure 7.4(b), where the uncertainty band for the expected exclusion appears to stop abruptly at $m_{\tilde{t}}$ =600 GeV. This behaviour does not occur in the sbottom scenario, as shown in Figure 7.4(c), where the limit in the $m_{\tilde{b}}, m_{\tilde{\chi}_1^0}$ mass plane is very similar to the limit in the m_{QL3}, μ phase space. In these scenarios stop masses are excluded between 320 and 560 GeV, and sbottom masses are excluded between 280 and 660 GeV, for neutralinos with mass 110 GeV.

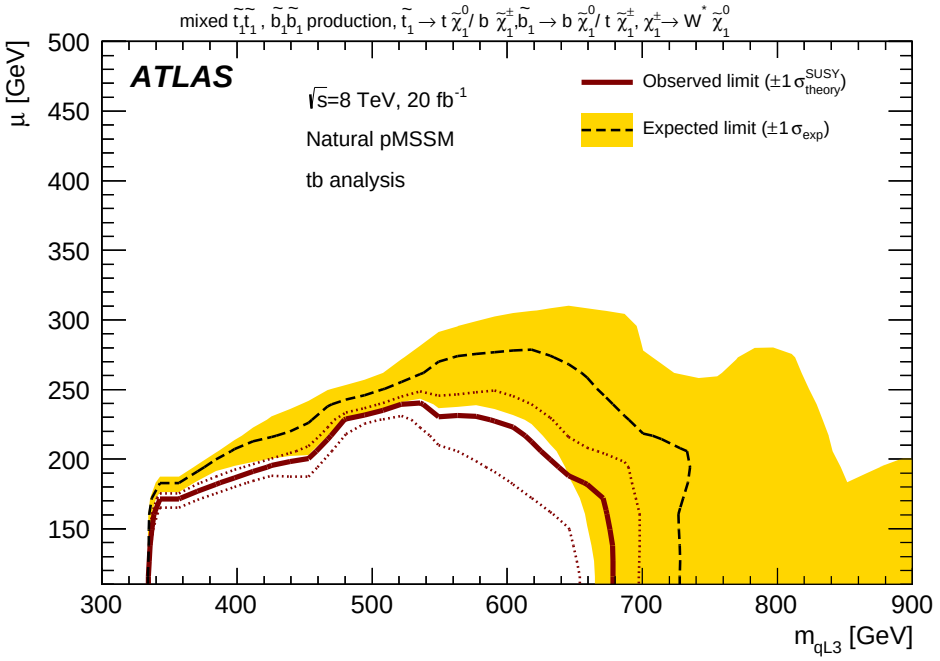

(a) m_{QL3}, μ

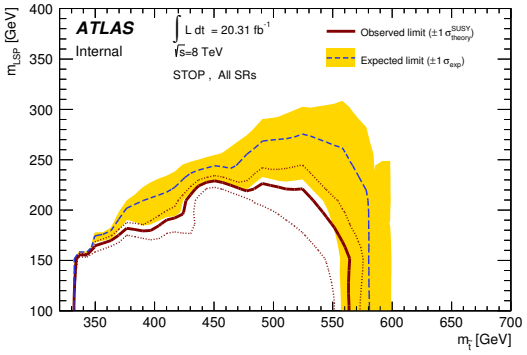

(b) $m_{\tilde{t}}, m_{\tilde{\chi}_1^0}$

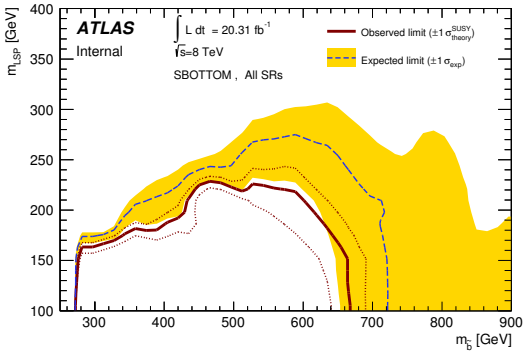

(c) $m_{\tilde{b}}, m_{\tilde{\chi}_1^0}$

FIGURE 7.4: Limits placed in (a) the natural pMSSM μ-m_{qL3} phase space, (b) the $m_{\tilde{t}}, m_{\tilde{\chi}_1^0}$ mass plane and (c) the $m_{\tilde{b}}, m_{\tilde{\chi}_1^0}$ mass plane. The blue curve shows the expected confidence level at 95%. The yellow band shows the expected confidence level at $\sigma = \pm 1$. The red curve shows the observed limit at 95% CLs with dashed-red curves representing the $\sigma = \pm 1$ theoretical limits on the signal cross section.

Figures 7.5(a) and 7.5(b) present the exclusion limits placed in the two simplified model scenarios with $\Delta m(\tilde{\chi}_1^{\pm}, \tilde{\chi}_1^0) = 5\,\mathrm{GeV}$ and $\Delta m(\tilde{\chi}_1^{\pm}, \tilde{\chi}_1^0) = 20\,\mathrm{GeV}$ respectively, assuming an equal BR for the $\tilde{t} \to t + \tilde{\chi}_1^0$ and $\tilde{t} \to b + \tilde{\chi}_1^{\pm}$ decays. The impact of the largest discrepancy observed in the SRexA region, is visible in the low mass diagonal region of Figure 7.5(a). For neutralinos with mass 110 GeV, stop quarks with masses between 300 and 510 GeV are excluded, leaving a large set of models uncovered to be targeted in Run 2.

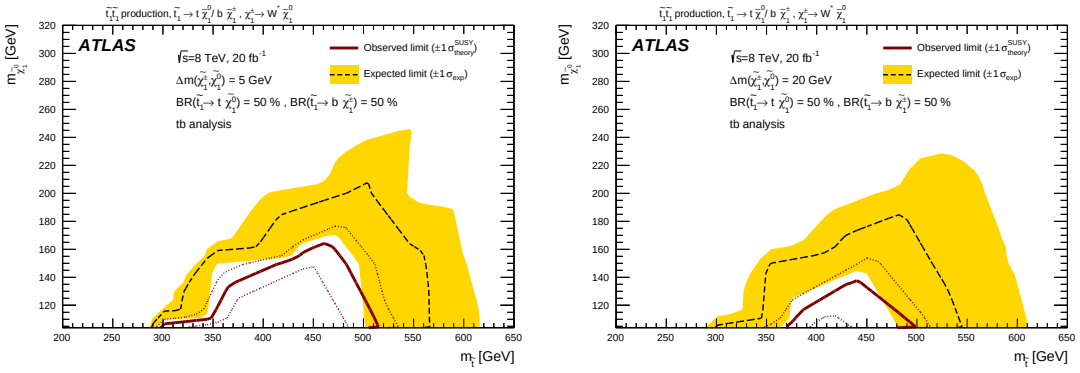

(a) $m_{\tilde{t}}$, $m_{\tilde{\chi}_1^0}$, $\Delta m(\tilde{\chi}_1^{\pm}, \tilde{\chi}_1^0) = 5\,\mathrm{GeV}$

(b) $m_{\tilde{t}}$, $m_{\tilde{\chi}_1^0}$, $\Delta m(\tilde{\chi}_1^{\pm}, \tilde{\chi}_1^0) = 20\,\mathrm{GeV}$

FIGURE 7.5: Combined SR limit plot in the asymmetric simplified model scenarios considered assuming $\mathrm{BR}(\tilde{t} \to t + \tilde{\chi}_1^0) = 50\%$. The red curve presents the observed limit at the 95% CL. The blue curve shows the expected confidence level at 95%. The yellow band shows the expected confidence level at $\sigma = \pm 1$.

Figure 7.5(b) presents the limits in the $\Delta m(\tilde{\chi}_1^{\pm}, \tilde{\chi}_1^0) = 20\,\mathrm{GeV}$ scenario. The significant differences between the kinematics of the $\Delta m(\tilde{\chi}_1^{\pm}, \tilde{\chi}_1^0) = 5\,\mathrm{GeV}$ and $\Delta m(\tilde{\chi}_1^{\pm}, \tilde{\chi}_1^0) = 20\,\mathrm{GeV}$ scenarios lead to weaker expected limits in the case of the $\Delta m(\tilde{\chi}_1^{\pm}, \tilde{\chi}_1^0) = 20\,\mathrm{GeV}$ scenario as the decay product of the W^* are visible, reducing the number of events passing the exclusive selection. Stop masses are excluded between 370 and 500 GeV for $m_{\tilde{\chi}_1^0} = 110\,\mathrm{GeV}$ in these scenarios.

7.3 $tb + E_{\mathrm{T}}^{\mathrm{miss}}$ Run 2 Analysis

The Run 2 search is optimised solely on the simplified model scenario, considering the pair production of sbottoms decaying asymmetrically via $\tilde{b}\tilde{b} \to b\tilde{\chi}_1^0 + t\tilde{\chi}_1^{\pm}$. The chargino-neutralino mass splitting is taken to be 1 GeV in these scenarios. This provides similar decay kinematics to the simplified models considered in the Run 1 analysis. The analysis was performed concurrently with the sbottom 2016 analysis, with a statistical combination of the $tb + E_{\mathrm{T}}^{\mathrm{miss}}$ and sbottom analyses foreseen to provide stronger constraints in

case of null results in the mixed scenario. As such, some analysis choices for the Run 2 $tb + E_{\mathrm{T}}^{\mathrm{miss}}$ analysis are designed to ease the statistical combination of the analyses.

In the following sections an overview of the updates to the Run 1 analysis are presented, including the definition of a new SR to target the models characterised by a small mass difference between $\tilde{b}$ and $\tilde{\chi}_1^0$ ($\approx m_t$) and the reoptimisation of the SRs that are based on the Run 1 analysis. The CR/VR strategy is presented for both the Run 1 based regions and the new region. The dominant systematic uncertainties are discussed briefly as they are calculated in an identical manner to the sbottom 2016 analysis. Finally the background-only fit results and the statistical interpretation of both the $tb + E_{\mathrm{T}}^{\mathrm{miss}}$ analysis on its own, and the combined sbottom and $tb + E_{\mathrm{T}}^{\mathrm{miss}}$ analyses are presented.

7.3.1 Signal kinematic studies

The optimisation studies for the analysis are focused on maximising the sensitivity to the mixed-decay scenarios, where one leg of the decay proceeds via $\tilde{b} \to b + \tilde{\chi}_1^0$ and the other leg proceeds via $\tilde{b} \to t\tilde{\chi}_1^{\pm}$, with the subsequent decay $\tilde{\chi}_1^{\pm} \to W^* + \tilde{\chi}_1^0$.

During the production of the samples to be used for the analysis, it was found that there are no noticable kinematic differences between the scenarios with mass splitting = 1 GeV or 5 GeV, and models with $\Delta m(\tilde{\chi}_1^{\pm}, \tilde{\chi}_1^0) = 1\,\mathrm{GeV}$ have been chosen. An additional check was performed to investigate if there were any significant differences in the pair production of $\tilde{t}$ or $\tilde{b}$ if both decay asymmetrically. The result of these studies was found to be that the decay kinematics are similar, regardless of which squark was produced at the production vertex.

The results of the above investigations allow the simplified scenarios used in Run 1 search to be placed on an even footing with the Run 2 signals. This implies that the regions used for the Run 1 analysis will be sensitive to the Run 2 signal scenarios and are used as a baseline for the Run 2 search.

As the search was performed in parallel with the sbottom 2016 analysis, the preselection used for the optimisation studies is identical to the preselection used in the sbottom analysis, as presented in Table 6.1. The choice of a common preselection is motivated by the aim of performing a statistical combination of the analyses.

7.3.2 Signal Region definitions

Similarly to the Run 1 analysis, the general SR strategy is to use the am_{T2} variable to reject the contribution from $t\bar{t}$, and m_{T} to reject W+jets. Table 7.19 presents an overview of the SRs defined for the analysis.

The A-type regions for the analysis use the inclusive regions defined in the Run 1 search as a baseline. These regions differed due to the m_{eff} selection, but also due to the $E_{\mathrm{T}}^{\mathrm{miss}}$ and $E_{\mathrm{T}}^{\mathrm{miss}}$ significance selections which were chosen to target different regions of the complex pMSSM phase space. In contrast, the regions defined for the Run 2 analysis use the same $E_{\mathrm{T}}^{\mathrm{miss}}$ and $E_{\mathrm{T}}^{\mathrm{miss}}$ significance selections whilst increasing the m_{eff} selection to target higher sbottom masses. When targeting large mass splitting between the sbottom and the neutralino, the invariant mass of the $b-$jets in the decay provides discrimination between signal and SM background hence a selection of $m_{\mathrm{bb}} > 200\,\mathrm{GeV}$ is introduced. It is found that extrapolating in m_{eff} provides sensitivity to higher mass sbottoms, however a minimum m_{eff} threshold of 450 GeV is used in the lowest m_{eff} SR (SRinA450), with two further SRs defined with $m_{\mathrm{eff}} > 600$ (SRinA600) and $> 750\,\mathrm{GeV}$ (SRinA750) respectively.

The B-type region (SRB) is designed to target the so-called compressed scenario, with $\Delta m(\tilde{b}, \tilde{\chi}_1^0) \approx m_t$. The m_{bb} selection introduced above is inverted and the selections on am_{T2} and the m_{T} variable are loosened to prevent signal event losses. A selection on the $\min m_{\mathrm{T}}(b, E_{\mathrm{T}}^{\mathrm{miss}})$ variable is introduced to provide additional discrimination between signal and the $t\bar{t}$ background.

In addition to the above SRs, a region kinematically close to the selection which exhibited the most significant excess in the Run 1 analysis is defined. This SR, labelled as SRA-300-2j is characterised by a stringent selection on the number of additional jets and is retained as it addresses a topology uncovered by other SUSY searches.

	SRinAx	SRA-300-2j	SRB
Pre-selection	✓	✓	✓
Signal Leptons (e, μ)	1	1	1
$p_{\mathrm{T}}(\ell)$	$> 27\,\mathrm{GeV}$	$> 27\,\mathrm{GeV}$	$> 27\,\mathrm{GeV}$
n_{jets}	≥ 2	$= 2$	≥ 2
$n_{b-\mathrm{jets}}$	2	2	2
$E_{\mathrm{T}}^{\mathrm{miss}}$	$> 200\,\mathrm{GeV}$	$> 200\,\mathrm{GeV}$	$> 200\,\mathrm{GeV}$
$E_{\mathrm{T}}^{\mathrm{miss}}$ significance	$> 8\,\mathrm{GeV}^{\frac{1}{2}}$	$> 8\,\mathrm{GeV}^{\frac{1}{2}}$	$> 8\,\mathrm{GeV}^{\frac{1}{2}}$
$m_{b,l}^{\mathrm{min}}$	$< 170\,\mathrm{GeV}$	$< 170\,\mathrm{GeV}$	$< 170\,\mathrm{GeV}$
$\min \Delta\phi(j, E_{\mathrm{T}}^{\mathrm{miss}})$	> 0.4	> 0.4	> 0.4
am_{T2}	$> 250\,\mathrm{GeV}$	$> 250\,\mathrm{GeV}$	$> 200\,\mathrm{GeV}$
m_{T}	$> 140\,\mathrm{GeV}$	$> 140\,\mathrm{GeV}$	$> 120\,\mathrm{GeV}$
m_{bb}	$> 200\,\mathrm{GeV}$	$> 200\,\mathrm{GeV}$	$< 200\,\mathrm{GeV}$
m_{eff}	$> 450, 600, 750\,\mathrm{GeV}$	$> 300\,\mathrm{GeV}$	$> 300\,\mathrm{GeV}$
$\min m_{\mathrm{T}}(b, E_{\mathrm{T}}^{\mathrm{miss}})$	–	–	$> 200\,\mathrm{GeV}$

TABLE 7.19: Summary of the Run 2 $tb + E_{\mathrm{T}}^{\mathrm{miss}}$ SRs. For the inclusive A regions, the x refers to the m_{eff} selection of the region.

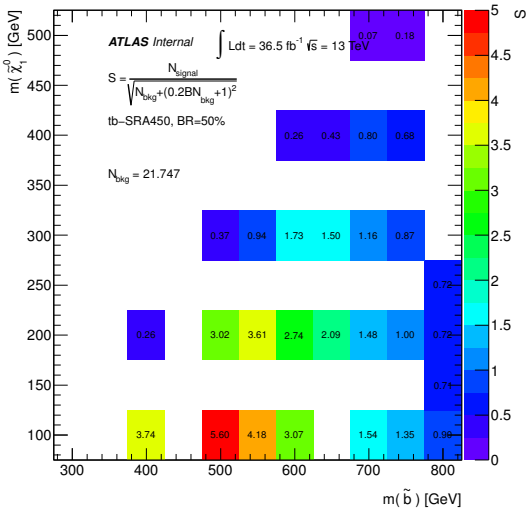

(a) tb-SRA450

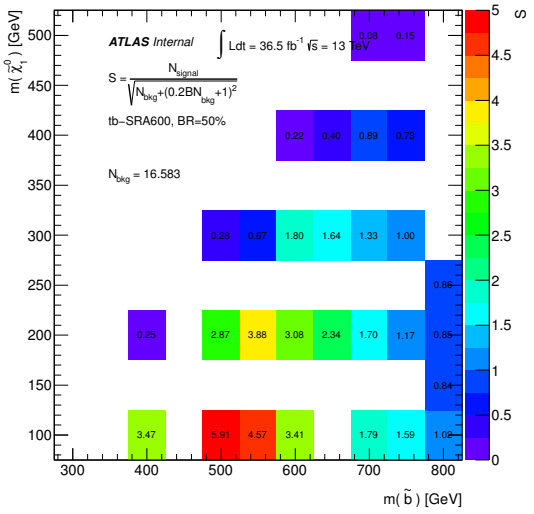

(b) tb-SRA600

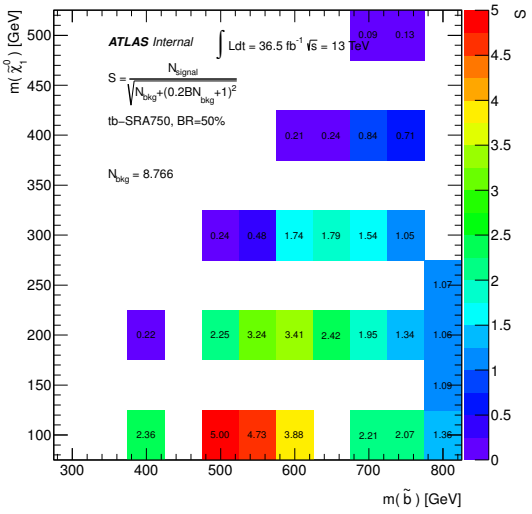

(c) tb-SRA750

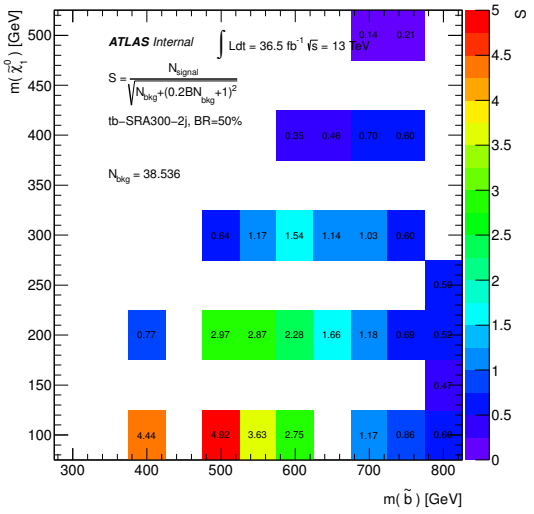

(d) tb-SRA300-2j

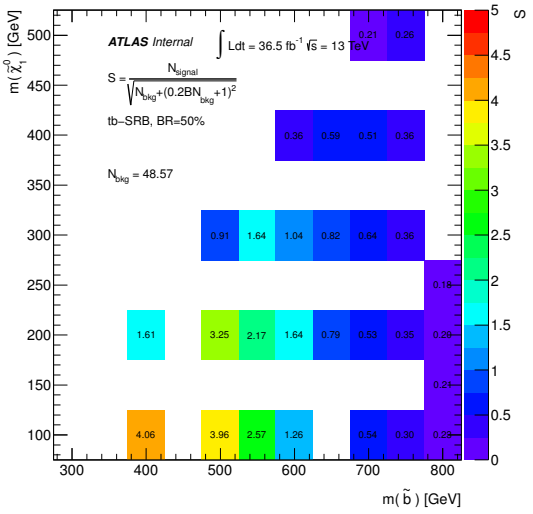

(e) tb-SRB

FIGURE 7.6: Significances for the Run 2 $tb + E_{\mathrm{T}}^{\mathrm{miss}}$ SRs, as defined in Table 7.19.

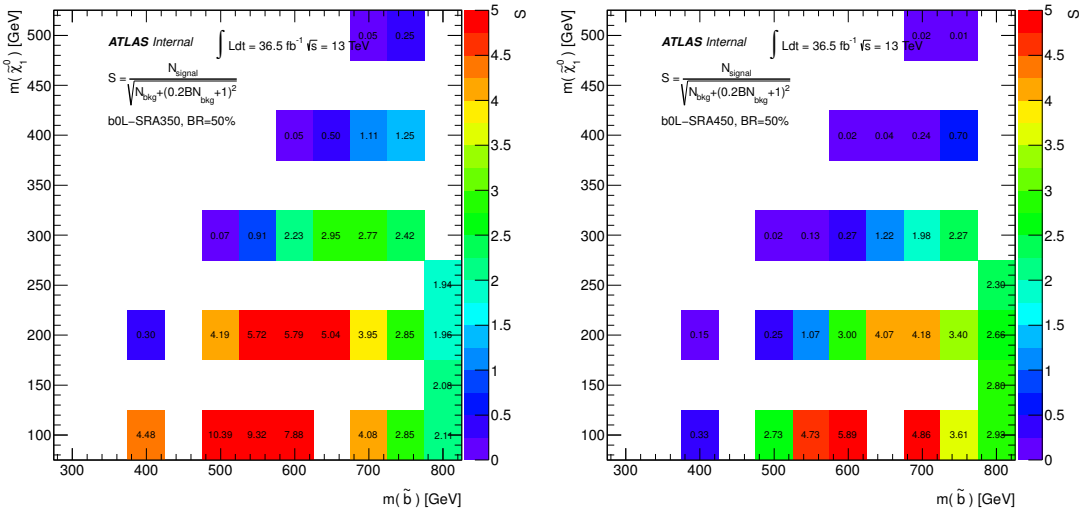

(a) (b)

FIGURE 7.7: Significance of the sbottom 2016 analysis SRA350 and SRA450 regions as defined in Table 6.21, when applied to the asymmetric decay scenario.

The significances obtained with the 50% BR assumption for the $tb + E_{\mathrm{T}}^{\mathrm{miss}}$ SRs are presented in Figure 7.6 for each of the regions defined in the analysis. It is seen that an increased m_{eff} selection targets higher sbottom mass scenarios, whilst the compressed selection Figure 7.6(e) provides the highest sensitivity to the $m_{\tilde{b}}, m_{\tilde{\chi}_1^0} = (400,200)$ mass point. Figure 7.7 presents the significance of the sbottom SRA350 and SRA450 selections when applied to the asymmetric scenario with a BR = 50%. It can be seen that there is a complimentarity between the sbottom and $tb + E_{\mathrm{T}}^{\mathrm{miss}}$ SRs, and a combination of the two would allow for exclusion up to around 800 GeV for scenarios with light neutralinos.

7.3.3 Control Region definitions

The analysis strategy related to the A-type SRs differs significantly to that of the Run 1 analysis. Only two CRs are defined to constrain the backgrounds for the A-type SRs. A dedicated CR for W+jets processes is no longer considered as W+jets events are expected to contribute less than 5% of the total SM background, while a CR is adaped to aid in the estimate of the single-top background. Investigations performed between Run 1 and Run 2 allowed for a selection to be defined which targets the single-top background.

Table 7.20 presents the CRs defined to constrain the $t\bar{t}$ and single-top backgrounds for the A-type regions. The $t\bar{t}$ region is defined with inverted am_{T2} and m_{bb} selections produce a pure $t\bar{t}$ region. As these regions are to be combined with the sbottom 2016

A-type regions, in addition to requiring orthogonality with the SRs, mutually exclusive requirements are also set with respect to the one-lepton sbottom CRs. For the $t\bar{t}$ CR, this is ensured using a selection of $m_{\mathrm{CT}} < 250\,\mathrm{GeV}$. In contrast to this, the single-top CR is identical to the sbottom CRstA region.

Variable	CRttA	CRstA
Pre-selection	✓	✓
n_{Leptons} (e, μ)	1	
$p_{\mathrm{T}}(\ell)$	$> 27\,\mathrm{GeV}$	
$n_{b-\mathrm{jets}}$	2	
$E_{\mathrm{T}}^{\mathrm{miss}}$	$> 200\,\mathrm{GeV}$	
$\min \Delta\phi(j, E_{\mathrm{T}}^{\mathrm{miss}})$	> 0.4	
$m_{b,l}^{\mathrm{min}}$	$< 170\,\mathrm{GeV}$	$> 170\,\mathrm{GeV}$
m_{CT}	$< 250\,\mathrm{GeV}$	$> 250\,\mathrm{GeV}$
m_{bb}	$< 200\,\mathrm{GeV}$	$> 200\,\mathrm{GeV}$
m_{eff}	$> 300\,\mathrm{GeV}$	✗
$E_{\mathrm{T}}^{\mathrm{miss}}$ significance	$> 8\,\mathrm{GeV}^{1/2}$	✗
am_{T2}	$< 250\,\mathrm{GeV}$	✗
$E_{\mathrm{T}}^{\mathrm{miss}}/m_{\mathrm{eff}}$	✗	> 0.25
m_{T}	$> 140\,\mathrm{GeV}$	✗
n_{jets}	> 2	$2, 3, 4$
$p_{\mathrm{T}}(j_1)$	> 35	> 130
$p_{\mathrm{T}}(j_2)$	> 35	> 50
$p_{\mathrm{T}}(j_4)$	> 35 (or $n_{\mathrm{jets}} < 4$)	$[35, 50]$ (or $n_{\mathrm{jets}} < 4$)
Leading $b-$jets	✗	✓

TABLE 7.20: Overview of the control regions associated to the SRinA selections.

There is significant contribution in the SRB region of $t\bar{t}$, single-top and W+jets events. Three CRs are defined, one for each of the main backgrounds. Table 7.21 presents the selections used to define the B-type CRs. The inclusion of the $\min \Delta\phi(b-\mathrm{jets}, E_{\mathrm{T}}^{\mathrm{miss}}) > 2.0$ selection ensures that the selection is mutually exclusive with respect to the sbottom B-type CRs.

The $t\bar{t}$ CR is defined by inverting the am_{T2} and $\min m_{\mathrm{T}}(b, E_{\mathrm{T}}^{\mathrm{miss}})$ selections with respect to the SR requirement. The single-top CR associated with SRB, requires $m_{b,l}^{\mathrm{min}} > 170\,\mathrm{GeV}$ to ensure a selection with high purity of single-top. In addition, the m_{bb} selection is also inverted to reduce the $t\bar{t}$ contributions. Finally the W+jets region is

defined requiring only one $b-$jet in the event. A window in m_{T} of [30, 120] GeV is used to further enhance the $W+$jets contribution in this region.

Variable	CRttB	CRstB	CRwB
Pre-selection	✓	✓	✓
n_{Leptons} (e, μ)		1	
$p_{\mathrm{T}}(\ell)$		$> 27\,\mathrm{GeV}$	
$n_{b-\mathrm{jets}}$	2	2	1
$E_{\mathrm{T}}^{\mathrm{miss}}$		$> 200\,\mathrm{GeV}$	
$\min \Delta\phi(j, E_{\mathrm{T}}^{\mathrm{miss}})$		> 0.4	
$m_{b,l}^{\mathrm{min}}$	$< 170\,\mathrm{GeV}$	$> 170\,\mathrm{GeV}$	$< 170\,\mathrm{GeV}$
m_{bb}	$< 200\,\mathrm{GeV}$	$> 200\,\mathrm{GeV}$	$> 200\,\mathrm{GeV}$
$E_{\mathrm{T}}^{\mathrm{miss}}$ significance		> 8	
am_{T2}	$< 200\,\mathrm{GeV}$	✗	$> 200\,\mathrm{GeV}$
m_{T}	$> 120\,\mathrm{GeV}$	[30, 120] GeV	[30, 120] GeV
n_{jets}		> 2	
$\min m_{\mathrm{T}}(b, E_{\mathrm{T}}^{\mathrm{miss}})$	$< 200\,\mathrm{GeV}$	$> 200\,\mathrm{GeV}$	$< 200\,\mathrm{GeV}$
$\min \Delta\phi(b-\mathrm{jets}, E_{\mathrm{T}}^{\mathrm{miss}})$	> 2.0	> 2.0	> 2.0

TABLE 7.21: Summary of the control regions associated to SRB.

$tb + E_{\mathrm{T}}^{\mathrm{miss}}$ **A-type CRs**	CRttA	CRstA
Observed events	975	118
Fitted bkg events	975.04 ± 31.23	118.01 ± 10.84
Fitted $t\bar{t}$ events	915.05 ± 33.06	17.87 ± 3.90
Fitted single-top events	20.87 ± 8.58	52.56 ± 20.84
Fitted W+jets events	15.20 ± 9.17	44.62 ± 15.95
Fitted Z+jets events	$0.34^{+0.37}_{-0.34}$	1.57 ± 0.26
Fitted diboson events	1.99 ± 1.42	0.94 ± 0.29
Fitted ttV events	21.58 ± 1.81	0.45 ± 0.08
MC exp. SM events	927.98	146.20
MC exp. $t\bar{t}$ events	856.38	16.73
MC exp. single-top events	32.50	81.88
MC exp. W+jets events	15.20	44.64
MC exp. Z+jets events	0.34	1.57
MC exp. diboson events	1.99	0.94
MC exp. ttV events	21.57	0.45

TABLE 7.22: Pre- and post-fit background expectations in the A-type control regions. The errors shown are the statistical plus systematic uncertainties.

Table 7.22 presents the pre- and post-fit yields for the A-type CRs. The pre-fit MC expectation in the CRstA region consists of a similar amount of single-top and W+jets. As there is not a specific CR designated to constraining the W+jets background, the W+jets contribution is allowed to float within its uncertainty in the fit. Table 7.24

$tb + E_{\mathrm{T}}^{\mathrm{miss}}$ **B-type CRs**	CRttB	CRstB	CRwB
Observed events	593	277	330
Fitted bkg events	592.97 ± 24.35	276.93 ± 16.61	330.09 ± 18.15
Fitted $t\bar{t}$ events	565.28 ± 24.78	47.75 ± 8.51	84.16 ± 8.88
Fitted single-top events	9.36 ± 3.25	123.62 ± 32.35	23.25 ± 7.46
Fitted W+jets events	8.64 ± 4.57	97.00 ± 23.97	208.77 ± 23.90
Fitted Z+jets events	$0.10^{+0.16}_{-0.10}$	0.78 ± 0.19	1.44 ± 0.50
Fitted diboson events	0.26 ± 0.18	5.66 ± 1.97	12.18 ± 6.28
Fitted ttV events	9.33 ± 0.75	2.12 ± 0.21	0.29 ± 0.08
MC exp. SM events	612.22	297.72	272.98
MC exp. $t\bar{t}$ events	583.52	49.31	86.82
MC exp. single-top events	13.27	175.19	32.94
MC exp. W+jets events	5.75	64.67	139.32
MC exp. Z+jets events	0.10	0.78	1.44
MC exp. diboson events	0.26	5.66	12.17
MC exp. ttV events	9.33	2.12	0.29

TABLE 7.23: Pre- and post-fit background expectations in the B-type control regions. The errors shown are the statistical plus systematic uncertainties.

Normalisation	A-type Fit result	B-type Fit result
$\mu_{t\bar{t}}$	1.07 ± 0.04	0.97 ± 0.05
$\mu_{\mathrm{single-top}}$	0.64 ± 0.25	0.71 ± 0.19
$\mu_{W+\mathrm{jets}}$	–	1.50 ± 0.22

TABLE 7.24: Normalisation parameters corresponding to the fit performed for the $tb + E_{\mathrm{T}}^{\mathrm{miss}}$ Run 2 analysis.

presents the normalisation parameters with the $t\bar{t}$ and single-top contributions both scaled up in the fit procedure. The uncertainty on the single-top normalisation is driven by the small statistics in the CRstA region.

The pre- and post-fit yields for the regions used in the B-type fit are presented in Table 7.23. Single-top is the dominant contribution to the CRstB region, comprising of 43% of the total pre-fit yield compared to 29% W+jets. The use of a 1 $b-$jet CR to constrain W+jets leads to a region dominated by W+jets with only a small contribution from the $t\bar{t}$ and single-top processes. Finally as in the A-type region, the CRttB region is dominated by $t\bar{t}$. The pre-fit MC yield in the CRttB region overestimates the data slightly, which causes the $t\bar{t}$ normalisation to be less than 1, as reported in Table 7.24.

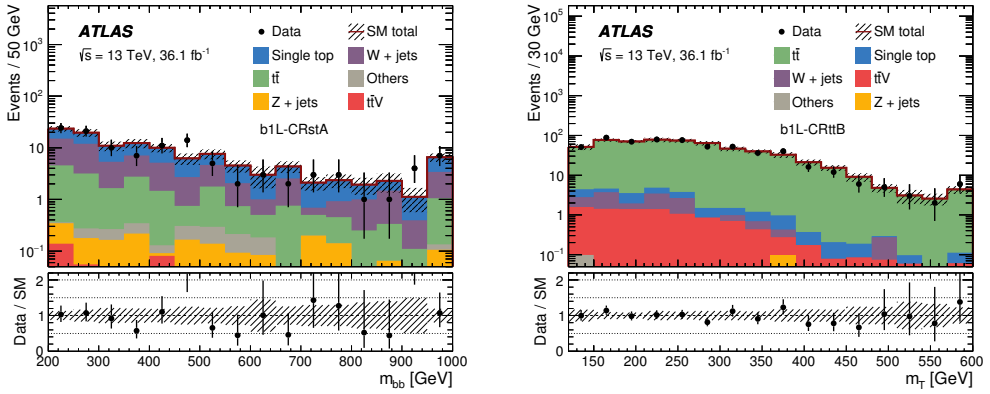

(a) CRstA m_{bb} (b) CRttB m_{T}

FIGURE 7.8: Distributions of key variables used in the definition of the $tb + E_{\mathrm{T}}^{\mathrm{miss}}$ CRs: (a) CRstA, m_{bb}; (b) CRttB, m_{T}. The error bars contain both statistical and systematic uncertainties.

Figure 7.8 presents distributions of: (a) the m_{bb} in the CRstA region; and (b) the m_{T} in the CRttB region. In both regions for both variables the post-fit background expectation is in very good agreement with the observed data.

7.3.4 Validation Region definitions

Two sets of VRs are defined to validate the SM background estimates resulting from the fit procedure for both A- and B-type regions.

The two A-type VRs are defined in Table 7.25. VRA-amT2 aims to validate the modelling of am_{T2} beyond the kinematic end-point by using the SR am_{T2} selection with an inverted m_{bb} requirement. The VRA_mbb uses the same selection as the SR on the m_{bb} variable but an inverted am_{T2} selection to validate the modelling of m_{bb}.

Variable	VRA_amT2	VRA_mbb
Pre-selection	✓	✓
n_{Leptons} (e, μ)	1	
$p_{\mathrm{T}}(\ell)$	$> 27\,\mathrm{GeV}$	
$n_{b-\mathrm{jets}}$	2	
m_{eff}	$> 300\,\mathrm{GeV}$	
$E_{\mathrm{T}}^{\mathrm{miss}}$	$> 200\,\mathrm{GeV}$	
$E_{\mathrm{T}}^{\mathrm{miss}}$ significance	$> 8\,\mathrm{GeV}^{1/2}$	
$\min \Delta\phi(j, E_{\mathrm{T}}^{\mathrm{miss}})$	> 0.4	
am_{T2}	$> 250\,\mathrm{GeV}$	$< 250\,\mathrm{GeV}$
$m_{b,l}^{\mathrm{min}}$	$< 170\,\mathrm{GeV}$	$< 170\,\mathrm{GeV}$
m_{T}	$[30, 140]\,\mathrm{GeV}$	$> 140\,\mathrm{GeV}$
m_{bb}	< 200	$> 200\,\mathrm{GeV}$

TABLE 7.25: Summary of the A-type VRs.

Two B-type regions are defined to validate the normalisations calculated for the B-type fit. These regions aim to validate the modelling of either the am_{T2} or m_{bb} variables.

The VRB_amT2 region is defined requiring the SR selections but with an inverted m_{bb} selection to validate the modelling of am_{T2}. A check of the signal contamination in this region is performed and it is found that the VR does not have a significant amount ($< 15\%$) of signal contamination.

The modelling of m_{bb} in MC simulation is validated in the VRB_mbb region which requires identical selections to the SR, but using a mass window in m_{T} of [30, 120] GeV to ensure orthogonality with the SR.

A-type Validation Regions	VRmbbA	VRamt2A
Observed events	878	89
Fitted bkg events	877.83 ± 339.72	64.97 ± 12.55
Fitted $t\bar{t}$ events	837.60 ± 339.99	19.44 ± 8.62
Fitted single-top events	21.34 ± 11.13	21.96 ± 11.36
Fitted W+jets events	1.62 ± 0.85	21.41 ± 8.41
Fitted Z+jets events	0.05 ± 0.01	0.25 ± 0.10
Fitted diboson events	0.15 ± 0.06	$0.90^{+4.48}_{-0.90}$
Fitted ttV events	17.06 ± 1.29	1.00 ± 0.13
MC exp. SM events	836.19	75.97
MC exp. $t\bar{t}$ events	784.06	18.20
MC exp. single-top events	33.24	34.20
MC exp. W+jets events	1.62	21.41
MC exp. Z+jets events	0.05	0.25
MC exp. diboson events	0.15	0.91
MC exp. ttV events	17.05	1.00

TABLE 7.27: Pre- and post-fit background expectations in the A-type validation regions. The errors shown are the statistical plus systematic uncertainties.

Variable	VRB_amT2	VRB_mbb
Pre-selection	✓	✓
n_{Leptons} (e, μ)	1	
$p_{\mathrm{T}}(\ell)$	$> 27\,\mathrm{GeV}$	
$n_{b-\mathrm{jets}}$	2	
$E_{\mathrm{T}}^{\mathrm{miss}}$	$> 200\,\mathrm{GeV}$	
$E_{\mathrm{T}}^{\mathrm{miss}}$ significance	$> 8\,\mathrm{GeV}^{1/2}$	
$\min \Delta\phi(j, E_{\mathrm{T}}^{\mathrm{miss}})$	> 0.4	
am_{T2}	$> 200\,\mathrm{GeV}$	
$m_{b,l}^{\mathrm{min}}$	$< 170\,\mathrm{GeV}$	
m_{T}	$> 120\,\mathrm{GeV}$	$[30, 120]\,\mathrm{GeV}$
m_{bb}	$> 200\,\mathrm{GeV}$	$< 200\,\mathrm{GeV}$
n_{jets}	> 2	
$\min m_{\mathrm{T}}(b, E_{\mathrm{T}}^{\mathrm{miss}})$	$> 200\,\mathrm{GeV}$	
$\min \Delta\phi(b-\mathrm{jets}, E_{\mathrm{T}}^{\mathrm{miss}})$	> 2.0	

TABLE 7.26: Summary of the B-type Validation Regions.

Table 7.27 displays the pre- and post-fit expectations for the VRA regions. The VRA_amT2 region can be seen pre-fit to consist of relatively equal amounts of $t\bar{t}$, single-top and W+jets. Post-fit there is a 1.6σ discrepancy between the observed number of

B-Type Validation Regions	tb_VRamt2B	tb_VRmbbB
Observed events	53	517
Fitted bkg events	41.08 ± 9.50	520.81 ± 136.09
Fitted $t\bar{t}$ events	16.71 ± 7.27	276.87 ± 128.31
Fitted single-top events	15.31 ± 6.74	46.88 ± 18.96
Fitted W+jets events	$1.38^{+1.84}_{-1.38}$	181.21 ± 65.08
Fitted Z+jets events	0.02 ± 0.00	1.09 ± 0.32
Fitted $t\bar{t} + V$ events	7.61 ± 0.66	3.85 ± 0.45
Fitted diboson events	0.05 ± 0.01	10.90 ± 1.81
MC exp. SM events	47.55	489.10
MC exp. $t\bar{t}$ events	17.26	286.10
MC exp. single-top events	21.70	66.47
MC exp. W+jets events	0.91	120.68
MC exp. Z+jets events	0.02	1.09
MC exp. $t\bar{t} + V$ events	7.61	3.86
MC exp. diboson events	0.05	10.91

TABLE 7.28: Pre- and post-fit background expectations in the SRB validation and signal regions. The errors shown are the statistical plus systematic uncertainties. Uncertainties on the fitted yields are symmetric by construction, where the negative error is truncated when reaching to zero event yield.

events and the expected number of background events. This has been studied in detail and found to be due to a mismodelling of the am_{T2} variable in MC simulation, which is observed also at the preselection level. This mismodelling is covered by the modelling uncertainties of the $t\bar{t}$ and single-top processes. The VRA_mbb region shows very good agreement between the data and the expected background estimate.

The fit results of the B-type VRs are presented in Table 7.28. A slight discrepancy is observed in the VRB_amT2 region used to validate the modelling of the am_{T2} variable, however this is the level of less than 1σ. The VRA_mbb region has good agreement bewtween the expected and observed number of events.

7.3.5 Systematic uncertainties

The systematic uncertainties considered in the analysis are identical to those in the sbottom 2016 analysis as reported in Section 6.3.5, including the single-top/$t\bar{t}$ interference systematic. Table 7.29 reports the effects of the major detector and modelling uncertainties for the analysis.

The dominant uncertainties are related to the jet energy scale and resolution and to the uncertainty on $b-$tagging, which have relatively similar contributions to the total

Source of uncertainty	SRinAs & SRA-300-2j	SRB
Detector uncertainties		
JES	6 - 12%	5%
JER	20 - 30%	4%
$b-$tagging	27 - 36%	11%
Theory uncertainties		
Single-top	30 - 54%	30%
W+jets	<5%	17%
$t\bar{t}$ production	52 - 74%	54%
Total background systematic (% of total background)	23 - 30%	22%

TABLE 7.29: Overview of the dominant detector and modelling uncertainties present in the Run 2 $tb + E_{\mathrm{T}}^{\mathrm{miss}}$ analysis. Due to the similarities between the A-type regions, and the fact that they overlap, a range of values are given for the uncertainties in these regions. The size of the total systematic uncertainty (as a % of the background expectation) is also given. As the uncertainties considered may be correlated, the total uncertainty may not simply be the sum in quadrature of the uncertainties.

overall systematic uncertainty as in the Run 1 analysis. The theoretical uncertainties are the main contributions to the total overall uncertainty, with the uncertainties from the $t\bar{t}$ and single-top modelling leading to the largest contributions.

7.3.6 Intepretation of Results

The results of the background-only fit procedure are presented in Table 7.30. The expected number of background events in the SRinA600 and SRinA750 regions models the observed data very well, whilst there are discrepancies observed in the SRs with the looser m_{eff} selections (SRinA450, SRA-300-2j and SRB). The region with the largest discrepancy between post-fit MC and data is the SRA-300-2j region, at the level of 1.3σ and is partially correlated with the SRinA discrepancy due to the overlapping m_{eff} and jet multiplicity selections of these two regions. The discrepancy in the SRB region is unrelated to the discrepancy in the other regions due to the m_{bb} selection. When compared to the excess in the SRA-300-2j region in Run 1, the excess has decreased from 1.4σ to 1.3σ in Run 2. Figure 7.9(a) presents an N-1 distribution of the m_{eff} in the SRinA600 region, which shows good agreement between the post-fit background expectation and the observed data. The m_{T} distribution in the SRB region is presented in 7.9(b), the post-fit background expectation generally agrees well with the data, however the slight discrepancy in the SRB region is noticable.

Exclusion limits are placed in both the model-independent scenario and in the asymmetric decay scenario assuming an equal BR for the $\tilde{b} \to b + \tilde{\chi}_1^0$ and $\tilde{b} \to t + \tilde{\chi}_1^{\pm}$ decay modes.

$tb + E_{\mathrm{T}}^{\mathrm{miss}}$ **Signal Regions**	SRinA450	SRinA600	SRinA750	SRA-300-2j	SRB
Observed events	33	21	13	12	69
Fitted bkg events	28.08 ± 6.83	22.99 ± 5.37	14.37 ± 3.61	6.28 ± 1.85	53.47 ± 12.04
Fitted $t\bar{t}$ events	12.15 ± 5.89	9.96 ± 4.69	5.46 ± 2.74	2.39 ± 1.32	15.82 ± 7.12
Fitted single-top events	9.07 ± 4.38	6.62 ± 3.23	4.20 ± 2.37	2.88 ± 1.60	10.15 ± 5.32
Fitted W+jets events	1.08 ± 0.54	0.94 ± 0.49	0.59 ± 0.27	0.40 ± 0.26	16.99 ± 8.33
Fitted Z+jets events	0.02 ± 0.00	0.02 ± 0.00	0.02 ± 0.00	0.02 ± 0.00	0.08 ± 0.02
Fitted $t\bar{t} + V$ events	5.68 ± 0.65	5.40 ± 0.65	4.03 ± 0.53	0.55 ± 0.14	8.74 ± 1.14
Fitted diboson events	0.07 ± 0.03	0.05 ± 0.01	0.05 ± 0.02	0.05 ± 0.02	1.68 ± 0.25
MC exp. SM events	26.08	21.45	13.44	5.73	52.54
MC exp. $t\bar{t}$ events	11.41	9.35	5.13	2.24	16.35
MC exp. single-top events	7.83	5.71	3.63	2.48	14.38
MC exp. W+jets events	1.07	0.93	0.59	0.39	11.31
MC exp. Z+jets events	0.02	0.02	0.02	0.02	0.08
MC exp. $t\bar{t} + V$ events	5.68	5.39	4.03	0.55	8.75
MC exp. diboson events	0.07	0.05	0.05	0.05	1.68

TABLE 7.30: Pre- and post-fit background expectations all signal regions. The errors shown are the statistical plus systematic uncertainties.

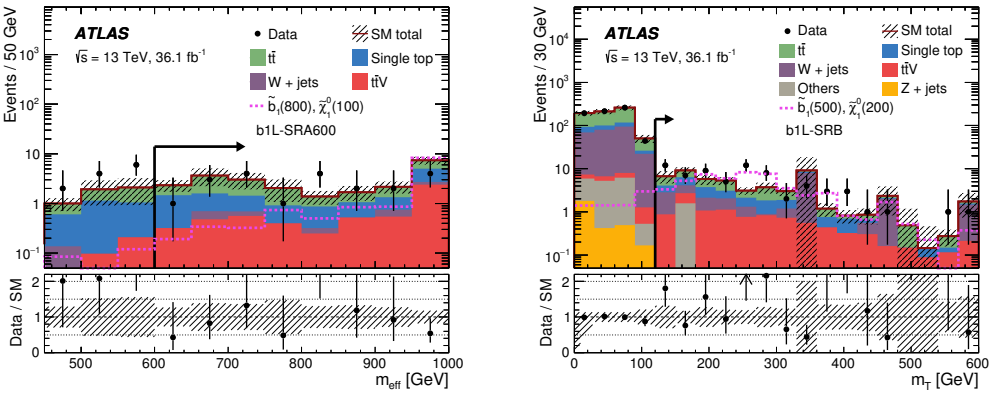

(a) SRinA600 m_{eff} (N-1) (b) SRB m_{T}

FIGURE 7.9: N-1 Distributions of key variables in the SRs: (a) SRinA600, m_{eff}; (b) SRB, m_{T}. The error bars consider both statistical and systematic uncertainties.

Signal Region	$\langle \epsilon A \sigma \rangle_{\mathrm{obs}}^{95}$[fb]	S_{obs}^{95}	S_{exp}^{95}
SRinA450	0.61	22.1	$18.7^{+7.5}_{-4.9}$
SRinA600	0.39	13.9	$15.1^{+5.5}_{-4.2}$
SRinA750	0.28	10.0	$11.9^{+4.2}_{-2.8}$
SRA-300-2j	0.40	14.3	$9.5^{+3.8}_{-2.8}$
SRB	1.14	41.3	$29.5^{+11.1}_{-8.3}$

TABLE 7.31: Model-independent upper limits on the cross section of a generic BSM process. Left to right: 95% CL upper limits on the visible cross section ($\langle \epsilon A \sigma \rangle_{\mathrm{obs}}^{95}$) and on the number of signal events (S_{obs}^{95}). The third column (S_{exp}^{95}) shows the 95% CL upper limit on the number of signal events, given the expected number of background events

Table 7.31 presents the model-independent limits at the 95% CL on the number of additional BSM events corresponding to an upper limit on the visible cross section. Due to the discrepancies in the SRinA450, SRA-300-2j and SRB regions the exclusion limit on the observed number of events is less stringent than the expected limit, whereas for SRinA600 and SRinA750 the exclusion limit on the observed number of events is better than the expected limit.

The model-dependent exclusion limits placed in the $(\tilde{b}, \tilde{\chi}_1^0)$ mass plane are presented in Figure 7.10. Figure 7.10(a) presents the limit using the best expected SR, which is driven in the high mass region by the SRinA600 and SRinA750 regions. In the compressed region the SRB region can be seen to provide exclusion power along the kinematic diagonal (beyond which the $\tilde{b} \to t + \tilde{\chi}_1^{\pm}$ decay is forbidden).

The limits for the SRA-300-2j region can be seen in Figure 7.10(e) where the effects of the discrepancy in this region can be appreciated as the observed limit is weaker than the expected limit. As the SRA-300-2j region is sub-optimal for these scenarios and was kept as a cross-check for the Run 1 discrepancy the signal sensitivity is weaker than the other regions.

7.4 Combination with Sbottom Analysis

As previously shown in Section 7.3.2, the sbottom 2016 analysis is also sensitive to the asymmetric decay scenarios targeted by the 1-lepton analysis. This is primarily due to the sensitivity of the sbottom analysis to the symmetric $\tilde{b} \to b + \tilde{\chi}_1^0$ decay, which occurs in 25% of signal events under the hypothesis of equal BRs for the $\tilde{b} \to b + \tilde{\chi}_1^0$ and $\tilde{b} \to t + \tilde{\chi}_1^{\pm}$. A model-dependent fit is performed using the sbottom 2016 analysis to place exclusion limits in the $(\tilde{b}, \tilde{\chi}_1^0)$ mass plane under such a hypothesis and is shown in Figure 7.11.

Upon comparing the exclusion contours of the two analyses good constraints can be obtained by performing a statistical combination of the $tb + E_{\mathrm{T}}^{\mathrm{miss}}$ and $bb + E_{\mathrm{T}}^{\mathrm{miss}}$ regions, as both analyses have similar reach in the $(\tilde{b}, \tilde{\chi}_1^0)$ mass plane.

The A-type sbottom SRs is combined with the A-type $tb + E_{\mathrm{T}}^{\mathrm{miss}}$ SRs, and the B-type sbottom SR are combined with the B-type $tb + E_{\mathrm{T}}^{\mathrm{miss}}$ SR. The statistical combination of the analyses was foreseen during the design of the $tb + E_{\mathrm{T}}^{\mathrm{miss}}$ analysis and, as mentioned, the regions used for the $tb + E_{\mathrm{T}}^{\mathrm{miss}}$ analysis are designed to be either orthogonal to the sbottom analysis, or to overlap completely to allow the same region to be used for

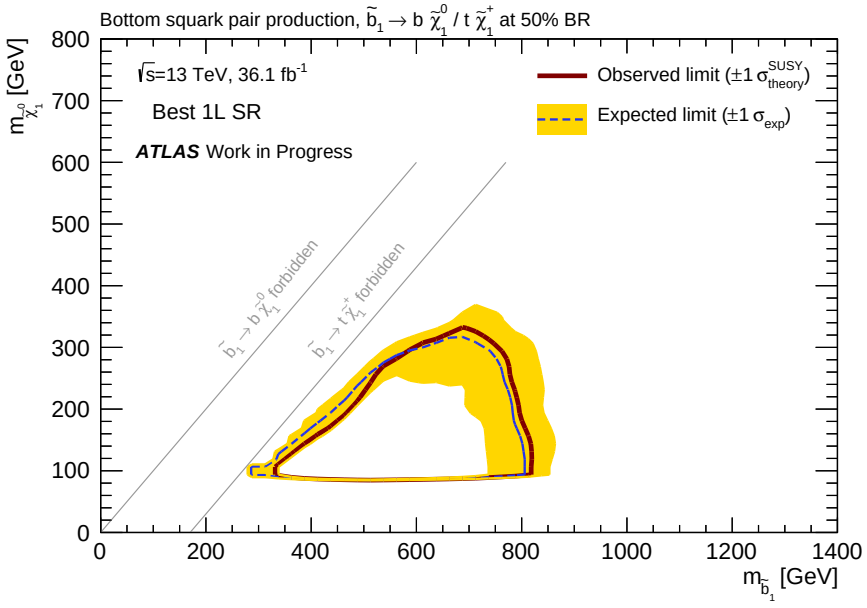

(a) Best Expected SR

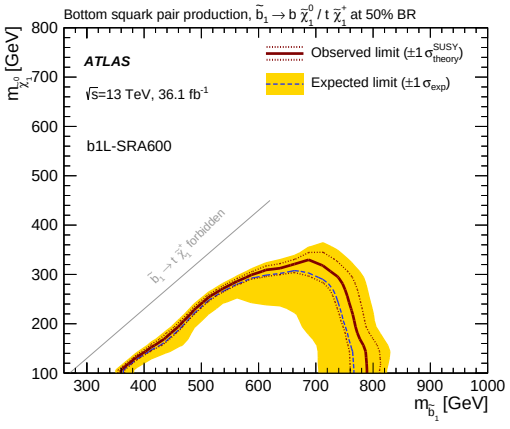

(b) SRinA600

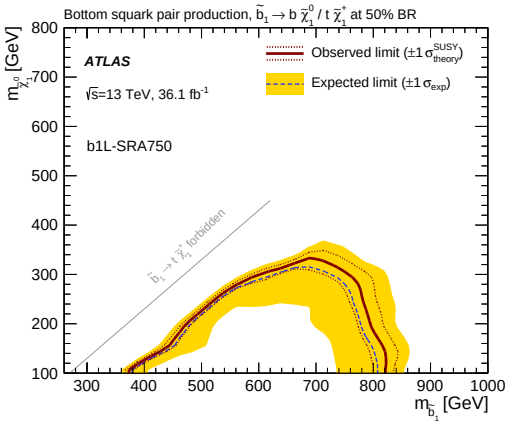

(c) SRinA750

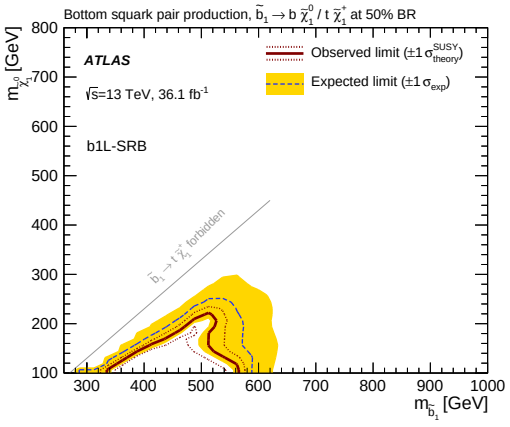

(d) SRB

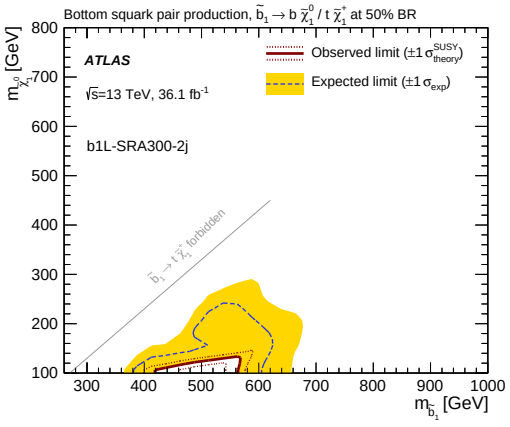

(e) SRA-300-2j

FIGURE 7.10: Expected and observed exclusion limits of the SRs at 95% CL in the $(m_{\tilde{b}}, m_{\tilde{\chi}_1^0})$ plane for the $BR(\tilde{b} \to b + \tilde{\chi}_1^0) = 50\%$ scenario. The dashed black and solid bold red lines show the 95% CL expected and observed limits respectively.

both analyses. When performing the combined fit for the A-type regions, the single-top CR definition is identical for both analyses, as such the same single-top normalisation parameter must be used, which is taken to be the single-top normalisation obtained using the sbottom 2016 fit (Table 6.29, $\mu_{\mathrm{single-top}} = 0.82 \pm 0.35$). This is consistent with the single-top normalisation parameter obtained considering the $tb + E_{\mathrm{T}}^{\mathrm{miss}}$ background-only fit which is $\mu_{\mathrm{single-top}} = 0.64 \pm 0.25$. With the single-top normalisation from the $bb + E_{\mathrm{T}}^{\mathrm{miss}}$ fit, the $\mu_{t\bar{t}}$ also varies within uncertainties. On the other hand, the combined fit for the B-type regions is straightforward as the SRs and CRs for both analyses are mutually exclusive and the fit is performed with the normalisation parameters reported in Tables 6.33 and 7.24.

The likelihood function (as in Equation 6.11) is built using the products of the probabilities from the individual regions in each analysis:

$$L(n, \theta^0 | \mu_{sig}, b, \theta) = P_{\mathrm{SR1}}^{bb+E_{\mathrm{T}}^{\mathrm{miss}}} \times P_{\mathrm{SR1}}^{tb+E_{\mathrm{T}}^{\mathrm{miss}}} \times P_{\mathrm{CRs}}^{bb+E_{\mathrm{T}}^{\mathrm{miss}}} \times P_{\mathrm{CR}}^{tb+E_{\mathrm{T}}^{\mathrm{miss}}} \times C_{\mathrm{syst}} \tag{7.2}$$

The results of the statistical combination are shown in Figure 7.12 for the BR($\tilde{b} \rightarrow b + \tilde{\chi}_1^0$) = 50% scenario, with the best expected SR from the individual analyses also shown as a reference. The statistical combination of the analysis provides exclusion up to larger sbottom masses. For example, compared to the individual analyses which extends to sbottom masses up to 800 GeV for $m_{\tilde{\chi}_1^0} = 110$ GeV, the combined exclusion excludes sbottom masses up to 880 GeV for the same neutralino mass. In the compressed region the sensitivity of the sbottom analysis to the symmetric sbottom decay contributes to the constraints of scenarios in the kinematic limit where the $\tilde{b} \rightarrow t + \tilde{\chi}_1^{\pm}$ decay is only just viable from the conservation of total energy. This region is difficult to target with the $tb + E_{\mathrm{T}}^{\mathrm{miss}}$ analysis as the signal is very similar to the $t\bar{t}$ background. The sensitivity of the $bb + E_{\mathrm{T}}^{\mathrm{miss}}$ analysis to the symmetric $\tilde{b} \rightarrow b + \tilde{\chi}_1^0$ scenario (which occurs in 25% of events) provides exclusion in this region.

7.5 Conclusions

This chapter presented the results from searches performed in Run 1 and Run 2 for stop/sbottom pair production where two decay modes are kinematically available: $\tilde{t}/\tilde{b} \rightarrow t/b + \tilde{\chi}_1^0$ and $\tilde{t}/\tilde{b} \rightarrow b/t + \tilde{\chi}_1^{\pm}$. As the mass splitting between the chargino and neutralino

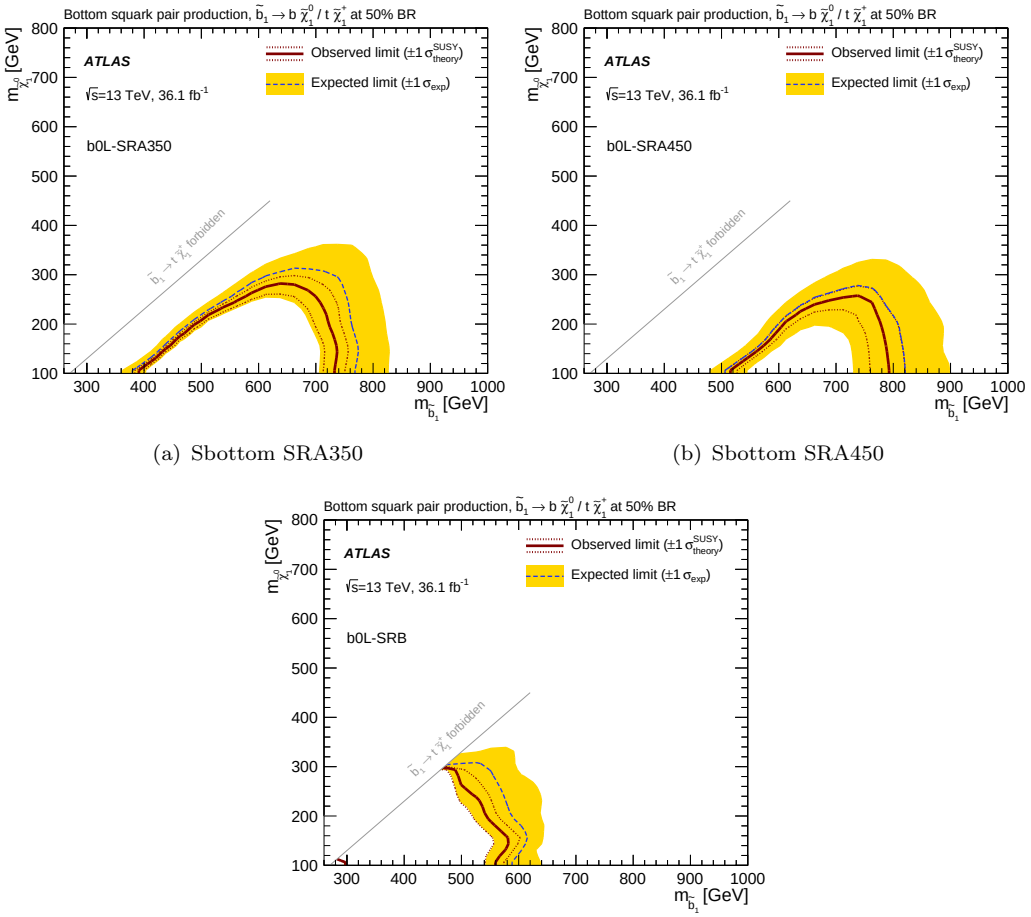

(a) Sbottom SRA350

(b) Sbottom SRA450

(c) Sbottom SRB

FIGURE 7.11: Expected and observed exclusion limits of the sbottom 2016 regions at 95% CL in the $(m_{\tilde{b}}, m_{\tilde{\chi}_1^0})$ plane for the $BR(\tilde{b} \to b + \tilde{\chi}_1^0) = 50\%$ scenario. The dashed black and solid bold red lines show the 95% CL expected and observed limits respectivelyExclusion limits of the three sbottom SRs which have sensitivity in the asymmetric decay scenario at 95% CL

is taken to be small in these scenarios, the chargino decay subsequently proceeds via $\tilde{\chi}_1^{\pm} \to W^* + \tilde{\chi}_1^0$. These searches were unique in that they were specifically optimised to target the asymmetric decay mode, which leads to a final state consisting of a top-quark, a bottom-quark and $E_{\mathrm{T}}^{\mathrm{miss}}$, provided that the W boson is off mass-shell.

The search performed using the $20\,\mathrm{fb}^{-1}$ Run 1 dataset was optimised targeting two signal scenarios. An optimisation was performed on a pMSSM scenario designed such that $\Delta m(\tilde{\chi}_1^{\pm}, \tilde{\chi}_1^0)$ is small, leading to an off-shell W boson, and so the BR of the symmetric decays lead to approximately 50% of events proceeding via the asymmetric final state. In this scenario limits are placed on the common mass parameter of the third generation squarks (m_{QL3}) and the higgsino mass parameter (μ). These limits can be related to direct limits on the stop/sbottom and neutralino masses, with stop masses

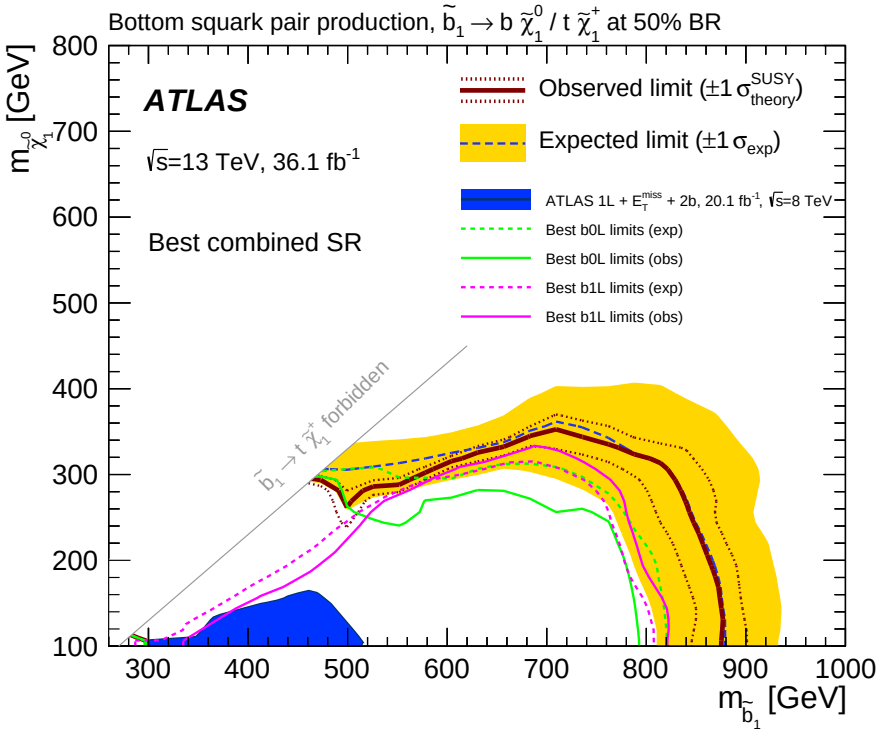

FIGURE 7.12: Exclusion limits produced using the combined fit procedure with the sbottom 2016 and $tb + E_{\mathrm{T}}^{\mathrm{miss}}$ Run 2 analyses, at 95% CL in the $(m_{\tilde{b}}, m_{\tilde{\chi}_1^0})$ plane for the asymmetric decay scenario with $\mathrm{BR}(\tilde{b} \to b + \tilde{\chi}_1^0) = 50\%$. The best expected exclusion for the sbottom analysis (green) and $tb + E_{\mathrm{T}}^{\mathrm{miss}}$ analysis (pink) are also shown for comparison.

excluded up to 560 GeV and sbottom masses excluded up to 660 GeV for neutralinos of mass 110 GeV. An optimisation was also performed targeting stop pair production in a simplified model scenario, with the $\mathrm{BR}(\tilde{t} \to t + \tilde{\chi}_1^0) = 50\%$, and the mass splitting of the lightest gauginos set to either 5, or 20 GeV. For the $\Delta m(\tilde{\chi}_1^{\pm}, \tilde{\chi}_1^0) = 5$ GeV scenario limits are placed on the stop mass up to 510 GeV for neutralinos of mass 110 GeV. When considering the $\Delta m(\tilde{\chi}_1^{\pm}, \tilde{\chi}_1^0) = 20$ GeV scenario the exclusion limits are less stringent and top squark masses are excluded between 370 and 500 GeV for neutralinos of mass 110 GeV.

Using the combined 2015+2016 Run 2 dataset a search was performed in the $tb + E_{\mathrm{T}}^{\mathrm{miss}}$ final state, investigating sbottom pair production with asymmetric decays in a simplified model scenario and assuming $\Delta m(\tilde{\chi}_1^{\pm}, \tilde{\chi}_1^0) = 1$ GeV. The search used the Run 1 analysis as a baseline to define the SRs, however the CR strategy was changed to reflect the different background composition of the SRs when moving from Run 1 to Run 2. Further to this an additional SR to specifically target the compressed region of the phase space was introduced. Exclusion limits are placed in the $\tilde{b}$, $\tilde{\chi}_1^0$ mass plane, with sbottom

masses of between 350 and 800 GeV excluded for neutralinos of mass 110 GeV.

The Run 2 version of the analysis was designed to allow for a statistical combination with the sbottom 2016 analysis. The statistical combination of the analyses provides greater exclusion in the $\tilde{b}$, $\tilde{\chi}_1^0$ phase space, with sbottom masses excluded up to 880 GeV for neutralino masses of 110 GeV. Further to this as the sbottom analysis is unaffected by the kinematic diagonal, beyond which the $\tilde{b} \to t + \tilde{\chi}_1^{\pm}$ decay is forbidden, the sbottom analysis provides additional exclusion in the compressed mass region.

Chapter 8

Search for direct Dark Matter production in association with $b-$jets

This chapter contains an overview of a search performed investigating direct dark matter production in association with $b-$jets using the full 2015 and partial 2016 dataset collected by ATLAS in Run 2, comprising a total luminosity of $13.3\,\text{fb}^{-1}$. The analysis focuses on searching for simplified models for DM production as introduced in Section 2.8. This chapter is heavily based upon the results presented in Ref. [3].

A brief overview of the signal models under investigation is introduced, the main background processes expected when considering the $bb + E_{\text{T}}^{\text{miss}}$ final state are discussed and the signal region is presented. The control regions associated with the SR are documented with the results of the background-only fit results normalisation parameters. These are subsequently validated in the validation regions. Finally the background-only fit results in the SR are shown and the statistical interpretations are given in both model-independent and model-dependent scenarios.

The author's contribution consisted of the development of the CR strategy, analysis cross-checks, the calculation of the modelling uncertainties, and validation of the signal samples.

8.1 Signal Model Overview

Searching for dark matter production using hadron collisions provides complementary results to direct and indirect dark matter detection experiments [144, 145, 146, 147]. When performing a search for dark matter production in hadron collisions the production mechanism for DM is unknown and must be modelled in some way. As discussed in Chapter 2.8, simplified model scenarios are considered when modelling the production of DM in hadron collisions. An important aspect of the models used is the Yukawa-like coupling between the mediator and the fermions, leading to interest in the production of DM in association with top or bottom quarks, the latter is presented in Figure 2.8. The mass-dependent LO cross section for the associated production of either a scalar or pseudoscalar mediator is presented in Figure 8.1 assuming $m_\chi = 1\,\text{GeV}$.

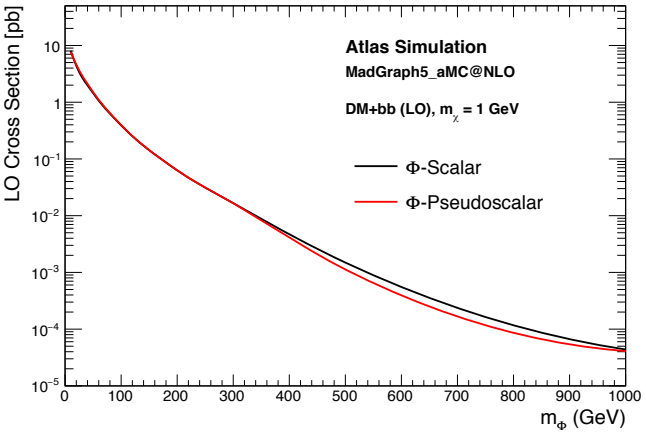

FIGURE 8.1: Leading-Order cross sections for simplified model production of DM in association with $b-$quarks

8.2 Event selection and Signal Region definition

The expected final state consists of 0 leptons, two $b-$jets and $E_{\text{T}}^{\text{miss}}$. The $E_{\text{T}}^{\text{miss}}$ in the event arises from the DM particles and is dependent upon the mass difference between the DM and the mediator, in some scenarios the optimal selection on $E_{\text{T}}^{\text{miss}}$ is lower than the recommended offline trigger threshold of 250 GeV, however it is found that a 2D-hyperbolic selection based upon the leading jet p_{T}, $p_{\text{T}}(j_1)$, and the $E_{\text{T}}^{\text{miss}}$ ensures the trigger is fully efficient:

$$p_{\text{T}}(j_1) > 85\,\text{GeV} \quad E_{\text{T}}^{\text{miss}} > \left(\frac{150 \cdot p_{\text{T}}(j_1) - 11700}{p_{\text{T}}(j_1) - 85}\right)\text{GeV} \tag{8.1}$$

The SM background processes contributing to this final state and passing the trigger requirements are similar to those in sbottom analysis. The dominant contribution arises from the Z+jets process with additional contributions from $t\bar{t}$, single-top, W+jets. Minor contributions are expected from the rare diboson and $t\bar{t}+V$ processes. The contribution from the multi-jet background can be reduced to a negligible level by the application of a selection on $\min \Delta\phi(j, E_{\mathrm{T}}^{\mathrm{miss}})$.

A single SR is defined based upon discriminating between signal and background events using the large separation expected in the (η, ϕ) phase space between the two $b-$jets in the signal. The signal topology suggests low jet multiplicity hence a selection of either 2 or 3 jets is used in addition to the final state requirement of two jets identified as having originated from a $b-$quark. The trigger requirements dictate the selection on $p_{\mathrm{T}}(j_1)$ and a further selection on the leading $b-$jet p_{T} is also used. Table 8.1 contains the full signal region selection employed by the analysis.

Quantity	SR
n_{lepton} (baseline)	0
n_{lepton} (signal)	0
$\min \Delta\phi(j, E_{\mathrm{T}}^{\mathrm{miss}})$	> 0.4
n_{jets}	$2-3$
$n_{\mathrm{b}-jets}$	$= 2$
$p_{\mathrm{T}}(j_1)$ [GeV]	> 100
$p_{\mathrm{T}}(j_2)$ [GeV]	> 20
$p_{\mathrm{T}}(j_3)$ [GeV]	< 60
$p_{\mathrm{T}}(b_1)$ [GeV]	> 50
$E_{\mathrm{T}}^{\mathrm{miss}}$ [GeV]	> 150
ΔR_{min}	> 2.8
$\Delta\eta(b_1, b_2)$	> 0.5
$\mathcal{I}(b_1, b_2)$	> 0.5
$\Delta\phi(b_1, b_2)$	> 2.2

TABLE 8.1: Summary of the signal region selections.

The ΔR_{min} variable is calculated between all jets in the event. In addition to this, the jet imbalance, $\mathcal{I}(b_1, b_2)$, is used to discriminate between the signal and the main Z+jets background as the $b-$jets arising from gluon splitting in the background are expected to have similar transverse momentum resulting in $\mathcal{I} \approx 0$.

SM process	Yield
$t\bar{t}$	5.8 ± 1.5
Z+jets	20.1 ± 6.0
W+jets	1.2 ± 0.8
single-top	2.7 ± 1.1
other	0.00 ± 0.00
Total Expected Background	29.8 ± 6.3

TABLE 8.2: Expected pre-fit background yields in the SR.

Table 8.2 presents the expected background yields in the SR. The dominant contribution is from the Z+jets background, with $Z \to \nu\nu$. The subdominant backgrounds in this region arise from $t\bar{t}$ pair production and single-top, with contributions from the W+jets background. These yields are used to guide the control region strategy.

8.3 Control Region definitions

The four main sources of background are estimated with the aid of three dedicated CRs. A two-lepton (same flavour opposite sign), one-b−jet region (CRZ1b) is defined to estimate contributions from the Z+jets process. The $t\bar{t}$ process is constrained in a one-lepton and two-b−jet region (CRW2b). Due to the similarities between the W+jets and single-top events a single control region, hence a single normalisation parameter, is considered for both processes. This CR (CRW1b) requires one-lepton and one-b−jet.

Regions with a different b−jet multiplicity with respect to the SR are used to keep the regions mutually exclusive to the SR and retain a sufficient number of events. In these regions other selections are loosened based upon the angular variables to further increase the number of events in the region. In the one-b−jet regions the calculation of the angular variables is performed using the non-b−tagged jet with the highest b−tagging weight as the second b−jet.

The CRZ1b region requires the invariant mass of the leptons to be in the Z-mass window [75-105] GeV. The SR selection on $E_{\mathrm{T}}^{\mathrm{miss}}$ is inverted and lowered to 100 GeV and a selection on $E_{\mathrm{T}}^{\mathrm{miss}\prime}$ (the lepton corrected $E_{\mathrm{T}}^{\mathrm{miss}}$ as introduced in Section 6.2.3) is used. A looser $E_{\mathrm{T}}^{\mathrm{miss}}$ selection is employed in the CRW1b region, with a selection of m_{T} between 30-100 GeV to enhance contributions from both W+jets and single-top events. The CRW2b region is very pure in $t\bar{t}$ from the requirement of one lepton and two b−jets. A lower bound of $m_{\mathrm{T}} > 30$ GeV is used to reject events with mismeasured leptons.

Quantity	CRZ1b	CRW1b	CRW2b
n_{lepton} (baseline)	2	1	1
n_{lepton} (signal)	2	1	1
$\min \Delta\phi(j, E_{\mathrm{T}}^{\mathrm{miss}})$	> 0.4	> 0.4	> 0.4
n_{jets}	$2-3$	$2-3$	$2-3$
$n_{\mathrm{b}jets}$	$= 1$	$= 1$	$= 2$
$p_{\mathrm{T}}(j_1)$ [GeV]	> 100	> 100	> 100
$p_{\mathrm{T}}(j_2)$ [GeV]	> 20	> 30	> 20
$p_{\mathrm{T}}(j_3)$ [GeV]	< 60	< 60	< 60
$p_{\mathrm{T}}(b_1)$ [GeV]	> 50	> 50	> 50
$E_{\mathrm{T}}^{\mathrm{miss}}$ [GeV]	< 100	> 130	> 120
$E_{\mathrm{T}}^{\mathrm{miss}\prime}$ [GeV]	> 120	-	-
ΔR_{min}	> 2.8	> 2.5	> 2.8
m_{T}	-	$[30, 100]$	> 30
$m_{\ell\ell}$	$[75, 105]$	-	-
$p_{\mathrm{T}}(\ell_1)$ [GeV]	> 30	> 30	> 30
$p_{\mathrm{T}}(\ell_2)$ [GeV]	> 25	-	-
$\Delta\phi(b_1, b_2)$	> 2.2	$[1, 2.2]$	> 2.2

TABLE 8.3: Summary of the selections of the control regions of the analysis.

Table 8.4 shows the results of the background only fit for the control regions. In each region, the diboson and $t\bar{t}+V$ events (listed collectively as "others") are shown to contribute minimally to the total event yield ($< 1\%$). The total expected pre-fit yields in each region are shown to model the observed number of events well. A relatively large difference arises in the CRW2b region where the MC overestimates the data, however this difference is expected when targeting $t\bar{t}$ events in this region of phase space using the nominal Powheg+Pythia6 sample. This effect has been found in other analyses targetting equally extreme regions of phase space [148]. Figure 8.2 presents key post-fit kinematic distributions in the CRs.

The normalisation parameters for the main backgrounds are presented in Table 8.5. The normalisation parameters further confirm the good modelling of the one-b−jet CRs as they are consistent with unity, whilst the CRW2b leads to $\mu_{t\bar{t}} < 1$. The normalisation parameters for the main backgrounds are validated in a set of VR regions with selections closer to the SR kinematics.

	CRW1b	CRZ1b	CRW2b
Observed	96	176	131
Total background	96.0 ± 9.8	176 ± 13	131 ± 11
W+jets	49.2 ± 7.8	$0.01^{+0.02}_{-0.01}$	4.3 ± 1.8
Z+jets	0.6 ± 0.5	168 ± 13	$0.03^{+0.04}_{-0.03}$
$t\bar{t}$	12.8 ± 2.7	5.8 ± 1.7	109 ± 13
single top	33.1 ± 6.0	1.5 ± 1.0	17.7 ± 4.0
others	$0.3^{+0.4}_{-0.3}$	1.2 ± 0.9	$0.03^{+0.06}_{-0.03}$
pre-fit total	101.2 ± 12.3	159.1 ± 24.1	158.1 ± 3.8
pre-fit W+jets	51 ± 11	$0.02^{+0.02}_{-0.02}$	4.4 ± 1.8
pre-fit Z+jets	0.6 ± 0.4	149 ± 24	$0.03^{+0.04}_{-0.03}$
pre-fit $t\bar{t}$	15.9 ± 2.5	7.2 ± 1.9	135.3 ± 1.6
pre-fit single top	34.3 ± 4.9	1.7 ± 1.1	18.3 ± 3.0
pre-fit others	$0.3^{+0.4}_{-0.3}$	1.2 ± 0.9	$0.07^{+0.08}_{-0.07}$

TABLE 8.4: Fit results in all control regions for an integrated luminosity of $13.3\,\text{fb}^{-1}$. The category "others" includes the very rare backgrounds dibosons and $t\bar{t}+V$.

Normalisation	Value
$\mu_{t\bar{t}}$	0.81 ± 0.1
$\mu_{W+\text{jets/single}-\text{top}}$	0.97 ± 0.2
$\mu_{Z+\text{jets}}$	1.12 ± 0.2

TABLE 8.5: Normalisation factors for the main backgrounds in the DM+bb analysis using the background-only fit with $13.3\,\text{fb}^{-1}$.

8.4 Validation Region definitions

When defining the CRs a significant number of kinematic selections were changed to produce regions enhanced in the dominant backgrounds. To validate the normalisation parameters a set of three VRs with selections more representitive of the SR are designed, described in Table 8.6.

The $t\bar{t}$, single-top and W+jets normalisation parameters are validated in a one lepton one $b-$jet region, VRW1b, which is orthogonal to the CRW1b region due to the requirement of $\Delta\phi(b_1, b_2) > 2.2$. The SR selection on $\Delta\eta(b_1, b_2)$ is also applied to more closely model the SR kinematics. The modelling of the Z+jets background is validated in a two lepton (same flavour, opposite sign), two $b-$jet region (VRZ2b). The invariant mass of the leptons is chosen to be in a tight Z-mass window of between 80-100 GeV. The usage of this tight $m_{\ell\ell}$ selection and requirement of two $b-$jets in the event reduces statistics, preventing the angular selections used in the SR being applied in this region.

The final VR is designed to validate the extrapolation from the one- and two-lepton CRs, to the final state by requiring zero leptons and two $b-$jets (VRLR). To ensure

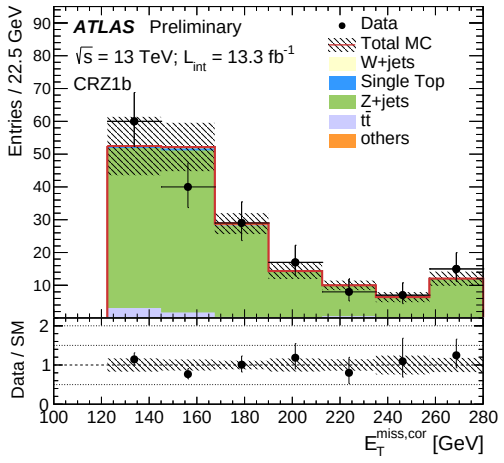

(a) CRZ1b, $E_{\mathrm{T}}^{\mathrm{miss}\,\prime}$

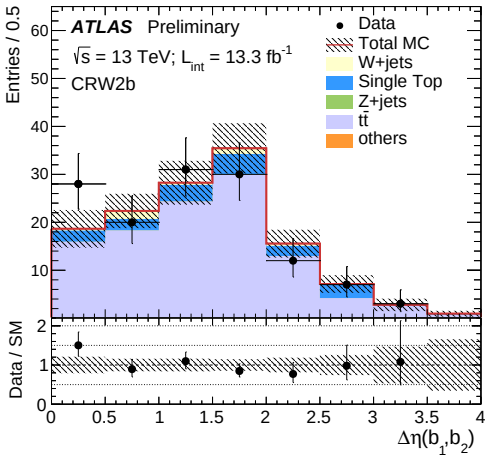

(b) CRW2b, $\Delta\eta(b_1, b_2)$

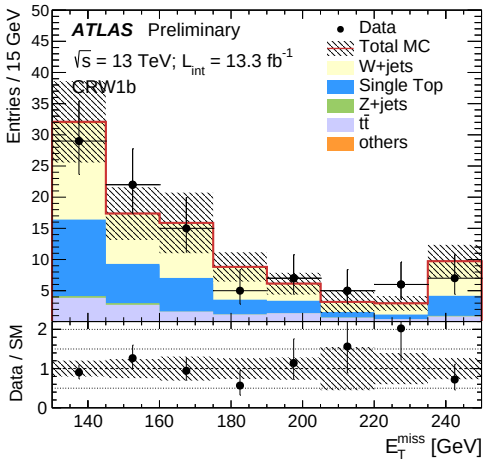

(c) CRW1b, $E_{\mathrm{T}}^{\mathrm{miss}}$

FIGURE 8.2: Post-fit distributions of key kinematic variables in the CRs: (a) CRZ1b $E_{\mathrm{T}}^{\mathrm{miss}\,\prime}$; (b) CRW2b $\Delta\eta(b_1, b_2)$; (c) CRW1b $E_{\mathrm{T}}^{\mathrm{miss}}$. Both systematic and statistical uncertainties are considered.

this region is orthogonal to the SR, a selection of $\Delta R_{\mathrm{min}} < 2.5$ is applied whilst the remainder of the selections used are identical to the SR.

Quantity	VRZ2b	VRW1b	VRLR
n_{lepton} (baseline)	2	1	0
n_{lepton} (signal)	2	1	0
$\min \Delta\phi(j, E_{\mathrm{T}}^{\mathrm{miss}})$	> 0.4	> 0.4	> 0.4
n_{jets}	$2-3$	$2-3$	$2-3$
$n_{\mathrm{b-}jets}$	$= 2$	$= 1$	$= 2$
$p_{\mathrm{T}}(j_1)$ GeV	> 85	> 100	> 100
$p_{\mathrm{T}}(j_2)$ GeV	> 20	> 30	> 20
$p_{\mathrm{T}}(j_3)$ GeV	< 60	< 60	< 60
$p_{\mathrm{T}}(b_1)$ GeV	> 50	> 50	> 50
$E_{\mathrm{T}}^{\mathrm{miss}}$ GeV	< 80	> 150	> 150
$E_{\mathrm{T}}^{\mathrm{miss}\prime}$ GeV	> 100	-	-
ΔR_{min}	> 2.8	> 2.8	< 2.5
$\Delta\eta(b_1, b_2)$	-	> 0.5	> 0.5
$\mathcal{I}(b_1, b_2)$	-	-	> 0.5
m_{T}	-	$[30, 100]$	-
$m_{\ell\ell}$	$[80, 100]$	-	-
$p_{\mathrm{T}}(\ell_1)$ GeV	> 30	> 30	-
$p_{\mathrm{T}}(\ell_2)$ GeV	> 25	-	-
$\Delta\phi(b_1, b_2)$	-	> 2.2	> 2.2

TABLE 8.6: Summary of the selections of the validation regions of the analysis.

	VRW1b	VRZ2b	VRLR
Observed	121	67	87
Total background	105 ± 20	58 ± 13	98 ± 18
W+jets	30.2 ± 8.3	-	3.4 ± 1.2
Z+jets	1.0 ± 0.6	49.7 ± 11.5	36.7 ± 9.2
$t\bar{t}$	26.0 ± 7.9	7.8 ± 2.6	47 ± 14
single top	47 ± 10	0.52 ± 0.44	10.7 ± 3.0
others	0.5 ± 0.3	$0.04^{+0.07}_{-0.04}$	0.1 ± 0.1
pre-fit total	113.6 ± 14.5	54.3 ± 12.4	105.6 ± 19.6
pre-fit W+jets	31.3 ± 8.4	-	3.5 ± 1.3
pre-fit Z+jets	0.9 ± 0.5	44 ± 12	33 ± 11
pre-fit $t\bar{t}$	32.3 ± 9.1	9.7 ± 2.9	58 ± 16
pre-fit single top	48.6 ± 7.6	0.54 ± 0.45	11.0 ± 2.6
pre-fit others	0.5 ± 0.3	$0.04^{+0.07}_{-0.04}$	0.1 ± 0.1

TABLE 8.7: Fit results in all validation regions for an integrated luminosity of 13.3 fb^{-1}. The category "others" includes the subdominant backgrounds such as diboson and $t\bar{t}$+V production.

Table 8.7 presents the background-only fit results for the validation regions. The observed yield and post-fit expectations are in agreement to within 1σ in all regions. Importantly the zero lepton VRLR region is modelled well, providing confidence in the

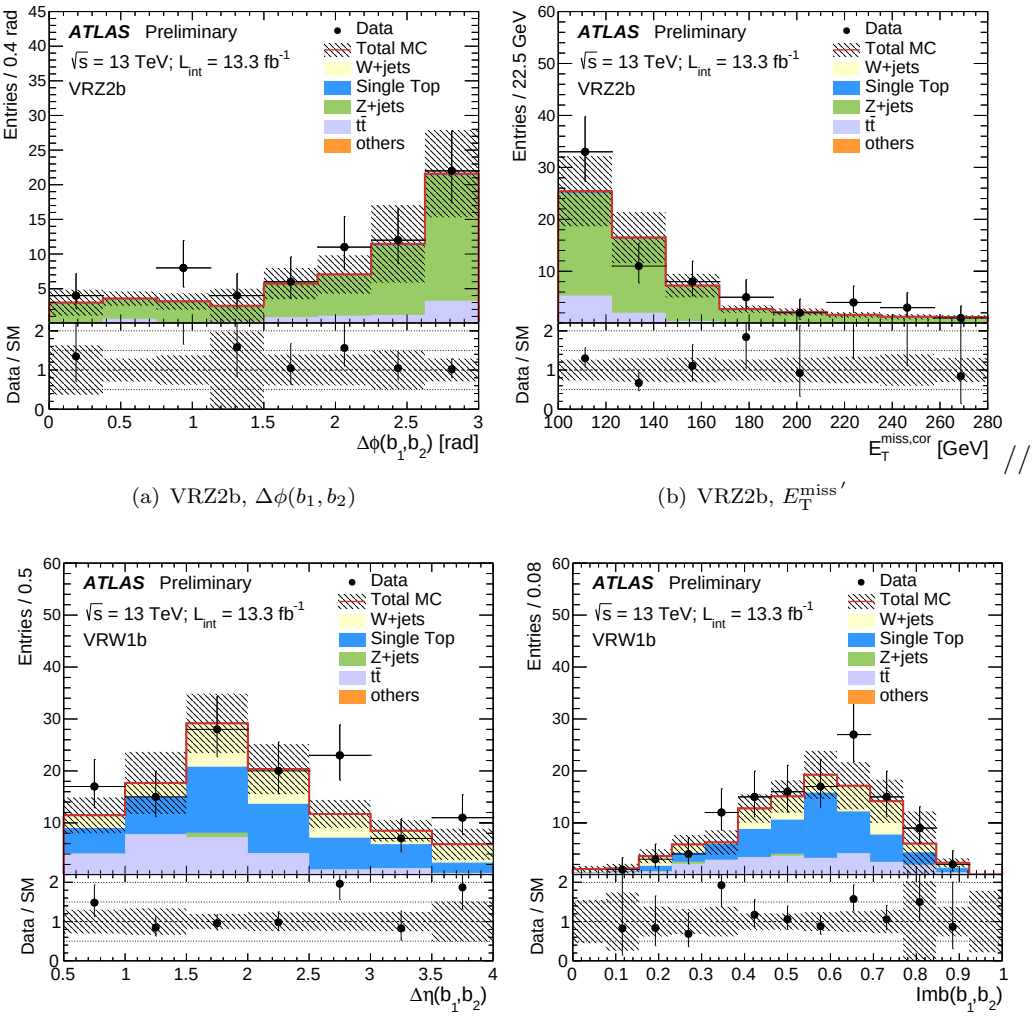

(a) VRZ2b, $\Delta\phi(b_1, b_2)$

(b) VRZ2b, $E_{\mathrm{T}}^{\mathrm{miss}\prime}$

(c) VRW1b, $\Delta\eta(b_1, b_2)$

(d) VRW1b, $\mathcal{I}(b_1, b_2)$

FIGURE 8.3: Post-fit distributions for key variables in the one- and two-lepton VRs. Both statistical and systematic uncertainties are considered.

extrapolation from the one/two lepton CRs to the zero lepton SR. Figure 8.3 presents a selection of post-fit distributions in the one- and two-lepton VRs showing very good agreement between the post-fit background expectation and the observed data.

8.5 Systematic uncertainties

The detector and modelling uncertainties considered for the analysis are evaluated in an identical manner to the uncertainties considered for both the sbottom analysis and the $tb + E_{\mathrm{T}}^{\mathrm{miss}}$ Run 2 analysis, as previously discussed in Section 6.2.6.

Table 8.8 contains an overview of the dominant systematic uncertainties in the analysis. As expected, with the final state under consideration, the main detector uncertainties

are jet related (JES and JER). A large contribution also arises from the flavour tagging uncertainty. The $E_{\mathrm{T}}^{\mathrm{miss}}$ uncertainty is a significant contribution which arises from the 2D-hyperbolic selection used to ensure events pass the trigger threshold.

The main modelling uncertainty is due to the modelling of the Z+jets process. The contributions from the subdominant backgrounds, $t\bar{t}$, single-top and W+jets, are a much smaller contribution to the overall modelling uncertainty.

Source of uncertainty	SR
Detector uncertainties	
JES	20.6%
JER	7.2%
$b-$tagging	36%
$E_{\mathrm{T}}^{\mathrm{miss}}$	43%
Modelling uncertainties	
Z+jets	62%
W+jets	6.4%
$t\bar{t}$	10%
single-top	6.3%
Total background systematic (% of expected background)	21%

TABLE 8.8: Overview of the dominant detector and modelling uncertainties present in the DM+bb analysis. The size of the total systematic uncertainty (as a % of the background expectation) is also given. As the uncertainties considered may be correlated, the total uncertainty may not simply be the sum in quadrature of the uncertainties.

8.6 Results and Interpretations

The results of the background-only fit procedure are presented in Table 8.9. The largest background in the region is the Z+jets process, which comprises of over 70% of the total post-fit yield. The observed number of events and expected background post-fit are in very good agreement. Both model-independent and model-dependent limits are placed at the 95% CL. The results are interpreted in the two model dependent scenarios considered and limits are placed on the production cross-section for both scalar and pseudoscalar mediators.

Figure 8.4 presents the distributions of $\mathcal{I}$ and ΔR_{min}, further confirming the good modelling in the SR.

Table 8.10 presents the model-independent limits on the cross-section of a generic BSM process in addition to the upper-limits on the number of additional BSM events given the observed and the background yields.

	SR
Observed	33
Total background	31.0 ± 6.2
W+jets	1.2 ± 0.8
Z+jets	22.6 ± 5.7
$t\bar{t}$	4.7 ± 1.4
single top	2.6 ± 1.1
others	-
pre-fit total	29.8 ± 6.3
pre-fit W+jets	1.2 ± 0.8
pre-fit Z+jets	20.1 ± 6.0
pre-fit $t\bar{t}$	5.8 ± 1.5
pre-fit single top	2.7 ± 1.1
pre-fit others	-

TABLE 8.9: Fit results in the SR for an integrated luminosity of $13.3\,\text{fb}^{-1}$. The category "others" includes the subdominant backgrounds such as diboson and $t\bar{t}+V$ production.

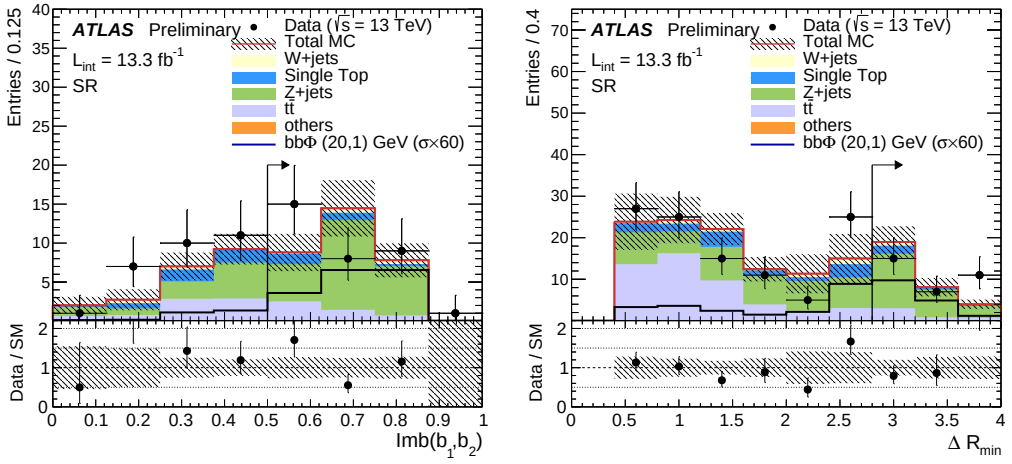

(a) $\mathcal{I}(b_1, b_2)$ (b) ΔR_{min}

FIGURE 8.4: Distributions of (a) p_{T} asymmetry $\mathcal{I}$ and (b) ΔR_{min} with all signal region selections applied except the selection on the variable, which is denoted by the arrow. One signal model with $(m_\phi, m_\chi) = (20, 1)\,\text{GeV}$ is shown, with the cross section scaled by a factor of 60. All statistical and systematic uncertainties are included.

Signal channel	$\langle \epsilon A \sigma \rangle^{95}_{\text{obs}}$[fb]	S^{95}_{obs}	S^{95}_{exp}
SR	1.38	18.3	$16.8^{+5.7}_{-4.3}$

TABLE 8.10: Left to right: 95% CL upper limits on the visible cross-section ($\langle \epsilon A \sigma \rangle^{95}_{\text{obs}}$) and on the number of BSM events (S^{95}_{obs}). The third column (S^{95}_{exp}) shows the 95% CL upper limit on the number of signal events, given the expected number of background events.

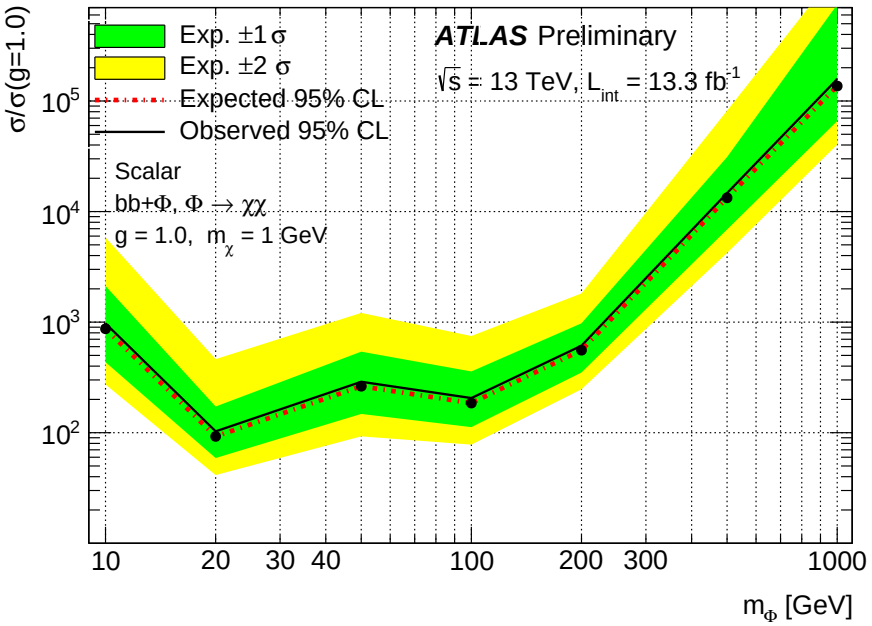

FIGURE 8.5: Cross section upper limits placed on the production of scalar mediators assuming a DM mass of 1 GeV for 13.3 fb^{-1} of data.

Figures 8.5 and 8.6 present the limits placed on the production cross sections of both scalar and pseudoscalar mediators respectively, with the assumption that $m_\chi = 1\,\text{GeV}$. As the observed and post-fit background yields agree to such a level the expected and observed 95% CL limits are very similar.

8.7 Conclusions

The chapter presented an overview of a search for direct dark matter production in association with $b-$jets using 13.3 fb^{-1} of Run 2 data collected by ATLAS. As previously discussed using an EFT approach to model the production of DM at LHC energies is not necessarily valid and this search uses simplified model scenarios with either a scalar or pseudoscalar mediator. The mediator provides a link between the fermionic sector and the dark sector and the free parameters in these models are the masses of the mediator

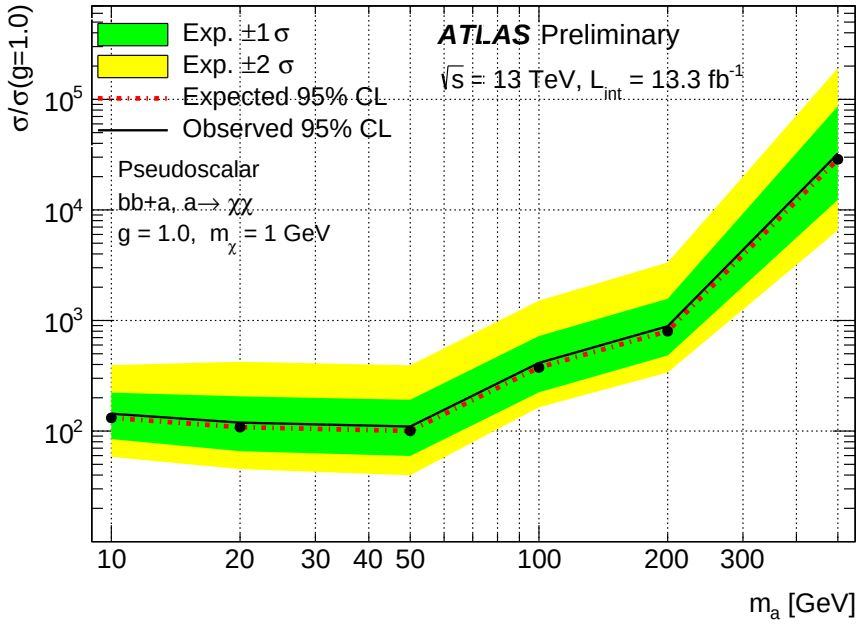

FIGURE 8.6: Cross section upper limits placed on the production of pseudoscalar mediators assuming a DM mass of 1 GeV for 13.3 fb^{-1} of data.

($m_{\phi/a}$), the DM mass (m_χ) and the couplings of the mediator to the fermionic sector (g_f) and dark sector (g_χ). No significant excesses are observed in the SR and limits are placed on the production cross section for scalar mediators with masses between 10-1000 GeV and pseudoscalar mediators with masses between 10 and 500 GeV, for a DM particle of mass 1 GeV.

Chapter 9

Summary

The high quality data collected by ATLAS over the course of both Run 1 and Run 2 has been used in a plethora of physics analyses including precision measurements of SM processes, the discovery of the Higgs boson, and many BSM searches. These analyses have returned results consistent with the predictions made by the SM. Analyses performed searching for the direct production of particles expected by a variety of BSM physics theories, such as SUSY, have so-far returned null results. This thesis contains the results of searches for three such BSM processes.

Chapter 6 contains two searches investigating the direct pair production of bottom squarks decaying via $\tilde{b} \to b + \tilde{\chi}_1^0$ at $\sqrt{s} = 13\,\text{TeV}$, in the 0-lepton, 2-$b$−jets and $E_{\text{T}}^{\text{miss}}$ final state. The first of these searches was performed using the $3.2\,\text{fb}^{-1}$ of luminosity collected during 2015 and, at the time, placed world-leading exclusion limits on sbottom pair production, with sbottom masses excluded up to 840 GeV, for massless neutralinos [1]. The second search improves upon the previous analysis and uses the full 2015 and 2016 dataset with a total luminosity of $36.1\,\text{fb}^{-1}$. This analysis provided additional sensitivity to more massive sbottoms, with an expected exclusion power of up to 1030 GeV for sbottom masses, and extended the exclusion limits to sbottom masses up to 950 GeV, assuming massless neutralinos.

Two searches for pair production of either top or bottom squarks decaying asymmetrically are presented in Chapter 7. These searches investigated scenarios where multiple decay modes are open for the sbottom/stop: $\tilde{t}\tilde{t}/\tilde{b}\tilde{b} \to tb + \tilde{\chi}_1^0\tilde{\chi}_1^{\pm}$. These scenarios lead to a complex final state consisting of a top quark, bottom quark and $E_{\text{T}}^{\text{miss}}$, and targeted the one-lepton, two-b−jets and $E_{\text{T}}^{\text{miss}}$ final state. The first search, performed in Run 1, targeted both pMSSM scenarios and simplified model scenarios characterised by

a small mass splitting between the $\tilde{\chi}_1^\pm$ and $\tilde{\chi}_1^0$. For the pMSSM scenarios, exclusion limits were placed on the m_{Ql3} and μ mass parameters with m_{Ql3} excluded between 340 and 680 GeV for $\mu = 110$ GeV. In the simplified model scenarios considered, exclusion limits are placed on stop masses assuming equal branching ratios for the $\tilde{t} \to t + \tilde{\chi}_1^0$ and $\tilde{t} \to b + \tilde{\chi}_1^\pm$ decays. For the $\Delta m(\tilde{\chi}_1^\pm, \tilde{\chi}_1^0) = 5$ GeV scenario, stop masses are excluded between 300 and 510 GeV for $m_{\tilde{\chi}_1^0} = 110$ GeV. Weaker limits are placed in the $\Delta m(\tilde{\chi}_1^\pm, \tilde{\chi}_1^0) = 20$ GeV scenario, where stop masses are excluded between 370 and 500 GeV for an equivalent neutralino mass. The second search was performed using the 2015 and 2016 data collected during Run 2, focusing on the pair production of sbottoms decaying asymmetrically. This search improved upon the Run 1 analysis, using an improved analysis strategy, setting exclusion limits on sbottom masses between 350 and 800 GeV for neutralinos of mass 110 GeV. A statistical combination of the sbottom and $tb + E_{\mathrm{T}}^{\mathrm{miss}}$ searches was performed, with the combination of the analyses excluding sbottom masses up to 880 GeV for $m_{\tilde{\chi}_1^0}$ =110 GeV.

Finally, Chapter 8 presents a search for direct dark matter production in association with $b-$jets in the 0-lepton, 2-$b-$jets and $E_{\mathrm{T}}^{\mathrm{miss}}$ final state. This search is performed investigating simplified model scenarios for dark matter production, and limits are placed, in both scalar and pseudoscalar mediator scenarios, on the production cross section for a range of mediator masses, assuming $m_\chi = 1$ GeV.

9.1 Future Outlook

While the null results reported by the searches for BSM physics may seem disheartening, especially considering the expectation that signs of BSM physics would be seen within days of the start of Run 1, there are still signs hinting towards BSM physics. The continued data-taking by ATLAS and CMS during the remainder of Run 2 and beyond, will provide further opportunities to investigate BSM physics using complementary methods.

Primarily, the increased luminosity allows for improvements to be made to the pre-existing analyses. Additional luminosity will allow for tighter selections when targeting signal scenarios, along with better modelling of the SM background processes. Investigating more complex models, many of which are currently uncovered, may provide hints of BSM physics which may have been missed with the simplified model scenarios currently investigated.

In addition to searches providing hints at BSM physics, the measurements of SM processes will be expected to reach an unprecedented precision. For example if the W-boson mass can be determined to a precision of 4 MeV, then the contributions from a variety of BSM physics models should be visible [149].

As the newest particle to be discovered, the Higgs boson also provides a tool to investigate BSM physics. Measurements of the Higgs couplings and branching ratios may provide the first concrete suggestions of BSM physics. The Higgs boson should also be used as a tool to discover new physics, considering models where a SM-like Higgs boson arises in the decay chains of new particles. The author is already actively working on searches for bottom squarks decaying via the second lightest neutralino, $\tilde{b} \to b + \tilde{\chi}_2^0$. In these models the second lightest neutralino subsequently decays via $\tilde{\chi}_2^0 \to h + \tilde{\chi}_1^0$. A variety of mass scenarios are considered for the mass splitting between the gauginos.

The search for new physics at the LHC has just commenced and inputs from non-collider experiments both currently collecting data and beginnning to do so in the near future (such as dark matter direct detection experiments, and the g-2 experiment at Fermilab) will also provide complementary information that might give further guidance to physicists in the search for the unknown.

Appendix A

Trigger selections and efficiencies

As introduced in Section 3.7, triggers are used to select interesting events depending upon the existence of leptons, jets and large $E_{\mathrm{T}}^{\mathrm{miss}}$ in the event. The efficiency of a given trigger is the number of accepted events collected by the trigger, relative to the total number of events produced that could be recorded by the trigger. Trigger efficiencies are calculated using data collected using a different trigger, to give the total number of events that could be recorded.

For example the efficiency of a single electron trigger is calculated using Equation A.1, where ϵ is the trigger efficiency, $N_{\mathrm{Collected}}$ is the total number of single electron events collected by the trigger, and N_{Total} is the total number of events with a single electron that could have been collected.

$$\epsilon = \frac{N_{\mathrm{Collected}}}{N_{\mathrm{Total}}} \tag{A.1}$$

When developing an analysis the efficiency of the triggers used needs to be taken into account when designing control, validation and signal regions. In the sbottom analysis (as described in Chapter 6) a $E_{\mathrm{T}}^{\mathrm{miss}}$ trigger is used to target the signal models under consideration. Figure A.1 presents the efficiency of the $E_{\mathrm{T}}^{\mathrm{miss}}$ trigger as a function of the $E_{\mathrm{T}}^{\mathrm{miss}}$ present in the event. As seen in the figure, the efficiency of the trigger is 100% when the $E_{\mathrm{T}}^{\mathrm{miss}}$ in the event is $\geq 250\,\mathrm{GeV}$. This motivates the $E_{\mathrm{T}}^{\mathrm{miss}}$ selection used when defining the sbottom SRs, ensuring the trigger is fully efficient.

The sbottom analysis, the tb+$E_{\mathrm{T}}^{\mathrm{miss}}$ analysis (as presented in Chapter 7) and the dark matter analysis (Chapter 8) use regions which require either one, or two leptons. For either 1-lepton selection or the 2-lepton selections defined in the analyses, single lepton triggers are used. The lepton p_{T} requirements in the analyses are driven by the

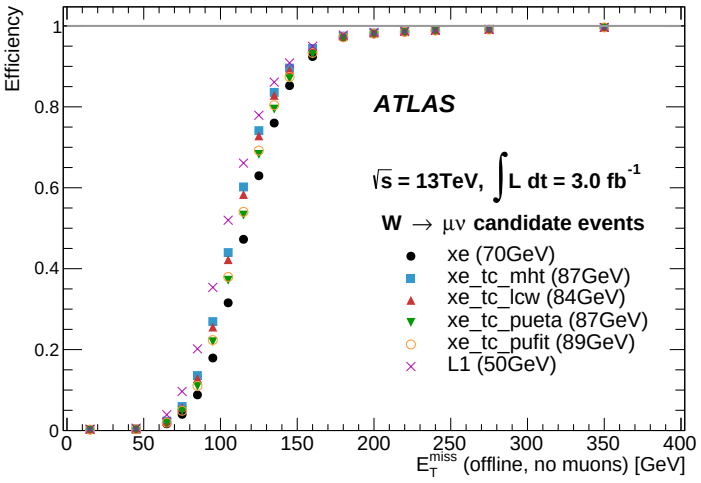

FIGURE A.1: Efficiency of the $E_{\mathrm{T}}^{\mathrm{miss}}$ trigger as a function of the $E_{\mathrm{T}}^{\mathrm{miss}}$ present in the event. Taken from [134].

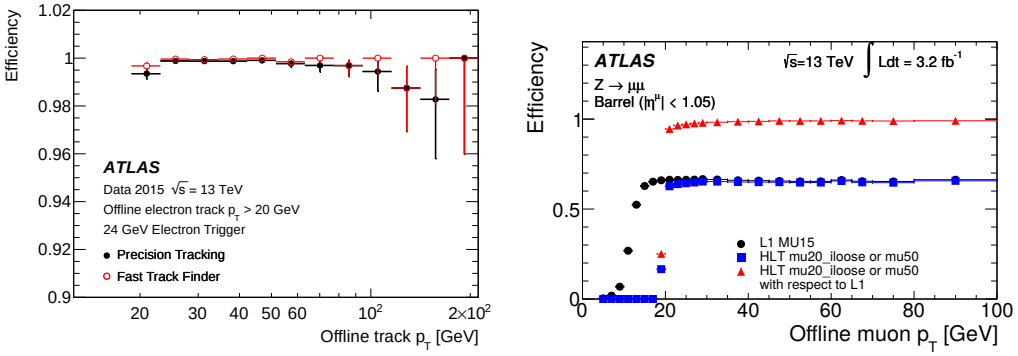

(a) Single electron trigger

(b) Single muon trigger

FIGURE A.2: Single lepton trigger efficiencies as a function of the lepton p_{T}. Taken from [134].

trigger efficiency to ensure the trigger is fully efficient. The electron and muon trigger efficiencies, as a function of the lepton p_{T} are shown in Figure A.2.

When defining the SR for the dark matter analysis it is found that a selection of $E_{\mathrm{T}}^{\mathrm{miss}}$ $> 250\,\mathrm{GeV}$, ensuring that the $E_{\mathrm{T}}^{\mathrm{miss}}$ trigger is fully efficient, removes a large amount of signal events. Due to the relationship between the $E_{\mathrm{T}}^{\mathrm{miss}}$ and the p_{T} of the leading jet in the signal a 2D selection on these two variables, to investigate if the $E_{\mathrm{T}}^{\mathrm{miss}}$ threshold could be lowered whilst still being in the region where the $E_{\mathrm{T}}^{\mathrm{miss}}$ filter is fully efficient.

Figure A.3 presents the efficiency of the $E_{\mathrm{T}}^{\mathrm{miss}}$ trigger as a function of the $E_{\mathrm{T}}^{\mathrm{miss}}$ and leading jet p_{T} for both data and MC. The black curve shows the hyperbolic selection as defined in Equation 8.1. It is seen that this selection allows the $E_{\mathrm{T}}^{\mathrm{miss}}$ selection to be loosened to $> 150\,\mathrm{GeV}$ (with respect to the $> 250\,\mathrm{GeV}$ required if applying a 1D

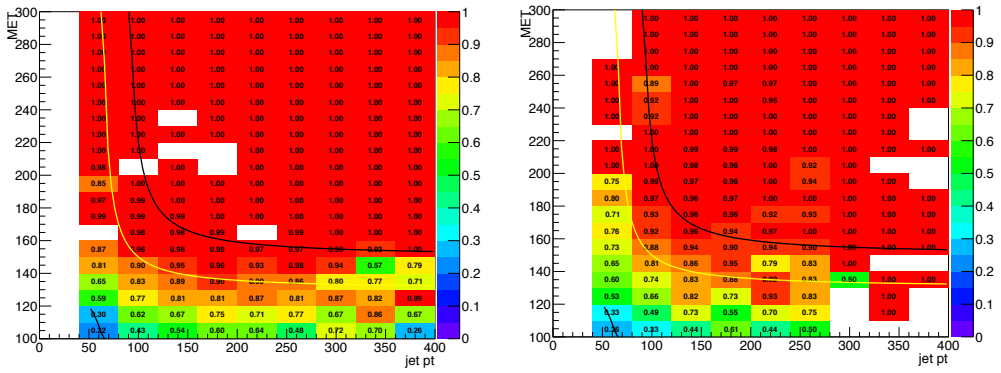

(a) Efficiencies calculated using $Z \to \nu\nu$ MC events (b) Single muon trigger

FIGURE A.3: 2-dimensional hyperbolic trigger efficiency as a function of the $E_{\mathrm{T}}^{\mathrm{miss}}$ and leading jet p_{T}.

selection as in Figure A.1) and still remaining fully efficient ($\epsilon > 0.95\%$).

The photon-replacement method used in the sbottom analysis uses a single photon trigger referred to as HLT_g120_loose which is found to be fully efficient with a selection of photon $p_{\mathrm{T}} \geq 130\,\mathrm{GeV}$, as seen in Figure A.4.

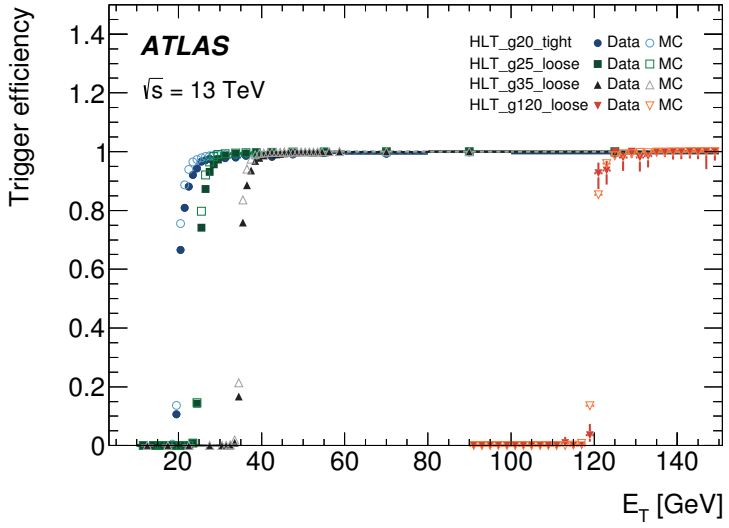

FIGURE A.4: Efficiency of the single photon trigger as a function of the photon p_{T}. The photon trigger used in the analysis is the HLT_g120_loose (orange curve), which is fully efficient at a photon $p_{\mathrm{T}} \geq 130\,\mathrm{GeV}$. Taken from [134].

Appendix B

Truth-level object definitions

When performing certain studies relevant for the analyses presented within this thesis, truth-level samples are used. These samples do not take into account any detector effects and are primarily used to calculate the modelling uncertainties. When using truth-level objects a series of selections are employed to attempt to reproduce the fiducial selections used for the analyses.

In addition to the selections used in Table B.1, all objects are required to be associated with the hard process, this removes bremstrahlung photons, muons from heavy flavour decays etc. An overlap removal corresponding to the Run 1 overlap removal introduced in Chapter 5 is also used. Finally the missing transverse momentum $E_{\mathrm{T}}^{\mathrm{miss}}$ is calculated using the vector sum of all non-interacting particles in the event.

Object	Baseline p_{T} requirement	Baseline $\lvert\eta\rvert$ requirement
Electron	$> 10\,\mathrm{GeV}$	< 2.4
Muon	$> 10\,\mathrm{GeV}$	< 2.4
Photon	$> 35\,\mathrm{GeV}$	< 2.37
Jets	$> 20\,\mathrm{GeV}$	< 2.8
$b-$jets	$> 20\,\mathrm{GeV}$	< 2.5

TABLE B.1: Overview of the truth-level object definitions.

The jets considered are anti-k_t truth jets with a jet radius $R = 0.4$, and the $b-$jets are identified by looping over the jets and checking the truth-label of the jet. To introduce a facsimile of the $b-$tagging algorithms used when considering detector effects, the $|\eta|$ requirement is tightened and a probability is assigned to the jet corresponding to the likelihood to tag (or mis-tag) the jet as a $b-$jet depending on the $b-$tagging efficiency of the algorithm that is being imitated. The mis-tag rate is also flavour dependent.

Appendix C

$t\bar{t}$ modelling uncertainties

During the calculation of the $t\bar{t}$ generator and parton shower uncertainties for the sbottom 2016 analysis (Chapter 6) and $tb+E_{\mathrm{T}}^{\mathrm{miss}}$ Run 2 analysis, it was found that there was lack of statistics for the alternative samples when considering the full analysis selections. A significant number of selections were loosened to produce a sensible estimate for the $t\bar{t}$ uncertainties.

To provide confidence in the estimate provided by the recommended method, an alternative comparison is made with a Sherpa $t\bar{t}$ sample. The Sherpa sample also suffers from a lack of statistics when tight selections of m_{eff} and m_{CT} are used, so instead a preselection level extrapolation is performed comparing the nominal Powheg sample to the Sherpa sample.

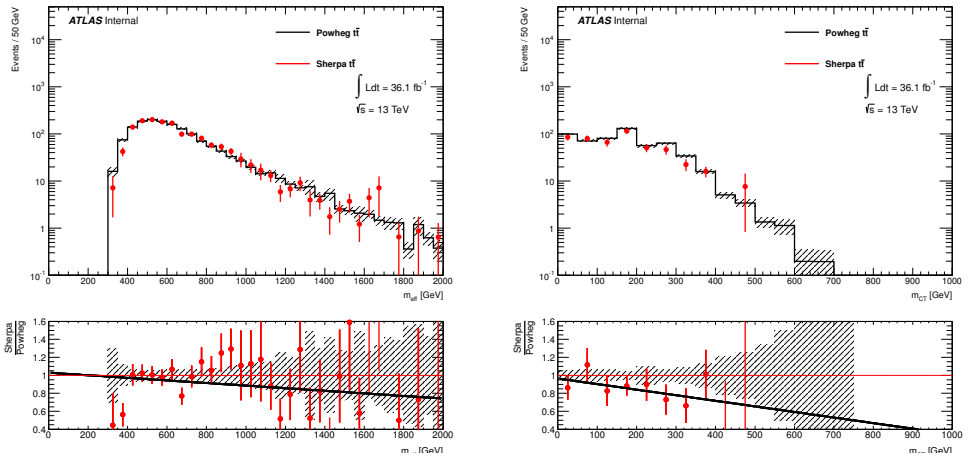

(a) $tb + E_{\mathrm{T}}^{\mathrm{miss}}$ Preselection, m_{eff}

(b) $bb + E_{\mathrm{T}}^{\mathrm{miss}}$ Preselelction, m_{CT}

FIGURE C.1: Comparisons between the nominal Powheg and the alternative Sherpa $t\bar{t}$ samples. The extrapolated line of best fit provides confidence in the nominal method for evaluating the $t\bar{t}$ modelling uncertainties.

Figure C.1 presents (left) the m_{eff} distribution using the $tb + E_{\text{T}}^{\text{miss}}$ preselection and (right) the m_{CT} distribution using the $bb + E_{\text{T}}^{\text{miss}}$ preselection. The line of best fit shown on the ratio plot for these comparisons is used to provide confidence in the nominal value calculated for the $t\bar{t}$ uncertainties, as ratio of the Sherpa sample to the nominal Powheg sample leads to a relatively similar uncertainty as calculated from the nominal method.

Further to this, both a Kolmogorov-Smirnov (KS) Test and a χ^2 test are performed on the two distributions to investigate the compatibility of the Powheg and Sherpa samples. For the $tb + E_{\text{T}}^{\text{miss}}$ distribution the result of the KS test is a probability of compatibility of 56% and a χ^2/NDF of 1.9. For the $bb + E_{\text{T}}^{\text{miss}}$ m_{CT} distribution the result of the KS is a probability of compatibility of 60%, with a χ^2/NDF of 1.5. The results of these tests suggest that a comparison between the Sherpa and Powheg samples, to calculate the $t\bar{t}$ modelling uncertainty, is well motivated.

Bibliography

[1] ATLAS Collaboration. Search for bottom squark pair production in proton–proton collisions at $\sqrt{s} = 13$ TeV with the ATLAS detector. *Eur. Phys. J. C*, 76:547, 2016.

[2] ATLAS Collaboration. ATLAS Run 1 searches for direct pair production of third-generation squarks at the Large Hadron Collider. *Eur. Phys. J. C*, 75:510, 2015.

[3] ATLAS Collaboration. Search for Dark Matter production associated with bottom quarks in 13.3 $\text{fb}^{-1}$of pp collisions at $\sqrt{s} = 13$ TeV with the ATLAS detector at the LHC. ATLAS-CONF-2016-086, 2016.

[4] ATLAS Collaboration. Monte Carlo Generators for the Production of a W or Z/γ^* Boson in Association with Jets at ATLAS in Run 2. ATL-PHYS-PUB-2016-003, 2016.

[5] C. Patrignani et al. Review of Particle Physics. *Chin. Phys.*, C40(10):100001, 2016.

[6] Michael E. Peskin and Daniel V. Schroeder. *An Introduction to quantum field theory*. Addison-Wesley, 1995.

[7] Chen-Ning Yang and Robert L. Mills. Conservation of Isotopic Spin and Isotopic Gauge Invariance. *Phys. Rev.*, 96:191–195, 1954.

[8] S. L. Glashow. Partial Symmetries of Weak Interactions. *Nucl. Phys.*, 22:579–588, 1961.

[9] Steven Weinberg. A Model of Leptons. *Phys. Rev. Lett.*, 19:1264–1266, 1967.

[10] Abdus Salam. Gauge Unification of Fundamental Forces. *Rev. Mod. Phys.*, 52:525–538, 1980. [Science210,723(1980)].

[11] Peter W. Higgs. Broken Symmetries and the Masses of Gauge Bosons. *Phys. Rev. Lett.*, 13:508–509, 1964.

[12] Peter W. Higgs. Broken symmetries, massless particles and gauge fields. *Phys. Lett.*, 12:132–133, 1964.

[13] F. Englert and R. Brout. Broken Symmetry and the Mass of Gauge Vector Mesons. *Phys. Rev. Lett.*, 13:321–323, 1964.

[14] John Ellis, Mary K. Gaillard, and Dimitri V. Nanopoulos. A Historical Profile of the Higgs Boson. pages 255–274, 2016.

[15] ATLAS Collaboration. Standard Model Production Cross Section Measurements. 2016. `http://atlas.web.cern.ch/Atlas/GROUPS/PHYSICS/CombinedSummaryPlots/SM/`.

[16] ATLAS Collaboration. Observation of a new particle in the search for the Standard Model Higgs boson with the ATLAS detector at the LHC. *Phys. Lett. B*, 716:1, 2012.

[17] CMS Collaboration. Observation of a new boson at a mass of 125 GeV with the CMS experiment at the LHC. *Phys. Lett.*, B716:30–61, 2012.

[18] ATLAS Collaboration. Evidence for the spin-0 nature of the Higgs boson using ATLAS data. *Phys. Lett. B*, 726:120, 2013.

[19] ATLAS and CMS Collaborations. Measurements of the Higgs boson production and decay rates and constraints on its couplings from a combined ATLAS and CMS analysis of the LHC pp collision data at $\sqrt{s} = 7$ and 8 TeV. *JHEP*, 08:045, 2016.

[20] Steven Weinberg. Implications of Dynamical Symmetry Breaking. *Phys. Rev.*, D13:974–996, 1976.

[21] Steven Weinberg. Implications of Dynamical Symmetry Breaking: An Addendum. *Phys. Rev.*, D19:1277–1280, 1979.

[22] Leonard Susskind. Dynamics of Spontaneous Symmetry Breaking in the Weinberg-Salam Theory. *Phys. Rev.*, D20:2619–2625, 1979.

[23] Eldad Gildener. Gauge Symmetry Hierarchies. *Phys. Rev.*, D14:1667, 1976.

[24] Katherine Garrett and Gintaras Duda. Dark Matter: A Primer. *Adv. Astron.*, 2011:968283, 2011.

[25] G. W. Bennett et al. Final Report of the Muon E821 Anomalous Magnetic Moment Measurement at BNL. *Phys. Rev.*, D73:072003, 2006.

[26] J. Grange et al. Muon (g-2) Technical Design Report. 2015.

[27] H. Miyazawa. Baryon Number Changing Currents. *Prog. Theor. Phys.*, 36(6):1266–1276, 1966.

[28] Pierre Ramond. Dual Theory for Free Fermions. *Phys. Rev.*, D3:2415–2418, 1971.

[29] A. Neveu and J. H. Schwarz. Factorizable dual model of pions. *Nucl. Phys.*, B31:86–112, 1971.

[30] A. Neveu and J. H. Schwarz. Quark Model of Dual Pions. *Phys. Rev.*, D4:1109–1111, 1971.

[31] D. V. Volkov and V. P. Akulov. Is the Neutrino a Goldstone Particle? *Phys. Lett.*, 46B:109–110, 1973.

[32] J. Wess and B. Zumino. A Lagrangian Model Invariant Under Supergauge Transformations. *Phys. Lett.*, 49B:52, 1974.

[33] J. Wess and B. Zumino. Supergauge Transformations in Four-Dimensions. *Nucl. Phys.*, B70:39–50, 1974.

[34] Pierre Fayet. Supersymmetry and Weak, Electromagnetic and Strong Interactions. *Phys. Lett.*, B64:159, 1976.

[35] Stephen P. Martin. A Supersymmetry primer. 1997. [Adv. Ser. Direct. High Energy Phys.18,1(1998)].

[36] Sidney R. Coleman and J. Mandula. All Possible Symmetries of the S Matrix. *Phys. Rev.*, 159:1251–1256, 1967.

[37] Michele Papucci, Joshua T. Ruderman, and Andreas Weiler. Natural SUSY Endures. *JHEP*, 09:035, 2012.

[38] Q. R. Ahmad et al. Direct evidence for neutrino flavor transformation from neutral current interactions in the Sudbury Neutrino Observatory. *Phys. Rev. Lett.*, 89:011301, 2002.

[39] A. Djouadi et al. The Minimal supersymmetric standard model: Group summary report. 1998.

[40] A. Arbey, M. Battaglia, A. Djouadi, and F. Mahmoudi. The Higgs sector of the phenomenological MSSM in the light of the Higgs boson discovery. *JHEP*, 09:107, 2012.

[41] Tim Gershon. Implications of LHCb measurements and future prospects. 2012.

[42] A. Arbey, M. Battaglia, F. Mahmoudi, and D. Martínez Santos. Supersymmetry confronts $B_s\mu^+\mu^-$: Present and future status. *Phys. Rev.*, D87(3):035026, 2013.

[43] C. L. Bennett et al. Nine-Year Wilkinson Microwave Anisotropy Probe (WMAP) Observations: Final Maps and Results. *Astrophys. J. Suppl.*, 208:20, 2013.

[44] Maria Beltran, Dan Hooper, Edward W. Kolb, Zosia A. C. Krusberg, and Tim M. P. Tait. Maverick dark matter at colliders. *JHEP*, 09:037, 2010.

[45] Patrick J. Fox, Roni Harnik, Joachim Kopp, and Yuhsin Tsai. Missing Energy Signatures of Dark Matter at the LHC. *Phys. Rev.*, D85:056011, 2012.

[46] Jessica Goodman, Masahiro Ibe, Arvind Rajaraman, William Shepherd, Tim M. P. Tait, and Hai-Bo Yu. Constraints on Dark Matter from Colliders. *Phys. Rev.*, D82:116010, 2010.

[47] Marco Laffranchi and Andre Rubbia. The ArDM project: A Liquid Argon TPC for Dark Matter Detection. 2007. [J. Phys. Conf. Ser.65,012014(2007)].

[48] Daniel Abercrombie et al. Dark Matter Benchmark Models for Early LHC Run-2 Searches: Report of the ATLAS/CMS Dark Matter Forum. 2015.

[49] Matthew R. Buckley, David Feld, and Dorival Goncalves. Scalar Simplified Models for Dark Matter. *Phys. Rev.*, D91:015017, 2015.

[50] G. Bachy, A. Hofmann, S. Myers, E. Picasso, and G. Plass. The LEP collider. *Part. Accel.*, 26:19–32, 1990.

[51] M. Benedikt, P. Collier, V. Mertens, J. Poole, and K. Schindl. LHC Design Report. 3. The LHC injector chain. 2004.

[52] Christiane Lefvre. The CERN accelerator complex. Complexe des accélérateurs du CERN. Dec 2008.

[53] Oliver S. Bruning, P. Collier, P. Lebrun, S. Myers, R. Ostojic, J. Poole, and P. Proudlock. LHC Design Report Vol.1: The LHC Main Ring. 2004.

[54] ATLAS Collaboration. Luminosity Determination Using the ATLAS Detector. ATLAS-CONF-2010-060, 2010.

[55] ATLAS Collaboration. The ATLAS Experiment at the CERN Large Hadron Collider. *JINST*, 3, 2008.

[56] ATLAS Collaboration. The ATLAS Inner Detector commissioning and calibration. *Eur. Phys. J.*, C70:787–821, 2010.

[57] S. Hassani, L. Chevalier, E. Lancon, J. F. Laporte, R. Nicolaidou, and A. Ouraou. A muon identification and combined reconstruction procedure for the ATLAS detector at the LHC using the (MUONBOY, STACO, MuTag) reconstruction packages. *Nucl. Instrum. Meth.*, A572:77–79, 2007.

[58] M Capeans et al. ATLAS Insertable B-Layer Technical Design Report. *CERN-LHCC-2010-013*, ATLAS-TDR-19, 2010.

[59] Giulia Ripellino. The alignment of the ATLAS Inner Detector in Run-2. *PoS*, LHCP2016:196, 2016.

[60] A Miucci. The ATLAS Insertable B-Layer Project. *IOP Journal of Instrumentation*, Volume 9, 2014.

[61] ATLAS Collaboration. Delivered Luminosity versus time for 2011-2016 (p-p data only) . 2016. `https://twiki.cern.ch/twiki/bin/view/AtlasPublic/LuminosityPublicResultsRun2/`.

[62] J. Stelzer. The ATLAS high level trigger configuration and steering: Experience with the first 7-TeV collision data. *J. Phys. Conf. Ser.*, 331:022026, 2011.

[63] G. Dissertori, I. G. Knowles, and M. Schmelling. High energy experiments and theory. *Oxford, UK: Clarendon (2003) 538 p*, 2003.

[64] H. Abramowicz et al. Combination of measurements of inclusive deep inelastic $e^{\pm}p$ scattering cross sections and QCD analysis of HERA data. *Eur. Phys. J.*, C75(12):580, 2015.

[65] H. Abramowicz and A. C. Caldwell. HERA collider physics. *Reviews of Modern Physics*, 71:1275–1409, October 1999.

[66] L. A. Harland-Lang, A. D. Martin, P. Motylinski, and R. S. Thorne. Parton distributions in the LHC era: MMHT 2014 PDFs. *Eur. Phys. J.*, C75(5):204, 2015.

[67] R. Devenish and A. Cooper-Sarkar. *Deep Inelastic Scattering*. Oxford University Press, 2004.

[68] Michiel Botje et al. The PDF4LHC Working Group Interim Recommendations. 2011.

[69] Andy Buckley et al. General-purpose event generators for LHC physics. *Phys. Rept.*, 504:145–233, 2011.

[70] John C. Collins. Sudakov form-factors. *Adv. Ser. Direct. High Energy Phys.*, 5:573–614, 1989.

[71] R. Keith Ellis, W. James Stirling, and B. R. Webber. QCD and collider physics. *Camb. Monogr. Part. Phys. Nucl. Phys. Cosmol.*, 8:1–435, 1996.

[72] Torbjorn Sjöstrand, Stephen Mrenna, and Peter Z. Skands. PYTHIA 6.4 Physics and Manual. *JHEP*, 05:026, 2006.

[73] M. Bahr et al. Herwig++ Physics and Manual. *Eur. Phys. J. C*, 58:639, 2008.

[74] Bo Andersson, G. Gustafson, G. Ingelman, and T. Sjostrand. Parton Fragmentation and String Dynamics. *Phys. Rept.*, 97:31–145, 1983.

[75] Jan-Christopher Winter, Frank Krauss, and Gerhard Soff. A Modified cluster hadronization model. *Eur. Phys. J.*, C36:381–395, 2004.

[76] T. Pierog, Iu. Karpenko, J. M. Katzy, E. Yatsenko, and K. Werner. EPOS LHC: Test of collective hadronization with data measured at the CERN Large Hadron Collider. *Phys. Rev.*, C92(3):034906, 2015.

[77] T. Gleisberg et al. Event generation with SHERPA 1.1. *JHEP*, 02:007, 2009.

[78] Tanju Gleisberg and Stefan Höche. Comix, a new matrix element generator. *JHEP*, 0812:039, 2008.

[79] Fabio Cascioli, Philipp Maierhofer, and Stefano Pozzorini. Scattering Amplitudes with Open Loops. *Phys. Rev. Lett.*, 108:111601, 2012.

[80] Steffen Schumann and Frank Krauss. A Parton shower algorithm based on Catani-Seymour dipole factorisation. *JHEP*, 0803:038, 2008.

[81] Stefan Höche, Frank Krauss, Marek Schönherr, and Frank Siegert. QCD matrix elements + parton showers: The NLO case. *JHEP*, 04:027, 2013.

[82] Marco Guzzi, Pavel Nadolsky, Edmond Berger, Hung-Liang Lai, Fredrick Olness, and C. P. Yuan. CT10 parton distributions and other developments in the global QCD analysis. 2011.

[83] Richard D. Ball et al. Parton distributions with LHC data. *Nucl. Phys. B*, 867:244, 2013.

[84] Paolo Nason. A new method for combining NLO QCD with shower Monte Carlo algorithms. *JHEP*, 11:040, 2004.

[85] Stefano Frixione, Paolo Nason, and Carlo Oleari. Matching NLO QCD computations with Parton Shower simulations: the POWHEG method. *JHEP*, 11:070, 2007.

[86] Simone Alioli, Paolo Nason, Carlo Oleari, and Emanuele Re. A general framework for implementing NLO calculations in shower Monte Carlo programs: the POWHEG BOX. *JHEP*, 06:043, 2010.

[87] Johan Alwall, Michel Herquet, Fabio Maltoni, Olivier Mattelaer, and Tim Stelzer. MadGraph 5 : Going Beyond. *JHEP*, 06:128, 2011.

[88] J. Alwall, R. Frederix, S. Frixione, V. Hirschi, F. Maltoni, et al. The automated computation of tree-level and next-to-leading order differential cross sections, and their matching to parton shower simulations. *JHEP*, 07:079, 2014.

[89] Torbjorn Sjöstrand, Stephen Mrenna, and Peter Z. Skands. A Brief Introduction to PYTHIA 8.1. *Comput. Phys. Commun.*, 178:852, 2008.

[90] J. Pumplin et al. New generation of parton distributions with uncertainties from global QCD analysis. *JHEP*, 07:012, 2002.

[91] F. Cascioli, S. Kallweit, P. Maierhfer, and S. Pozzorini. A unified NLO description of top-pair and associated Wt production. *Eur. Phys. J.*, C74(3):2783, 2014.

[92] Stefano Frixione, Eric Laenen, Patrick Motylinski, Bryan R. Webber, and Chris D. White. Single-top hadroproduction in association with a W boson. *JHEP*, 07:029, 2008.

[93] Rikkert Frederix. Top Quark Induced Backgrounds to Higgs Production in the $WW^{(*)} \to ll\nu\nu$ Decay Channel at Next-to-Leading-Order in QCD. *Phys. Rev. Lett.*, 112(8):082002, 2014.

[94] Matteo Cacciari, Gavin P. Salam, and Gregory Soyez. The anti-k_t jet clustering algorithm. *JHEP*, 04:063, 2008.

[95] Oxford University. ATLAS Detector layers overview, 2016. `http://collider.physics.ox.ac.uk/img/layers.png`.

[96] ATLAS Collaboration. Electron efficiency measurements with the ATLAS detector using 2012 LHC proton–proton collision data. *Eur. Phys. J. C*, 77:195, 2017.

[97] ATLAS Collaboration. Muon reconstruction efficiency and momentum resolution of the ATLAS experiment in proton–proton collisions at $\sqrt{s} = 7$ TeV in 2010. *Eur. Phys. J. C*, 74:3034, 2014.

[98] ATLAS Collaboration. Measurement of the photon identification efficiencies with the ATLAS detector using LHC Run-1 data. 2016.

[99] ATLAS Collaboration. Electron reconstruction and identification efficiency measurements with the ATLAS detector using the 2011 LHC proton–proton collision data. *Eur. Phys. J. C*, 74:2941, 2014.

[100] ATLAS Collaboration. Electron efficiency measurements with the ATLAS detector using the 2012 LHC proton–proton collision data. ATLAS-CONF-2014-032, 2014.

[101] ATLAS Collaboration. Electron identification measurements in ATLAS using $\sqrt{s} = 13$ TeV data with 50 ns bunch spacing. ATL-PHYS-PUB-2015-041, 2015.

[102] ATLAS Collaboration. Muon reconstruction performance in early $\sqrt{s} = 13$ TeV data. ATL-PHYS-PUB-2015-037, 2015.

[103] ATLAS Collaboration. Measurement of the muon reconstruction performance of the ATLAS detector using 2011 and 2012 LHC proton–proton collision data. *Eur. Phys. J. C*, 74:3130, 2014.

[104] ATLAS Collaboration. Non-collision backgrounds as measured by the ATLAS detector during the 2010 proton–proton run. ATLAS-CONF-2011-137, 2011.

[105] ATLAS Collaboration. Muon reconstruction performance of the ATLAS detector in proton–proton collision data at $\sqrt{s} = 13$ TeV. *Eur. Phys. J. C*, 76:292, 2016.

[106] ATLAS Collaboration. Performance of pile-up mitigation techniques for jets in pp collisions at $\sqrt{s} = 8$ TeV using the ATLAS detector. *Eur. Phys. J. C*, 76:581, 2016.

[107] D W Miller, A Schwartzman, and D Su. Jet-Vertex Association Algorithm. (ATL-COM-PHYS-2008-008), Jan 2008.

[108] ATLAS Collaboration. Topological cell clustering in the ATLAS calorimeters and its performance in LHC Run 1. 2016.

[109] ATLAS Collaboration. Jet energy measurement and its systematic uncertainty in proton–proton collisions at $\sqrt{s} = 7$ TeV with the ATLAS detector. *Eur. Phys. J. C*, 75:17, 2015.

[110] ATLAS Collaboration. Jet energy scale measurements and their systematic uncertainties in proton-proton collisions at $\sqrt{s} = 13$ TeV with the ATLAS detector. 2017.

[111] ATLAS Collaboration. Tagging and suppression of pileup jets with the ATLAS detector. ATLAS-CONF-2014-018, 2014.

[112] ATLAS Collaboration. Performance of the ATLAS Secondary Vertex b-tagging Algorithm in 900 GeV Collision Data. ATLAS-CONF-2010-004, 2010.

[113] ATLAS Collaboration. Calibration of b-tagging using dileptonic top pair events in a combinatorial likelihood approach with the ATLAS experiment. ATLAS-CONF-2014-004, 2014.

[114] ATLAS Collaboration. Expected performance of the ATLAS b-tagging algorithms in Run-2. ATL-PHYS-PUB-2015-022, 2015.

[115] ATLAS Collaboration. Optimisation of the ATLAS b-tagging performance for the 2016 LHC Run. ATL-PHYS-PUB-2016-012, 2016.

[116] ATLAS Collaboration. Performance of b-Jet Identification in the ATLAS Experiment. *JINST*, 11:P04008, 2016.

[117] W Lampl, S Laplace, D Lelas, P Loch, H Ma, S Menke, S Rajagopalan, D Rousseau, S Snyder, and G Unal. Calorimeter Clustering Algorithms: Description and Performance. ATL-LARG-PUB-2008-002, 2008.

[118] ATLAS Collaboration. Expected photon performance in the ATLAS experiment. ATL-PHYS-PUB-2011-007, 2011.

[119] ATLAS Collaboration. Photon identification in 2015 ATLAS data. ATL-PHYS-PUB-2016-014, 2016.

[120] ATLAS Collaboration. Performance of missing transverse momentum reconstruction in proton–proton collisions at $\sqrt{s} = 7$ TeV with ATLAS. *Eur. Phys. J. C*, 72:1844, 2012.

[121] ATLAS Collaboration. Expected performance of missing transverse momentum reconstruction for the ATLAS detector at $\sqrt{s} = 13$ TeV. ATL-PHYS-PUB-2015-023, 2015.

[122] ATLAS Collaboration. Performance of missing transverse momentum reconstruction with the ATLAS detector in the first proton–proton collisions at $\sqrt{s} = 13$ TeV. ATL-PHYS-PUB-2015-027, 2015.

[123] ATLAS Collaboration. Data-Quality Requirements and Event Cleaning for Jets and Missing Transverse Energy Reconstruction with the ATLAS Detector in Proton–Proton Collisions at a Center-of-Mass Energy of $\sqrt{s} = 7$ TeV. ATLAS-CONF-2010-038, 2010.

[124] Partha Konar, Kyoungchul Kong, Konstantin T. Matchev, and Myeonghun Park. Dark Matter Particle Spectroscopy at the LHC: Generalizing M(T2) to Asymmetric Event Topologies. *JHEP*, 04:086, 2010.

[125] C. G. Lester and D. J. Summers. Measuring masses of semiinvisibly decaying particles pair produced at hadron colliders. *Phys. Lett.*, B463:99–103, 1999.

[126] Daniel R. Tovey. On measuring the masses of pair-produced semi-invisibly decaying particles at hadron colliders. *JHEP*, 04:034, 2008.

[127] ATLAS Collaboration. Search for direct third-generation squark pair production in final states with missing transverse momentum and two b-jets in $\sqrt{s} = 8\,\text{TeV}$ pp collisions with the ATLAS detector. *JHEP*, 1310, 2013.

[128] ATLAS Collaboration. Measurement of differential production cross-sections for a Z boson in association with b-jets in 7 TeV proton–proton collisions with the ATLAS detector. *JHEP*, 10:141, 2014.

[129] Reinhard Schwienhorst, on behalf of the ATLAS, CMS, and CDF. Top cross-sections and single top. *Int. J. Mod. Phys. Conf. Ser.*, 31:1460277, 2014.

[130] ATLAS Collaboration. Expected sensitivity studies for gluino and squark searches using the early LHC 13 TeV Run-2 dataset with the ATLAS experiment. ATL-PHYS-PUB-2015-005, 2015.

[131] S. van der Meer. Calibration of the Effective Beam Height in the ISR. CERN-ISR-PO-68-31, 1968.

[132] ATLAS Collaboration. Single hadron response measurement and calorimeter jet energy scale uncertainty with the ATLAS detector at the LHC. *Eur. Phys. J. C*, 73:2305, 2013.

[133] ATLAS Collaboration. A method for the construction of strongly reduced representations of ATLAS experimental uncertainties and the application thereof to the jet energy scale. ATL-PHYS-PUB-2015-014, 2015.

[134] ATLAS Collaboration. Jet energy measurement with the ATLAS detector in proton–proton collisions at $\sqrt{s} = 7$ TeV. *Eur. Phys. J. C*, 73:2304, 2013.

[135] ATLAS Collaboration. Jet energy resolution in proton–proton collisions at $\sqrt{s} =$ 7 TeV recorded in 2010 with the ATLAS detector. *Eur. Phys. J. C*, 73:2306, 2013.

[136] ATLAS Collaboration. Forward Jet Vertex Tagging: A new technique for the identification and rejection of forward pileup jets. ATL-PHYS-PUB-2015-034, 2015.

[137] ATLAS Collaboration. Measurement of the cross section for the production of a W boson in association with b-jets in pp collisions at $\sqrt{s} = 7$ TeV with the ATLAS detector. *Phys. Lett. B*, 707:418, 2012.

[138] M. Baak, G. J. Besjes, D. Côte, A. Koutsman, J. Lorenz, and D. Short. HistFitter software framework for statistical data analysis. *Eur. Phys. J.*, C75:153, 2015.

[139] ATLAS Collaboration. Search for top squark pair production in final states with one isolated lepton, jets, and missing transverse momentum in $\sqrt{s} = 8$ TeV pp collisions with the ATLAS detector. *JHEP*, 11:118, 2014.

[140] ATLAS Collaboration. Search for direct pair production of the top squark in all-hadronic final states in proton–proton collisions at $\sqrt{s} = 8$ TeV with the ATLAS detector. *JHEP*, 09:015, 2014.

[141] The DELPHI Collaboration. Searches for supersymmetric particles in e+e- collisions up to 208 GeV and interpretation of the results within the MSSM. *Eur. Phys. J. C*, 31:421,479, 2003.

[142] J.M. Butterworth, Jeffrey R. Forshaw, and M.H. Seymour. Multiparton interactions in photoproduction at HERA. *Z. Phys. C*, 72:637, 1996.

[143] B. P. Kersevan and E. Richter-Waş. The Monte Carlo event generator AcerMC versions 2.0 to 3.8 with interfaces to PYTHIA 6.4, HERWIG 6.5 and ARIADNE 4.1. *Computer Physics Communications*, 184:919–985, March 2013.

[144] D. S. Akerib et al. LUX-ZEPLIN (LZ) Conceptual Design Report. 2015.

[145] Michael Klasen, Martin Pohl, and Günter Sigl. Indirect and direct search for dark matter. *Prog. Part. Nucl. Phys.*, 85:1–32, 2015.

[146] Jan Conrad. Indirect Detection of WIMP Dark Matter: a compact review. In *Interplay between Particle and Astroparticle physics (IPA2014) London, United Kingdom, August 18-22, 2014*, 2014.

[147] Teresa Marrodán Undagoitia and Ludwig Rauch. Dark matter direct-detection experiments. *J. Phys.*, G43(1):013001, 2016.

[148] ATLAS Collaboration. Measurement of top quark pair differential cross sections in the dilepton channel in pp collisions at $\sqrt{s} = 7$ and 8 TeV with ATLAS. *Phys. Rev. D*, 94:092003, 2016.

[149] D. de Florian et al. Handbook of LHC Higgs Cross Sections: 4. Deciphering the Nature of the Higgs Sector. 2016.